2015

Development of advanced materials for rechargeable lithium-ion batteries

Zhijia Zhang
University of Wollongong

UNIVERSITY OF WOLLONGONG

Development of Advanced Materials for Rechargeable Lithium-Ion Batteries

This thesis is presented as part of the requirements for the

Award of the Degree of

Doctor of Philosophy

from the

University of Wollongong

by

Zhijia Zhang, B. Eng., M. Eng.

Institute for Superconducting and Electronic Materials (ISEM)

Faculty of Engineering

January 2015

Dedication

To my parents, brother, and Yingguang, who have always been there when I needed them.

Acknowledgements

I would like to express my utmost gratitude to my supervisors, A/Prof. Jiazhao Wang, Prof. Huijun Li, and Dr Shulei Chou, for their encouragement, understanding, invaluable advice, and constructive expert supervision of my PhD career during my study at the University of Wollongong (UOW). I also wish to thank Prof. Huakun Liu for her supervision and guidance. Special Thanks to Dr. Tania Silver, who always critically read every manuscript during my PhD study.

I would also like to thank the UOW and China Scholarship Council (CSC) for my international postgraduate tuition award (IPTA) and scholarship support, respectively.

I am grateful to my collaborators, especially Prof. Kiyoshi Ozawa (NIMS), Dr. Qinfen Gu (Australian Synchrotron), Dr. Jingfa Li (Shandong University), and Dr Zidong Zhang (Shandong University), who provided important contributions to our joint publications during my PhD study.

Technical assistance from various people at UOW, such as Dr. Kosta Konstantinov (TGA, BET), Dr. Germanas Peleckis (XRD), Dr. Dongqi Shi (XPS), Dr. Darren Attard (FESEM), Dr. Tony Romeo (FESEM), and Dr. Gilberto Casillas-Garcia (TEM), is also highly appreciated. I am also very eager to thank the University staff, especially at ISEM, especially Ms. Crystal Mahfouz *(*Administrative Assistant), Ms. Narelle Badger **(**Administrative Assistant), and Ms. Joanne George (Laboratory and Safety Operations Officer), who gave me a great deal of administrative and safety education assistance.

I also would like to thank my good friends during my PhD study at ISEM, who have contributed in different ways throughout my doctoral degree. I really hope that we can stay together to have great fun and build up our very strong friendship.

Many thanks to Dr. MD Mokhlesyr Rahman, Dr. Nurul Hayayi Idris, Dr. Lin Lu, Dr. Chao Zhong, Dr. Lukman Noerochim, Dr. Yi Shi, Dr. Xuanwen Gao, Dr. Jiantie Xu, Dr. Qi Li, Ms. Yunxiao Wang, Mr. Jun Wang, Ms. Xin Liang, Ms. Weijie Li, Mr. Wenbin Luo, Mr. Rejaul Kaiser, and Ms. Lanling Zhao, for their readiness to share their knowledge and valuable suggestions.

Finally, I would like to thank my parents and my brother for their love and support. My special thanks go to my wonderful wife, Mrs. Yingguang Liu, who is always there and has given me great support during my PhD study.

Table of Contents

Abstract

As well as being one of the most promising candidates for power sources in electric vehicles (EVs) and hybrid electric vehicles (HEVs), lithium-ion batteries (LIBs) have been widely used as power sources for portable electronic devices due to their high voltage, long cycle life, and operation at ambient temperature. Compared to portable electronic devices, large-scale energy storage systems, used for EVs or HEVs, require high power and high energy density, and need to be further improved by solving problems related to safety issues, high costs, and low rate capability. The electrode materials play a decisive role in the performance of LIBs. For enhancing the lithium diffusion coefficient and conductivity, preparing nanosized materials and surface modification are the most popular and highly effective methods to achieve improved electrochemical performance. In this doctoral work, several nanosized materials and conductive (electronic and ionic conductivity) composites have been synthesized, including $LiNbO_3$ coated $Li_{1.08}Mn_{1.92}O_4$ composite, $LiNbO_3/LiNi_{0.5}Mn_{1.5}O_4$ composite, polypyrrole-coated α-$LiFeO_2$ nanocomposite, V_2O_3/C composite, and three-dimensional (3D) TiO_2 nanotube/Ti mesh (TiO_2/Ti mesh). The high ionic conductivity $LiNbO_3$, and electronically conductive polypyrrole and amorphous carbon were also introduced into these electrode materials to form composites. Furthermore, the effects of the structure, morphology, and physical and chemical properties of these composites towards improvement of electrochemical performance have also been systematically investigated.

Cathode materials for LIBs

To study the influence of solid state electrolyte coating layers on the performance of cathode materials for lithium-ion batteries in combination with organic liquid electrolyte, $LiNbO_3$-coated $Li_{1.08}Mn_{1.92}O_4$ cathode materials were synthesized by using a facile solid-state reaction method. The $0.06LiNbO_3$-$0.97Li_{1.08}Mn_{1.92}O_4$ cathode exhibited an initial discharge capacity

of 125 mAh g^{-1}, retaining a capacity of 119 mAh g^{-1}, at 25 ^{o}C, while at 55 ^{o}C, it exhibited an initial discharge capacity of 130 mAh g^{-1}, retaining a capacity of 111 mAh g^{-1}, both at a current density of 0.5 C (where 1 C is 148 mAh g^{-1}). Very good rate capability has been demonstrated, with the $0.06LiNbO_3$-$0.97Li_{1.08}Mn_{1.92}O_4$ cathode showing more than 85% capacity at the rate of 50 C compared with the capacity at 0.5 C. The $0.06LiNbO_3$-$0.97Li_{1.08}Mn_{1.92}O_4$ cathode showed a high lithium diffusion coefficient (1.6×10^{-10} cm^2 s^{-1} at 55 ^{o}C), and low apparent activation energy (36.9 kJ mol^{-1}). The solid state electrolyte coating layer is effective for preventing Mn dissolution and maintaining the high ionic conductivity between the electrode and the organic liquid electrolyte.

Due to its high ionic conductivity, $LiNbO_3$ has been used as a novel additive for $LiNi_{0.5}Mn_{1.5}O_4$ cathode material. The *in-situ* synchrotron X-ray diffraction (SXRD) results confirmed that $LiNi_{0.5}Mn_{1.5}O_4$ crystal structure is highly reversible, and the $LiNbO_3$ additive phase structure remains stable throughout the charge-discharge process. The $0.04LiNbO_3/LiNi_{0.5}Mn_{1.5}O_4$ cathode delivers an initial discharge capacity of 125 mAh g^{-1} and retain a capacity of 117.9 mAh g^{-1} after 200 cycles, with capacity retention of 94 %, at 25 ^{o}C and a rate of 0.5 C (where 1 C = 147 mAh g^{-1}). Even at the high rate of 20C, the $0.04LiNbO_3/LiNi_{0.5}Mn_{1.5}O_4$ cathode exhibits more than 80 % of the capacity at 0.5 C. The $0.04LiNbO_3/LiNi_{0.5}Mn_{1.5}O_4$ cathode showed a high lithium diffusion coefficient (3.6×10^{-10} cm^2 s^{-1} at 25 ^{o}C). $LiNbO_3$ acts as bifunctional additive in LIBs with organic liquid electrolyte, which not only improves the lithium diffusion coefficient, but also protects the electrolyte from oxidative side reactions at high voltage.

A conducting α-$LiFeO_2$-polypyrrole (α-$LiFeO_2$-PPy) nanocomposite material was prepared by the chemical polymerization method as a cathode material for lithium-ion batteries. The porous α-$LiFeO_2$ was prepared via the microwave hydrothermal method and a post-annealing. The X-ray diffraction, Fourier transform infrared spectroscopy, and field emission

scanning electron microscopy measurements showed that the α-$LiFeO_2$ nanoparticles were coated with PPy. The polypyrrole coating improves the reversible capacity and cycling stability (104 mAh g^{-1} at 0.1 C after 100 cycles) for lithium-ion batteries. Even at the high rate of 10 C, the electrode showed more than 40% of the capacity at low rate (0.1 C). The PPy can prevent the formation of cracks in electrodes during the charge/discharge process. The conductive PPy serves as both a conducting matrix and a protective coating.

Anode materials for LIBs

V_2O_3/C composites were synthesized by the one-pot hydrothermal method in conjunction with an oxygen corrosive and carbon coating process. The resultant composite reveals a unique morphology in which porous V_2O_3 is coated by carbon. The porous structure could mitigate the stress/strain of Li^+ insertion/de-insertion, increase the surface area of the material, and reduce the effective diffusion distance for lithium ions, all of which would lead to improved capacity, rate capability, and cycling performance. It delivers more than two times the capacity of V_2O_3 and an impressive capacity of 283 mAh g^{-1} at the current density of 25 A g^{-1}. Furthermore, this carbon-coated nano-architecture ensures not only high electronic conductivity for both facile mass transfer and facile charge transfer, but also protection from the agglomeration of nanoparticles. As one of the first reported composites of V_2O_3/C, it has highly desirable properties: a high specific capacity, reduced resistance, and exceptionally good rate capability.

3D TiO_2 nanotube arrays grown on Ti mesh were prepared via the anodization process. The diameters of the Ti and TiO_2/Ti wires and the length of the TiO_2 nanotubes have linear relationships with the anodization processing time. When the anodization processing time was 600 min, the TiO_2/Ti mesh anode materials showed good capacity retention and high specific area capacity, without the need for a current collector or binder, due to their high

surface area, high substrate utilization, and large active material loading rate per unit area. At the current density of 50 μA cm^{-2}, TiO_2/Ti mesh with 600 min anodization processing time has a stable discharge platform at 1.78 V, and the specific area capacity is 1745.5 μAh cm^{-2} over 100 cycles. By tuning the geometric parameters of the TiO_2/Ti mesh and the anodization processing time, we can pave the way to finding TiO_2/Ti mesh electrodes for lithium-ion batteries with high capacity per unit area and outstanding mechanical behavior.

Nomenclature

List of Abbreviations

Abbreviation	Full name
3D	Three dimensional
a.u.	Arbitrary unit
BET	Brunauer Emmett Teller
CEI	cathode electrolyte interface
cm	Centimeter
CMC	Sodium carboxymethyl cellulose
CPE	Constant phase-angle element
CV	Cyclic voltammetry
DEC	Diethyl carbonate
DMC	Dimethyl carbonate
EC	Ethylene carbonate
EDS	Energy dispersive X-ray spectroscopy
EIS	Electrochemical impedance spectroscopy
EV	Electric vehicle
FESEM	Field emission scanning electron microscopy
FTIR	Fourier transform infrared Spectroscopy
JCPDS	Joint committee on powder diffraction standards
HEV	Hybrid electric vehicle
HRTEM	High-resolution transmission electron microscopy
LIB	Lithium-ion battery
LNMO	$LiNi_{0.5}Mn_{1.5}O_4$

Abbreviation	Full name
LNO	$LiNbO_3$
mm	Millimeter
nm	Nanometer
NMP	1-methyl-2-pyrrolidinone
PPy	Polypyrrole
*p*TS	*p*-toluenesulfonate
PVDF	Polyvinylidene fluoride
Py	Pyrrole
SAED	Selected area electron diffraction
SEI	Solid electrolyte interphase
SEM	Scanning electron microscopy
SXRD	Synchrotron X-ray diffraction
TEM	Transmission electron microscopy
TGA	Thermogravimetric analysis
XPS	X-ray photoelectron spectroscopy
XRD	X-ray diffraction

List of Symbols

Symbol	Name	Unit
2θ	Detection angle in XRD	Degree
C-rate	Charge or discharge rate	mA g^{-1}
E_a	Apparent activation energies	kJ mol^{-1}
f	Frequency in the EIS test	Hz

Symbol	Name	Unit
F	Faraday's constant = 96485	C
I	Current density	A cm^{-2}
i_0	Exchange currents	A
L	Crystal size	nm
m	Active material mass	g
N	Avogadro's number = 6.022×10^{-23}	mol^{-1}
P	Relative pressure	Pa
P_0	Saturation pressure	Pa
PD	Power density	W L^{-1}/ W kg^{-1}
Q	Specific capacity	mAh g^{-1}
Q_c	Specific charge capacity	mAh g^{-1}
Q_d	Specific discharge capacity	mAh g^{-1}
Q_{TSC}	Theoretical specific capacity	mAh g^{-1}
R	Gas constant = 8.319	J K^{-1} mol^{-1}
R_{ct}	Charge transfer resistance	Ω
S_{BET}	Specific BET surface area	m^2 g^{-1}
SE	Specific energy	Wh kg^{-1}
SP	Specific power	W kg^{-1}
T	Temperature	K or °C
t	Time	h or s
W	Warburg impedance	Ω
Z_{im}	Imaginary part of the impedance	Ω
Z_{re}	Real part of the impedance	Ω
σ	Ionic conductivity	S cm^{-1}

Symbol	Name	Unit
η	Coulombic efficiency	%
λ	X-ray wavelength	Å

List of Organizations

Abbreviation	Full name
AIIM	Australian Institute for Innovative Materials
CSC	China Scholarship Council
AS	Australian Synchrotron
EMC	Electron Microscopy Centre
ISEM	Institute for Superconducting and Electronic Materials
UOW	University of Wollongong

List of Figures

first cycle at 25 ^{o}C at current density of 0.5 C (1 C = 148 mAh g^{-1}); (b) rate performance and (c) capacity retention rate of xLiNbO$_3$-(1-x/2)Li$_{1.08}$Mn$_{1.92}$O$_4$ electrodes at different current densities from 0.5 C to 50 C at 25 ^{o}C. The rate capability in (c) is expressed as a relative specific discharge rate compared to that obtained at the low rate of 0.5 C.

Figure 4.10 *In situ* SXRD patterns of 0.06LiNbO$_3$-0.97Li$_{1.08}$Mn$_{1.92}$O$_4$ during the first cycle at 0.5C. (a) Selected individual diffraction patterns during the first cycle stacked against the charge/discharge curve. The main peaks of Li$_{1.08}$Mn$_{1.92}$O$_4$ correspond to the (b) (111), (d) (400), and (e) (511) reflections. These regions are highlighted in the bottom columns, and peaks corresponding to the Li$_{1.08}$Mn$_{1.92}$O$_4$ and λ-MnO$_2$ (Li$_{0.04}$Mn$_{0.96}$O$_2$) phases are marked by black dotted lines and purple dotted lines, respectively. For the LiNbO$_3$ phase, the main peak that corresponds to the (012) reflection is also highlighted in the bottom columns (c). LMO: Li$_{1.08}$Mn$_{1.92}$O$_4$; MO: Li$_{0.04}$Mn$_{0.96}$O$_2$ (λ-MnO$_2$); LNO: LiNbO$_3$.

Figure 4.11 *In situ* SXRD patterns of 0.06LiNbO$_3$-0.97Li$_{1.08}$Mn$_{1.92}$O$_4$ during the first cycle at 0.5 C. (a) Image plot of diffraction pattern reflections during the first cycle. The horizontal axis represents the selected 2θ region, and time is on the vertical axis. The diffraction intensity is color coded, with the scale bar shown on top. The corresponding charge/discharge curve is plotted to the right. (b) Selected individual diffraction patterns during the first cycle stacked against the charge/discharge curve. The main peaks correspond to the (111), (311), (222), (400), (331), and (440) reflections.

Figure 4.12 Phase transformation from Li$_{1.08}$Mn$_{1.92}$O$_4$ (blue) to Li$_{0.04}$Mn$_{0.96}$O$_2$ (λ-MnO$_2$, red) and the structural relations between Li$_{1.08}$Mn$_{1.92}$O$_4$ and Li$_{0.04}$Mn$_{0.96}$O$_2$ (λ-MnO$_2$) with the corresponding lattice parameter changes. The lattice parameter changes with charge/discharge time correspond to the selected individual diffraction patterns [Figure 5(b)]. The delithiation/lithiation proceeds at 0.5 C via the formation of a non-equilibrium solid solution

phase, $Li_{x+0.08}Mn_{1.92}O_4$ (intermediate pink color). When the charge/discharge process is finished, the particles have reached their equilibrium configuration corresponding to the $Li_{0.04}Mn_{0.96}O_2$ (λ-MnO_2) and $Li_{1.08}Mn_{1.92}O_4$ structures.

Figure 4.13 Structure of $LiNbO_3$ (space group *R3c*).

Figure 4.14 Cycling performance (a, b) and capacity retention rate (c, d) for xLiNbO$_3$-(1-x/2)$Li_{1.08}Mn_{1.92}O_4$ electrodes (x = 0, 0.03, 0.06, and 0.1) at current density of 0.5 C with a potential window of 4.5-3.2 V: (a) and (c) at 25 ^oC, (b) and (d) at 55 ^oC. The cycling retention rate is expressed as a relative specific discharge capacity compared to that obtained from the first cycle.

Figure 4.15 Nyquist plots of xLiNbO$_3$-(1-x/2)$Li_{1.08}Mn_{1.92}O_4$ (x = 0, 0.03, 0.06, and 0.1) electrodes after cycling over 5 cycles at a discharge potential of 4.0 V vs. Li/Li^+ at different temperatures and frequencies from 100 kHz to 10 mHz. The equivalent circuit is shown in the insets.

Figure 4.16 Real part of the complex impedance for the electrodes versus $\omega^{-1/2}$ at a series of temperatures at discharge potential of 4.0 V vs. Li/Li^+.

Figure 4.17 Electrochemical kinetics for xLiNbO$_3$-(1-x/2)$Li_{1.08}Mn_{1.92}O_4$ (x = 0, 0.03, 0.06, and 0.1) electrodes at a discharge potential of 4.0 V vs. Li/Li^+: (a) Arrhenius plots of lg i_0 versus 1/T. The lines are the linear fitting results; (b) lithium diffusion coefficients at different temperatures; (c) Lg D versus 1/T plots during lithium insertion, with the solid lines indicating the linear fitting results; (d) comparison of E_a and E_{aD} (activation energy based on the Arrhenius equation and on the lithium diffusion coefficient, respectively).

Figure 4.18 Images of electrodes collected after 100 cycles at 0.5 C and 25 ^oC: FESEM images of (a) 0.06LiNbO$_3$-0.97$Li_{1.08}Mn_{1.92}O_4$ sample and (b) pristine $Li_{1.08}Mn_{1.92}O_4$ sample.

Figure 5.9 Charge-discharge curves of *x*LNO/LNMO (*x* = 0.02, 0.04, and 0.06) electrodes for the first cycle at 25 ^{o}C at a current density of 0.5 C (1 C = 148 mAh g^{-1}) (a); rate performance (b), and the corresponding capacity retention rate at different current densities from 0.5 C to 50 C at 25 ^{o}C (c). The rate capability in (c) is expressed as a relative specific discharge rate compared to that obtained at 0.5 C.

Figure 5.10 Cycling performance (a) and capacity retention rate (b) for *x*LNO/LNMO (*x* =0, 0.02, 0.04, and 0.06) electrodes at current density of 0.5 C with a potential window of 4.95-3.5 V at 25 ^{o}C. The cycling retention rate represents a relative specific discharge capacity compared to the discharge capacity at the first cycle.

Figure 5.11 *In situ* SXRD patterns of 0.04LNO/LNMO electrode during the first cycle at 0.5C and 25 ^{o}C. (a) Selected individual diffraction patterns during the first cycle stacked against the charge/discharge curve. The main peaks of LNMO correspond to (b) (111), (d) (220), and (e) (331) reflections. These regions are highlighted in the bottom columns and peaks corresponding to the $LiNi_{0.5}Mn_{1.5}O_4$ and $Ni_{0.5}Mn_{1.5}O_4$ phases are marked by black dotted lines and purple dotted lines, respectively. For the LNO phase, the main peak that corresponds to the (012) reflection is also highlighted in the bottom columns (c).

Figure 5.12 *In situ* SXRD patterns of 0.04LNO/LNMO electrode during the first cycle at 0.5 C.

Figure 5.13 (a) Impedance plots of pristine LNMO and 0.04LNO/LNMO electrodes at discharge voltage of 4.7 V vs. Li/Li^+ after 5 cycles and frequencies from 100 kHz to 10 mHz. The equivalent circuit is shown in the lower right inset and the upper left inset is an enlargement of the higher frequency region. (b) Real part of the impedance for the electrodes versus $\omega^{-1/2}$ at discharge potential of 4.7 V vs. Li/Li^+.

densities.

Figure 8.6 (a) Impedance plots of the TiO_2/Ti-60min mesh and TiO_2/Ti-600min mesh anodes after cycling over 10 cycles at a discharge potential of 1.7 V vs. Li/Li^+ at 25 °C at frequencies from 100 kHz to 10 mHz. The equivalent circuit is shown in the inset. (b) Real part of the complex impedance versus $\omega^{-1/2}$ at 25 °C at a discharge potential of 1.7 V vs. Li/Li^+.

Figure 8.7 FESEM images of TiO_2/Ti mesh after 100 cycles: (a) top view of theTiO_2/Ti-60min mesh; (b) cross-sectional image of the TiO_2/Ti-60min mesh; (c) high magnification image of the TiO_2 nanotubes from (b); (d) top view of the TiO_2/Ti-600min mesh; (e) cross-sectional image of the TiO_2/Ti-600min mesh; (f) high magnification image of TiO_2 nanotubes from (e).

List of Tables

Chapter 1 Introduction

1.1 General Background

With rapid development around the world, fossil fuel consumption has been increasing exponentially in the past few decades, so that the human living environment has been greatly threatened by emissions of greenhouse gases and pollutants such as carbon dioxide, nitrogen oxides, sulfur dioxide, and particulate materials [1]. The development of clean and renewable energy resources has become a more important task than ever. Although the technology for harvesting sustainable energy has made impressive progress in recent years, such as with better wind turbines, photothermal receivers, and photovoltaic cells, the development of large-scale energy storage devices is still unsatisfactory, especially for electric and hybrid electric vehicles (EVs and HEVs) [2-4]. Currently, huge numbers of combustion engines, used for driving automobiles, ships, and airplanes, are burning fossil fuels and emitting greenhouse gases and pollutants. It is highly desirable to develop large-scale energy storage devices for EVs and HEVs instead of using fossil fuel vehicles, as these have low emissions of greenhouse gases and pollutants.

The lithium ion battery (LIB) is one of the most promising candidate power sources for EVs and HEVs compared with other types of batteries, due to its high voltage, long cycle life, and operation at ambient temperature. Furthermore, LIBs have been widely used as power sources for portable electronic devices, such as mobile phones, cameras, and laptop computers [5-7]. Compared to portable electronic devices, EVs and HEVs require significant improvements in various aspects of LIBs' electrochemical performance, including power and energy density, safety issues, high costs, and low rate capability [8, 9]. The key to success in the development of LIBs for large-scale applications is the electrode materials. In this doctoral work, the general purpose is to improve electrode electrochemical performance

though surface modifications and nanotechnology.

1.2 Statement of the Problem

As with other types of batteries, a LIB includes an anode, a cathode, and a porous separator that is soaked in electrolyte between these two electrodes, in which lithium ions move from the negative electrode to the positive electrode during discharge, and back when charging. Apart from the active material, the electrodes consist of an electrical conductor and a binder due to its poor electronic conductivity and viscosity. Usually, the electrolyte is an organic liquid solution with dissolved lithium salt. Although LIBs have had outstanding commercial success in portable devices, those are still need to significant improvements for meeting the large-scale applications. Effective research is ongoing on LIBs, including on anode materials, cathode materials, electrolytes, and battery construction.

1.2.1 Cathode Materials

Cathode materials play a key role in the working voltage, capacity, and rate capability of LIBs. Actually, considerable efforts are presently being devoted to the cathode to increase energy density and power density, and decrease costs. Currently, the cathode materials with layered structures ($LiMO_2$ with M = Co, Fe) and spinel structures (LM_2O_4 with M = Mn, Ni) are being widely studied due to their excellent delithiation/lithiation properties. Layered $LiCoO_2$ has been widely used in commercial LIBs, however, it shows a limited specific capacity (140 mAh g^{-1}), is partially toxic, and has a high cost [10]. Layered $LiFeO_2$ shows extremely low ionic conductivity because the lithium diffusion pathways blocked by the iron ions on lithium sites [11, 12]. In the case spinel $LiMn_2O_4$, it is challenging to control the capacity decay during cycling, which is associated with Mn dissolution and Jahn-Teller distortion of Mn^{3+} ions with high spin [13, 14]. The electrochemical performance of $LiNi_{0.5}Mn_{1.5}O_4$ (LNMO) is restricted by many factors related to the material itself, including

the crystalline structure (cation mixing and stoichiometry), particle morphology and size, and type of electrolyte [15, 16]. Meanwhile, rate capability and safety issues need to be considered for the next generation of cathode materials.

1.2.2 Anode Materials

Most commercial LIBs use graphitic carbon as the anode material. Graphite electrode shows good cycling stability, a low operational voltage, and low cost, but with a low theoretical specific capacity (372 mAh g^{-1}) [17]. In additional, there are safety concerns for this material, because the lithium dendrites that grow after repeated charge-discharge cause irreversible damage to the LIB. A series of new anode materials have been developed with high theoretical specific capacity, i.e. Si, Sn, and transition metal oxides [18-21]. Unfortunately, there are volume changes that accompany with the delithiation/lithiation reactions, which severely reduce the capacity retention and cycle life for the electrode. Surface modification and designing special nanostructures are the most viable options to solve the problem of capacity loss and low cycling stability. It is worth noting that the alloy and transition metal oxide anode materials should be coupled with high-voltage cathode materials, which maintain LIB voltages exceeding 3.5 V.

1.2.3 Electrolyte

Currently, flammable organic electrolytes are those mostly used in traditional LIBs. Organic electrolytes lead to the formation of cathode electrolyte interphase and lithium dendrites, so that the safety issues are already restricting the development of large-scale batteries [22-24]. Solid-state electrolyte is a possible replacement for the flammable organic electrolytes, which simplify the battery design and increase the cycle life and safety of the batteries. Low ionic conductivity is the crucial problem for the solid-state electrolyte. Although the ionic conductivity of solid-state electrolyte can approach the level of commercial organic liquid

electrolytes (10^{-2} S cm^{-1}), and even more than 10^{-2} S cm^{-1} (1.2×10^{-2} S cm^{-1} for $Li_{10}GeP_2S_{12}$) [25], the low mechanical strength and poor electrode/electrolyte interface contact restrict the development of this type of electrolyte [26].

1.3 Importance of Study

Nanotechnology and surface modification are the most viable options to achieve significant development of LIBs for EVs and HEVs. In this doctoral work, systematic investigations were carried out to develop advanced materials for LIBs based on the surface modification of composites and nanostructured materials. The foreseeable advantages for the use of surface modified composites and nanostructured materials as electrode are summarized as follows:

Firstly, improvement in rate capability: The special nanostructures provide a larger specific surface area and shorten the lithium ion diffusion and electron transport distances. On the other hand, the conductive surface of the active materials is also beneficial for lithium ion diffusion and electron transportation.

Secondly, improvement in capacity retention: Nanostructured materials are able to accommodate the volume changes during charge/discharge processes. Meanwhile, the modified surface of the electrode materials can prevent contact between the active material and the electrolyte, so that it effectively reduces the active material oxidation and solid state interphase formation.

Thirdly, enhancement of the high temperature performance: The surface of electrode materials modified with a protective layer can tolerate temperature changes and keep the active materials stable.

It is also necessary to understand how the surface modification and nanostructure influence the electrochemical performance of LIBs when the composites and nanostructured materials

are applied as electrode. In addition, the electrolyte is also crucial for improving LIB safety. Therefore, it is of the most importance to carry out these investigations for the development of LIBs which are suitable for next-generation large-scale applications.

1.4 Objectives and Scope of Research

In this doctoral work, the initial objective was to improve the electrochemical performance of LIBs through nanotechnology and surface modification. Once the composite/nanostructured materials were identified as electrode materials for LIBs, the next objective was to further improve the performance by means of electrode engineering, such as by using a different electrolyte or different current collector, or even *in-situ* analysis for kinetics and thermodynamics studies. Therefore, the overall objective of this doctoral work is to synthesize composite/nanostructured materials and apply them in LIBs, with the emphasis on the morphological, structural, physical, and key electrochemical changes.

Meanwhile, the scope of the research that is carried out in this doctoral thesis is briefly outlined below as follows:

In Chapter 1, the general background, major problems, and some approaches for improving the electrochemical performance of LIBs are simply introduced. The importance and objectives of the study are also discussed.

Chapter 2 presents a thorough literature review on LIBs, especially with respect to the role of composite/nanostructured materials, surface modification, and possible techniques for the synthesis of these materials.

Chapter 3 presents the chemicals and methods used to synthesize composite/nanostructured materials. This chapter also presents the instrumental analysis techniques used to characterize the electrode materials, including X-ray diffraction (XRD), synchrotron X-ray diffraction

(SXRD), thermogravimetric analysis (TGA), Raman spectroscopy, Fourier transform infrared (FTIR) spectroscopy, scanning electron microscopy (SEM), field emission scanning electron microscopy (FESEM), transmission electron microscopy (TEM), selected area electron diffraction (SAED), energy dispersive X-ray spectroscopy (EDS), Brunauer-Emmet-Teller (BET) surface area measurements, cyclic voltammetry (CV), galvanostatic charge-discharge testing, and electrochemical impedance spectroscopy (EIS).

Chapter 4 and 5, investigate the influence of solid state electrolyte on the performance of spinel structured cathode materials for LIBs in combination with organic liquid electrolyte, which are $LiNbO_3$-$Li_{1.08}Mn_{1.92}O_4$, and $LiNbO_3$-$LiNi_{0.5}Mn_{1.5}O_4$, respectively.

Chapter 6 and 7 investigate the influence of nanostructured coated layers on the performance of electrode materials for LIBs, for α-$LiFeO_2$-PPy, and V_2O_3/C, respectively.

Chapter 8 describes the synthesis techniques and electrochemical properties that were investigated for a three-dimensional nanotube arrays anode material (TiO_2/Ti mesh).

Chapter 9 summarizes the overall doctoral work and provides some suggestions for further research work related to these composite/nanostructured materials

Chapter 2 Literature Review

2.1 Lithium-Ion Batteries

Over the past several decades, energy storage and conversion have drawn a great deal of attention from the scientific community and industry. Lithium ion batteries (LIBs) have been demonstrated to be one of the most successful examples in commercial applications, ever since they were commercialized by SONY in 1991 [27, 28]. Currently, LIBs remain the major power sources for portable electronic devices, such as power tools, mobile phones, laptop computers, and telecommunication devices. LIBs possess many advantages over other competing battery systems, including lead-acid batteries, nickel-cadmium batteries, nickel metal-hydride batteries, sodium-sulphur, and sodium metal-chloride batteries (Figure 2.1) [1]. LIBs have around four times the energy and twice the power density of the nickel-cadmium batteries. Meanwhile, LIBs show a 50% longer cycle life, and there is no memory effect for recharging. Compared with lead-acid batteries, LIBs have triple the energy density, and they are environmentally friendly. Furthermore, lithium has a low density (ρ = 0.53 g cm^{-3}), small ionic radius (76 pm), and low redox potential compared to other elements (-3.04 V vs. standard hydrogen electrode (SHE) potential), so that LIBs have a high energy density and average voltage of 3.6 V, which makes them ideal for powering portable electronic devices. LIBs also show a low self-discharge capability.

Currently, however, the technologies for producing LIBs cannot meet the rapidly developing requirements of industry. In particular, the large-scale batteries needed for electric vehicles (EVs), hybrid EVs (HEVs), and power grid storage systems are still in the research and development stages. In recent decades, great efforts have been devoted to improvements in LIB electrochemical performance, such as in power and energy density, safety issues, and low rate capability. Vinodkumar Etacheri et al. present an optimistic review of the challenges

to the development of LIBs [2]. There are mainly three areas of challenges: developing advanced nanostructured materials for improving both anode and cathode performance; applying new *in-situ* characterization techniques for identifying electrode material problems and giving a rapid assessment of possible solutions; and developing advanced computer simulation modeling for optimizing the new combinations of electrode materials and geometries. In this doctoral work, LIBs will be investigated and discussed in detail.

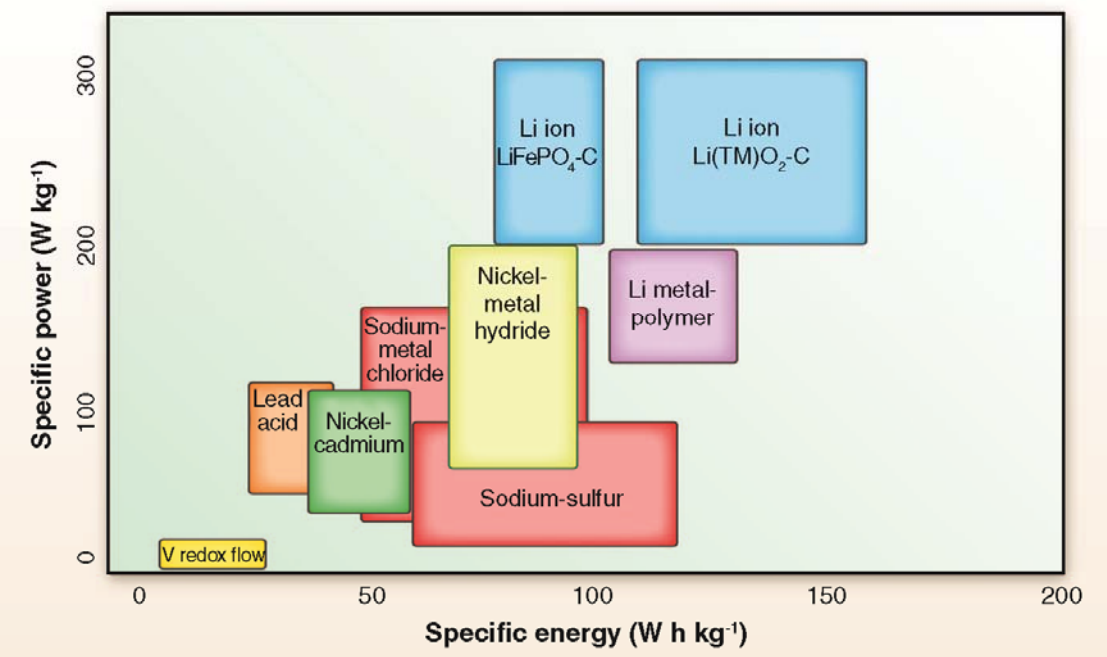

Figure 2.1 Gravimetric power and energy densities for different types of rechargeable batteries [1].

2.1.1 Brief History

Benjamin Franklin first used the word "battery" to describe a group of electrical devices, multiple Leyden jars, in 1748, by analogy to a battery of cannons. After the discovery of "animal electricity" by Luigi Galvani in 1780, the first modern electrochemical cell was developed by Alessandro Volta in 1800. The "galvanic cell" or "voltaic cell" is a stack of copper and zinc plates, separated by brine soaked paper disks, which could produce a steady current for a considerable length of time. Subsequently, many types of primary or

rechargeable batteries were developed, such as the lead-acid battery, zinc-carbon battery, nickel-cadmium battery, zinc-air battery, alkaline battery, and lithium battery [29, 30]. Figure 2.2 shows the historical timeline for batteries over the centuries.

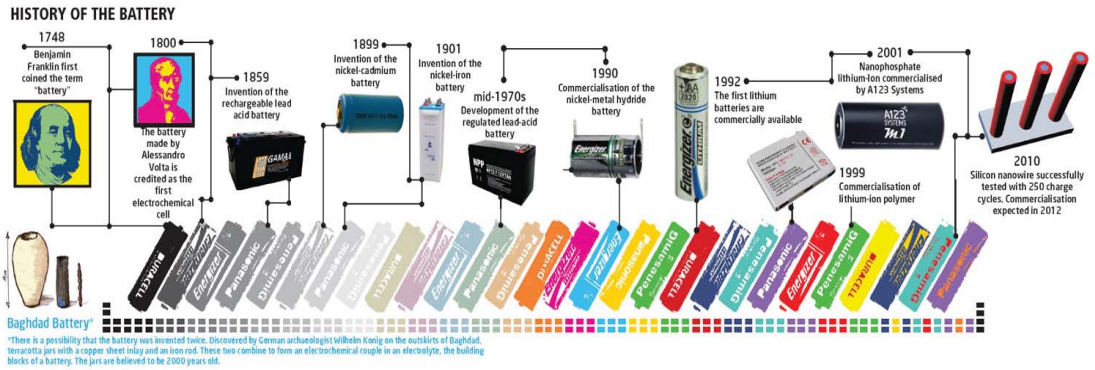

Figure 2.2 Schematic representation of battery development over the centuries [31].

The first lithium battery was proposed by Harris in his doctoral thesis in 1958 [32]. After the efforts of many scientists and engineers on the lithium battery during the early days, primary lithium cells (non-rechargeable) were commercialized in the 1970s and are still in use today, as they have high capacity and variable discharge rates. The most prominent early lithium battery systems mainly include lithium/sulphur dioxide (Li/SO_2), lithium/thionyl chloride ($Li/SOCl_2$), lithium/polycarbon monofluoride ($Li/(CF_x)_n$), and lithium/manganese dixiode (Li/MnO_2) [33]. The invention of the LIB was not an accidental event, because numerous inorganic compounds were shown to reversibly react with alkali metals. Whittingham, who worked for Exxon in the 1970s, proposed and investigated the use of titanium sulfide (TiS_2) as a cathode in lithium batteries, because lithium ions could be intercalated into the layered dichalcogenides and could be form a single phase over the entire composition range of Li_xTiS_2 ($0 \leqslant x \leqslant 1$) [34]. The commercialization eventually failed, however, due to the safety problem, as well as the low potential and high production costs. Those features have led to the study of layered oxide materials. Vanadium pentoxide (V_2O_5) and molybdenum trioxide (MoO_3) were two of the earliest studied oxides [35, 36]. MoO_3 showed a low rate

capability so researchers are not very interested in this material. V_2O_5 has been investigated for 40 years. It has a layered structure with weak vanadium-oxygen bonds between the layers and is now known to react by an intercalation mechanism. Unfortunately, this material also is unsuitable for commercial application, due to the multiphase transitions and rapid capacity loss on cycling. In the 1980s, Goodenough and his co-workers discovered that $LiCoO_2$ had a similar structure to the layered structured dichalcogenides and showed that the lithium could be inserted and de-inserted electrochemically, thus making it a very promising cathode material [37]. Furthermore, Goodenough's group proposed the open framework Li_xMO_2 (M = Co, Ni, and Mn) family of compounds, which is still used in LIBs today [38]. On the other hand, the electrochemical properties of lithium intercalation in graphite were first proposed in a Sanyo patent in 1981 [39]. The graphite anode is much safer than if pure lithium is used for the battery, and it forms the compound LiC_6 on reaction with lithium ions. The safety issue for the pure lithium anode arises from the easy formation of lithium dendrites, leading to a short circuit. The graphitic carbon anode can only result in the loss of 100-300 mV in cell potential, which is negligible when it is coupled with higher potential $LiCoO_2$ cathode [40]. Eventually, the first commercial LIB was proposed by the SONY Corporation in 1991, which combined $LiCoO_2$ cathode with a graphite anode and had an open circuit potential of 4.2 V and an operational voltage of 3.6 V. This led to the so called lithium-ion or rocking-chair batteries [41]. Since then, many electrode materials have been investigated, such as spinel $LiMn_2O_4$, olivine $LiFePO_4$ for cathode, and Si, Sn, and transition metal oxides for anode. Currently, LIBs have an irreplaceable influence on the battery community all over the world, and they have rapidly come into use in portable electronic devices, especially mobile phones and laptop computers, over the past two decades.

2.1.2 Working Mechanism

A battery is commonly a stack of one or more electrochemical cells, where individual cells

are electrically connected in series or parallel. As shown in Figure 2.3, a electrochemical cell can be packed in many types of shapes, such as cylindrical, coin, prismatic, and plastic cells. Although the shapes are different, the basic components are similar to each other, including the anode (negative electrode), cathode (positive electrode), electrolyte with lithium salt, and separator [42]. The anode releases electrons to the external circuit during the discharge process, corresponding to oxidative chemical reactions. The cathode gains electrons from the external circuit during the discharge process, corresponding to reductive chemical reactions. The electrolyte shows high ionic conductivity and low electrical conductivity between the anode and cathode in the cell. The separator is a physical barrier between the anode and cathode to prevent an electrical short circuit. In addition, aluminium and copper are usually used as the current collectors at the cathode and anode, respectively. In some special cases, nickel also can be chosen for the current collector. The collector materials require good electrical conductivity and inertness to any electrochemical lithium reaction at the respective electrodes.

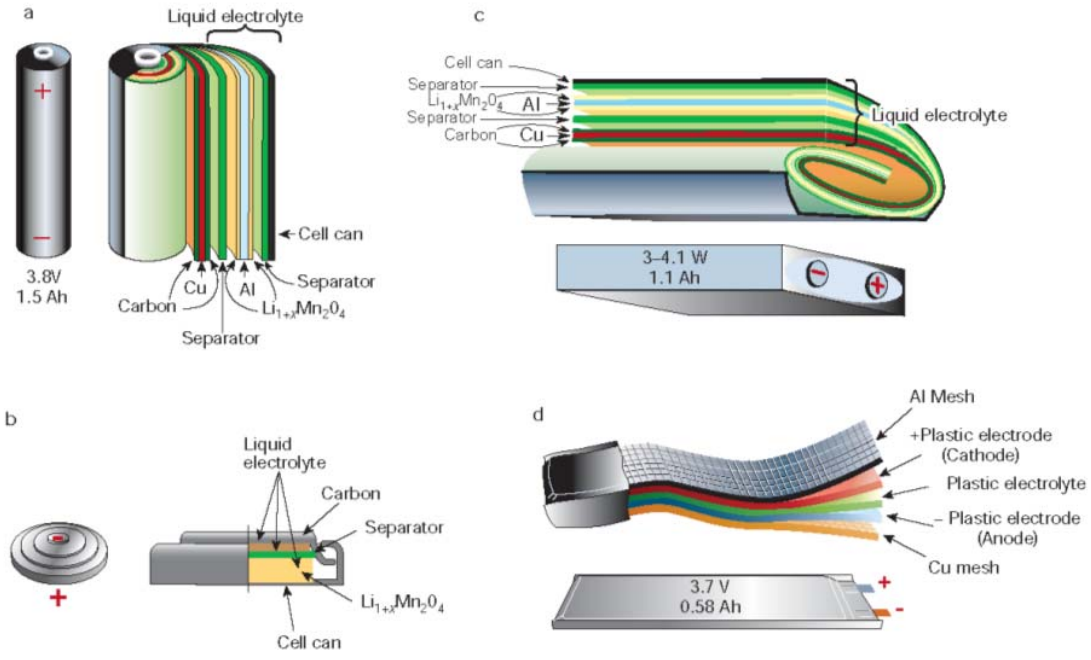

Figure 2.3 Schematic diagrams of the shapes and components of various LIB configuration:

a) cylindrical; b) coin; c) prismatic; d) thin and flat plastic cell [41].

The LIB works by means of lithium ions rocking between the anode and cathode through the electrolyte, while energy is release or replenished inside the cell. Taking the conventional lithium-ion cell (graphite/$LiCoO_2$) as an example (Figure 2.4), during the discharge process, lithium ions move from the anode (graphite) to the cathode ($LiCoO_2$) via the electrolyte, while the electrons go through the external circuit in the same direction, converting the electrochemical energy into electrical energy. During the charge process, an external electrical power source forces lithium ions to move back from the cathode ($LiCoO_2$) to the anode (graphite) via the electrolyte, while the electrical energy is stored as electrochemical energy. The reaction mechanisms are shown as follows:

$$LiCoO_2 \leftrightarrow Li_{1-x}CoO_2 + xLi^+ + xe^- \quad (2.1)$$

$$C + xLi^+ + xe^- \leftrightarrow Li_xC \quad (2.2)$$

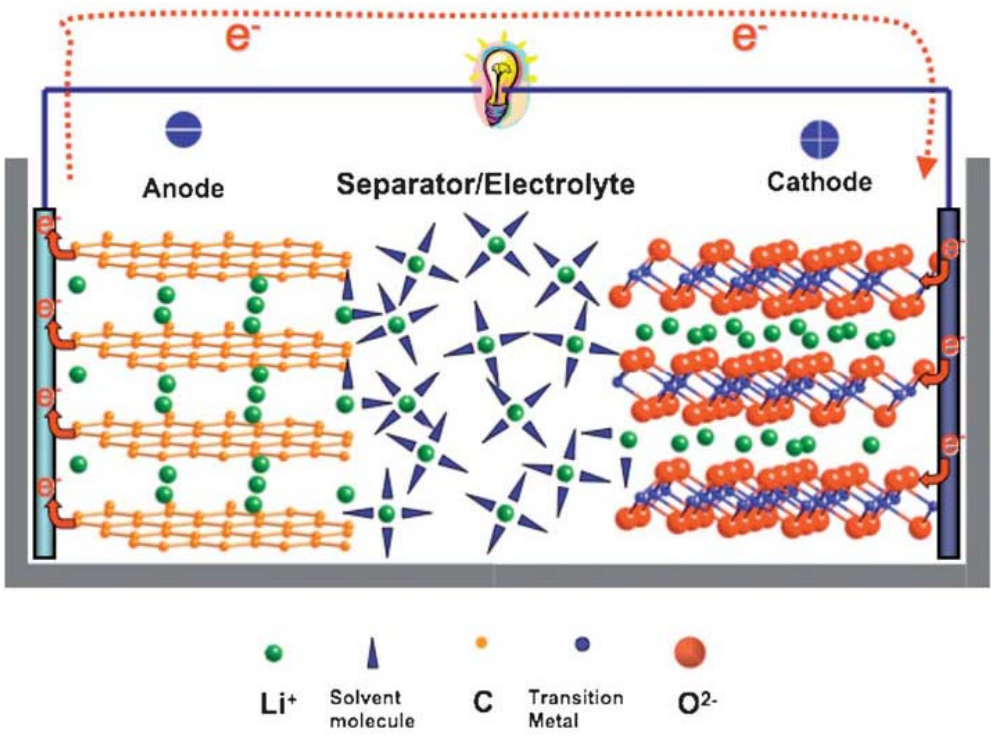

Figure 2.4 Schematic illustration of the working mechanism in a rechargeable LIB [43].

2.1.3 Basic Concepts

In order to evaluate the properties of electrodes in LIBs, definitions, basic concepts, and theories are discussed below:

Voltage

The open circuit voltage (V_{oc}) is the voltage measured across the terminals of a cell without external current flow. It is determined by the difference in electrochemical potential between the anode and the cathode.

$$V_{oc} = (\mu_A - \mu_C)/(-nF) \quad (2.3)$$

where $\mu_A - \mu_C$ is the difference in the electrochemical potential between the anode and cathode, n is the numbers of the electrons involved in the chemical reaction of the cell, and F is the Faraday constant (96485 C/mol).

The operating voltage of the cell can be described as:

$$V = V_{oc} - IR \quad (2.4)$$

where I is the working current in the circuit and R is the internal resistance of the cell.

Capacity

Capacity (Q) is the total amount of charge on the electrode for the redox reaction during the charge/discharge process of the cell.

$$Q = \int_{t1}^{t2} I(t)\, dt = nzF \quad (2.5)$$

where $I(t)$ is the current; t is the time; n is the number of the ions (mol), z is the valence of the ions, F is the Faraday constant.

Specific capacity (Q_s) can be divided into charge specific capacity (Q_{sc}) and discharge specific capacity (Q_{sd}), which can be described in terms of gravimetric specific capacity (ampere hour per kilogram; Ah g^{-1}), volumetric specific capacity (ampere hour per litre; Ah L^{-1}), and superficial specific capacity (ampere hour per litre; Ah m^{-2}). The specific capacity can be calculated based on the capacity per unit weight of the active material, capacity per unit density of the active material, and capacity per unit area of the active material.

Irreversible capacity

The irreversible capacity is the capacity lost after one cycle, which resultsfrom irreversible lithium reactions.

For anode materials:

$$\text{Irreversible capacity} = {}^{n^{th}}Q_d - {}^{n^{th}}Q_c \tag{2.6}$$

For cathode materials:

$$\text{Irreversible capacity} = {}^{n^{th}}Q_c - {}^{n^{th}}Q_d \tag{2.7}$$

where n is the cycle number, Q_d is the discharge capacity, Q_c is the charge capacity.

Coulombic efficiency

Coulombic efficiency (η_e) is the ratio of the charge capacity to the discharge capacity at the n^{th} cycle, which represents the cycling stability.

$$\eta_e = \frac{n^{th}Q_d}{n^{th}Q_c} \tag{2.8}$$

Energy

The specific energy can be expressed in watt-hours per kilogram (Wh Kg^{-1}) and watt-hours

per litre (Wh L^{-1}). This value expresses the energy content of a cell.

Power

The specific power can be expressed in watts per kilogram (W Kg^{-1}) and watts per litre (W L^{-1}). This value expresses the rate capability of a cell.

Rate capability

Rate capability (C-rate) is used to evaluate how fast lithium-ions can be transferred. C represents either the theoretical charge capacity of a cell or the nominal capacity of a cell. For example, C/2 means a current allowing a full charge/discharge in 2 hours.

Charge-transfer resistance

Charge-transfer resistance (R_{ct}) quantitatively characterizes the speed of an electrode reaction. Generally, a large charge-transfer resistance corresponds to a slow electrochemical reaction. The R_{ct} can be calculated from electrochemical impedance spectroscopy (EIS).

Apparent activation energy

The apparent activation energy (E_a) is a very important kinetic parameter. Normally, a low activation energy corresponds to a short lithium-ion diffusion path. The apparent activation energy (E_a) can be calculated from the following equations.

$$i_0 = RT / nFR_{ct} \tag{2.9}$$

$$i_0 = A\exp(-E_a / RT) \tag{2.10}$$

where R is the gas constant (8.314 J mol^{-1} K^{-1}) , T (K) is the absolute temperature, n is the number of transferred electrons, F is the Faraday constant, A is a temperature-independent coefficient.

$$E_a = -Rk\ln 10 \quad (2.11)$$

where k is the slope of the fitting line in the Arrhenius plot of log i_0 as a function of $1/T$.

2.2 Cathode Materials

Cathode materials for lithium-ion batteries and lithium batteries have been considered one of the biggest obstacle to the aim of improving electrochemical performance since the advent of the commercial LIBs in 1991. A wide range of materials can be chosen as cathode for LIBs, while the ideal cathode material is one that exhibits no structural change during cycling. Several reviews have been published recently, which have mainly focused on the cathode materials for LIBs, such as reviews by Yair Ein-Eli's group [3, 44], Doron Aurbach's group [45], and Goodenough's group [46]. Typical delithiation/lithiation compounds are unanimously considered as the preferred candidates. For these cathode materials, the topotactic delithiation/lithiation process is without structural change. The key requirements for choosing cathode materials must be considered carefully, however [47]:

a) high free energy of reaction with lithium,

b) wide range of x (amount of lithium-ion insertion),

c) reasonable power density and energy density,

d) small structural changes from reactions,

e) rapid diffusion of lithium within the host lattice.

f) good electronic conductivity,

g) non-solubility in electrolyte,

h) low cost and ease of synthesis.

As shown in Figure 2.5, the potential alternative cathode materials for LIBs can be divided into three major categories, including layered, spinel, and olivine structured oxides. Here, a review is presented on selected developments in the area of cathode materials for LIBs and lithium batteries in the past decade.

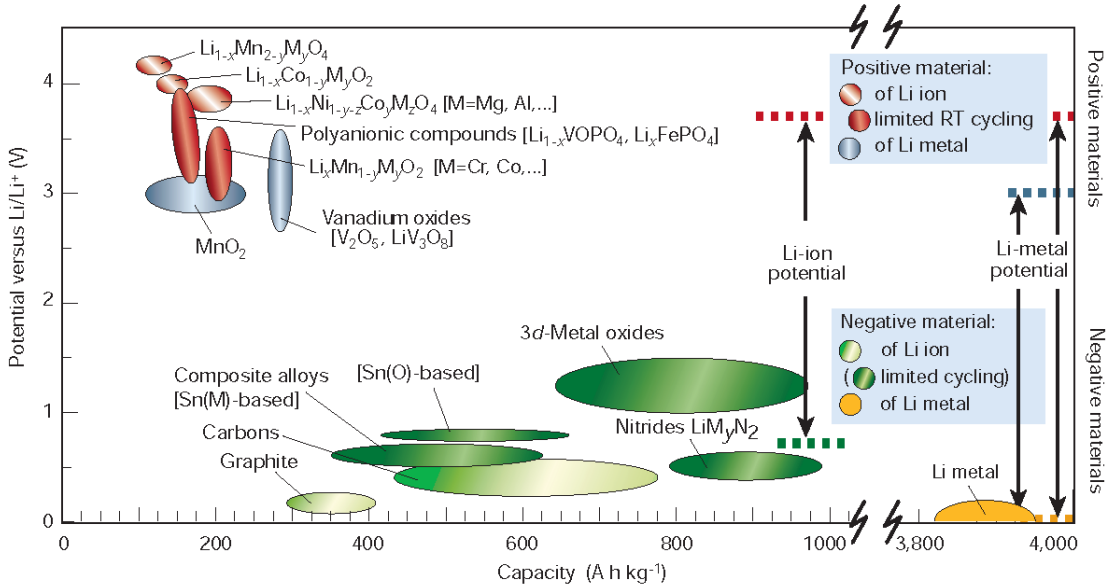

Figure 2.5 Electrode materials and corresponding electrochemical performances in the current LIB technologies [41].

2.2.1 Layered Oxides

$LiCoO_2$, with the α-$NaFeO_2$ structure, has been extensively studied and widely used as cathode electrode materials in commercial LIBs, due to its good cycling performance and the simplicity of preparation [48]. $LiCoO_2$ can be described as having a distorted rock salt superstructure (Figure 2.6). In a cubic close-packed oxygen array, the Li and Co atoms occupy the octahedral interstitial sites, so that CoO_2 layers are formed and consist of edge-sharing octahedra (CoO_6). Lithium atoms are located between the CoO_2 layers and reside in the octahedral coordination (LiO_6), which results in alternating (111) planes of the cubic rock salt structure. The layered structure provides a two dimensional path, allowing for lithium ion

extraction and insertion. Alternatives to $LiCoO_2$, however, are being constantly studied. This is because $LiCoO_2$ shows limited specific capacity (~ 140 mAh g^{-1}, theoretical capacity of 273 mAh g^{-1}), high costs, toxicity, and poor safety, which prevent application in large-scale energy-storage systems such as for EVs and HEVs [49].

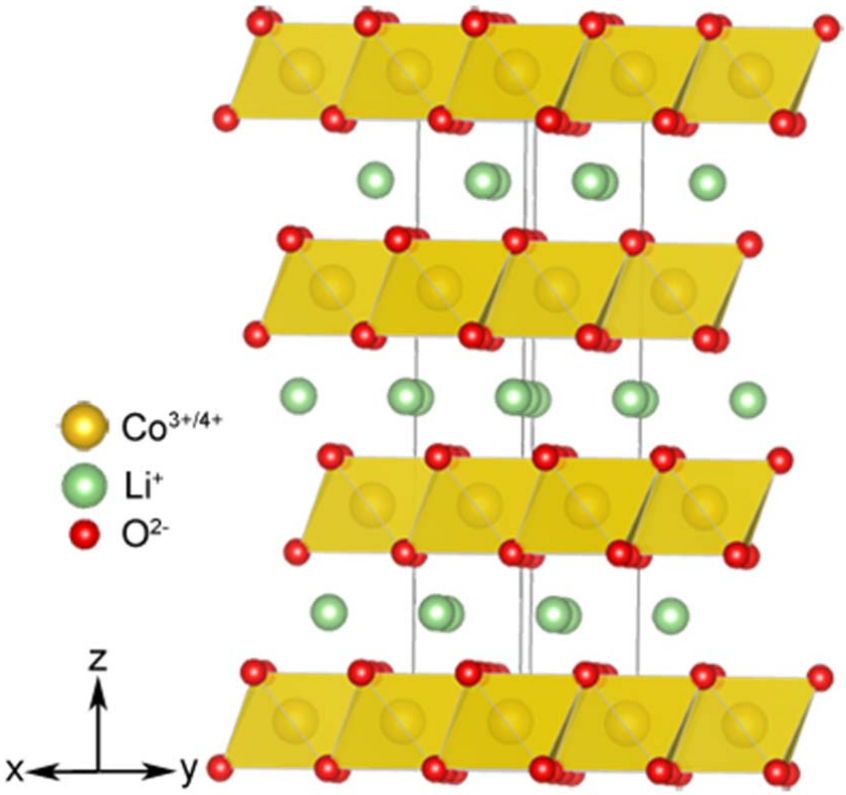

Figure 2.6 Layered crystal structure of $LiCoO_2$ (R-3m) [50].

As early as 1991, Dahn et al. proposed the isostructural $LiNiO_2$ as an alternative to $LiCoO_2$. Compared with $LiCoO_2$, $LiNiO_2$ is low cost, and has lower toxicity and higher reversible capacity (~ 200 mAh g^{-1}) [51]. The safety issues hinder the further development of $LiNiO_2$, however, which are associated with structural change and the generation of O_2 during the charge process. Layered $LiMnO_2$ is regarded as a very promising cathode material, just in terms of its low cost and environmental friendliness [52]. Unfortunately, layered $LiMnO_2$ is a metastable phase, which is not only unstable at high temperature, but also impossible to

synthesize using the solid-state method. Although some researchers have reported that layered $LiMnO_2$ can be prepared by ion exchange of thermodynamically stable layered $NaMnO_2$ with lithium-ions, layered $Li_{0.5}MnO_2$, produced during charge/discharge processes, is prone to convert into thermodynamically more stable spinel phase ($LiMn_2O_4$) [53]. The phase conversion makes the electrochemical properties unstable and causes a spinel-like drop in the voltage profile. Lithium ferrite, $LiFeO_2$, has also been widely studied as a potential alternative to $LiCoO_2$ cathode material, due to its non-toxicity, environmental friendliness, low cost, low cycling efficiency, and low operating voltage. The low electronic conductivity, however, and the poor cycling performance have restricted the development of $LiFeO_2$ cathode materials [54, 55]. The unstable layered structure of $LiNiO_2$, $LiMnO_2$ and $LiFeO_2$ during charge/discharge process have diverted researchers' attention to the investigation of "mixed oxide" layered structures, such as $LiNi_xMn_yO_2$, $LiNi_xCo_yO_2$, $LiMn_xCoyO_2$, and $LiNi_xMn_yCo_zO_2$ [56-62]. $LiCo_{1/3}Ni_{1/3}Mn_{1/3}O_2$ in particular exhibited promising electrochemistry and intriguing structural behaviour, as it had an α-$NaFeO_2$-type structure, and Ni, Co, and Mn ions adopting valence states of 2^+, 3^+, and 4^+, respectively [63-65]. This type of material can be further modified to improve its safety, which has made it a very promising candidate for large-scale energy storage.

2.2.2 Spinel Oxides

Spinel $LiMn_2O_4$ is another popular cathode material for LIBs, on which the earlier investigations have been concentrated. Spinel $LiMn_2O_4$ cathode material has mainly the following four advantages over layered $LiCoO_2$ or $LiNiO_2$ cathode materials: 1) low cost and abundant raw materials, 2) higher thermal stability, especially during overcharge, 3) higher discharge voltage (4.1 V vs. Li^+/Li), 4) environmental friendliness [66-69]. It remains challenging, however, to improve its electrochemical performance, due to the following problems: 1) low specific capacity (theoretical capacity of 148 mAh g^{-1}), 2) low power

density compared with layered cathode materials, 3) poor cycling stability, especially at elevated temperatures (> 50 ^{o}C) [14, 70-72].

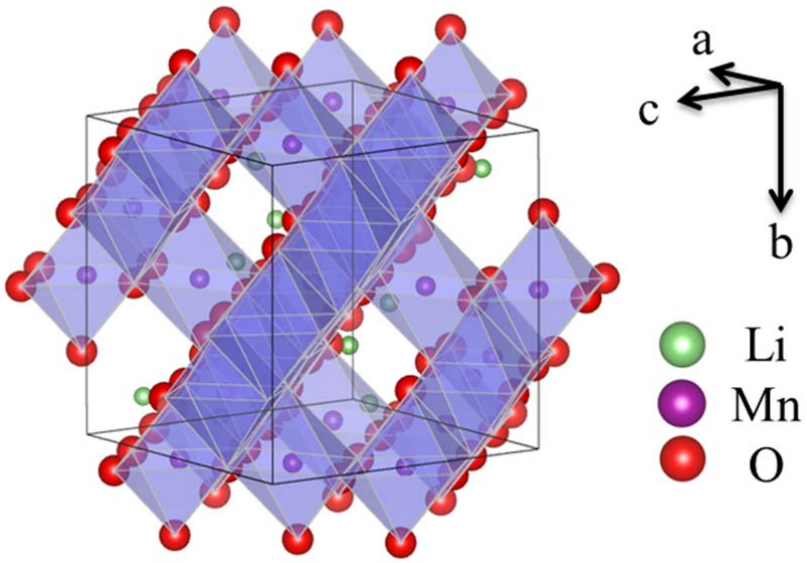

Figure 2.7 Spinel crystal structure of $LiMn_2O_4$ (Fd3m).

As can be seen from Figure 2.7, $LiMn_2O_4$ has a cubic spinel structure, which can be described as a cubic close-packed oxygen array with oxygen anions on the crystallographic *32e* sites of the *Fd3m* space group [14]. The manganese cations reside in half of the octahedral interstitial sites (*16d*), and the lithium cations are located at one eighth of the tetrahedral sites (*8a*). The interstitial spaces in the Mn_2O_4 framework are relative to a diamond-type network of tetrahedral *8a* and surrounding octahedral *16c* sites, so that these vacant tetrahedral and octahedral sites are interconnected with each other by common faces and edges to form the lithium-ions' three-dimensional (3D) diffusion pathways. The 3D framework structure of $LiMn_2O_4$ possesses several advantages compared with the two-dimensional (2D) layered structures of other cathode materials, such as avoiding the co-insertion of bulky species (solvent molecules), the smaller degree of volume change of the framework structure during lithiation/delithiaton processes, and suitability for large-scale

batteries due to the large size of the lithium-ion channels to sufficiently accommodate the ions [73-75].

The capacity decay during cycling, however, is still plaguing the application of $LiMn_2O_4$ cathodes. Researchers have proposed several mechanisms for explaining this phenomenon, such as Jahn-Teller distortion of Mn^{3+} ions, Mn dissolution into electrolyte, loss of crystallinity, the microstrain due to lattice mismatch between two distinct cubic phases during cycling, and increasing oxygen deficiency or oxygen loss during cycling [76-78]. Mn dissolution via the disproportionation reaction ($2Mn^{3+}_{(solid)} \rightarrow Mn^{4+}_{(solid)} + Mn^{2+}_{(solution)}$) is unanimously considered to be the predominant reason. A recent study has confirmed the Mn dissolution mechanism according to the dissolution reaction by free energy calculations through first principles [79-81].

To improve the capacity retention, on the one hand, there are some reports on the use of nanostructured spinel and the surface modification of the $LiMn_2O_4$ cathode materials, such as ordered mesoporous $LiMn_2O_4$ [82, 83], $LiMn_2O_4$ nanorods [84, 85], and M-coated $LiMn_2O_4$ (M= different forms of carbon, oxides, and polymers) [86-90]. On the other hand, spinel $LiMn_2O_4$, replaced by different elements (Fe, Co, Ni, Mg, Cr, and Cu), has been investigated to improve the electrochemical performance [72, 91-95]. Spinel $LiFe_xMn_{2-x}O_4$ is a kind of 5 V cathode material and shows poor capacity and cycling performance, whereas $LiCo_xMn_{2-x}O_4$, also a 5 V cathode material, has much better conductivity and cycling stability than $LiCoMn_2O_4$ [96, 97]. Another high voltage cathode material, $LiNi_{0.5}Mn_{1.5}O_4$, is a very promising candidate in the spinel oxide family. $LiNi_{0.5}Mn_{1.5}O_4$ is characterized by a two-phase electrochemical process that is reflected in a high-voltage plateau (~ 4.7 V vs. Li/Li) [15, 98-100]. Also, the theoretical capacity of $LiNi_{0.5}Mn_{1.5}O_4$ is similar to that of $LiMn_2O_4$, 147 and 148 mAh g^{-1}, respectively. Apart from the same advantages as $LiMn_2O_4$, $LiNi_{0.5}Mn_{1.5}O_4$ shows high working potential, which provides more than 30 % higher energy

density than that of $LiMn_2O_4$. A promising new generation of 12 V batteries was reported by Ohzuku et al.[101], which use $LiNi_{0.5}Mn_{1.5}O_4$ and $LiMn_2O_4$ spinel as cathode in combination with an elevated potential anode, such as spinel $Li_4Ti_5O_{12}$. The high voltage cathodes are expected to be suitable for high-energy and large-scale batteries.

2.2.3 Olivines

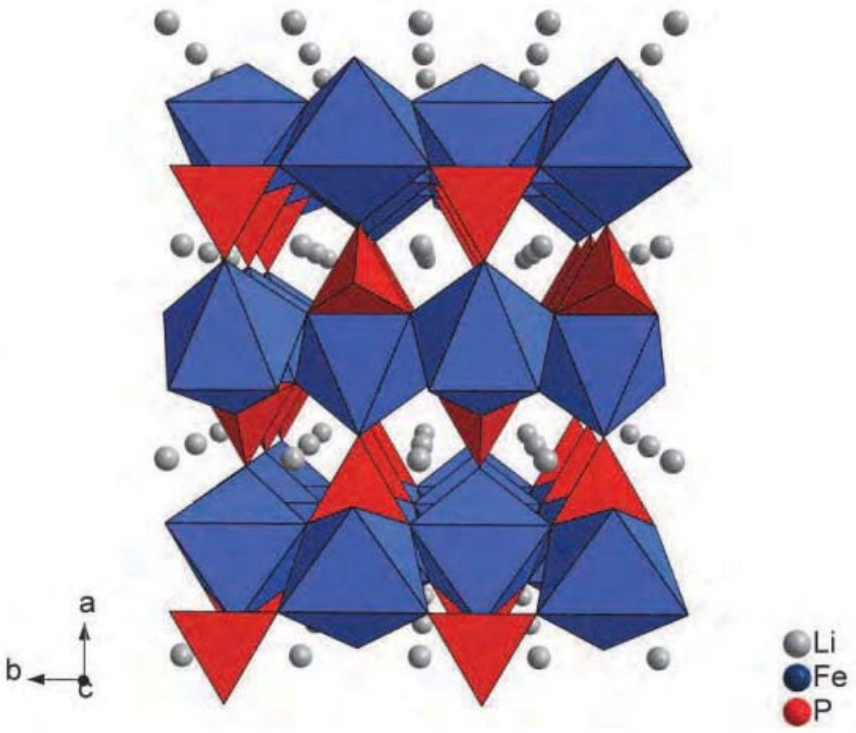

Figure 2.8 Olivine crystal structure of $LiFePO_4$ (Pnma) [110].

Padhi's group's [102] discovery of the $LiMPO_4$ (M = Fe, Ni, Mn etc.) compounds in 1997 have had a definite impact on cathode material research. Among the $LiMPO_4$ (M = Fe, Ni, Mn etc.) cathode materials, $LiFePO_4$ has attracted a considerable amount of researchers' attention [103-107]. This is because the olivine $LiFePO_4$ can be discharged to 90 % of its theoretical capacity (170 mAh g^{-1}) at a stable voltage of ~ 3.4 V [108, 109]. Pure $LiFePO_4$ shows a very low conductivity (10^{-9} S cm^{-1}), so that this cathode material requires a small particle size (< 1 μm) and is well dispersed in a conductive carbon matrix when it is used in

LIBs. $LiFePO_4$ cathode materials also possess the advantages of low cost, non-toxicity, natural abundance, and environmental friendliness.

Figure 2.8 shows the olivine structure of $LiFePO_4$. Olivine $LiFePO_4$ consists of corner-sharing FeO6 octahedra and $PO4^{-3}$ tetrahedral anions, with lithium cations located at the octahedral holes. The cation arrangement of $LiFePO_4$ is totally different from the arrangements of the layered and spinel structures. The olivine structure has no continuous network of FeO_6 edge-sharing octahedral, rather, the Fe^{2+} ions occupy corner-sharing octahedra. These structures are considered to have a negative impact on electronic conductivity [111]. In addition, the phosphorus ions occupy the tetrahedral sites, and the lithium-ions reside in chains of edge-sharing octahedra [112].

For improving electronic conductivity, on the one hand, doped $Li_{1-x}M_xFePO_4$ (M = Mg, Al, Ti, Nb, or W) was synthesized via solid-state reaction method [113-119]. The solid solution doping by metals increases the electronic conductivity of $LiFePO_4$ (approximately 10^8 S cm^{-1}). Nanosizing and carbon coating can effectively increase the electrochemical performance, especially improving the electronic conductivity. Carbon-coated $LiFePO_4$ cathode materials synthesized with a carbon aerogel or graphene wrapped $LiFePO_4$ cathode materials demonstrated high rate capability and cycling stability [120, 121]. Monodisperse nanofibers of $LiFePO_4$ cathode materials mixed with conductive carbon could delivered nearly the full theoretical capacity at 3 C, and 36 % of theoretical capacity at the enormous discharge rate of 65 C [122]. Thus, the performance of nanosized $LiFePO_4$ and conductive $LiFePO_4$ composites make $LiFePO_4$ cathode materials suitable for use in EVs and HEVs, due to their high energy density and high power.

On the other hand, olivine $LiMnPO_4$, which is isostructural with $LiFePO_4$, also has a similar theoretical capacity (171 mAh g^{-1}), but show a higher voltage plateau (~ 4.1 V vs. Li^+/Li),

offering high energy density [123, 124]. Up to now, olivine $LiMnPO_4$ has been handicapped by several critical disadvantage for LIB applications. The olivine $LiMnPO_4$ system shows very poor electronic conductivity and structural distortions with oxidation to $MnPO_4$, which prevent lithium-ion transport, so that numerous reports of this material show very poor capacity and cycling stability. Researchers have attempted many methods to enhance the electrochemical properties of $LiMnPO_4$, including preparing nanosized powder, doping with metal cations, and coating with various types of carbon [125-129].

2.2.4 Vanadates

Vanadium oxides have gained attention for use as the cathode material in LIBs for many years, due to their lithium storage properties [130-133]. Figure 2.9 shows the structure of this cathode material. There are actually many kinds of vanadium oxides. Because the V-O bonds and VO_6 octahedra of their layered structures can be distorted, they provide large bond length variations. Vanadium pentoxide (V_2O_5) has attracted the most interest among the vanadium oxides species, owing to its low cost and high theoretical capacity (437 mAh g^{-1}) [134]. The crystal structure of V_2O_5 consists of VO_5 square pyramids, which share the corners of their bases to form a sheet. In the absence of any vacancies, the V_2O_5 crystal has the composition V_2O_4 (Figure 2.9). Nanostructured V_2O_5 anodes have been extensively studied to improve their electrochemical properties, due to their short lithium-ion diffusion lengths, high surface area and large tolerance for volume change caused by lithiation/delithiation, in various forms, including nanofibers [135], nanotubes [136, 137], nanobelts [138], nanorods [139], and nanowires [140]. The weak point of this material, however, is its widely reported limited cycling stability. The reason for the capacity fading is owing to the decomposition of electrolyte (especially the solvent) or the dissolution of V_2O_5, which generates irreversible phases [ε-$Li_xV_2O_5$ ($0.35 < x < 0.7$) and δ-LiV_2O_5] during cycling [141]. While dopant

cations could improve the cycling stability of the vanadium oxides, the doped materials suffer from lower capacity [142, 143].

Other kinds of vanadium oxides have also attracted considerable attention as electrode materials for LIBs, such as V_2O_3, V_6O_{13}, $LiVO_2$, LiV_3O_8, and Li_3VO_4. More details on these vanadium oxides can be found in references [144-148].

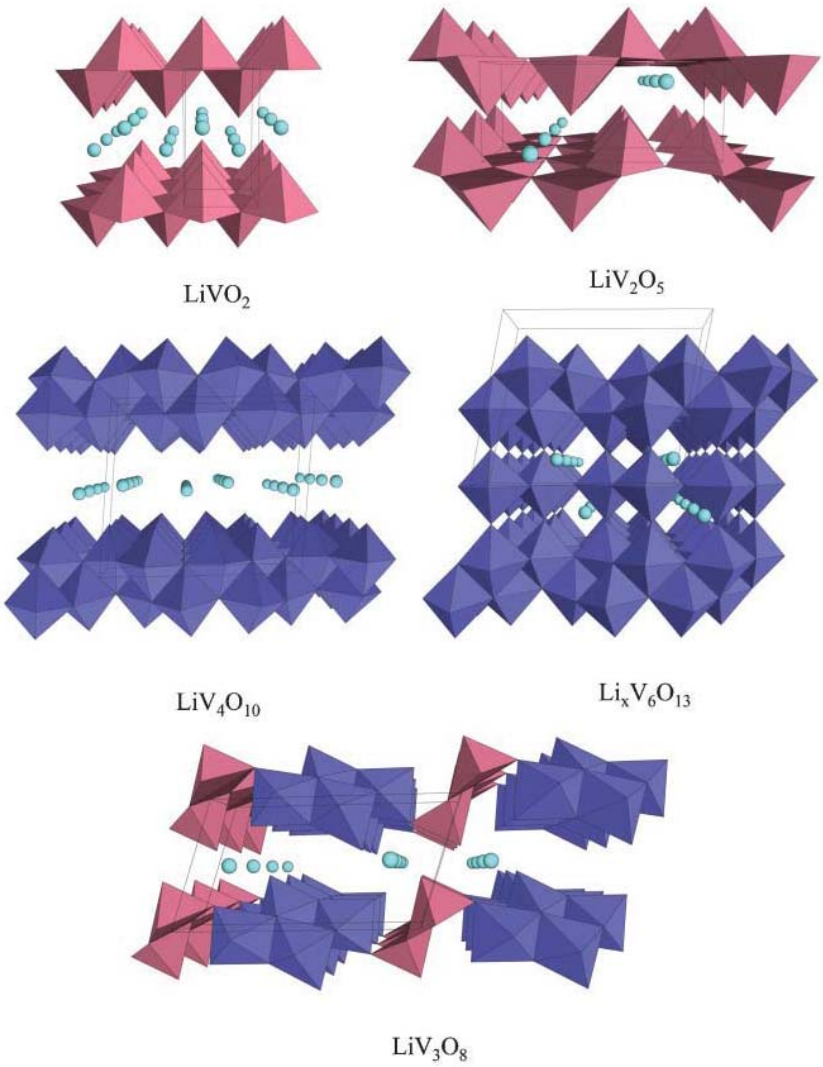

Fig. 2.9 Structures of layered $LiVO_2$, LiV_2O_5, double sheet LiV_4O_{10}, V_6O_{13}, and LiV_3O_8. VO_5 square pyramids are pink, VO_6 octahedra are blue, and lithium atoms are green [149].

2.3 Anode Materials

Graphitic carbon anodes have been and still are being used as the main anode materials in the commercial LIBs due to their extremely low cost, excellent cycling stability and reliability, and environmental friendliness since their advent at the end of the 1980s [150]. With the increasing requirement for larger capacity and higher lithium diffusion rates in LIBs, researchers have changed their focus to finding alternative anode materials in recent years. The alternative materials for anode in LIBs can be divided into three major groups: carbonaceous materials, metal alloy materials, and metal oxides [151, 152]. The target for developing new anode materials is to obtain higher specific capacity than that of the current 372 mAh g^{-1}, while keeping the excellent properties of carbonaceous materials including low cost, cycling stability, and good safety features.

2.3.1 Carbonaceous Materials

Carbonaceous materials, which have been widely studied, are the most promising candidate anode materials for LIBs. Carbon is one of the few elements known since antiquity, which has various forms, such as graphite, diamond, and carbon nanotube (CNT) (Figure 2.10) [153-155]. The discovery of graphene has propelled the research on carbon into a new era, especially on its use in LIBs [156, 157]. In addition, disordered carbon and amorphous carbon have also been the objects of great efforts for developing high capacity anode materials.

Graphite is regarded as the first successful example of LIB anode among the carbonaceous anode materials [158]. Lithium-ions are inserted into the graphitic layers, forming the compound LiC_6 without any major resulting structural changes. In the half-cell reaction coupled with lithium, the discharge process involves lithium-ion intercalation into carbon, while in contrast, the lithium-ion de-intercalation process corresponds to the charge step:

$$C_n + xLi^+ + xe^- \leftrightarrow Li_xC_n \quad (0 \le n \le 6) \tag{2.12}$$

The theoretical capacity is 372 mAh g^{-1}, and the discharge plateau voltage is ~ 0.1 V *vs.* Li^+/Li, which is close to the metallic lithium voltage (0 V *vs.* Li^+/Li). It worth noted that irreversible capacity loss occurs during the first charge step of all types of carbonaceous materials. The reason is that the electrolyte decomposition results in the formation of solid electrolyte interphase (SEI) on the electrode surface [159, 160]. The SEI mainly forms at the first cycle and prevents further electrolyte decomposition, which maintains the continuous operation of the carbon anode. The main drawback of the graphite anodes is the poor thermal stability of the lithiated graphite, which prevents its using for large-scale batteries such as for EVs and HEVs.

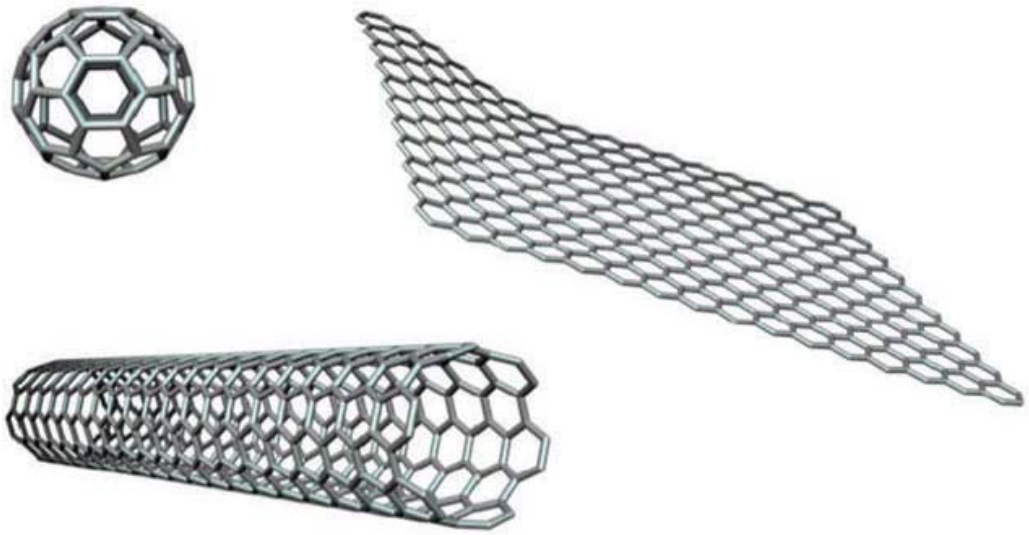

Figure 2.10 Chemical structures of fullerenes (0D), single wall carbon nanotubes (1D), and graphene (2D) [161].

The CNTs, with high length-to-diameter ratio (diameter less than 100 nm), represent a potential new paradigm in carbonaceous-based battery electrode materials due to their high capacity (exceeding 600 mAh g^{-1}) [162]. The CNTs can be either single-walled carbon nanotubes (SWCNTs), double-walled carbon nanotubes (DWCNTs), or multi-walled carbon nanotubes (MWCNTs) [163]. These one-dimensional (1D) anode materials have high

surface-to-volume ratios and a nanosized lithium-ion diffusion length, which will efficiently increase the kinetic properties of LIBs. These properties would radically improve the cycling stability, capacity retention, and rate capability of LIBs. It is reported that it is possible to charge SWCNTs up to one lithium for every three carbon atoms and higher [164, 165]. The CNTs show high capacity of up to 1400 mAh g^{-1} in the first cycle. Although a large amount of this capacity is irreversible, lithium capacities of CNT anode material have been determined experimentally to reach higher than 600 mAh g^{-1} [166]. The large hysteresis in voltage during charge and discharge processes, however, currently restricts the application of CNTs.

Graphene was first isolated and characterized by Nobel Prize winners Andre Geim and Konstantin Novoselov in 2004 through an adhesive tape method [167]. Graphene is pure carbon in the form of a very thin, nearly transparent sheet, one atom thick. Graphene is widely used in the semiconductor, electronics, battery, energy, and composites industries, and sales reached $9 million by 2014. As a single sheet of graphitic carbon, graphene shows great advantages due to its high surface area, good conductivity, and good mechanical properties [168]. In 1958, Hummers used a simple oxidation method to obtain graphitic oxide [169], which paved the way to achieving large-scale production of graphene. Yoo's group first tested the LIB performance of graphene nanosheets in 2008 [7]. Although graphene shows the capacity of 540 mAh g^{-1} which is much shorter than that of the theoretical capacity of 744 mAh g^{-1}, the capacity of graphene with 2-3 layers reached 650 mAh g^{-1}, as reported by Wang's group in 2009 [170, 171]. From then on, research based on graphene and graphene composite materials has increased exponentially, especially for LIBs and other types of electrochemical energy storage systems.

2.3.2 Lithium-Metal Alloy Materials

Lithium can electrochemically react with a number of metallic and semi-metallic elements to form lithium-metal alloys. The reaction is usually described by the following reversible process:

$$Li_xM \leftrightarrow M + xLi^+ + xe^- \quad (2.13)$$

where *M* represents the elements from the groups IV and V, such as Si, Sn, Ge, Pb, P, As, Sb, and Bi, as well as other metal elements, such as Al, Au, In, Ga, Zn, Cd, Ag, and Mg [5, 172]. Among them, Si, Sn, and Ge are the three most popular anode materials (Figure 2.11) [173-175]. The main problem with these lithium-metal-alloy materials, however, is the huge volume change during in the lithiation/delithiation processes. The significant volume changes result in an unstable SEI layer, which makes it prone to cracks caused by the mechanical stress and further degrades the cycling stability of LIBs.

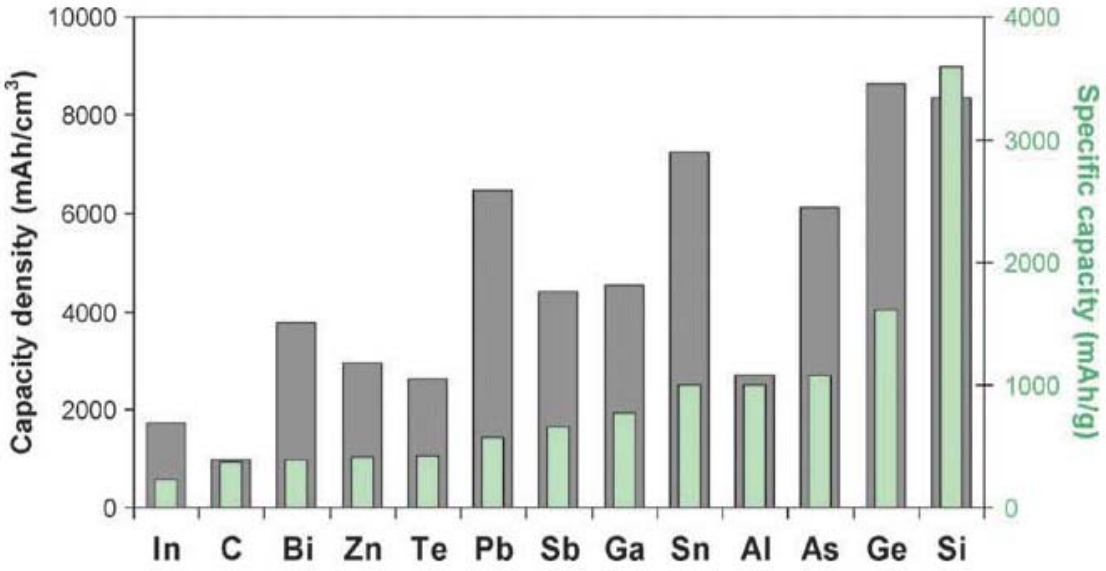

Figure 2.11 Specific volumetric and gravimetric capacities for selected alloying reactions. Values for graphite are given as a reference [176].

Si is regarded as the most studied anode material for high energy density LIBs, due to its low

discharge potential (0.06 V vs. Li^+/Li) and high theoretical specific capacity (4200 mAh g^{-1}, $Li_{22}Si_5$ phase) [177]. The large volume changes (up to 420 % for the $Li_{22}Si_5$ phase), however, and low Coulombic efficiency at the initial cycle prevent the large-scale commercial application of Si anode materials in LIBs. The reason for the low Coulombic efficiency is that new SEI layers are prone to form on the fresh surfaces arising from the cracks and pulverization. After great research efforts, three main strategies have been proposed to overcome the huge volume changes and maintain the structural integrity: 1) preparing unique nanostructures, 2) introducing a second component to form nanocomposites, 3) preparing an alloy with a second phase, which is there to absorb the massive volume changes during charge/discharge processes [178-180]. In 2008, Chan and co-workers successfully synthesized Si nanowires, and the recorded capacity of the Si nanowire anode was more than 3000 mAh g^{-1} and remained stable for 10 cycles with negligible capacity fading [173]. Unfortunately, its cycle life still needs to improve. Ni-Si alloy, dispersed in a conductive carbon matrix, shows higher cycling stability. Ni-Si/graphite anode exhibited a reversible capacity of 830 mAh g^{-1} and still retained 730 mAh g^{-1} after 40 cycles [181, 182]. Moreover, Cui and his co-workers introduced an additional mechanical clamping layer to tolerate the volume changes and form a stable SEI layer [183]. The double-wall Si nanotube anode demonstrated high electrochemical performance with long cycle life (6000 cycles with 88 % capacity retention), as well as high specific charge capacity (2970 mAh g^{-1} at 0.2 C) and high rate capability (up to 20 C). Additionally, high performance binder is also a new choice for improving the cycling performance of the Si and Si composite anode materials.

Germanium is regarded as the least studied element for application in LIBs, due to its expensive price. Germanium shows superior electrochemical properties, however, as an anode material for LIBs in comparison with Si anode materials [184]. The theoretical capacity of germanium (1620 mAh g^{-1}, corresponding to $Li_{22}Ge_5$ phase) is much higher than

that of graphite. Germanium is also exhibits high electronic conductivity (104 times greater) and lithium diffusion efficiency (400 times greater) compared to silicon. Additionally, the surface of germanium is stable in air as compared to Si. These features give germanium anode high power and high energy density. Nevertheless, germanium anode also encounters the problem of the volume changes during discharge/charge processes, which results in capacity decay. The approaches for resolving the volume changes are similar to those used for other lithium-metal-alloy materials, including preparing nanosized materials [185], intermetallic alloys [186], and carbon-coated germanium composites [187]. Seng and his group prepared hollow germanium/carbon nanostructured anode by a facile method, which shows high electrochemical performance with high specific charge capacity (1200 mAh g^{-1} at 0.2 C), long cycle life (120 cycles with 900 mAh g^{-1} capacity remaining), and high rate capability (up to 40 C) [188].

2.3.3 Metal Oxides

Various metal oxides have been intensively studies for development as potential anode materials for LIBs, because these materials show different chemical and physical properties. Usually, metal oxide anodes can deliver high reversible capacities (500 - 1000 mAh g^{-1}). Metal oxide anode materials can be divided into three categories according to their reaction mechanisms: 1) lithium alloy reaction mechanism, 2) lithium-ion insertion/extraction reaction mechanism, and 3) conversion reaction mechanism, which involves the formation and decomposition of Li oxide (Li_2O) [21]. The three reaction mechanisms are listed as follows:

Lithium alloy reaction mechanism:

$$M_xO_y + 2yLi^+ + 2ye^- \rightarrow xM + yLi_2O \quad (2.14)$$

$$M + zLi^+ + ze^- \leftrightarrow Li_zM \quad (2.15)$$

Insertion reaction mechanism:

$$MO_x + yLi^+ + ye^- \leftrightarrow Li_yMO_x \quad (2.16)$$

Conversion reaction mechanism:

$$M_xO_y + 2yLi^+ + 2ye^- \leftrightarrow xM + yLi_2O \quad (2.17)$$

Lithium alloy reaction mechanism

SnO_2 is the representative metal oxide in this group. On the first discharge process, SnO_2 reacts with lithium-ions to form Li_2O and metallic Sn, a reaction which is irreversible and consumes lithium-ions [189, 190]. Then, the metallic Sn reacts with lithium-ions to form an alloy with an upper-limit of $Li_{4.4}Sn$, corresponding to the theoretical capacity of 783 mAh g^{-1}. During the continuous cycling, however, the Sn phase particles generated from the delithiation of the lithium-tin alloy are prone to aggregate with each other and form clusters. This phenomenon causes irreversible capacity fading. This is because the volume changes of Sn destroy the Li_2O matrix that sustains the reduced Sn particles. Considerable efforts has been made to improve the cycling stability of the SnO_2 anode materials, including preparing porous SnO_2 nanostructured materials [191], SnO_2-based nanocomposites [192, 193], and hollow core-shell mesospheres [194-196].

Porous SnO_2 with nanostructures can tolerance volume changes, because the pores act as a structural buffer for the huge volume changes during charge/discharge processes [197]. Hyeon and co-workers prepared SnO_2 microspheres using $SnCl_4 \cdot 5H_2O$ and resorcinol-formaldehyde gel [198]. The SnO_2 microsphere anode achieved a discharge capacity of 952 mAh g^{-1}. The large surface area results in a large irreversible capacity, however. Recently, Zhang and co-workers synthesized carbon-SnO_2 core-sheath composite nanofibers through electrospinning and an electrodeposition method [199]. The resultant anode delivered a

discharge capacity of 800 mAh g^{-1} at the first cycle at 50 mA g^{-1}, retaining 69 % of the capacity after 100 cycles.

Insertion reaction mechanism

Metal oxide anodes with the insertion reaction mechanism are used for LIBs due to their low cost and non-toxicity [20]. The weak point of these anodes is that the number of lithium-ions involved in the insertion reaction is generally less than one per formula unit because lithium can only occupy the vacant sites in the frameworks of these crystals. So, this kind of metal oxide shows low specific capacity. TiO_2 is a typical metal oxide which can store lithium through the insertion reaction mechanism. The reaction can be described as follows:

$$TiO_2 + xLi^+ + xe^- \leftrightarrow Li_xTiO_2 \quad (0 \le x \le 1) \tag{2.18}$$

TiO_2 has the theoretical capacity of 336 $mAhg^{-1}$ and a high lithium intercalation potential (1.75 V vs. Li^+/Li), enabling it to avoid the deposition of metallic lithium. TiO_2 has different phases including anatase, rutile, and TiO_2-B [200-202]. Anatase is the most promising anode material because it is the most electroactive lithium-ion host and has fast lithium-ion insertion/extraction kinetics. Anatase TiO_2 nanotube anode is generally considered the most attractive anode material. Wang and co-workers synthesized TiO_2 nanotubes with mesoporous walls, which delivered a discharge capacity of 340 mAh cm^{-3} [203]. The TiO_2 nanotube structure provided the fast lithium-ion and electron transfer pathways which have a strong influence on the rate capability of LIBs.

Conversion reaction mechanism

Poizot and co-workers proposed another series of anode candidates based on transition metal oxides (M_xO_y, where M = Fe, Co, Ni, Cu, Mn, Mo, Ru, etc.) with high reversibility and cycling stability [20]. According to Equation (2.17), transition metal oxides react with

lithium-ions to form Li_2O and metallic nanoparticles during the lithiation process, and then the reaction product are reversibly returned to their initial states after delithiation.

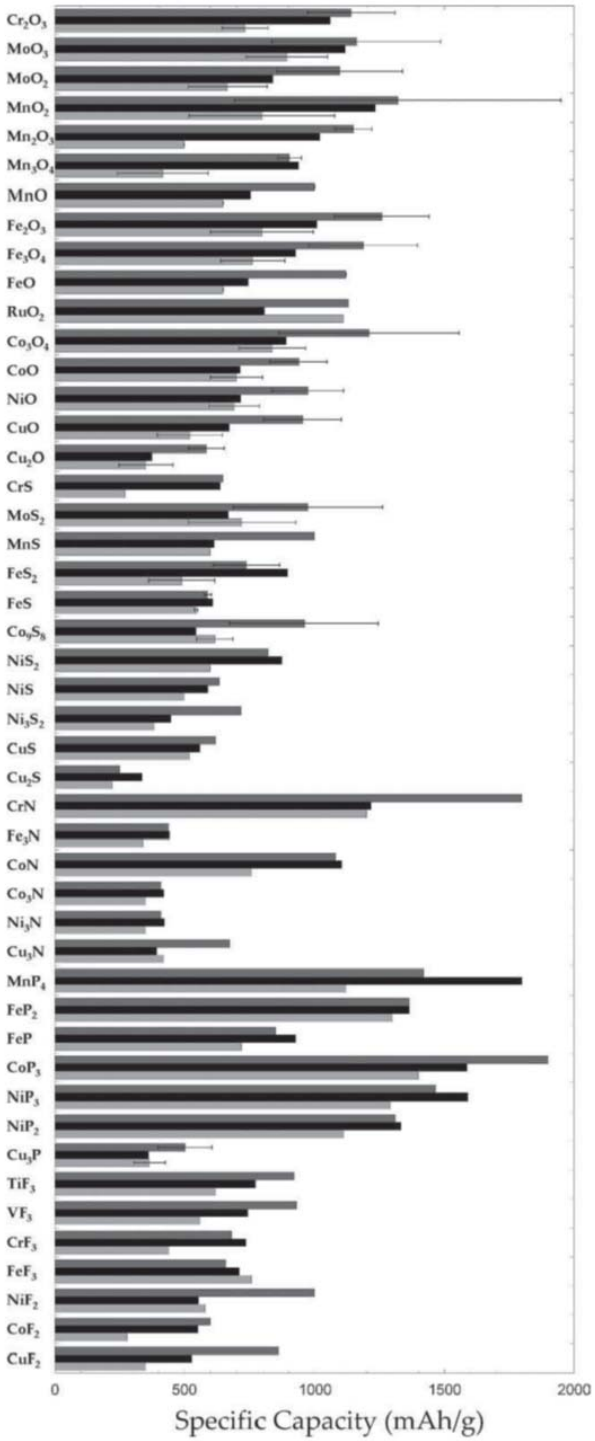

Figure 2.12 Theoretical (black bars), first discharge (dark grey), and first charge (light grey) specific gravimetric capacities of different compounds that react with lithium through a

conversion reaction. The "error" bars are provided as an indication of the dispersion of values observed in the literature [204].

Generally, the oxidation state utilizes more than one electron in the conversion reaction, so that the transition metal oxide anodes show high energy density and high discharge capacity (Figure 2.12) [152]. Transition metal oxide anodes still faces several challenges, however, so that their cannot achieve commercial application in LIBs. The disadvantages include: 1) low Coulombic efficiency at the first cycle (> 20%), consuming large amounts of lithium; 2) unstable SEI film formation, resulting from the large volume expansion accompanying the conversion reaction; 3) large voltage hysteresis during discharge/charge processes [31, 204]. Preparing nanostructured transition metal oxides and transition metal oxide nanocomposites are effective solutions to improve the electrochemical performance of transition metal oxide anodes.

Fe_2O_3 has a total theoretical capacity of 1007 mAh g^{-1} by the formation of Fe^0 from Fe^{3+}. Lou's group synthesized polycrystalline α-Fe_2O_3 nanotubes by a one-step template-engaged precipitation method [205]. These nanotube anodes exhibited the large discharge capacity of 1377 mAh g^{-1} at the first cycle at 0.5 C and over 1000 mAh g^{-1} after 50 cycles. Cobalt oxide (Co_3O_4) also has relatively high theoretical capacity of 890 mAh g^{-1}. Self-supported Co_3O_4 nanowire arrays were reported as anode materials by Wu and co-workers [206], which exhibited large discharge capacities of approximately 1124 mAh g^{-1} at the first cycle at 1 C, maintaining a stable capacity of 700 mAh g^{-1} after 20 cycles. V_2O_3 is another transition metal oxide with a Li insertion storage mechanism, which shows a a high theoretical capacity of 1070 mAh g^{-1} as an anode material in LIBs [144, 207, 208]. The first discharge process vause amorphization of the host structures, however, which shows the poor kinetics associated with the energy barrier and breakage of the metal-oxygen (M-O) bonds. This poor

kinetic performance causes large electrode polarization. Although the potential applicability of the transition metal oxides need to be confirmed, the important role of nanomaterials and nacomposites has been clearly elaborated.

2.4 Electrolyte

The role of the electrolyte is to ensure effective lithium-ions transport while possessing the feature of electronic insulation. In terms of LIBs, the electrochemical stability of the electrolyte during charge/discharge processes is highly related to kinetic rather than thermodynamic factors. Also, the electrolyte need to endure the strong oxidizing and reducing characteristics of the electrodes. As a main component of the LIB, the choice of electrolyte is critically important for the cell operation. For LIB application, electrolytes can be divided into numerous categories, such as organic liquid electrolyte, inorganic liquid electrolyte, ionic liquid electrolyte, organic solid electrolyte, and inorganic solid electrolyte [45, 176, 209-215]. Table 2.1 shows the typical electrolytes and their key properties. The key requirements must be considered carefully for choosing electrolytes, and the requirements below should be fulfilled as far as possible:

1) stability of the electrolyte/electrode interface during cycling,

2) high ionic conductivity ($\sigma_{Li} > 10^{-4}$ S cm^{-1}) and low electronic conductivity ($\sigma_e < 10^{-10}$ S cm^{-1}),

3) transference number $\sigma_{Li+}/\sigma_{total} \approx 1$, where σ_{total} is the sum of the conductivities of all the other ions in the electrolyte ($\sigma_{Li} + \sigma_e$),

4) suitability for large ambient temperature ranges,

5) the ability to rapidly form a passivating SEI layer,

6) safety (non-toxic, non-flammable, and environmentally friendly),

7) low cost.

Table 2.1 Non-aqueous electrolyte systems for LIBs [31].

Electrolytes	Classical electrolytes	Ionic conductivity (10^{-3} s cm^{-1}, 25 °C)	Electrochemical Windows vs. Li^+/Li		Remark
			Reduction	Oxidation	
Liquid organic	1M $LiPF_6$ in EC : DEC (1:1)	7	1.3	4.5	Flammable
	1M $LiPF_6$ in EC:DMC (1:1)	10	1.3	> 5.0	
Liquid ionic	1M LiTFSI in EMI-TFSI	2.0	1.0	5.3	Non-flammable
	1M $LiBF_4$ in EMI-BF_4	8.0	0.9	5.3	
Polymer	LiTFSI-(PEO/MEEGE)	0.1	< 0.0	4.7	Flammable
	$LiClO_4$-PEO_8 + 10 wt. % TiO_2	0.02	< 0.0	5.0	
Inorganic solid	$Li_{4-x}Ge_{1-x}P_xS4$ (x = 0.75)	70	< 0.0	> 5.0	Non-flammable
	0.05 $Li4SiO_4$ + 0.57Li_2S + 0.38 SiS_2		< 0.0	> 8.0	
Inorganic liquid	$LiAlCl_4$ + SO_2	4.2	--	4.4	Non-flammable
Inorganic liquid + Polymer	0.04 $LiPF_6$ + 0.2 EC + 0.62 DMC + 0.14 PAN	3.0	--	4.4	Flammable
	$LiClO_4$ + EC + PC + PVdF		--	5.0	
Ionic liquid + Polymer	1M LiTFSI + P13TFSI + PVdF-HFP	0.18	< 0.0	5.8	Less Flammable
Ionic liquid + Polymer + Liquid organic	56 wt. % LiTFSI-Py24TFSI + 30 wt. % PVdF-HFP + 14 wt. % EC/PC	0.81	1.5	4.2	Less Flammable
Polymer +Inorganic solid	2 vol % $LiClO_4$-TEC-19 + 98 vol% 95 (0.6Li_2S + 0.4Li_2S) + 5$Li4SiO_4$	0.03	< 0.0	> 4.5	Non-flammable
Ionic liquid + Liquid organic		--	--	--	Non-flammable

2.4.1 Lithium Salts

The typical lithium salts which used as the solutes in the electrolytes along with their basic physical properties are listed in Table 2.2. Most of the lithium salts are suitable for use in carbonate solvent, and each of them exhibits some specific properties. $LiBF_4$ is a kind of salt with an inorganic super acid anion, which shows stable ionic conductivity in non-aqueous solvents [216]. $LiAsF_6$ is similar to $LiBF_4$, whereas the toxicity of As restricts its commercial

application [217]. $LiClO_4$ shows satisfactory solubility and high chemical stability (toward ambient moisture), as well as high ionic conductivity (~ 9.0 mS cm^{-1} in ethylene carbonate/ dimethyl carbonate (EC/DMC) at 20 ^oC) [218]. Li-triflate also exhibits excellent chemical stability, however, the property of serious aluminum corrosion is a real obstacle to LIB application [219]. Li-imide also possesses good electrochemical performance, including a high dissociation constant, high safety, thermal stability, and high ionic conductivity [220]. Regrettably, Li-imide results in severe Al corrosion in electrolytes. Among these numerous salts used for LIBs, $LiFP_6$ (lithium hexafluorophosphate) is the obvious winner and the most commonly used salt in commercial LIBs, which exhibits the best combination of the above-mentioned properties [221].

Table 2.2 Lithium salts as electrolyte solutes [209].

Salt	Structure	M. Wt. g mol^{-1}	T_m ^oC	$T_{Decomp.}$ ^oC In solution	Al corrosion	σ/mS m^{-1} (1.0M, 25^oC)	
						In EC	DMC
$LiBF_4$	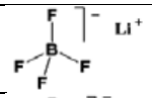	93.9	293	> 100	N	3.4	4.9
$LiPF_6$	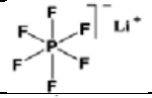	151.9	200	~ 80	N	5.8	10.7
$LiAsF_6$	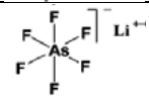	195.9	340	> 100	N	5.7	11.1
$LiClO_4$	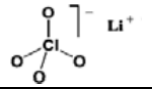	106.4	236	>100	N	5.6	8.4
Li Triflate	$Li^+CF_3SO_3^-$	155.9	> 300	> 100	Y	1.7	
Li Imide	$Li^+[N(SO_2CF_3)_2]^-$	286.9	234	> 100	Y	5.1	9.0
Li Beti	$Li^+[N(SO_2CF_2CF_3)_2]^-$				N		

2.4.2 Organic Liquid Electrolytes

Carbonates are the most popular solvents for commercial LIBs, which have an oxidation potential [highest occupied molecular orbital (HOMO)] at 4.7 V vs. Li^+/Li and a reduction potential [lowest unoccupied molecular orbital (LUMO)] at ~ 1.0 V vs. Li^+/Li [222-224].

Also, the carbonate solvents show a relatively low viscosity, resulting in low activation energy for lithium-ion diffusion. The most commonly used electrolyte solvents are alkyl carbonates or alkyl carbonate blends containing one or more of the following: ethylene carbonate (EC) and either dimethyl carbonate (DMC), diethyl carbonate (DEC), ethyl methyl carbonate (EMC) or propylene carbonate (PC) [225, 226]. Figure 2.13 shows the structural formulae for these electrolyte solvents. These alkyl carbonates, combined with the lithium salt ($LiPF_6$), are regarded as the basic standard electrolyte solutions for LIBs.

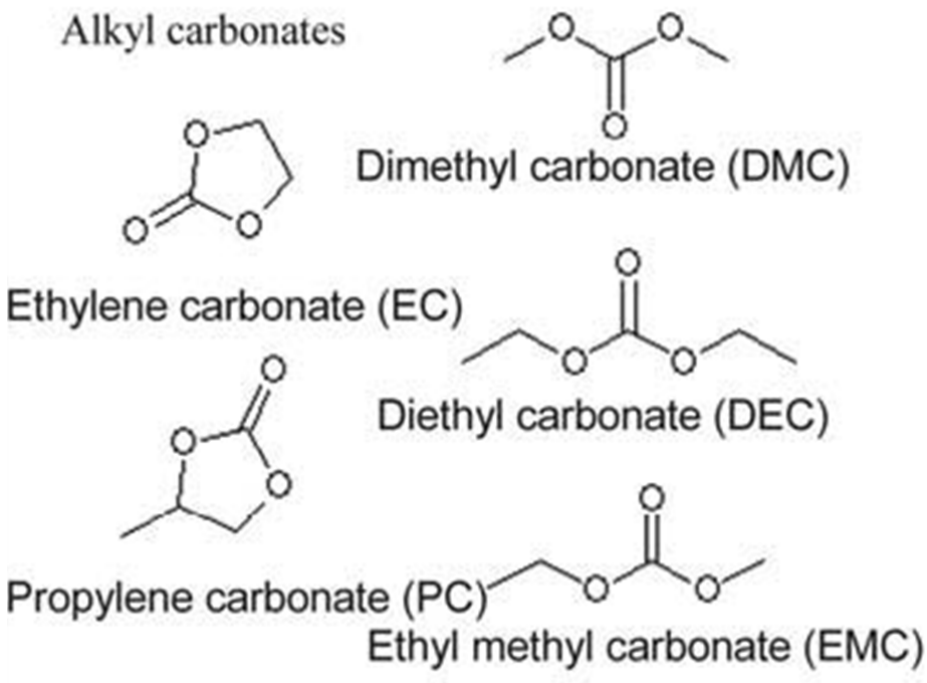

Figure 2.13 Typical alkyl carbonate solvents used in electrolyte in Li-ion batteries [2].

The alkyl carbonate electrolytes exhibit the following advantages: 1) high ionic conductivity, 2) high anodic stability, and 3) high chemical stability. Aluminum foil is the most common current collector for cathodes in LIBs. In $LiPF_6$ solutions, the PF_6 anions can react with aluminum and generate a passivated layer (AlF_3 and $Al(PF_6)_3$) on the surface of the active aluminum metal. The passivated layer shows a high polarization voltage (up to 5 V vs. Li^+/Li), even at 60 ^oC. Another important advantage is: 4) highly conductive SEI formation. Taking the $LiFP_6$ in EC/DMC electrolyte as an example, $ROCO_2Li$ and ROLi will generate

and form a stable precipitate network on the anode, which is highly passivating (Table 2.3) [227-229].

Table 2.3 Major reduction products of non-aqueous Li salt solutions [21].

Solution species	Main reduction products (not all)	Potential range vs. Li^+/Li
O_2	LiO_2, Li_2O_2	1.5 – 2 V
H_2O	LiOH	1.5 – 1.2 V
HF, PF_5	LiF, Li_xPF_y	1.8 V and below
Ethers	ROLi	Below 0.5 V
Esters	$ROCO_2Li$	Below 1.2 V
Alkyl carbonates	$ROCO_2Li$, ROLi	Below 1.5 V
EC	$(CH_2OCO_2Li)_2$, C_2H_4	Below 1.5 V
PC	$CH_3CH(OCO_2Li)$ CH_2OCO_2Li $CH_3CH=CH_2$	Below 0.5 V
DMC	CH_3OCO_2Li,CH_3OLi	Below 1.2 V
$LiClO_4$	LiCl, $LiClO_x$	Below 1 V
$LiPF_6$	LiF, Li_xPF_y	Below 1 V
LiN $(SO_2CF_3)_2$	LiF, $LiCF_3$, $LiSO_2CF_3$ $Li_2NSO_2CF_3$	Below 1 V

Alkyl carbonate electrolytes are also handicapped by several disadvantages, however, including: 1) The ionic conductivity is temperature sensitive. For example, the ionic conductivity of EC drops significantly below -20 ^oC. 2) The carbonate-based solvents are flammable. 3) $LiPF_6$ is vulnerable to decomposition in these electrolytes. Some of the $LiPF_6$ is prone to decompose into LiF and PF_5 (strong Lewis acid). PF_5 is sensitive to trace amounts of H_2O, resulting the formation of HF and PF_3O (strong Lewis acid), which will reduce the cell life.

2.4.3 Inorganic Liquid Electrolytes

Stassen and Hambitzer proposed the inorganic liquid electrolytes, which have good ionic conductivity (7×10^{-2} S cm^{-1} at room temperature) and are non-flammable [230]. The inorganic liquid electrolytes suffer from a very low electrochemical window (~ 1.2 V, SHE), since they are subject to water decomposition. This feature restricts the application of the

inorganic liquid electrolytes.

2.4.4 Ionic Liquid Electrolytes

Room-temperature ionic liquids (RTILs) have been regarded as promising alternative electrolytes for LIBs due to their high oxidation potential (~5.3 V vs Li^+/Li), non-flammability, low vapor pressure, good chemical and thermal stability, and high Li-salt solubility [231, 232]. Several typical families of relevant RTILs are listed, including the structural formulae and physical properties. RTILs usually exhibit high viscosity, however, which reduces their lithium-ion conductivity and the wettability of the electrodes and separator. RTILs based on imidazolium-based cations are the predominant candidates for LIBs because of their lower viscosity and high Li-salt solubility. Nevertheless, RTILs show unsatisfactory stability at voltages below 1.1 V vs. Li^+/Li [233, 234]. One approach to overcome this is the use of additives [fluorinated EC or vinylene carbonate (VC)] to form a stable SEI layer on a carbon anode. Another alternative approach is to increase the concentration of lithium-ions, such as by adding a liquid carbonate to RTILs. Additionally, the high price of RTILs also limits their large-scale application in LIBs.

Table 2.4 Important families of ionic liquids and their physical properties [2].

Cation	Anion	Melting point (°C)	Density/g cm^{-3} (20°C)	Viscosity/mPa s (25 °C)	Conductivity σ, 10^{-4} S cm^{-1} (25 °C)
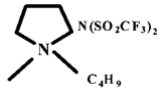	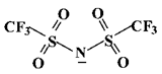	-18	1.41	85	22
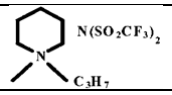	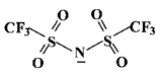	8.7	1.43	117	15.1
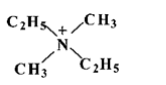	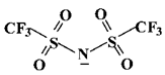	-14	1.41	83	12
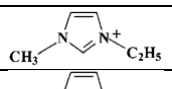	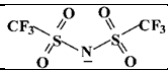	-15	1.52	34	87
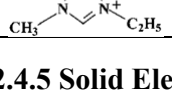	BF_4	13	1.28	37	140

2.4.5 Solid Electrolytes

Solid electrolytes have attracted much attention because they simplify the battery design and increase the lifetime and safety of the batteries [235]. Solid electrolyte is a kind of fast lithium ion conductor. Solid electrolytes possess a regular structure with immobile ions, while liquid electrolytes have no regular structure and fully mobile ions. Solid electrolytes for LIBs include many materials such as oxide, sulfide, and polymer materials [236]. The ionic conductivity of typical oxide, sulfide, and polymer solid electrolytes are listed in Table 2.8. Solid electrolytes can be divided into two categories: inorganic solid electrolytes and solid polymer electrolytes.

Table 2.5 Conductivity of oxide, sulfide, and polymer-based solid electrolytes for all-solid-state LIBs [45, 211-215].

Composition (oxide)	**Conductivity at 25°C (S cm^{-1})**	**Classification**	**Reference**
$LiNbO_3$	1×10^{-5}	Amorphous (thin film)	45
$LiTaO_3$	8×10^{-8}	Crystalline (thin film)	
$Li_{1.3}Al_{0.3}Ti_{1.7}(PO_4)_3$	7×10^{-4}	Crystal (NASICON)	211
$La_{0.51}Li_{0.34}TiO_{2.94}$	1.4×10^{-3}	Crystal (perovskite)	
$Li_7La_3Zr_2O_{12}$	3×10^{-4}	Crystal (garnet)	
$50Li_4SiO_4 \cdot 50Li_3BO_3$	4.0×10^{-6}	Glass	
$Li_{2.9}PO_{3.3}N_{0.46}$	3.3×10^{-6}	Amorphous (thin film)	
$Li_{3.6}Si_{0.6}P_{0.4}O_4$	5.0×10^{-6}	Amorphous (thin film)	
$Li_{1.07}Al_{0.69}Ti_{1.46}(PO_4)_3$	1.3×10^{-3}	Glass–ceramic	
$Li_{1.5}Al_{0.5}Ge_{1.5}(PO_4)_3$	4.0×10^{-4}	Glass–ceramic	
Composition (sulfide)	**Conductivity at 25°C (S cm^{-1})**	**Classification**	
$Li_{10}GeP_2S_{12}$	1.2×10^{-2}	Crystal	212
$Li_{3.25}Ge_{0.25}P_{0.75}S_4$	2.2×10^{-3}	Crystal	
Li_6PS_5Cl	1.3×10^{-3}	Crystal (argyrodite)	
$30Li_2S \cdot 26B_2S_3 \cdot 44LiI$	1.7×10^{-3}	Glass	
$50Li_2S \cdot 17P_2S_5 \cdot 33LiBH_4$	1.6×10^{-3}	Glass	
$63Li_2S \cdot 36SiS_2 \cdot 1Li_3PO_4$	1.5×10^{-3}	Glass	
$70Li_2S \cdot 30P_2S_5$	1.6×10^{-4}	Glass	
$Li_7P_3S_{11}$	1.1×10^{-2}	Glass–ceramic	
$Li_{3.25}P_{0.95}S_4$	1.3×10^{-3}	Glass–ceramic	
Composition (polymer based)	**Conductivity at 25°C (S cm^{-1})**	**Classification**	
21PAN-33PC-38BL-8$LiClO_4$	3.71×10^{-3}	Polymer	213
21PAN-33PC-10EC-18BL-10NMP 8$LiClO_4$	2.57×10^{-3}	Polymer	
21PAN-33PC-20EC-18BL-8$LiAsF_6$	3.87×10^{-3}	Polymer	
MEEP-$(LiClO_4)_{0.25}$	1.7×10^{-5}	Polymer	
MEEP-$(LiBF_4)_{0.25}$	1.5×10^{-5}	Polymer	214
MEEP-$Li(CF_3SO_3)_{0.25}$	1.5×10^{-5}	Polymer	

MEEP-$[LiN(CF_3SO_2)_2]_{0.13}$	6.5×10^{-5}	Polymer	
55MEEP/45PEO-$(LiClO_4)_{0.13}$	1.3×10^{-6}	Polymer	
55MEEP/45PEO-$(LiBF_4)_{0.13}$	2.4×10^{-5}	Polymer	
55MEEP/45PEO-$(LiCF_3SO_3)_{0.13}$	1.0×10^{-5}	Polymer	
55MEEP/45PEO-$(LiNCF_3SO_2)_{0.13}$	6.7×10^{-5}	Polymer	
55aMEEP/45PEO-(LiAsF6)0.13	1.9 · 107	Polymer	
87aMEEP/13PEGDA-(LiClO4)0.13	1.2 · 106	Polymer	
87aMEEP/13PVP-(LiClO4)0.13	4.0 · 106	Polymer	
ALPE 1	0.09× 10−3	Polymer	215
ALPE 2A-1 DEC.	0.11× 10−3	Polymer	
ALPE 2A-6 DEC.	0.12× 10−3	Polymer	
ALPE 3A-1 DMC.	0.20× 10−3	Polymer	
ALPE 4A-1 EC.	1.90× 10−3	Polymer	
ALPE 5A-1 PC.	1.00× 10−3	Polymer	

Inorganic solid electrolytes

In contrast to the more robust technology for liquid electrolytes, the inorganic solid electrolytes for LIBs are still in their infancy. The inorganic solid electrolytes cannot compare with the commercial liquid electrolytes. Although the ionic conductivity of selected inorganic solid electrolytes (1.2×10^{-2} S cm^{-1} for $Li_{10}GeP_2S_{12}$) has theoretically approached the level of commercial organic liquid electrolytes (10^{-2} S cm^{-1}), in practice, grain boundary resistance and electrode/electrolyte interface resistance decrease it to less than 10^{-5} S cm^{-1} [210]. Perovskite $Li_{3x}La_{(2/3)-x}TiO_3$ exhibits ionic conductivity as high as 10^{-3} S cm^{-1} at room temperature, which is also restricted by the grain boundary resistance that is essentially associated with the high temperature synthesis method [237]. $Li_{1+x}M_{2-x}A_x(PO_4)_3$ (M = Ti, Ge, Hf and Zr; A = Sc, Al) species are also fascinating candidates due to their high conductivities (up to 7×10^{-4} S cm^{-1}) [238]. Regretfully, these inorganic solid electrolytes suffer from titanium reduction at low potential. $Li_7La_3Zr_2O_{12}$ is another potential electrolyte for use in all-solid-state LIBs, and it is a garnet type fast lithium ion conductor with conductivity of 5×10^{-4} S cm^{-1}. $Li_7La_3Zr_2O_{12}$ exhibits stable electrochemical properties at potentials as high as 5.5 V vs Li^+/Li [222]. In addition, glass ceramic sulfides (Li_2S-P_2S_5) have also attracted great

interest, due to their high ionic conductivity (10^{-3} S cm^{-1}) [239]. It is worth noting that glass ceramic sulfides are sensitive to air and moisture.

Recently, $LiNbO_3$ and $LiTaO_3$ have recently gained attention because these materials can be applied as buffer layers in all-solid-state LIBs. Glass et al. reported that $LiNbO_3$ and $LiTaO_3$ could be considered as a solid state electrolyte (SSE) in 1978, because they exhibit high room-temperature ionic conductivity (10^{-5} S cm^{-1} and 10^{-8} S cm^{-1}, respectively) and low electronic conductivity (10^{-11} S cm^{-1}) [240]. Meanwhile, these materials show excellent optical and electrical properties, so that numerous methods have been reported for the synthesis of these materials, including the so-gel method, pulsed laser deposition, chemical vapor deposition, sputter deposition, and the solid-state reaction method. The $LiNbO_3$ and $LiTaO_3$ electrolytes are handicapped by several crucial problems for battery application, relating to such factors as their Li-ion transference number, mechanical strength, and electrode/electrolyte interface contact. Ohta and co-workers reported that a $LiNbO_3$ buffer layer interposed between $LiCoO_2$ and the sulfide electrolyte significantly decreases the interfacial resistance [241]. Furthermore, Haruyama and co-workers theoretically elucidated the characteristics of this buffer layer in all-solid-state LIBs [242]. The results show that the $LiNbO_3$ buffer layer provides smooth lithium-ion transport paths free from the possible bottlenecks that exist at the electrode/electrolyte interface.

Solid polymer electrolytes

Solid polymer electrolytes can be generally divided into gel polymer electrolytes, dry polymer electrolytes, and solid ceramic-polymer electrolytes. The gel electrolyte is a polymer membrane impregnated with a lithium salt solution [212]. The gel electrolytes have already been used in large-scale and rechargeable macrobatteries, owing to their high ionic conductivity, which is comparable to the performance of liquid electrolyte. The liquid

electrolytes (solvents) incorporated in them restrict the application of gel polymer electrolytes, because they are highly flammable and prone to form a SEI layer resulting in volume change. Therefore, the dry polymer electrolytes were developed, which do not use liquid electrolyte solution [243]. The dry polymer electrolytes often consist of a polymer with high dielectric constant (poly(ethylene oxide), poly(methyl methacrylate), polyacrylonitrile, polyphosphazenes, siloxanes) and a salt with low lattice energy ($LiPF_6$ or $LiAsF_6$), which shows good chemical stability, but low lithium ion conductivity, with $\sigma_{Li+} < 10^{-5}$ S cm^{-1} at room temperature. To further improve the mechanical strength and conductivity of dry polymer electrolytes, solid ceramic-polymer electrolytes were proposed, which consist of a ceramic phase (e.g., $A_{l2}O_3$, TiO_2, SiO_2, or ZrO_2) and a dry polymer matrix [244]. There are two major classes of such electrolytes: polymer-in-ceramic, and ceramic-in-polymer.

Chapter 3 Experiments

3.1 Chemicals and Materials

The chemicals and materials used in this doctoral work are listed in Table 3.1. The details of the suppliers are provided for reference.

Table 3.1 Chemicals and materials used in this thesis.

Materials/Chemicals	Formula	Purity (%)	Supplier
1-methyl-2-pyrrolidinone (NMP)	C_5H_9NO	99.5	Sigma Aldrich
Acetone	CH_3COCH_3	99	Ajax Finechem
Ammonia	$NH_3 \cdot H_2O$	~30	Sigma Aldrich
Aluminium foil	Al	N/A	China
Ammonium fluoride	NH_4F	98+	Sigma Aldrich
Carbon black (Acetylene carbon)	C	N/A	Carbot
Carbon black (Super P)	C	N/A	Timcal Belgium
Carboxymethyl cellulose sodium (CMC)	$C_8H_{16}NaO_8$	N/A	Sigma Aldrich
Citric Acid	$C_6H_8O_7$	99.5	Sigma Aldrich
Copper foil	Cu	N/A	China
CR2032 type coin cells	N/A	N/A	China
Cyclohexane	C_6H_{12}	99.5	Sigma Aldrich
Diethyl carbonate (DEC)	$C_5H_{10}O_3$	99+	Sigma Aldrich
Dimethyl carbonate (DMC)	$C_3H_6O_3$	99+	Sigma Aldrich
Ethanol	C_2H_5OH	99	Ajax Finechem
Ethylene carbonate (EC)	$C_3H_4O_3$	99+	Sigma Aldrich

Materials/Chemicals	**Formula**	**Purity (%)**	**Supplier**
Ethylene glycol	$(CH_2OH)_2$	99.8	Sigma Aldrich
Glucose	$C_6H_{12}O_6$	99	Sigma Aldrich
Iron(III) chloride	$FeCl_3$	97	Sigma Aldrich
Lithium acetate	CH_3COOLi	99.99	Sigma Aldrich
Lithium carbonate	$LiCO_3$	99+	Sigma Aldrich
Lithium hexafluorophosphate	$LiPF_6$	99.99	Sigma Aldrich
Lithium metal	Li	99.9	Sigma Aldrich
Manganese acetate tetrahydrate	$Mn(CH_3COO)_2{\cdot}4H_2O$	99+	Sigma Aldrich
Monomer pyrrole		98	Sigma Aldrich
Milli-Q water	H_2O	5 ppb (TOC)	Millipore USA
Nickel acetate tetrahydrate	$Ni(CH_3COO)_2{\cdot}4H_2O$	99+	Sigma Aldrich
Niobium pentoxide	Nb_2O_5	99.8+	CBMM-Brazil
Polypropylene separator	$(C_3H_6)_n$	Celgard2500	Hoechst Celanese
Polyvinylidene difluoride (PVDF)	$(CH_2CF_2)_n$	N/A	Sigma Aldrich
Pure ethanol	C_2H_5OH	99.95	Sigma Aldrich
Sodium *p*-toluenesulfonate (pTSNa)	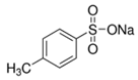	95	Sigma Aldrich
Ti mesh	Ti	99.5	China

3.2 Experimental Procedures

Figure 3.1 presents the experimental procedures used in this doctoral work. This PhD research work mainly consists of two parts: the first part describes the fabrication and

characterization of the as-synthesized nanostructured/composite materials; and in the second part, the as-prepared electrode materials were assembled into coin-type cells, and their electrochemical properties were tested in LIBs.

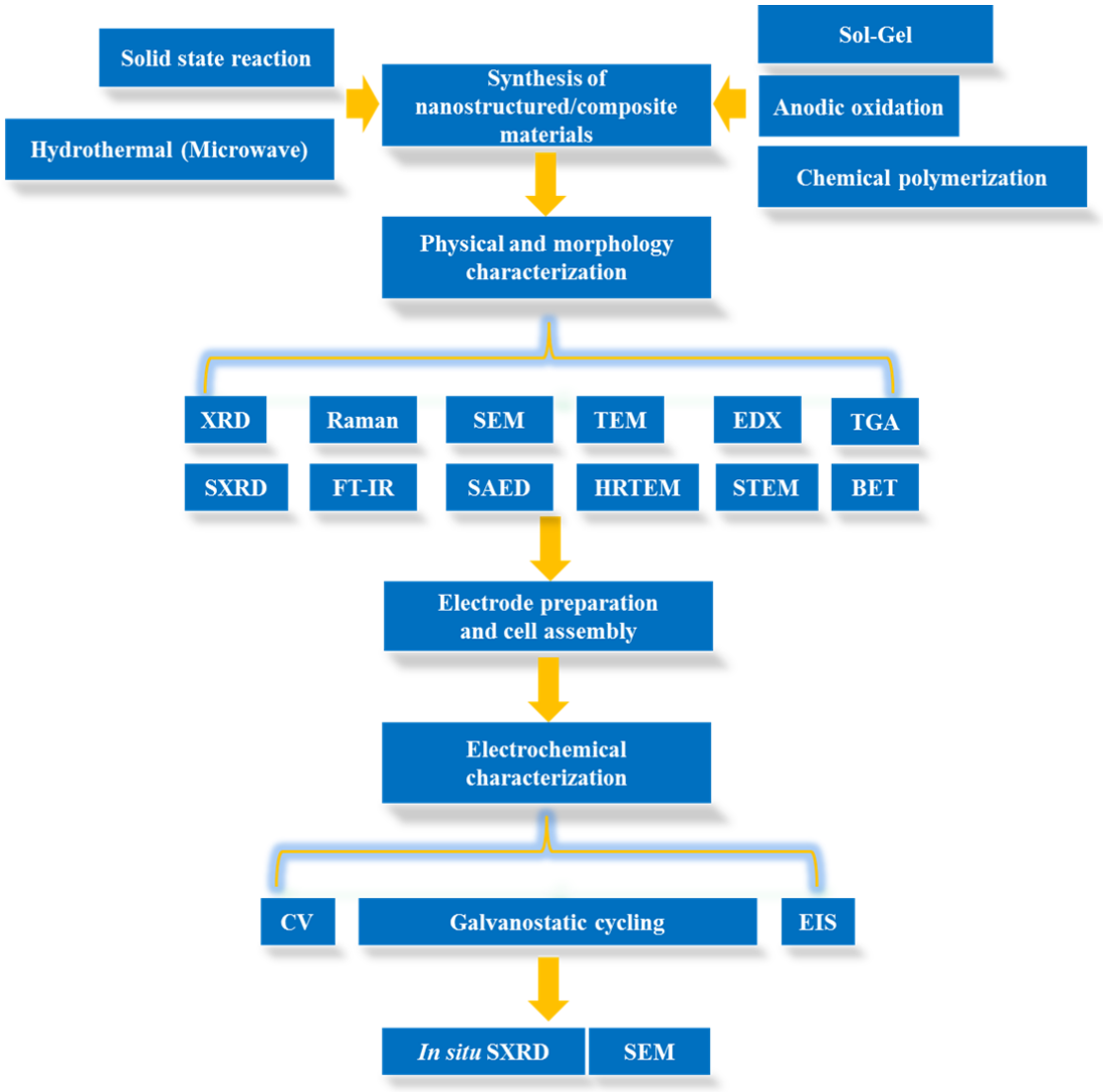

Figure 3.1 Outline of the experimental procedures.

3.3 Synthesis Method

The electrode materials used in this doctoral work were prepared via different methods, including the hydrothermal method, solid state reaction, chemical polymerization, the sol-gel method, and anodic oxidation. The details of these experimental methods and procedures are

explained in this subsection.

3.3.1 Hydrothermal Method

The hydrothermal method is one of the most popular experimental methods for synthesizing crystal and nanostructured materials at comparatively low temperature and high pressure [245-247]. Generally, the hydrothermal method can be defined as a method for the synthesis of materials in hot water under high pressure. In this experimental work, the hydrothermal autoclaves are 4748 Acid Digestion Bombs with 125 ml capacity from the Parr Instrument Company (Figure 3.2). These hydrothermal autoclaves including two parts: the outside parts are made of stainless steel; and the inside parts are the polytetrafluoroethylene (PTFE) cups. The maximum working temperature is 250 ^{o}C. In terms of composition, morphology, and crystal structure, the products of the hydrothermal reaction are influenced by many factors, including the amount of solution relative to the pressure, the concentration of the reaction solution, the temperature, and the surfactant. To control the morphology and crystal structure of the products, all the parameters need to be further investigated.

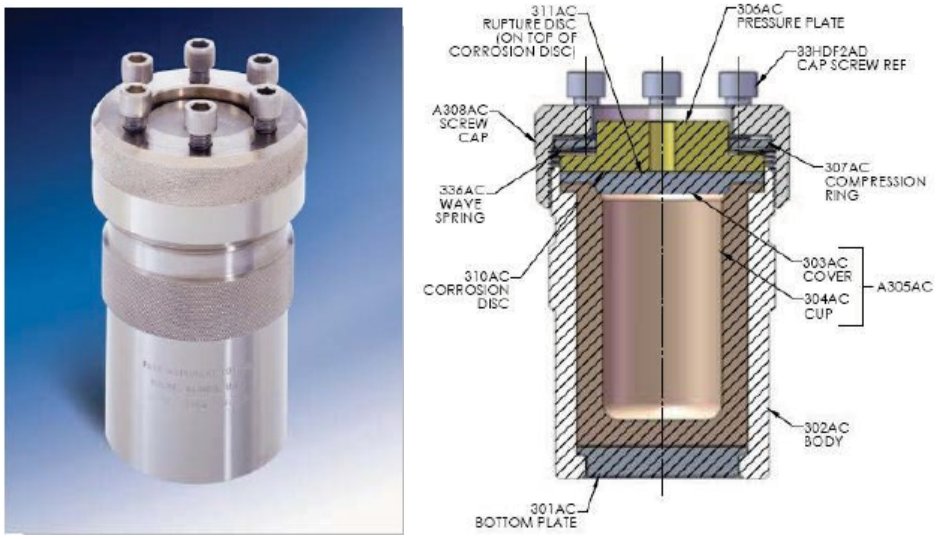

Figure 3.2 Hydrothermal autoclave (4748 Acid Digestion Bombs) from Parr Instruments (left) with a cross-sectional view (right).

3.3.2 Microwave Hydrothermal Method

The working principles of the microwave hydrothermal method are similar to those of the conventional hydrothermal method. The difference between these two methods is in the source of the heat. The microwave hydrothermal method uses microwave irradiation as the heat-source. Microwaves act as high frequency electric fields and will heat the material containing mobile electric charges, such as metals, solutions containing polar molecules, and solids containing conducting ions, in an ultra-fast way [248]. Microwave heating only heats the target conductive materials without heating the experimental container/device, which saves time and energy [249].

Figure 3.3 MicroSYNTH microwave system (Milestone) with a Labthermal 800 controller. The working frequency is 2.45 GHz.

The MicroSYNTH microwave system (Milestone) is applied in this doctoral work, which is controlled by a Labthermal 800 controller (Figure 3.2). The MicroSYNTH microwave system has a frequency of (2.45 GHz), and the maximum working power is 1 kW. The reaction container is a 100 ml PTFE vessel, which is sealed in a safety shield during the hydrothermal

reaction. The safety shield features built-in-pressure control via a preloaded spring with a vent and resealing mechanism. The hydrothermal autoclaves contain thermal sensors which can control the reaction temperature up to 250 ^{o}C. The PTFE vessel can work at high pressure (40 bar). The typical experimental procedure consists of two steps: 1) the precursor solution is transferred into the PTFE vessel, and the temperature and pressure sensors are assembled; 2) the sealed vessels are mounted inside the microwave oven, followed by setting up the reaction time, temperature, and pressure.

3.3.3 Solid State Reaction

Solid state reaction is considered to be the most widely used method for the synthesis of polycrystalline solids from a mixture of solid starting materials. Solid state reaction is mainly affected by the solid diffusion, controlled by Fick's Law:

$$J = -D(\frac{dc}{dx}) \tag{3.1}$$

where J is the flux of diffusing species, D is the diffusion coefficient, increasing with temperature, and dc/dx is the concentration gradient. Solid state reactions usually require high treatment temperatures and long heating time, due to the low diffusion in solids. In order to accelerate diffusion, the starting materials are usually pressed into pellets before sintering. For some reactions, the steps of grinding, pressing, and sintering must be repeated several times to obtain pure phase products.

3.3.4 Chemical Polymerization

In polymer chemistry, polymerization is the gathering together of the starting monomer molecules via a chemical reaction to form polymer chains or three-dimensional networks [250]. In chemical compounds, polymerization reactions include a variety of mechanisms due

to functional groups present in the reacting compounds and their inherent steric effects. Alkene, a straightforward polymerization product, is relatively stable due to the σ bonding between carbon atoms. The relevant reaction is a simple radical reaction. In contrast, polyurethane, involving substitution at carbonyl groups, a relatively complex polymerization product, requires more complex synthesis due to the way in which reacting molecules polymerize [251, 252]. There are two basic ways to form polymers: 1) linking small molecules together, such as polyethylene and polyvinyl chloride (PVC); 2) combining two molecules (the same or different types) with the elimination of a stable small molecule such as water. The latter is defined as a condensation reaction. Generally, synthesizing a polymer consists of two steps: 1) dispersing monomer precursors and catalyst into the solvent at the required temperature; 2) adding the oxidant at a constant speed.

3.3.5 Sol-Gel Method

The sol-gel method is a low-cost and effective wet-chemical technique to synthesize glassy and ceramic materials [253-255]. The sol-gel process generally consists of four steps, including solution, gelation, drying, and densification. In this process, the sol (or solution) evolves gradually towards the formation of a uniform gel-like network including both a liquid phase and a solid phase. The possible morphologies of the gel range from discrete particles to continuous polymer networks. The purpose of the drying process is to remove the liquid, so that the gel contracts into a three-dimensional network. The dried gel is defined as a xerogel, which is influenced by the removal rate of the liquid. Generally, the xerogel needs to be heat-treated (sintering process) to obtain fine products. The thermal treatment of the xerogel is also conducive to further poly-condensation, and the structural stability is also increase via post treatments such as sintering, densification, and grain growth. Therefore, the sol-gel method shows several advanced features: 1) low reaction temperature and facile synthesis process; 2) controllable morphology of the product; 3) homogeneous product ingredients; 4)

potential to synthesize compounds which are difficult to acquire by conventional methods. For example, the starting materials are volatile or exhibit mutual incompatibility.

3.3.6 Anodic oxidation

Anodic oxidation is an electrolytic passivation process used to increase the thickness of the oxide layer on the surface of metal parts. In this PhD thesis work, anodic oxidation was used to prepare three- dimensional (3D) TiO_2 nanotube arrays on Ti mesh.

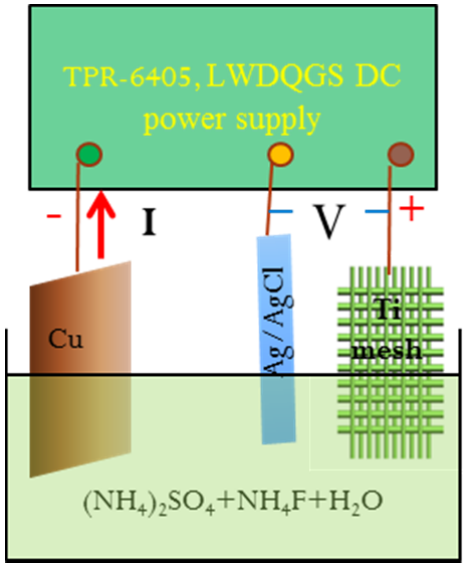

Figure 3.4 Schematic illustration of TiO_2/Ti mesh synthesis using the anodic oxidation method.

Figure 3.4 shows a schematic illustration of the experimental set-up for titanium (Ti) oxidation. A piece of Ti mesh acts as the positive electrode connected to a laboratory DC power supply, while the copper plate serves as the counter electrode. When the voltage was applied, Ti mesh was oxidized to TiO_2, which grew on the surface of the Ti mesh. Meanwhile TiO_2 would dissolve into the solution because of the presence of HF. In a typical anodic oxidation process, the reactions can be expressed as follows:

$$Ti + 2H_2O \rightarrow TiO_2 + 4H^+ \quad (3.2)$$

$$H^+ + F^- \rightarrow HF \quad (3.3)$$

$$TiO_2 + 6HF \rightarrow [TiF_6]^{2-} + 2H_2O + 2H^+ \quad (3.4)$$

Many factors can control the rate of TiO_2 formation to that of TiO_2 dissolution, including temperature, acidity, ion flux, and reaction time [256-258].

3.4 Physical and Morphology Characterization

The physical and morphology characterizations of the as-prepared nanostructured/composite materials are described in detail in the following section. These characterizations are used for understanding the physical nature and features of the morphology of the as-prepared electrode materials and their relationship to the improvement of the electrochemical properties. Most of the characterizations were achieved in our institute and the Intelligent Polymer Research Institute (IPRI) under the Australian Institute of Innovative Materials (AIIM), with the exception of those at the Australian Synchrotron (AS).

3.4.1 X-Ray Diffraction

Laboratory X-Ray Diffraction

X-ray diffraction (XRD) is widely used to study the bulk structure of materials. XRD is a non-destructive technique, which can reveal information on the crystallographic structure, chemical composition, and physical properties of a sample. X-rays are generated from an X-ray tube when the anode material (usually copper) is irradiated with a beam of high-energy electrons. The high-energy electrons are accelerated by a high voltage electric field. X-ray radiation is a type of electromagnetic wave with wavelengths ranging from 10 to 0.01 nanometers, which is on the same order as the lattice spacing in crystals. Therefore, the X-rays can be scattered by each set of lattice planes at a characteristic angle, and the scattering

patterns are related to the crystal structure of the given material. This is because each material has a set of unique *d*-spacings, which correspond to the XRD pattern. Bragg's law presents the diffraction condition from planes with a given *d*-spacing:

$$n\lambda = 2d \sin \theta \tag{3.5}$$

where n is an integer, λ is the wavelength of the incident X-ray beam, d is the distance between atomic planes in a crystal, and θ is the angle of the incidence. In this doctoral work, X-ray powder diffraction was commonly used to characterize crystalline materials. The powder sample is placed on a small disk-shaped sample holder with a flattened surface. The sample holder is mounted on the axis of the diffractometer at an angle θ. A detector rotates around the diffractometer on an arm at the corresponding angle 2θ. Figure 3.6 shows the interference between waves scattered from two adjacent planes of atoms in a crystal.

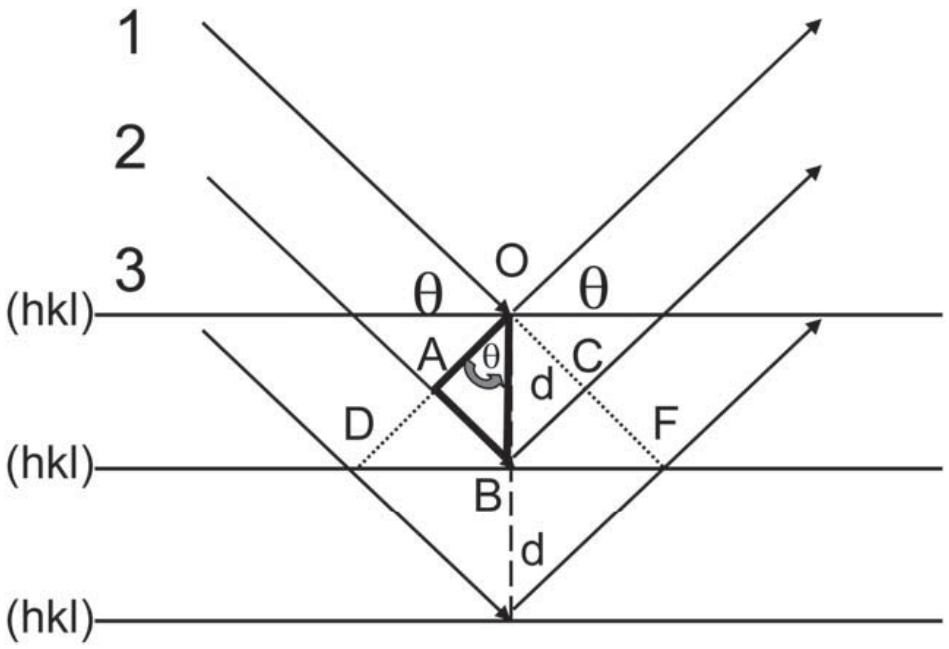

Figure 3.5 Bragg's law can be derived from the geometrical relation between the interplanar spacing *d* and the diffraction angle θ [259].

The crystal size of crystallographic materials can be calculated from the broadening of the

peaks using the Scherrer formula:

$$B(2\theta) = \frac{K\lambda}{L\cos\theta} \tag{3.5}$$

where B is the full width at half maximum (FWHM) in radians, 2θ is the peak position, K is the shape factor of the average crystallite ($K \approx 0.9$), and λ is the X-ray wavelength, and L is the crystal size (nm). In this PhD research work, a Philips PW 1730 diffractometer (Cu K_α radiation, $\lambda = 1.5418$ Å) was used for collecting XRD patterns.

Synchrotron X-Ray Diffraction

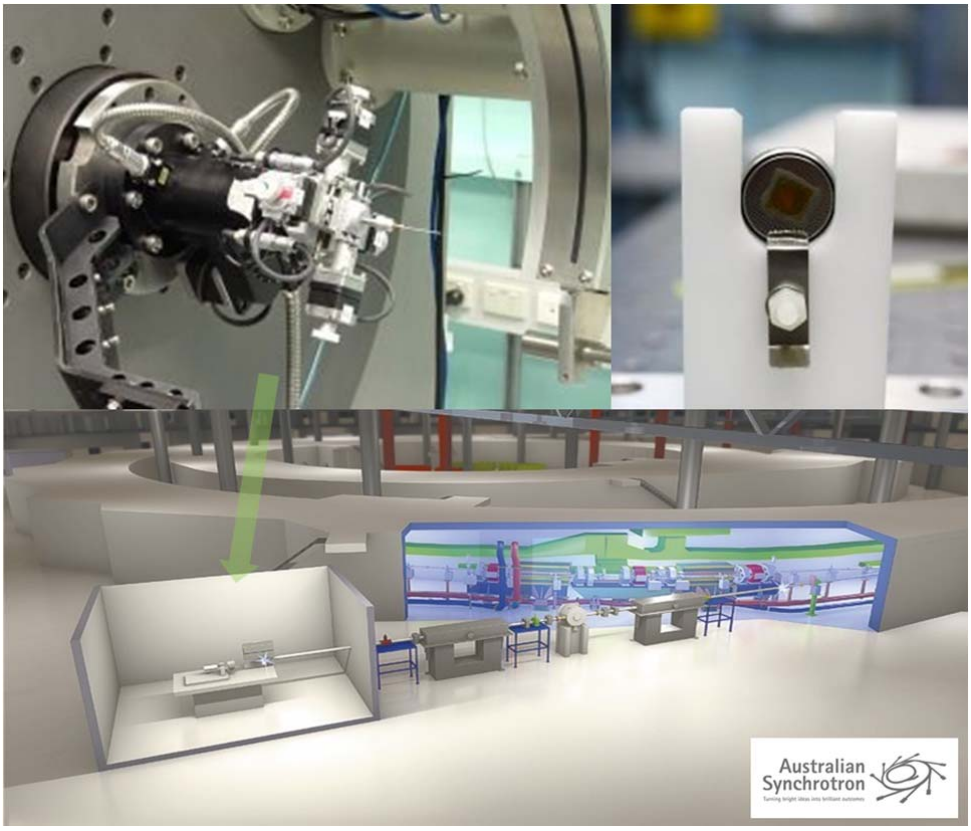

Figure 3.6 Australian Synchrotron Powder Diffraction Beamline and the *in situ* battery tester.

Synchrotron X-rays are the electromagnetic radiation emitted when charged particles are accelerated radially. Synchrotron radiation may be generated naturally by fast electrons

moving through magnetic fields, or artificially in accelerators (synchrotron or storage rings) as a deliberately produced radiation source for laboratory applications. Synchrotron X-rays show high resolution, which can determine and refine accurate structures of even moderately complex materials from powder samples. Synchrotron X-ray diffraction (SXRD) allows more accurate information to be acquired from crystalline materials, because it has numerous advantages over conventional powder XRD, including high signal-to-noise ratio, good time resolution, high angular and energy resolution due to the large and accessible *d*-space range, narrower peak width, and simple shape. SXRD also has tunable and monochromatic X-rays with the ability to penetrate bulky sample cells while avoiding or exploiting absorption edges. Additionally, *in situ* SXRD can collect dynamic information which accurately elucidates any phase transformations that are not resolved in the *ex-situ* experiments (Figure 3.6). SXRD measurements were conducted at the Australian Synchrotron Powder Diffraction Beamline (Figure 3.6).

3.4.2 Raman Spectroscopy

Raman spectroscopy is considered an important characterization method to study vibrational, rotational, and other low frequency modes in a structure. Raman measurements usually use a laser (monochromatic light source) to interact with the molecular vibrations, phonons, or other excitations of the sample to provide characteristic shifts in laser energy. The energy shift is detected and recorded in the form of frequency or wavelength, and the spectrum contains chemical and structural information on the sample materials. In this study, Raman spectroscopy was used as a complementary tool to XRD for identification of the as-prepared electrode materials. Raman spectroscopy measurements were conducted at IPRI using a JOBIN Yvon Horiba Raman Spectrometer model HR800 with a laser at 632.8 nm and a charge-coupled detector (CCD)

3.4.3 Fourier Ttransform Infrared Spectroscopy

Infrared spectroscopy (IR spectroscopy) is the type of spectroscopy that deals with the infrared region of the electromagnetic spectrum. Infrared radiation is light with a longer wavelength and lower frequency than visible light. Fourier transform infrared spectroscopy (FTIR) is a common laboratory method, which is based on absorption spectroscopy. FTIR is similar to Raman spectroscopy, but provides complementary information. In this experimental work, FTIR spectra were collected using a Nicolet Avatar 360 FTIR Fourier transform infrared spectrometer. The samples were mixed with KBr powder. KBr acts as the background file. The mixed samples were then placed in a sample cup and measured using the Nicolet Avatar 360 FTIR Fourier transform infrared spectrometer. All spectra were measured from 4000 to 500 $cm^{-1}$with a resolution of 2 cm^{-1}.

3.4.4 Thermogravimetric Analysis

Thermogravimetric analysis (TGA) is thermal analysis method for investigating the changes in physical and chemical properties of materials. TGA curves are measured as a function of increasing temperature (with constant heating rate), or as a function of time (with constant temperature and/or constant mass loss). TGA can collect information on various physical phenomena, such as second-order phase transitions, including vaporization, sublimation, absorption, adsorption, and desorption. Also, TGA can provide information on chemical phenomena, including chemisorption, desolvation (especially dehydration), decomposition, and solid-gas reactions. TGA was used to determine the polypyrrole (PPy) and carbon contents in composite samples in this doctoral work. TGA was performed on a SETARAM Thermogravimetric Analyzer (France). The sample was placed in an alumina crucible with loading mass of 5-20 mg, depending on the density of the composite materials. The samples were then heated to 800 ^{o}C in air or argon with a rate of 10 ^{o}C per min.

3.4.5 Brunauer-Emmett-Teller Surface Area Analysis

Brunauer-Emmett-Teller (BET) is an important analysis technique for the measurement of the specific surface area of a material. The BET surface area analysis is based on the theory of physical adsorption of gas molecules on a solid surface, which was first proposed by Stephen Brunauer, Paul Hugh Emmett, and Edward Teller in 1938 [260]. The BET theory is an extension of the Langumuir theory, which is a theory for monolayer molecular adsorption. For explaining multilayer adsorption, the BET theory proposed the following hypotheses: 1) gas molecules are physically adsorbed on the surface of a solid in potentially infinite layers; 2) there is no interaction between various adsorption layers; and (iii) the Langmuir theory can be applied to each layer. In this study, a Quanta Chrome Nova 1000 instrument was used to measure the specific surface area of the as-prepared electrode materials. The analysis is carried out in a liquid nitrogen environment (77 K), and the adsorption in 15-point mode. The as-prepared electrode materials were first dried in an evacuated oven for 12 h for degassing purposes and the loading weight of the sample was in a range of 100 mg to 500 mg.

3.4.6 Scanning Electron Microscopy

The scanning electron microscope (SEM) is primarily a tool for investigating the morphology of various materials. The SEM is a type of electron microscope that produces images of a sample by scanning it with a focused beam of electrons. The high energy electrons interact with the atoms in the sample, which generate various signals such as secondary electrons, back-scattered electrons (BSE), characteristic X-rays, light (cathodoluminescence), and transmitted electrons. These signals can be detected and contain the information on the sample's surface topography and composition. The secondary electron detector is commonly used in all SEM. The secondary electrons come from interactions of the electron beam with atoms at or near the surface of the sample, so the secondary electron image displays the

topography of the materials' surface. The morphologies of the materials or electrodes were collected on a JEOL JSM 6460A SEM and a field-emission SEM (FESEM, JEOL 7500). For SEM observations, the powder sample was either dispersed in ethanol or directly loaded onto carbon conductive tape which was mounted with adhesive on an aluminium holder.

3.4.7 Transmission Electron Microscopy

Transmission electron microscopy (TEM) is a microscopy technique where a beam of electrons is transmitted through an ultra-thin specimen, interacting with the specimen as it passes through. TEM can be used to observe the morphology, crystal structure, and electronic structure through the signals which are generated from the interaction of the electrons transmitted through the specimen. TEMs are capable of imaging at a significantly higher resolution than light microscopes, because the beam electrons have a small de Broglie wavelength. Selected area electron diffraction (SAED) is a crystallographic experimental technique that can be performed inside a transmission electron microscope (TEM). When the high energy electrons are transmitted through the ultra-thin crystalline sample, part of the electrons will be scattered at different angles depending on the crystal structure. The scattering signal will generate a characteristic pattern of diffraction spots. SAED is a very useful tool to investigate crystallographic information, which was used as a complementary technique to XRD for identification of crystalline samples. In this doctoral work, the TEM results were collected by using a JEOL 2011, 200 kV TEM and JEOL ARM200F, 200 kV scanning TEM (STEM).

3.4.8 Energy Dispersive X-ray Spectroscopy

Energy dispersive X-ray spectroscopy (EDS) is an analytical technique used for the elemental analysis or chemical characterization of a sample, which is one of the variants of X-ray fluorescence spectroscopy. EDS can be used for analysing the characteristic X-rays generated

from the sample after it is bombarded by electrons. The EDS patterns exhibit qualitative and quantitative information on the chemical composition and elements. EDS systems included in SEM and TEM. In this work, EDS patterns were collected from both SEM and TEM microscopes.

3.5 Electrode Preparation and Coin-Cell Assembly

Figure 3.7 Stacking sequence of components of a CR2032 coin cell [261].

The working electrodes were prepared by mixing the as-synthesised nanostructured/composite materials with 10-30 wt.% carbon black [acetylene black (AB) or Super P] and 5 wt.% sodium carboxymethyl cellulose (CMC) or polyvinylidene fluoride (PVDF) in a solvent of distilled water or N-methyl-2-pyrrolidone (NMP), respectively. The slurry was spread onto aluminium (cathode) or copper (anode) foil substrates. The coated electrodes were dried at 60-150 ^{o}C in a vacuum oven for 24 h. The electrode was then pressed

using a disc with a diameter of 14 mm to enhance the contact between the substrate, active materials, and conductive carbon. Subsequently, the electrodes were cut to a 1×1 cm^2 size. The average active material loading rate was 2-5 mg cm^{-2}. After weighing, the electrodes were then transferred into an argon-filled glove box for coin-cell assembly.

The cells were assembled in an argon-filled glove box (Mbraun, Unilab, Germany) with O_2 and H_2O levels less than 1 ppm. CR2032 coin type cells were used in this doctoral work with lithium foil serving as counter electrode and a porous Celgard polypropylene membrane as separator. The electrolytes chosen for these cells were 1 M $LiPF_6$ in a 1:1 (v/v) mixture of ethylene carbonate (EC) and dimethyl carbonate (DMC), and 1 M $LiPF_6$ in a 1:1 (v/v) mixture of ethylene carbonate (EC) and diethyl carbonate (DEC). Figure 3.7 presents the coin-cell components in their stacking sequence.

3.6 Electrochemical Measurements

Electrochemical measurements, including cyclic voltammetry, galvanostatic charge-discharge testing, and electrochemical impedance microscopy, were used to investigate the electrochemical properties of the as-prepared electrode materials in LIBs.

3.6.1 Cyclic Voltammetry

Cyclic voltammetry (CV) is as widely used technique for investigating the thermodynamics and kinetics of electron transfer at the electrode-electrolyte interface. In a CV experiment, the working electrode potential is ramped linearly versus time, and the corresponding current is recorded. The CV curve is a function of current value versus potential. When an electrochemical redox reaction occurs, a distinct peak will be generated at both the forward and reverse scans due to the current changes. The scan rate is a function of time versus the change of potential, which is the main parameter for CV measurements. The Randles-Sevcik

equation describes the relationship between the peak current (i_p) and the scan rate:

$$I_p = (2.69 \times 10^5) n^{2/3} A C D^{1/2} v^{1/2} \quad (3.6)$$

Where n is the number of moles of electrons transferred in the electrochemical reaction, A is the area of the electrode, C is the bulk concentration of the redox species, D is the diffusion coefficient, and v is the scan rate. In this work, the CV measurements were carried out on a Biologic VMP-3 electrochemical work station in ISEM.

3.6.2 Galvanostatic Charge-Discharge

The capacity and cycling stability of the as-prepared electrode materials were studied using galvanostatic charge-discharge tests in a constant current mode. The discharge/charge capacity (Q) can be calculated based on the discharge/charge time according to the formula $Q = I \times t$, where I is the current and t is the time. The rate capability of these electrodes can also be tested by setting up varying current densities applied over a number of cycles. All the cells were tested on a Land battery tester at room temperature or 55 ^{o}C in ISEM.

3.6.3 Electrochemical Impedance Spectroscopy

Electrochemical impedance spectroscopy (EIS) is an experimental method for characterizing the energy storage and dissipation properties of electrochemical systems [262]. EIS measures the impedance of a system over a range of frequencies, which can be carried out in potentiostaic (PEIS) or galvanostatic (GEIS) mode. A common type EIS spectrum consists of a low-frequency semicircle and a high-frequency tail. The PEIS are conducted by using a sine wave around a potential (E). E can be set to a fixed value or a value relative to the working electrode equilibrium potential over a range of frequencies. A typical PEIS consists of a low-frequency semicircle related to the kinetic process and a high-frequency tail resulting from the diffusion process. Usually, the high-frequency tail for the LIB system has a 45° angle

(Figure 3.8). The GEIS is similar to the PEIS. The only difference is that the current is controlled instead of the potential. In this thesis work, EIS spectra were collected on a Biologic VMP-3 electrochemical work station in potentiostatic mode in ISEM.

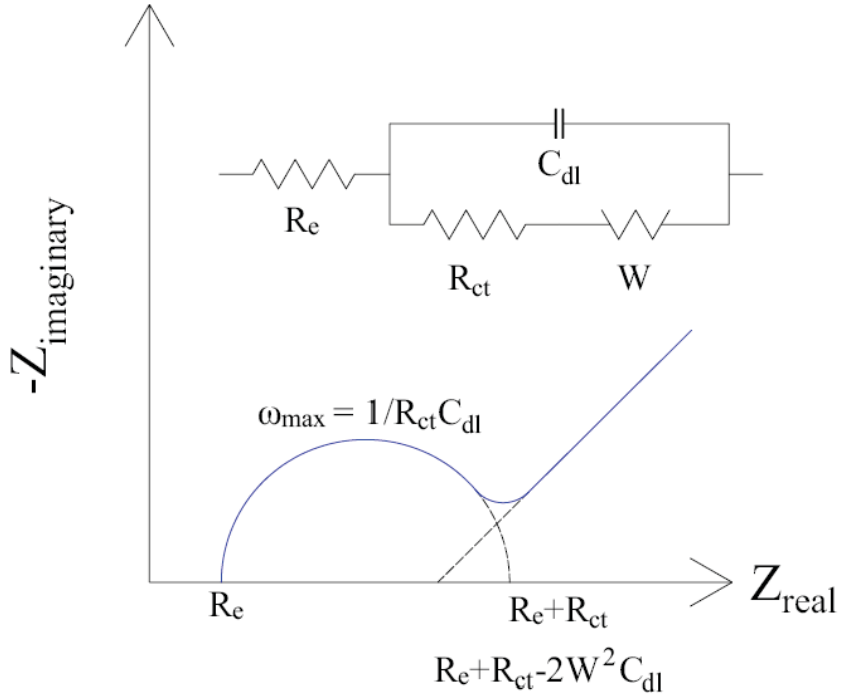

Figure 3.8 Typical EIS curve and the corresponding equivalent circuit for LIBs [263]. R_e is the uncompensated resistance, R_{ct} is the charge transfer resistance, C_{dl} is constant phase angle element, W is the Warburg impedance.

Chapter 4 Enhancing the High Rate Capability and Cycling Stability of $LiMn_2O_4$ by Coating of Solid-State Electrolyte $LiNbO_3$

4.1 Introduction

As one of the most promising candidates for power sources in electric vehicles (EVs) and hybrid electric vehicles (HEVs), LIBs need to be further improved by solving problems related to safety issues, high costs, low rate capability, and low energy density [2, 264, 265]. Cathode materials play a decisive role in LIBs because they can contribute to low cost, as well as high energy and high power densities. Lithium manganese oxide with a spinel structure has been widely studied as a promising candidate cathode for safe and high power LIBs, and $Li_{1-x}Mn_{2-y}O_4$ with the proper degree of cation mixing [excess lithium atom ($x < 0.1$) occupying the manganese sites (16 sites) and Mn ions in the tetrahedral sites (8 sites) in the spinel structure] has shown high cycling performance [266-269]. It remains challenging, however, to control capacity decay during cycling, which is well-known to be associated with Mn dissolution via the disproportionation reaction ($2Mn^{3+}_{(solid)} \rightarrow Mn^{4+}_{(solid)} + Mn^{2+}_{(solution)}$) and the crystallographic structural transformation from cubic to tetragonal phase by Jahn-Teller distortion of Mn^{3+} ions with high spin [270-272]. Meanwhile, organic liquid electrolyte (OLE) is another reason for the restricted development of large-scale batteries, because it is flammable and prone to the growth of lithium dendrites [45, 209, 213]. Solid state electrolyte (SSE) has been proposed to replace the OLE, because it simplifies the battery design and increases the lifetime and safety of the batteries [210, 212, 215, 273]. SSE is handicapped by several crucial problems for battery applications, however, relating to the Li-ion transference number, mechanical strength, and electrode/electrolyte interface contact [214, 242, 274]. Therefore, combining the advantages of the SSE and OLE is a possible solution for designing next-generation large-scale LIBs with lithium manganese oxide cathode.

For combining the advantages of the cathode, SSE, and OLE, one viable option is modification of the electrode by surface coating, which is a popular and highly effective method to achieve improved electrochemical performance. Usually, oxides (MgO [275], Al_2O_3 [276], SiO_2 [277], ZrO_2 [278]), polymers (polypyrrole (PPy) [279], polyacrylonitrile (Pan) [280]), and different forms of carbon (amorphous carbon [281], graphene [282], graphite [283]) are used as coating layers. The coating layers can: (1) prevent direct contact with the electrolyte solution, (2) suppress phase transitions and/or prevent dendrite growth, (3) improve the structural stability, and (4) decrease the disorder of cations in crystal sites, but at the expense of compromising the theoretical capacity and/or the energy density [284].

Furthermore, as a coating layer on the electrode surface, SSE is required to have easy synthesis and a simple structure. $LiNbO_3$, a kind of SSE, can be synthesized by solid state reaction and has the *R3c* crystal structure. Glass et al. reported that $LiNbO_3$ could be considered as a SSE in 1978, because it exhibits high room-temperature ionic conductivity and low electronic conductivity (10^{-5} S cm^{-1} and 10^{-11} S cm^{-1}, respectively) [240]. Recently, Ohta et al. [241] reported that $LiNbO_3$ could be applied in all-solid-state lithium secondary batteries as the buffer layer between the $LiCoO_2$ cathode and the sulphide electrolyte ($Li_{3.25}Ge_{0.25}P_{0.75}S_4$, denoted as thio-LISICON), due to its high ionic conductivity and ease of synthesis and coating on the $LiCoO_2$ cathode surface. The resultant battery exhibited low interfacial resistance and high-rate capability, as well as revealing a feasible method to increase the ionic conductivity at the interface between the electrode and the bulk SSE.

As an attempt to introduce an SSE coating layer into LIBs in combination with OLE, herein, I have developed a novel LIB system which consists of a manganese spinel cathode, an SSE $LiNbO_3$-coating layer, OLE, and a lithium foil anode (Figure 4.1). In this report, $LiNbO_3$-coated-$Li_{1.08}Mn_{1.92}O_4$ was synthesized by a simple solid-state reaction method. The influence

of the $LiNbO_3$ coating layer on the $Li_{1.08}Mn_{1.92}O_4$ spinel cathode has been investigated, including the influence on the crystal structure and electrochemical performance. The SSE $LiNbO_3$-coating layer effectively prevents Mn dissolution and maintains the high ionic conductivity between the OLE and the cathode.

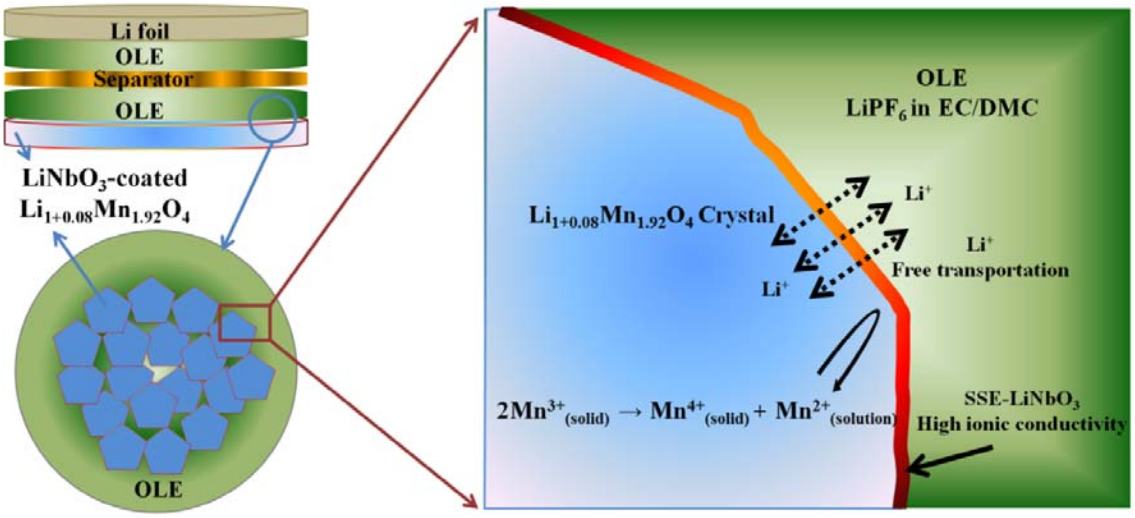

Figure 4.1 Schematic illustration of cathode-electrolyte interface in a lithium-ion battery containing both an SSE-$LiNbO_3$ coating layer and organic liquid electrolyte. OLE: organic liquid electrolyte; SSE: solid-state electrolyte; EC: ethylene carbonate; DMC: dimethyl carbonate.

4.2 Experimental Section

4.2.1 Material Synthesis

The $LiNbO_3$-coated $Li_{1.08}Mn_{1.92}O_4$ composite materials were synthesized by solid-state reaction. The starting materials, niobium pentoxide (Nb_2O_5, 99.8% purity, CBMM-Brazil), lithium carbonate ($LiCO_3$, ≥ 99% purity, Sigma-Aldrich), and manganese acetate ($Mn(CH_3COO)_2 \cdot 4H_2O$, ≥ 99% purity，Sigma-Aldrich) were ground in an agate mortar with a pestle in the predetermined ratio Nb : Li : Mn = x : 1.15 : 1.92-x (x = 0, 0.03, 0.06, and 0.1)

until the mixture became homogeneous. After that, the mixture was pressed into pellets and preheated at 650 ^oC in air for 5 h in a tube furnace. Then, the mixture was again ground, pressed into pellets, and heated at 750 ^oC in air for 24 h in the same tube furnace. All the samples were cooled to room temperature at the cooling rate of 1 ^oC/min after the second heat-treatment. The details of the compositions and synthesis conditions for the $LiNbO_3$-coated $Li_{1.08}Mn_{1.92}O_4$ composite materials are summarized in Table 4.1.

Table 4.1 Summary of preparation conditions for x^*LiNbO_3-(1-x/2)$Li_{1.08}Mn_{1.92}O_4$ composite materials.

Sample	**Nb/Li/Mn ratio**	**Target composite**	**Preparation conditions**	
	x : 1.1 : 1.92-x	**$xLiNbO_3$-(1-x/2)$Li_{1.08}Mn_{1.92}O_4$**	**Preheating**	**2nd heating**
x=0	0 : 1.1 : 1.92	$Li_{1.08}Mn_{1.92}O_4$	650 ^oC for 5 h	750 ^oC for 24 h
x=0.03	0.03 : 1.1 : 1.89	$0.03LiNbO_3$-$0.985Li_{1.08}Mn_{1.92}O_4$	650 ^oC for 5 h	750 ^oC for 24 h
x=0.06	0.06 : 1.1 : 1.86	$0.06LiNbO_3$-$0.97Li_{1.08}Mn_{1.92}O_4$	650 ^oC for 5 h	750 ^oC for 24 h
x=0.1	0.1 : 1.1 : 1.82	$0.1LiNbO_3$-$0.95Li_{1.08}Mn_{1.92}O_4$	650 ^oC for 5 h	750 ^oC for 24 h

4.2.2 Material Characterization

The structures and morphologies of the as-prepared materials were characterized by X-ray diffraction (XRD; GBC MMA) with Cu Kα radiation, synchrotron X-ray diffraction (SXRD) with *in situ* SXRD conducted at the Powder Diffraction Beamline (wavelengths: 0.7747 Å, and 0.6888 Å; Australian Synchrotron, Clayton, Australia) with a Mythen detector, field emission scanning electron microscopy (FESEM; JEOL 7500, 30 kV), transmission electron microscopy (TEM; JEOL JEM-2011, 200 kV) with high-resolution TEM (HRTEM), and Brunauer-Emmett-Teller (BET) analysis (Quanta Chrome Nova 1000). To test the electrodes after cycling, the cells were opened, and the electrodes were taken out and washed with dimethyl carbonate (DMC) three times. For the *in situ* synchrotron X-ray diffraction, Kapton film was used as a window to allow the penetration of the synchrotron beam into the *in situ*

cell, which was assembled under the same conditions as the other cells in this work.

4.2.3 Electrochemical measurements

To test the electrochemical performance, the electrodes were prepared by mixing xLiNbO$_3$-(1-x/2)Li$_{1.08}$Mn$_{1.92}$O$_4$ (x = 0, 0.03, 0.06, and 0.1, with x : 1-x/2 is the molar ratio of LiNbO$_3$: Li$_{1.08}$Mn$_{1.92}$O$_4$) composite materials with acetylene black (AB) and polyvinylidene fluoride (PVDF) in *N*-methyl-2-pyrrolidone (NMP), with a weight ratio of 80:10:10. The slurry was spread onto aluminum foil substrates with an area of 1 × 1 cm^2 and dried at 100 °C in a vacuum oven for 24 h to remove water molecules. The electrode was then pressed using a disc with a diameter of 14 mm to enhance the contact between the aluminum foil, active materials, and conductive carbon. The average active material loading rate was ~ 5 mg cm^{-2}. CR 2032 coin-type cells were assembled in an Ar-filled glove box (Mbraun, Unilab, Germany), using lithium metal foil as the counter electrode. The electrolyte was 1 M $LiPF_6$ in a mixture of ethylene carbonate (EC) and dimethyl carbonate (DMC) (1:1 by volume, provided by MERCK KGaA, Germany). The cells were galvanostatically charged and discharged in the voltage range of 4.5-3.2 V at different current densities using a computer-controlled charger system manufactured by Land Battery Testers. A Biologic VMP-3 electrochemical work station was used to perform cyclic voltammetry (CV; scanning rate 0.1 mV s^{-1}) and electrochemical impedance spectroscopy (EIS; ac amplitude 5 mV, frequency range 100 kHz - 0.01 Hz).

Table 4.2 Rietveld refinement results based on SXRD data for xLiNbO$_3$-(1-x/2)Li$_{1.08}$Mn$_{1.92}$O$_4$ (x = 0, 0.03, 0.06, and 0.1) composite materials.

Sample	Composite formula	Nb/Li/Mn ratio
x=0	Li$_{1.079}$Mn$_{1.920}$O$_4$	0 : 1.079 : 1.920
x=0.03	0.029LiNbO$_3$-0.986Li$_{1.072}$Mn$_{1.928}$O$_4$	0.029 : 1.057 : 1.901
x=0.06	0.060LiNbO$_3$-0.970Li$_{1.087}$Mn$_{1.912}$O$_4$	0.060 : 1.054 : 1.855
x=0.1	0.089LiNbO$_3$-0.956Li$_{1.099}$Mn$_{1.901}$O$_4$	0.089 : 1.051: 1.817

Table 4.3 Lattice parameters for the $xLiNbO_3$-(1-x/2)$Li_{1.08}Mn_{1.92}O4$ (x = 0, 0.03, 0.06, and 0.1) composite materials.

Samples		a(Å)	b(Å)	c(Å)	Volume (Å^3)	Rwp[a] (%)
x=0	Phase1[b]	8.21895	8.21895	8.21895	555.200	9.84
	Phase2[c]	/	/	/	/	
x=0.03	Phase1	8.22392	8.22392	8.22392	556.207	11.21
	Phase2	5.14837	5.14837	13.8477	317.851	
x=0.06	Phase1	8.22869	8.22869	8.22869	557.175	8.08
	Phase2	5.1503	5.1503	13.8462	318.075	
x=0.10	Phase1	8.23028	8.23028	8.23028	557.499	11.26
	Phase2	5.14993	5.14993	13.8460	318.024	

[a] R_{wp} is the agreement factor for the xLiNbO$_3$-(1-x/2)$Li_{1.08}Mn_{1.92}O_4$ (x = 0, 0.03, 0.06, 0.1) refinement. [b] is $Li_{1.08}Mn_{1.92}O_4$ phase. [c] is $LiNbO_3$ phase.

Table 4.4 Atomic sites and coordinates x, y, z, with N (number of atoms) for $Li_{1.08}Mn_{1.92}O_4$ compound.

Atom	x	y	z	N	Occupancy
Li1	0.12500	0.12500	0.12500	8	1.0
Mn1	0.50000	0.50000	0.50000	16	0.9602
O1	0.26030	0.26030(2)	0.26030	32	1.0
Li12	0.50000	0.50000	0.50000	16	0.0397

Table 4.5 Atomic sites and coordinates x, y, z, with N (number of atoms) for 0.03$LiNbO_3$-0.985$Li_{1.08}Mn_{1.92}O_4$ composite material.

Atom	x	y	z	N	Occupancy
Li1	0.12500	0.12500	0.12500	8	1.0
Mn1	0.50000	0.50000	0.50000	16	0.9639(2)
O1	0.26249(2)	0.26249(2)	0. 26249(2)	32	1.0
Li12	0.50000	0.50000	0.50000	16	0.0361(2)
Li2	0.0	0.0	0.282(21)	6	1.0
Nb2	0.0	0.0	0.002(10)	6	1.0
O2	0.044(11)	0.310(16)	0.074(13)	18	1.0

Table 4.6 Atomic sites and coordinates x, y, z, with N (number of atoms) for 0.06$LiNbO_3$-0.97$Li_{1.08}Mn_{1.92}O_4$ composite material.

Atom	X	y	z	N	Occupancy
Li1	0.12500	0.12500	0.12500	8	1.0
Mn1	0.50000	0.50000	0.50000	16	0.9561(2)
O1	0.26321(2)	0.26321(2)	0.26321(2)	32	1.0
Li12	0.50000	0.50000	0.50000	16	0.0438(2)
Li2	0.0	0.0	0.311(4)	6	1.0
Nb2	0.0	0.0	0.006(5)	6	1.0
O2	0.037(6)	0.314(9)	0.079(5)	18	1.0

Table 4.7 Atomic sites and coordinates *x*, *y*, *z*, with *N* (number of atoms) for $0.1LiNbO_3$-$0.95Li_{1.08}Mn_{1.92}O_4$ composite material.

Atom	x	y	z	N	Occupancy
Li1	0.12500	0.12500	0.12500	8	1.0
Mn1	0.50000	0.50000	0.50000	16	0.9503(2)
O1	0.26317(2)	0.26317(2)	0.26317(2)	32	1.0
Li12	0.50000	0.50000	0.50000	16	0.0496(7)
Li2	0.0	0.0	0.2809(1)	6	1.0
Nb2	0.0	0.0	0.0017(1)	6	1.0
O2	0.037(4)	0.331(7)	0.0587(1)	18	1.0

4.3 Results and Discussion

The structures and phases of the as-prepared xLiNbO$_3$-(1-x/2)$Li_{1.08}Mn_{1.92}O_4$ (x = 0, 0.03, 0.06, and 0.1) samples were analyzed by XRD (Figure 4.2 in the Supporting Information) and SXRD (Figure 4.3 and Figure 4.4). The diffraction patterns can be indexed as mixed phases with a slight amount of peak shifting compared with the standards in the database [$LiMn_2O_4$ $Fd\bar{3}m$ spinel structure (JPCDS card no. 35-0782) and $LiNbO_3$ *R3c* structure (JPCDS card no. 20-0631)]. As can be seen from SXRD Rietveld refinement results in Figure 4.3a, the spinel $Li_{1.08}Mn_{1.92}O_4$ sample can be written as $Li_{1.079}Mn_{1.920}O_4$, matching well with the target value (Table 4.2-4.7). After the Nb element is added, the $LiNbO_3$ phase materials maintains a stable structure and the lattice constant of $Li_{1.08}Mn_{1.92}O_4$ compared with $LiMn_2O_4$ is slightly increased, corresponding to the partial replacement by lithium ions of manganese ions in octahedral sites (lattice parameter details shown in Table 4.3) [285, 286]. It needs to be pointed out, however, that the refined formula for $0.1LiNbO_3$-$0.95Li_{1.08}Mn_{1.92}O_4$ composite material cannot match the target value, indicating that the amount of $LiNbO_3$ should be less than 0.1 mol for maintaining effective cation mixing in $Li_{1-x}Mn_{2-x}O_4$ (Table 4.1) [287-289]. As shown in Table 4.2, the amount of lithium ions is less than 1.15 mol. The small amount of lithium ion loss in the composite is owing to the natural presence of lithium vapor at around

650 °C [290]. The vapor component of the lithium ions can react with niobium ions when the amount of niobium is high enough, according to the results of Table 4.2.

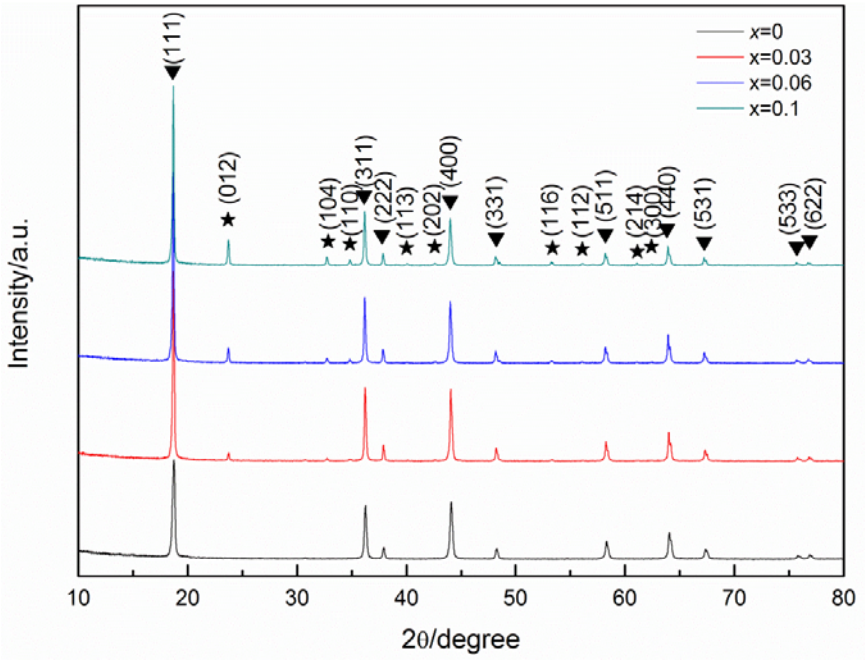

Figure 4.2 XRD patterns of as-prepared $xLiNbO_3$-(1-x/2)$Li_{1.08}Mn_{1.92}O_4$ (x = 0, 0.03, 0.06, and 0.1) composite materials.

Typical FESEM and TEM observations of the xLiNbO$_3$-(1-x/2)$Li_{1.08}Mn_{1.92}O_4$ (x = 0, 0.03, 0.06, and 0.1) composite materials are shown in Figure 4.5 and 4.6. The particles of the pristine $Li_{1.08}Mn_{1.92}O_4$ sample showed very smooth edges, and there is no other layer on the surface. After introducing the Nb element, the particle sizes of the xLiNbO$_3$-(1-x/2)$Li_{1.08}Mn_{1.92}O_4$ (x = 0.03, 0.06, and 0.1) composite materials are slightly increased, however, the particle sizes gradually decrease as the amount of Nb element increases, and the 0.06LiNbO$_3$-0.97$Li_{1.08}Mn_{1.92}O_4$ composite material features an almost uniform coating layer on the surface of the $Li_{1.08}Mn_{1.92}O_4$ particles. The specific surface areas of the as-prepared samples were measured by the 15-point Brunauer-Emmett-Teller (BET) N_2 adsorption method. The specific surface areas of the xLiNbO$_3$-(1-x/2)$Li_{1.08}Mn_{1.92}O_4$ (x = 0, 0.03, 0.06, and 0.1) composite materials were 2.9, 1.8, 2.3, and 2.5 m^2 g^{-1}, respectively. The specific

surface areas of the $LiNbO_3$ coated samples are lower than for the sample without $LiNbO_3$, because the $LiNbO_3$ coating layer acts as a connecting layer between some tiny $Li_{1.08}Mn_{1.92}O_4$ particles.

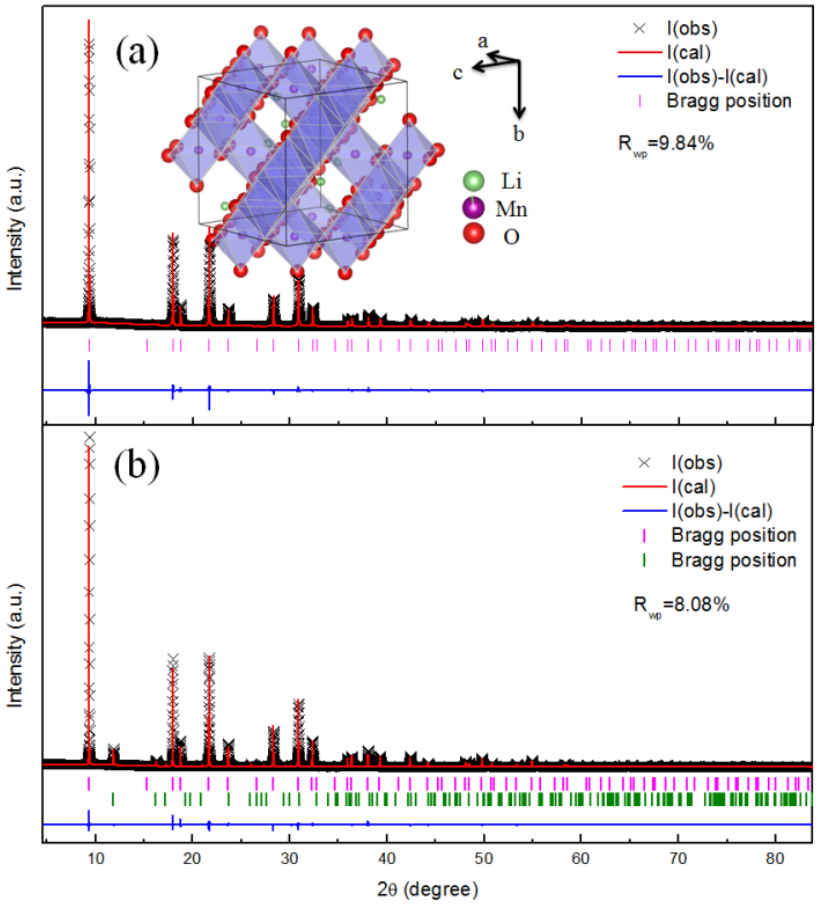

Figure 4.3 Rietveld refined SXRD patterns of (a) $Li_{1.08}Mn_{1.92}O_4$, with the spinel structure of $Li_{1.08}Mn_{1.92}O_4$ shown in the inset (space group $Fd\bar{3}m$); (b) $0.06LiNbO_3$-$0.97Li_{1.08}Mn_{1.92}O_4$. I(obs) is observed data, I(cal) is calculated data, I(obs)-I(cal) is the difference curve between the observed and calculated intensities. R_{wp} is the weighted profile factor.

To confirm the thickness and crystal structure of the coating layer and matrix, HRTEM images and the corresponding electron diffraction patterns are shown in Figure 4.7. The pristine $Li_{1.08}Mn_{1.92}O_4$ sample shows lattice fringes with a lattice spacing of 4.76 Å along the [111] direction, and the selected area electron diffraction (SAED) pattern presents well-

defined spots which can be well indexed to the cubic spinel structure [Figure 4.7(a-c)].

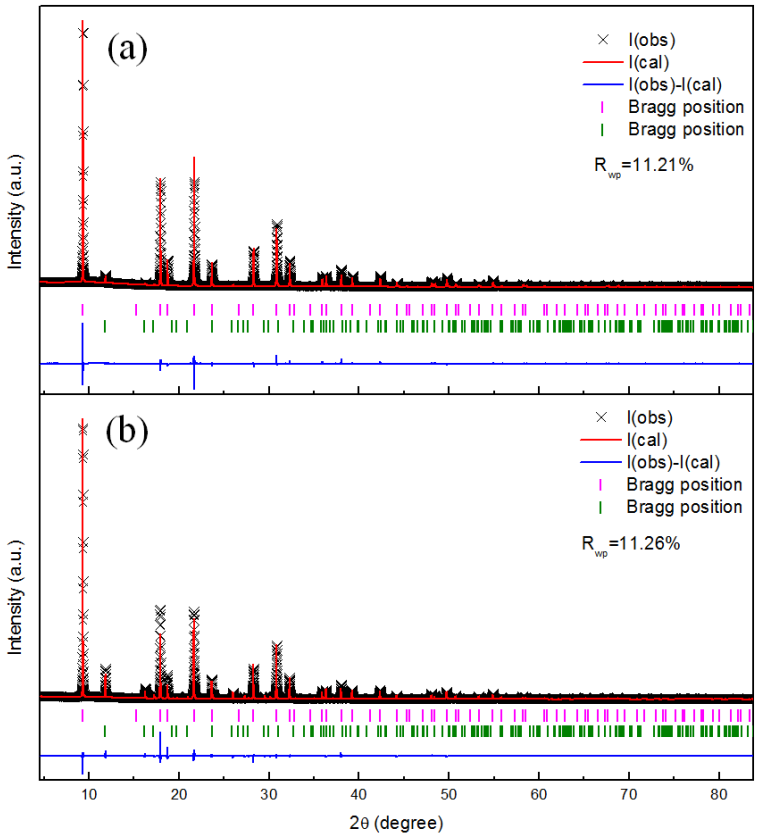

Figure 4.4 Rietveld refined SXRD patterns of (a) $0.03LiNbO_3$-$0.985Li_{1.08}Mn_{1.92}O_4$, (b) $0.1LiNbO_3$-$0.95Li_{1.08}Mn_{1.92}O_4$. I(obs) is observed data, I(cal) is calculated data, I(obs)-I(cal) is the difference curve between the observed and calculated intensities.

As observed in Figure 4.7(d), the thickness of the $LiNbO_3$ coating layer is 5-8 nm, and the $LiNbO_3$ coating layer consists of nanocrystalline structures with different crystallographic directions (such as the [104] direction with a lattice spacing of 2.75 Å and the [110] direction with a lattice spacing of 2.58 Å). Furthermore, the SAED pattern for the $0.06LiNbO_3$-$0.97Li_{1.08}Mn_{1.92}O_4$ composite material clearly shows two sets of diffraction spots: 1) well-defined bright spots indexed to the cubic spinel structure; 2) polycrystalline diffraction rings corresponding to the $LiNbO_3$ coating layer and indexed as (104), (110), and (006) from the inside out, respectively [Figure 4.7(e) and (f)]. Therefore, it is found that the $0.06LiNbO_3$-

$0.97Li_{1.08}Mn_{1.92}O_4$ composite material has the proper concentration of Nb element, with a thin and uniform $LiNbO_3$ coating layer acquired during the solid-state reaction. The solid-state reaction should consist of a two-phase synergistic nucleation and growth process and the small amount of $LiNbO_3$ has a preference for nucleation and growth at $Li_{1.08}Mn_{1.92}O_4$ lattice defects which are located at the crystal surface.

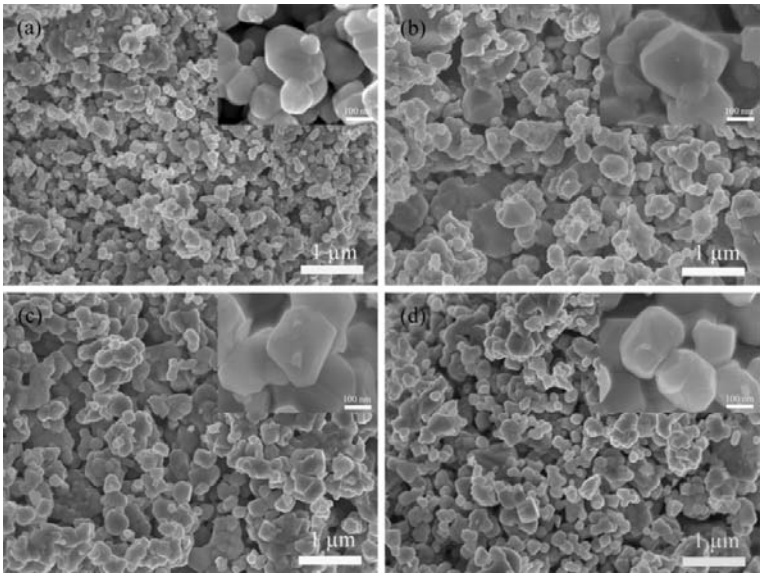

Figure 4.5 FESEM images of as-prepared xLiNbO$_3$-(1-x/2)$Li_{1.08}Mn_{1.92}O_4$ composite materials: (a) $Li_{1.08}Mn_{1.92}O_4$; (b) $0.03LiNbO_3$-$0.985Li_{1.08}Mn_{1.92}O_4$; (c) $0.06LiNbO_3$-$0.97Li_{1.08}Mn_{1.92}O_4$; (d) $0.1LiNbO_3$-$0.95Li_{1.08}Mn_{1.92}O_4$. The corresponding high magnification images are shown in the insets.

The influence of the SSE-coating layer on LIBs was investigated as follows. The electrochemical performance of the xLiNbO$_3$-(1-x/2)$Li_{1.08}Mn_{1.92}O_4$ (x = 0, 0.03, 0.06, and 0.1) composite materials was initially investigated by cyclic voltammetry (CV) (Figure 4.8). In all of the four samples, the typical two redox peaks can be observed, corresponding to a two-step reversible intercalation reaction, leading to λ-MnO_2/$Li_{0.5}Mn_2O_4$ and $Li_{0.5}Mn_2O_4$/$LiMn_2O_4$ [291-293]. Meanwhile, apart from the first cycle (electrode activation), no significant alteration in the CV curves is observed from the second cycle onwards. An

additional peak at 3.8 V - 3.9 V appears in Figure 4.8(a-c). Chen's group reported that the peak at 3.8 V - 3.9 V is caused by the disordered structure of the lithium-rich spinel manganese oxide and that this peak is present in the first discharge curve [294]. Tarascon's group also reported that the cation mixing in spinel $LiMn_2O_4$ between lithium octahedral sites (8 sites) and manganese tetrahedral sites (16 sites), gives rise to high discharge capacity [287]. As can be seen from the xLiNbO$_3$-(1-x/2)Li$_{1.08}$Mn$_{1.92}$O$_4$ (x = 0.03 and 0.06) electrodes [Figure 4.8(b) and (c)], the peak at 3.8 V - 3.9 V shows no significant alteration from the second cycle onwards. The reason might be that the SSE-$LiNbO_3$ coating layer prevents change in the disordered structure.

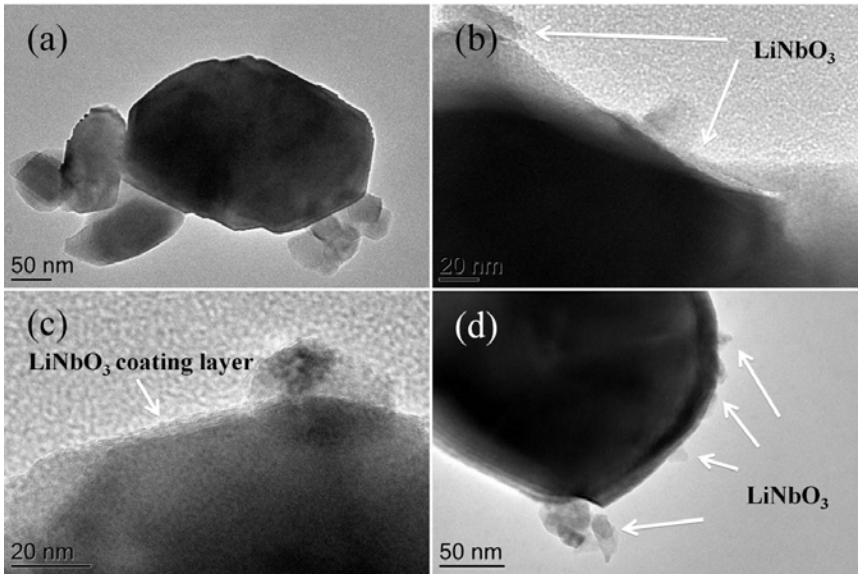

Figure 4.6 TEM images of as-prepared xLiNbO$_3$-(1-x/2)Li$_{1.08}$Mn$_{1.92}$O$_4$ composite materials: (a) Li$_{1.08}$Mn$_{1.92}$O$_4$; (b) 0.03LiNbO$_3$-0.985Li$_{1.08}$Mn$_{1.92}$O$_4$; (c) 0.06LiNbO$_3$-0.97Li$_{1.08}$Mn$_{1.92}$O$_4$; (d) 0.1LiNbO$_3$-0.95Li$_{1.08}$Mn$_{1.92}$O$_4$.

Charge/discharge curves for the first cycle are shown in Figure 4.9(a). In good agreement with the CV results, all of the xLiNbO$_3$-(1-x/2)Li$_{1.08}$Mn$_{1.92}$O$_4$ electrodes show two distinguishable pseudoplateaus (at ~4.15 V and ~4.0 V) and the 0.06LiNbO$_3$-0.97Li$_{1.08}$Mn$_{1.92}$O$_4$ electrode shows an extra plateau at 3.8 V-3.9 V, resulting in a higher

discharge capacity than for the other SSE-coated electrodes (126.1 mAh g^{-1}, 124.9 mAh g^{-1}, and 119.1 mAh g^{-1}, corresponding to x = 0.03, 0.06, and 0.1, respectively). The pristine $Li_{1.08}Mn_{1.92}O_4$ electrode shows the highest discharge capacity with 131.5 mAh g^{-1}, agreeing well with those of other reported lithium-rich manganese oxides [289, 295, 296]. To further evaluate the rate capability, the xLiNbO$_3$-(1-x/2)$Li_{1.08}Mn_{1.92}O_4$ electrodes were cycled at various current densities ranging from 0.5 C to 50 C within a potential window of 4.5-3.2 V at 25 ^oC, followed by a return to 0.5 C. A rate of n C corresponds to a full charge/discharge rate of the theoretical capacity in 1/n hours, and 1 C is 148 mAh g^{-1} for $LiMn_2O_4$. As shown in Figure 4.9(b) and (c), the 0.03LiNbO$_3$-0.985$Li_{1.08}Mn_{1.92}O_4$ electrode and 0.06LiNbO$_3$-0.97$Li_{1.08}Mn_{1.92}O_4$ electrode exhibit excellent rate capability, such that when the C-rate increases, even up to 50 C, the cell still retains 83.3% and 87.9% of the original capacity of 124.9 mAh g^{-1} and 126.1 mAh g^{-1}, respectively. Whereas, the pristine

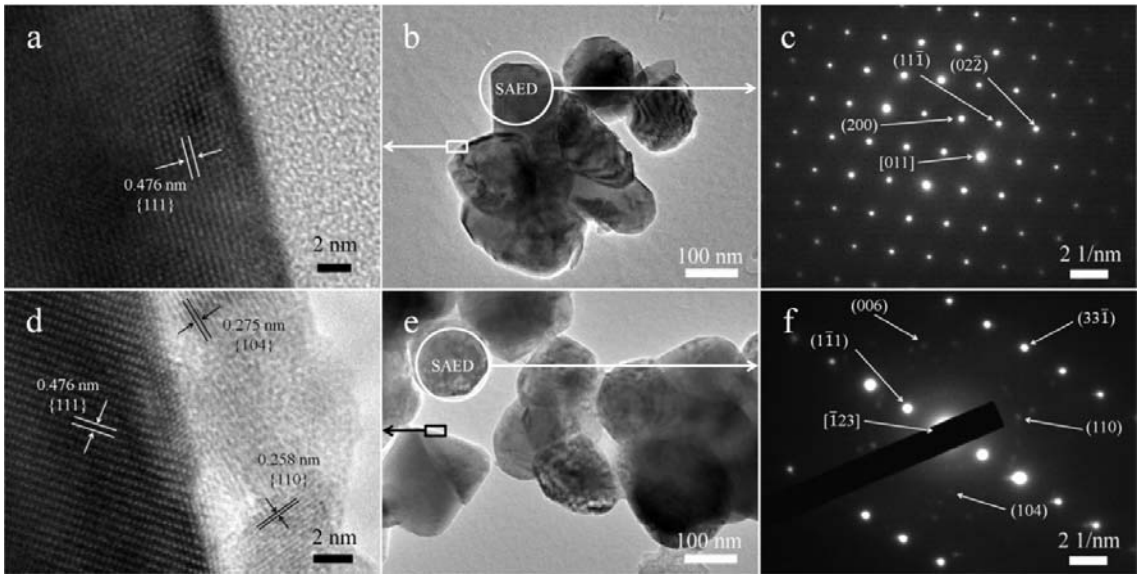

Figure 4.7 HRTEM images of a) $Li_{1.08}Mn_{1.92}O_4$ and d) 0.06LiNbO$_3$-0.97$Li_{1.08}Mn_{1.92}O_4$; b) and f) are the corresponding low magnification TEM images; c) and f) are the corresponding SAED patterns.

$Li_{1.08}Mn_{1.92}O_4$ electrode and the 0.1LiNbO$_3$-0.95$Li_{1.08}Mn_{1.92}O_4$ electrode show inferior rate

capability of only 41.4% and 70.7% of the original capacity of 131.5 mAh g^{-1} and 119.1 mAh g^{-1}, respectively, under the same conditions of increasing C-rate. The rate plots [Figure 4.9(c)] show that the high rate capability of the electrode containing the $0.06LiNbO_3$-$0.97Li_{1.08}Mn_{1.92}O_4$ composite materials is better than those of the electrodes containing the other xLiNbO$_3$-(1-x/2)$Li_{1.08}Mn_{1.92}O_4$ composite materials (x = 0, 0.03, and 0.1), suggesting that the solid state electrolyte $LiNbO_3$ coating layer plays an important role in the rate capability. Electrodes with partially $LiNbO_3$ coated lithium-rich manganese oxide also show good rate capability, however, the rate capability is inferior when the $LiNbO_3$ is in the form of clusters, not layers, due to excess Nb element (x = 0.1 for xLiNbO$_3$-(1-x/2)$Li_{1.08}Mn_{1.92}O_4$). It should be noted that the rate capability of the xLiNbO$_3$-(1-x/2)$Li_{1.08}Mn_{1.92}O_4$ composite materials (x = 0.03, 0.06, and 0.1) is better than that of the pristine $Li_{1.08}Mn_{1.92}O_4$.

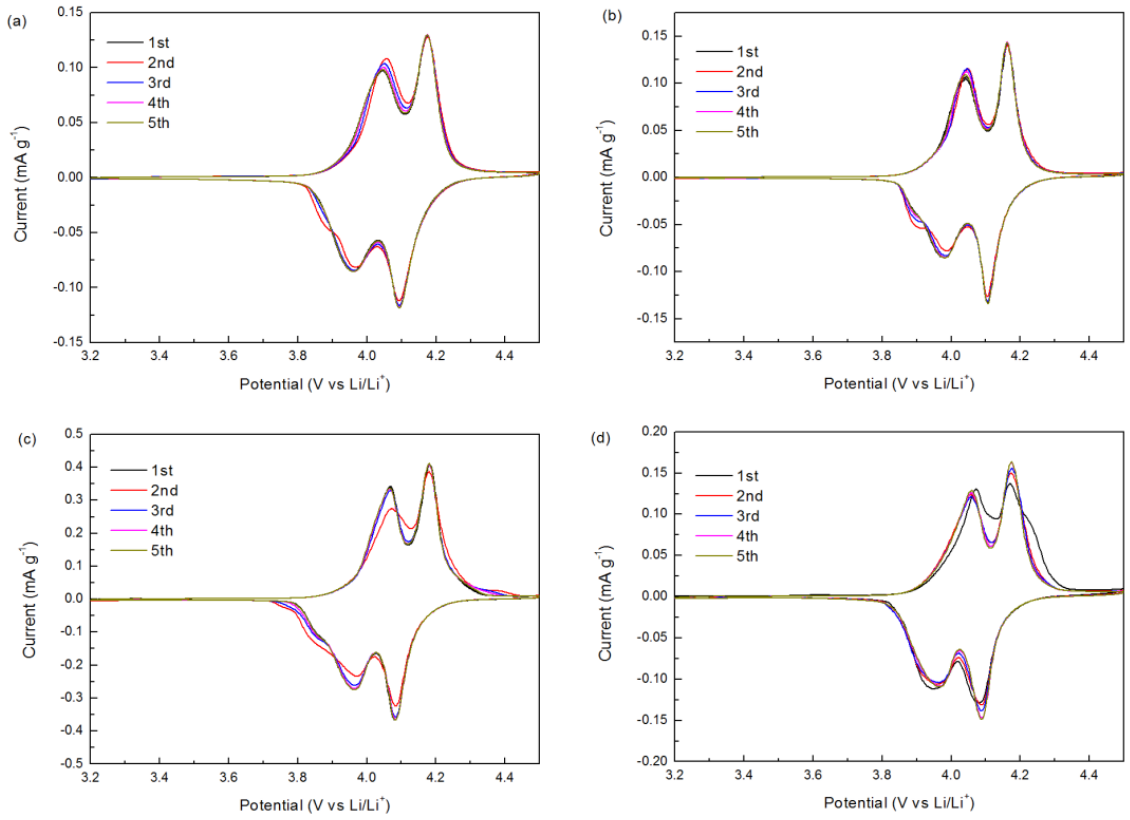

Figure 4.8 Cyclic voltammograms of the xLiNbO$_3$-(1-x/2)$Li_{1.08}Mn_{1.92}O_4$ electrodes for the first 5 cycles at a scan rate of 0.1 mV s^{-1}: (a) $Li_{1.08}Mn_{1.92}O_4$; (b) $0.03LiNbO_3$-

$0.985Li_{1.08}Mn_{1.92}O_4$; (c) $0.06LiNbO_3$-$0.97Li_{1.08}Mn_{1.92}O_4$; (d) $0.1LiNbO_3$-$0.95Li_{1.08}Mn_{1.92}O_4$.

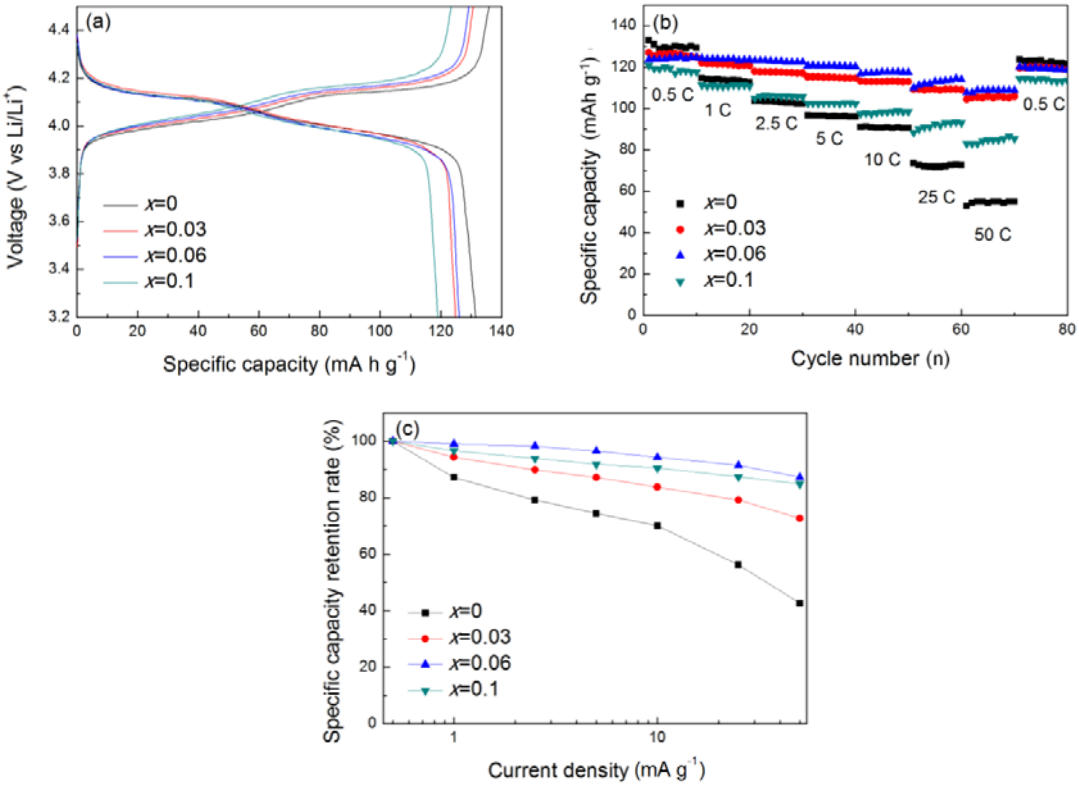

Figure 4.9 (a) Charge-discharge curves of xLiNbO$_3$-(1-x/2)Li$_{1.08}$Mn$_{1.92}$O$_4$ electrodes for the first cycle at 25 ^{o}C at current density of 0.5 C (1 C = 148 mAh g^{-1}); (b) rate performance and (c) capacity retention rate of xLiNbO$_3$-(1-x/2)Li$_{1.08}$Mn$_{1.92}$O$_4$ electrodes at different current densities from 0.5 C to 50 C at 25 ^{o}C. The rate capability in (c) is expressed as a relative specific discharge rate compared to that obtained at the low rate of 0.5 C.

The electrochemical delithiation/lithiation processes were also investigated via *in situ* SXRD. As can be seen from Figure 4.10 and Figure 4.11, the $0.06LiNbO_3$-$0.97Li_{1.08}Mn_{1.92}O_4$ composite material has undergone highly reversible changes in crystal structure at 0.5C and room temperature. During the charge process, the lattice constant of $Li_{1.08}Mn_{1.92}O_4$ gradually decreases from a = 8.228 Å (voltage = 3.22 V, open circuit potential) to a = 8.066 Å (Voltage = 4.5 V), with the SXRD peaks corresponding to shifts in the peaks of $Li_{1.08}Mn_{1.92}O_4$ to

higher angles [Figure 4.10(b), (d), and (e)]. A similar phenomenon appears during the discharge process, in which the SXRD peaks are shifted backward from their initial position

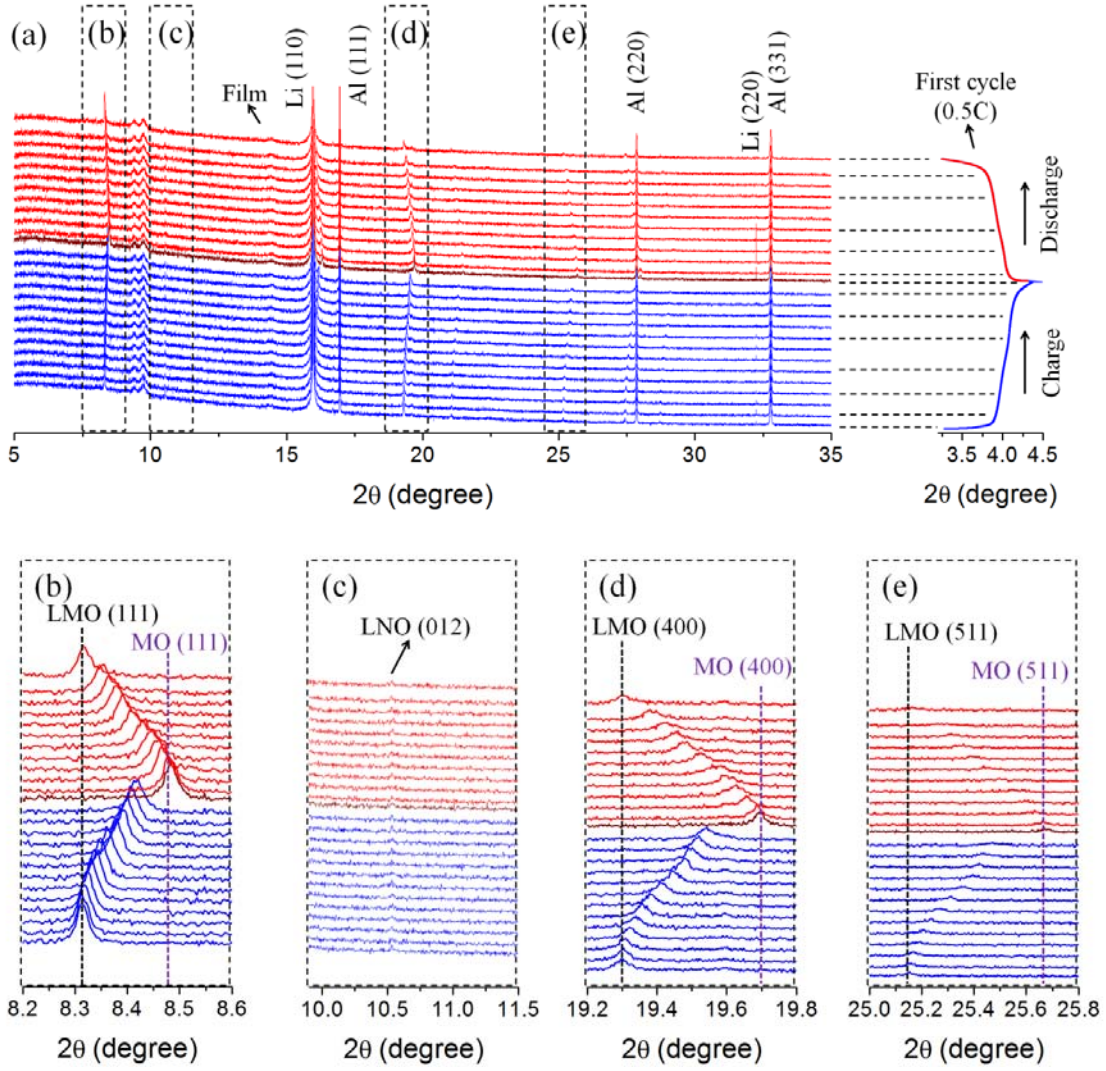

Figure 4.10 *In situ* SXRD patterns of $0.06LiNbO_3$-$0.97Li_{1.08}Mn_{1.92}O_4$ during the first cycle at 0.5C. (a) Selected individual diffraction patterns during the first cycle stacked against the charge/discharge curve. The main peaks of $Li_{1.08}Mn_{1.92}O_4$ correspond to the (b) (111), (d) (400), and (e) (511) reflections. These regions are highlighted in the bottom columns, and peaks corresponding to the $Li_{1.08}Mn_{1.92}O_4$ and λ-MnO_2 ($Li_{0.04}Mn_{0.96}O_2$) phases are marked by black dotted lines and purple dotted lines, respectively. For the $LiNbO_3$ phase, the main peak that corresponds to the (012) reflection is also highlighted in the bottom columns (c). LMO:

$Li_{1.08}Mn_{1.92}O_4$; MO: $Li_{0.04}Mn_{0.96}O_2$ (λ-MnO_2); LNO: $LiNbO_3$.

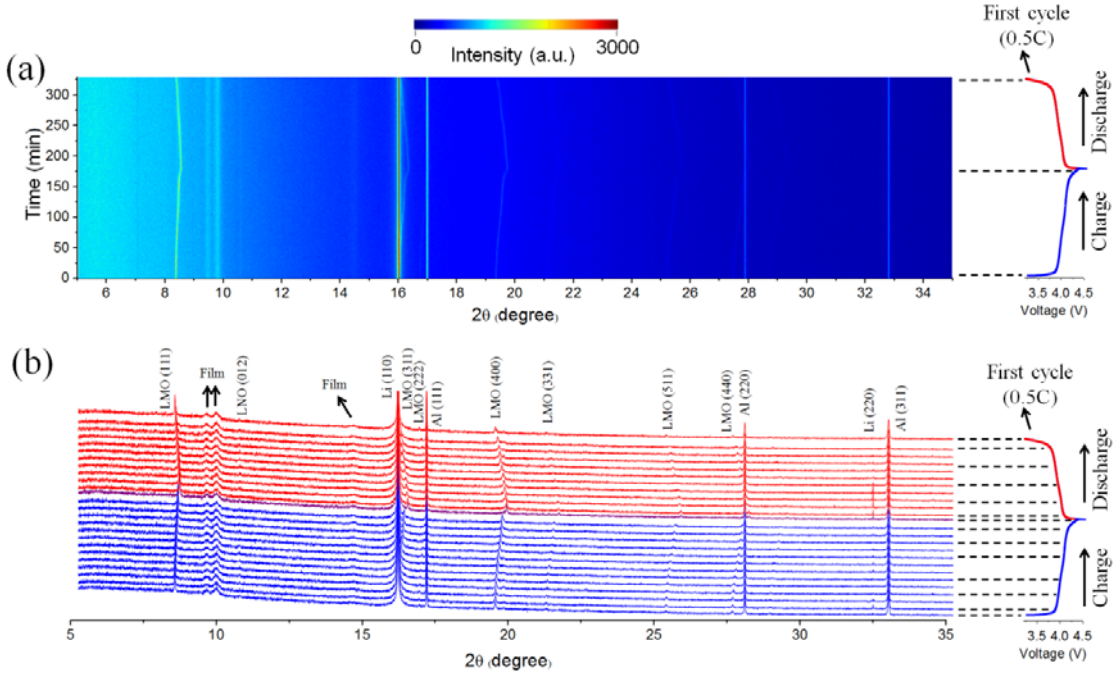

Figure 4.11 *In situ* SXRD patterns of $0.06LiNbO_3$-$0.97Li_{1.08}Mn_{1.92}O_4$ during the first cycle at 0.5 C. (a) Image plot of diffraction pattern reflections during the first cycle. The horizontal axis represents the selected 2θ region, and time is on the vertical axis. The diffraction intensity is color coded, with the scale bar shown on top. The corresponding charge/discharge curve is plotted to the right. (b) Selected individual diffraction patterns during the first cycle stacked against the charge/discharge curve. The main peaks correspond to the (111), (311), (222), (400), (331), and (440) reflections.

(a = 8.225 Å, voltage = 3.2 V). No new crystal structure is generated during the delithiation/lithiation processes. That is to say, there is no nucleation and growth of a second phase, so that the spinel structure avoids rearrangement and large volume changes [297-300]. It should be pointed out that lithium shows preferred nucleation and growth orientation during the charge/discharge process [lithium (220) reflection, Fig 4.10(a)]. As can be seen from Figure 4.12, a non-equilibrium solid solution phase, $Li_{x+0.08}Mn_{1.92}O_4$ ($0 < x < 1$), spans

the entire composition between the two thermodynamic phases, $Li_{1.08}Mn_{1.92}O_4$ and $Li_{0.04}Mn_{0.96}O_2$ (λ-MnO_2). An analogous phenomenon has also been reported in $Li_{1.06}Mn_2O_4$ and $LiFePO_4$ cathode materials for LIBs [285, 297]. From Figure 4.10(c), we can see that the SSE coating layer of $LiNbO_3$ shows a weak (012) reflection. No peak shifts of $LiNbO_3$ appear throughout the charge/discharge process. The dual structure of the cathode material, a stable $LiNbO_3$ structure (Figure 4.13) and a non-equilibrium solid solution phase [$Li_{x+0.08}Mn_{1.92}O_4$ ($0 < x < 1$)], effectively prevents the soluble Mn^{2+} from being generated and diffusing to the OLE, and avoids the splitting up of $Li_{1.08}Mn_{1.92}O_4$ particles caused by the slight crystal volume change. Although SSE presents a low Li-ion transfer rate in all solid state batteries, there is no obvious evidence that the thin $LiNbO_3$ SSE coating layer affects the Li-ion transfer rate from the *in situ* SXRD results. Therefore, the low-energy non-equilibrium solid solution phase [$Li_{x+0.08}Mn_{1.92}O_4$ ($0 < x < 1$)] and the stable SSE coating layer of $LiNbO_3$ can increase the high-rate capability and cycling stability.

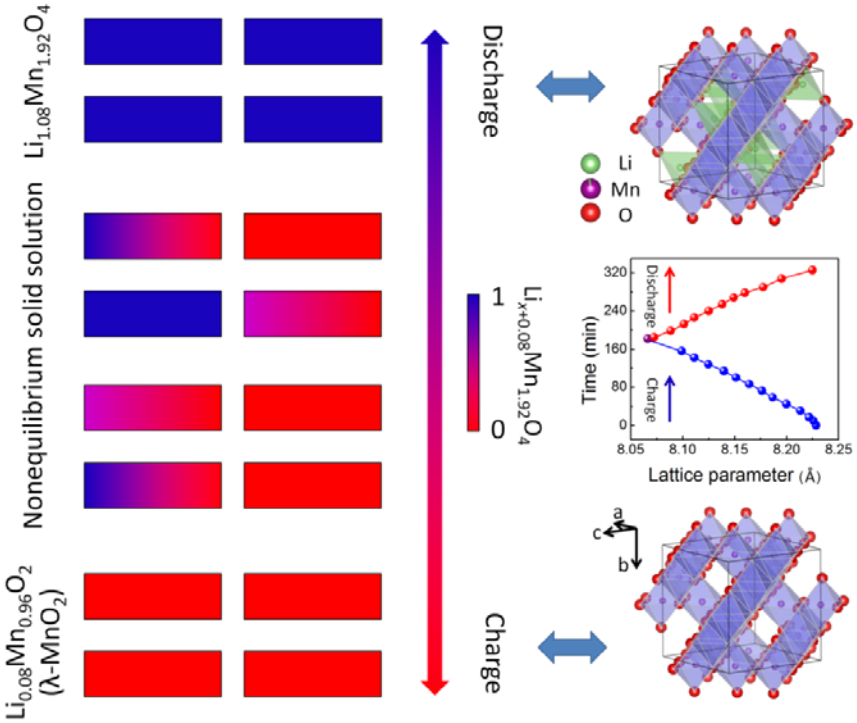

Figure 4.12 Phase transformation from $Li_{1.08}Mn_{1.92}O_4$ (blue) to $Li_{0.04}Mn_{0.96}O_2$ (λ-MnO_2, red)

and the structural relations between $Li_{1.08}Mn_{1.92}O_4$ and $Li_{0.04}Mn_{0.96}O_2$ (λ-MnO_2) with the corresponding lattice parameter changes. The lattice parameter changes with charge/discharge time correspond to the selected individual diffraction patterns [Figure 5(b)]. The delithiation/lithiation proceeds at 0.5 C via the formation of a non-equilibrium solid solution phase, $Li_{x+0.08}Mn_{1.92}O_4$ (intermediate pink color). When the charge/discharge process is finished, the particles have reached their equilibrium configuration corresponding to the $Li_{0.04}Mn_{0.96}O_2$ (λ-MnO_2) and $Li_{1.08}Mn_{1.92}O_4$ structures.

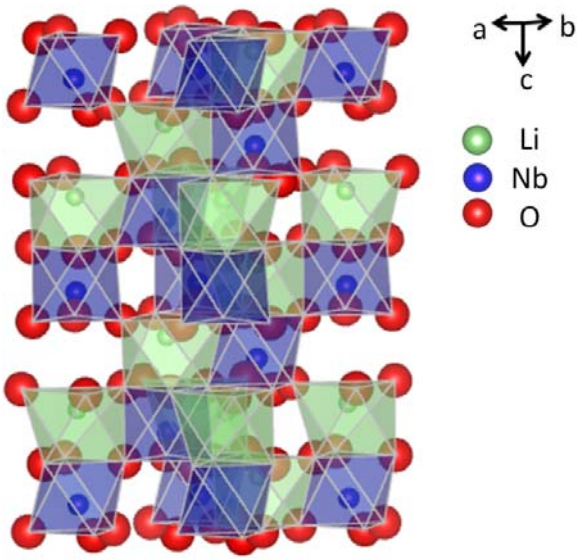

Figure 4.13 Structure of $LiNbO_3$ (space group *R3c*).

To investigate the cycling stability, the variation in the discharge capacity of the electrodes over 100 cycles is shown in Figure 4.14, where there is a comparison between $Li_{1.08}Mn_{1.92}O_4$ samples containing different amounts of SSE-$LiNbO_3$. The initial discharge specific capacities, at a rate of 0.5 C, are 131.9 mAh g^{-1}, 123.8 mAh g^{-1}, 124.7 mAh g^{-1}, and 119.7 mAh g^{-1} for $x$$LiNbO_3$-(1-$x$/2)$Li_{1.08}Mn_{1.92}O_4$ electrodes with x = 0, 0.03, 0.06, and 0.1, respectively [Figure 4.14(a)]. The retained discharge capacity was 91.4%, 94.1%, 95.7%, and 93.1%, respectively, after 100 cycles, in comparison with the initial capacity (corresponding discharge capacity: 120.6 mAh g^{-1}, 116.5 mAh g^{-1}, 119.4 mAh g^{-1}, and 111.5 mAh g^{-1})

[Figure 4.14(c)]. The behavior of xLiNbO$_3$-(1-x/2)Li$_{1.08}$Mn$_{1.92}$O$_4$ (x = 0, 0.03, 0.06, and 0.1) at high temperature (55 ^{o}C) has also been investigated and is shown in Figure 4.14(b) and (d). The pristine Li$_{1.08}$Mn$_{1.92}$O$_4$ shows a higher initial capacity than that of the same electrode at 25 ^{o}C and there was a 23.7% capacity loss after 100 cycles from 135 mAh g^{-1} to 103 mAh g^{-1}. In contrast, 0.06LiNbO$_3$-0.97Li$_{1.08}$Mn$_{1.92}$O$_4$ exhibits much greater cycling stability than the pristine compound, with only 14.3% capacity loss after 100 cycles from 139.1 mAh g^{-1} to 111.0 mAh g^{-1}. All of the samples with the LiNbO$_3$ coating layer show stable cycling performance at 55 ^{o}C, although the capacity exhibits more fading compared with the pristine Li$_{1.08}$Mn$_{1.92}$O$_4$ when the mol ratio of LiNbO$_3$ is 0.1 in the xLiNbO$_3$-(1-x/2)Li$_{1.08}$Mn$_{1.92}$O$_4$ composite materials. In accordance with those cycling stability results, a thin and uniform LiNbO$_3$-coating layer on the surface of Li$_{1.08}$Mn$_{1.92}$O$_4$ increases the high rate capability, prevents capacity fading and decrease the capacity loss caused by the weight percentage of LiNbO$_3$, especially at high temperature. The cycling performance of 0.06LiNbO$_3$-0.97Li$_{1.08}$Mn$_{1.92}$O$_4$ at 25 ^{o}C and 55 ^{o}C is not only in sharp contrast to that of the pristine Li$_{1.08}$Mn$_{1.92}$O$_4$, but also compares favorably with the widely reported results for cycling stability of Li$_{1+x}$Mn$_{2-x}$O$_4$ with or without a coating layer (Table 4.8).

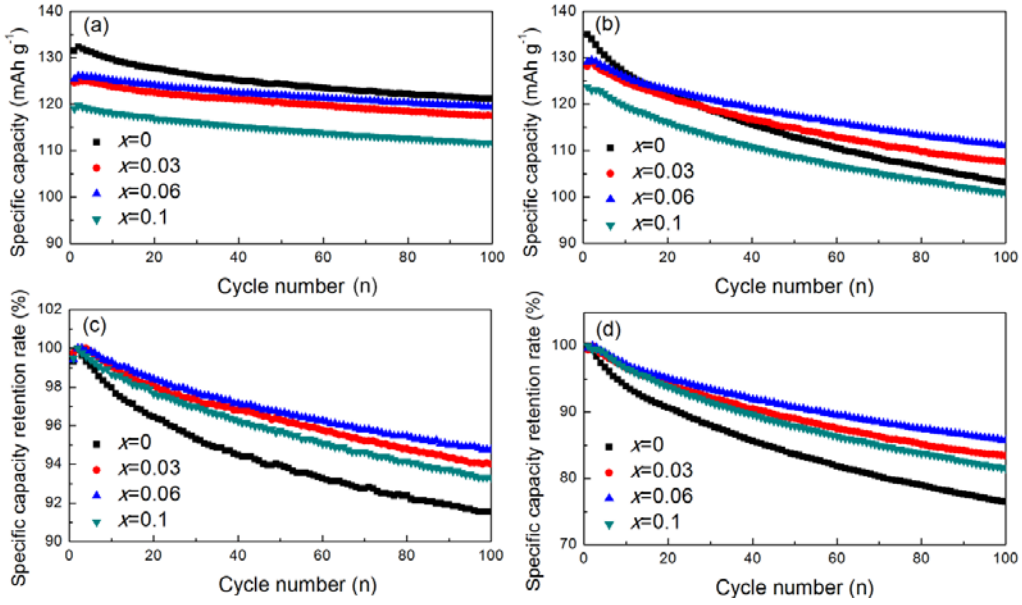

Figure 4.14 Cycling performance (a, b) and capacity retention rate (c, d) for xLiNbO$_3$-(1-

$x/2)Li_{1.08}Mn_{1.92}O_4$ electrodes (x = 0, 0.03, 0.06, and 0.1) at current density of 0.5 C with a potential window of 4.5-3.2 V: (a) and (c) at 25 ^oC, (b) and (d) at 55 ^oC. The cycling retention rate is expressed as a relative specific discharge capacity compared to that obtained from the first cycle.

Table 4.8 Cycling and rate performance of $Li_{1+x}Mn_{2-x}O_4$ spinel cathodes in the literature [a].

Composition	Initial capacity		Capacity retention [b]		Rate capability [c]		Reference
	(mAh g^{-1}) and (C)		(%) and (cycles)		(C) and (%)		
$0.06LiNbO_3$-$0.97Li_{1.08}Mn_{1.92}O_4$	125	0.5	96	100	50	88	Current work
$LiMn_2O_4$	~ 135	0.33	~ 92	50	/	/	41
$LiMn_2O_4$	~ 115	10	~ 91	400	100	81	49
$LiMn_2O_4$	105	10	/	/	30	52	50
$Li_{1.03}Mn_{1.97}O_4$	127	1	91	100	10	84	42
$Li_{1.05}Mn_2O_4$	~ 120	10	~ 75	200	/	/	39
$Li_{1.05}Mn_{1.95}O_4$	116	0.2	~ 91	150	/	/	51
$Li_{1.08}Mn_2O_4$	123	0.2	84	25	/	/	52
$Li_{1.05}Mn_2O_{4.1}$	119	0.33	92	50	/	/	34
$LiMn_2O_4$-6.3wt%Ag	123	1	94	50	10	94	53
$Li_{1.08}Mn_2O_4$-0.1wt%LBO	122	0.2	87	25	/	/	52
$LiMn_2O_4$-7mol%$LiCoO_2$	~ 122	0.2	92	100	/	/	54

[a] Comparisons may only be approximate due to the diversity of cell assembly techniques in different laboratories. [b] Capacity after 100 cycles compared with the initial capacity at room temperature and the corresponding discharge current density. [c] High rate current density and capacity retention compared with the capacity at around 0.5 C and room temperature.

Table 4.9 R_f, R_{ct}, and R_l values for the xLiNbO$_3$-(1-x/2)$Li_{1.08}Mn_{1.92}O_4$ (x = 0, 0.03, 0.06, and 0.1) electrodes calculated by Zview.

Temperature (K)	R_f (Ω)	R_{ct} (Ω)	R_l (Ω)
$Li_{1.08}Mn_{1.92}O_4$			
297.15	327.9	563.6	0.5
303.15	195.4	288.2	0.6
311.15	139.3	133.8	0.7
316.15	118	89.9	0.7
328.15	84.6	37.1	0.9
$0.03LiNbO_3$-$1.985Li_{1.08}Mn_{1.92}O_4$			
297.15	146.2	144.3	2.6
303.15	116.1	121	3.6
310.15	90.7	77.6	1.9
316.15	84.6	53	1.8
324.15	80.6	26.9	1.6
$0.06LiNbO_3$-$1.97Li_{1.08}Mn_{1.92}O_4$			
297.15	75.2	164.3	2.8
303.15	56.9	126.3	1.9
310.15	45.6	99.1	2.2

Temperature (K)	R_f (Ω)	R_{ct} (Ω)	R_l (Ω)
316.15	38.1	67.4	1.8
323.19	36.9	56.2	1.9
$0.1LiNbO_3$-$1.95Li_{1.08}Mn_{1.92}O_4$			
297.15	121.2	214.5	4.6
303.15	89.7	164.6	3.6
309.15	77.5	128.7	2.2
316.15	66.6	95.9	2
325.19	54.1	52.9	2.3

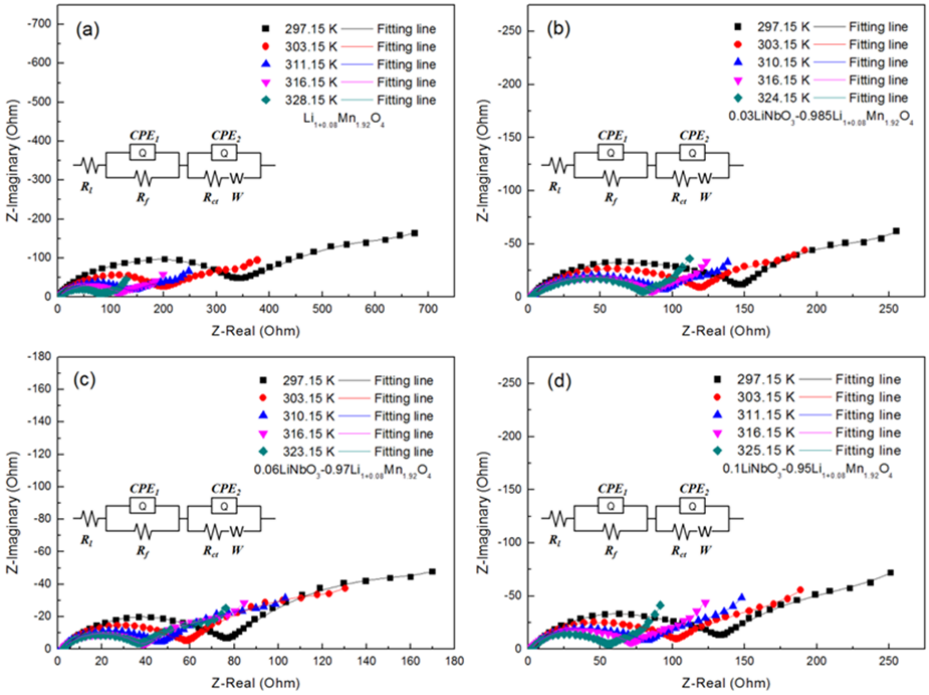

Figure 4.15 Nyquist plots of xLiNbO$_3$-(1-x/2)Li$_{1.08}$Mn$_{1.92}$O$_4$ (x = 0, 0.03, 0.06, and 0.1) electrodes after cycling over 5 cycles at a discharge potential of 4.0 V vs. Li/Li$^+$ at different temperatures and frequencies from 100 kHz to 10 mHz. The equivalent circuit is shown in the insets.

To further investigate the influence of the SSE coating layer on the LIBs when combined with OLE, the electrochemical kinetics for the xLiNbO$_3$-(1-x/2)Li$_{1.08}$Mn$_{1.92}$O$_4$ (x = 0, 0.03, 0.06, and 0.1) electrodes was examined by electrochemical impedance spectroscopy (EIS). Figure 4.15 shows the Nyquist plots at discharge potential of 4.0 V vs. Li/Li$^+$ at different temperatures after 5 cycles. All the impedance curves show two partially overlapping semicircles in the high to medium frequency region, which could be assigned to the film resistance (R_f), associated with the solid electrolyte interphase (SEI), and the charge transfer

resistance (R_{ct}), respectively. A line inclined at approximately 45° reflects the Warburg impedance (W), which is associated with the lithium-ion diffusion in the $Li_{1.08}Mn_{1.92}O_4$ compound. The high-frequency intercept of the semicircle reflects the uncompensated resistance (R_l), which includes the particle-particle contact resistance, the electrolyte resistance, and the resistance between the cathode materials and the current collector [105]. The R_f, R_{ct}, and R_l values for the xLiNbO$_3$-(1-x/2)$Li_{1.08}Mn_{1.92}O_4$ (x = 0, 0.03, 0.06, and 0.1) electrodes were obtained using the equivalent circuit shown in the inset of Figure 4.15(a) (calculated by Zview and shown in Table 4.9). The R_l of the $LiNbO_3$-coated $Li_{1.08}Mn_{1.92}O_4$ electrodes is slightly higher than that of the pristine $Li_{1.08}Mn_{1.92}O_4$ electrode, whereas the R_f is apparently decreased after coating with $LiNbO_3$. This indicates that the $LiNbO_3$ coating layer effectively hinders SEI formation. The lithium diffusion coefficients and apparent activation energies of the xLiNbO$_3$-(1-x/2)$Li_{1.08}Mn_{1.92}O_4$ (x = 0, 0.03, 0.06, and 0.1) electrodes were calculated from EIS results using a previously reported method [134, 301].

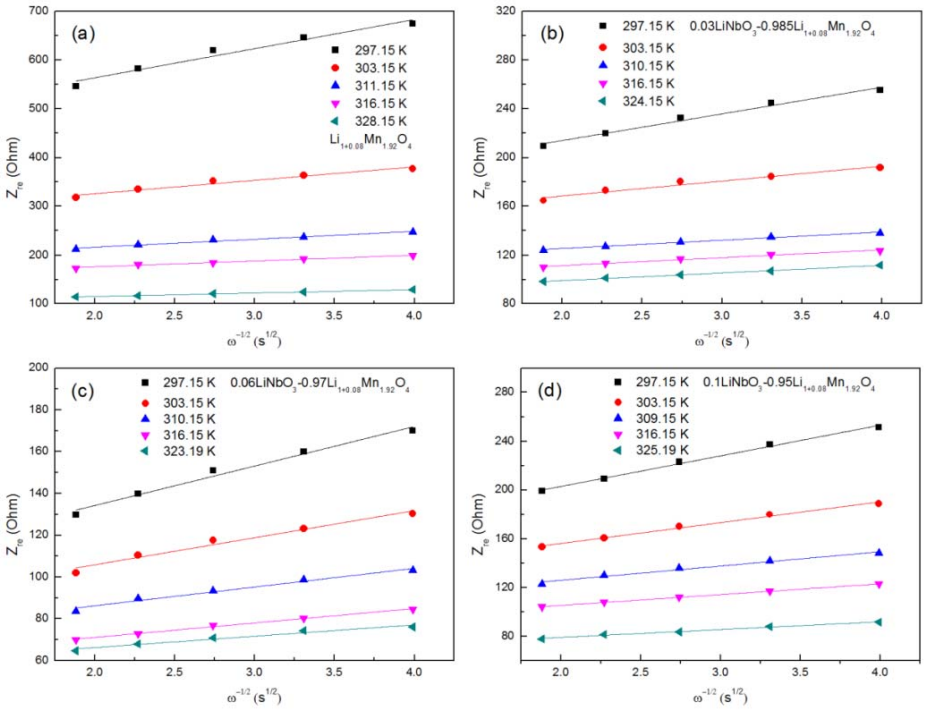

Figure 4.16 Real part of the complex impedance for the electrodes versus $\omega^{-1/2}$ at a series of

temperatures at discharge potential of 4.0 V vs. Li/Li^+.

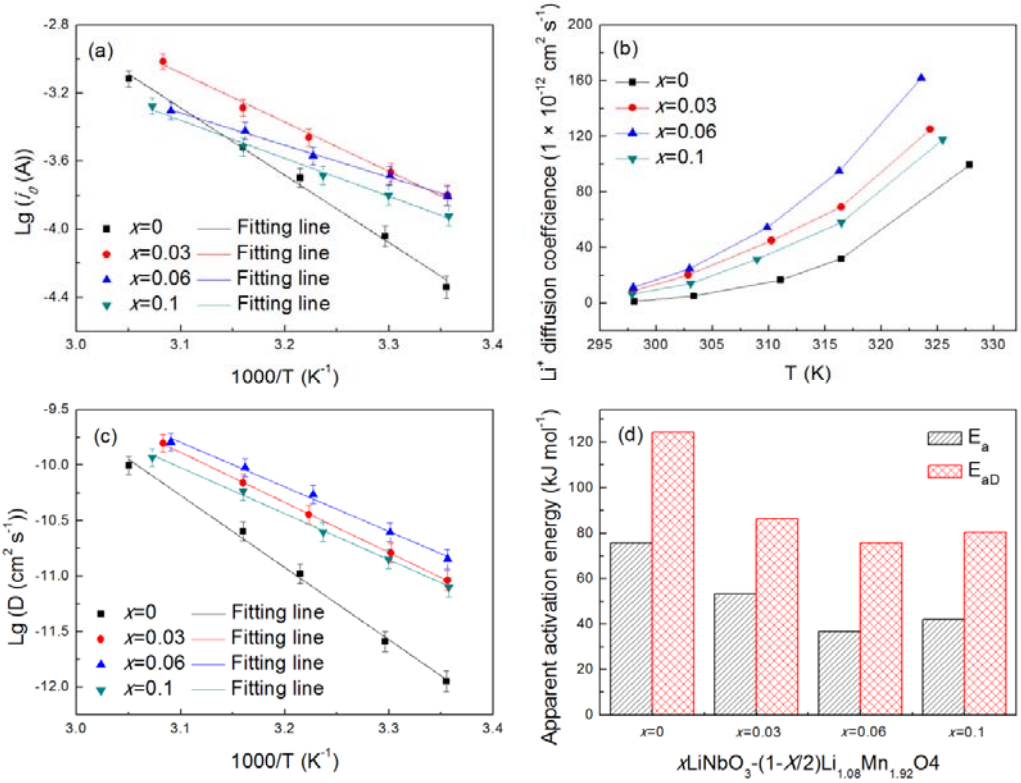

Figure 4.17 Electrochemical kinetics for xLiNbO$_3$-(1-x/2)Li$_{1.08}$Mn$_{1.92}$O$_4$ (x = 0, 0.03, 0.06, and 0.1) electrodes at a discharge potential of 4.0 V vs. Li/Li^+: (a) Arrhenius plots of lg i_0 versus 1/T. The lines are the linear fitting results; (b) lithium diffusion coefficients at different temperatures; (c) Lg D versus 1/T plots during lithium insertion, with the solid lines indicating the linear fitting results; (d) comparison of E_a and E_{aD} (activation energy based on the Arrhenius equation and on the lithium diffusion coefficient, respectively).

The lithium diffusion coefficient can be used to calculate using the following Equation (4.1) [302, 303]:

$$D = R^2T^2/2A^2n^4F^4C^2\sigma^2 \quad (4.1)$$

where D is the diffusion coefficient (cm^2 s^{-1}), R is the gas constant, T is the absolute temperature, A is the surface area of the cathode (1 cm^2), n is the number of electrons

transferred in the half-reaction for the redox couple, which is equal to 1, F is the Faraday constant, C is the concentration of Li ions in the solid $Li_{1.08}Mn_{1.92}O_4$ (2.99×10^{-3} mol cm^{-3}), and σ is the Warburg factor, which is relative to Z_{re} [304]. σ can be obtained from the slope of the lines in Figure 4.16.

$$Z_{re} = R_l + R_{ct} + \sigma\omega^{-1/2} \quad (4.2)$$

The lithium diffusion coefficients are calculated to be (1.1, 9.1, 11.3, and 6.3) $\times 10^{-12}$ cm^2 s^{-1} for the $x$$LiNbO_3$-(1-$x$/2)$Li_{1.08}Mn_{1.92}O_4$ (x = 0, 0.03, 0.06, and 0.1) electrodes, respectively, at 24 ^oC. The 0.06$LiNbO_3$-0.97$Li_{1.08}Mn_{1.92}O_4$ composite material with a thin and uniform coating layer exhibits the highest lithium diffusion coefficient. The high lithium diffusion coefficient is also owing to the high ionic conductivity of the SSE-$LiNbO_3$ coating layer. During the sintering process at high temperature, the primary particles (around 500 nm in size) were merged into secondary particles (about 1 μm), as shown in Figure 4.5 and Figure 4.6. The portion of $LiNbO_3$ that is located in the interior of the secondary particles (due to the coating on the primary particles) effectively improves the lithium diffusion coefficient. The lithium diffusion coefficient increases with increasing of $LiNbO_3$ uniformity on the surface of the $Li_{1.08}Mn_{1.92}O_4$ crystal. When the primary $Li_{1.08}Mn_{1.92}O_4$ particles have a thin and uniform coating layer, there will be a three-dimensional (3D) $LiNbO_3$ net structure. This 3D $LiNbO_3$ net structure effectively decreases the lithium diffusion distance and increases the lithium diffusion coefficient. The lithium diffusion coefficient was also calculated at different temperatures [Figure 4.17(b)]. The lithium diffusion coefficient increases as the temperature increases.

The exchange current (i_0) and the apparent activation energy (E_a) for lithium intercalated into the $Li_{1.08}Mn_{1.92}O_4$ spinel structure can be calculated from Equation (4.1) and the Arrhenius equation, Equation (4.2), respectively.

$$i_0 = RT/nF\ R_{ct} \quad (4.3)$$

$$i_0 = A \exp(- E_a/ RT) \quad (4.4)$$

where A is a temperature-independent coefficient, R is the gas constant, T (K) is the absolute temperature, n is the number of transferred electrons, and F is the Faraday constant. Figure 4.17(a) shows the Arrhenius plots of lg i_0 as a function of $1/T$. The apparent activation energies [E_a = - Rk ln 10, where k is the slope of the fitting line in Figure 4.17(a)] of the $x$$LiNbO_3$-(1-$x$/2)$Li_{1.08}Mn_{1.92}O_4$ (x = 0, 0.03, 0.06, and 0.1) electrodes are shown in Figure 4.17(d). The $0.06LiNbO_3$-$0.97Li_{1.08}Mn_{1.92}O_4$ composite material with a thin and uniform coating layer exhibits the lowest E_a (36.9 kJ, error within 1.5%).

The diffusion apparent activation energy (E_{aD}) can also be calculated from the plots of log D *vs.* $1/T$ using the equation: E_{aD} = - Rk ln (10), where k is the slope of the fitting line in Figure 4.17(c). The diffusion apparent activation energy is shown in Figure 4.17(d), and the trend in the values as the amount of Nb element increases is similar to that for E_a (based on the Arrhenius equation). The lowest E_{aD} (75.8 kJ, error within 1%) appears for the $0.06LiNbO_3$-$0.97Li_{1.08}Mn_{1.92}O_4$ composite material with a thin and uniform coating layer, corresponding to the lithium diffusion coefficient results.

The excellent electrochemical stability of the $0.06LiNbO_3$-$0.97Li_{1.08}Mn_{1.92}O_4$ composite material is also confirmed by the images of electrodes, which were collected after 100 cycles at 0.5 C and 25 ^oC (Figure 4.18). As can be seen from the optical digital photographs (Figure 4.18: the right sides of the FESEM images), the morphology of the $0.06LiNbO_3$-$0.97Li_{1.08}Mn_{1.92}O_4$ cathode electrode after 100 charge-discharge cycles is still smooth and flat, and the counter anode (lithium foil) and separator do not show manganese deposition from cathode dissolution, whereas the pristine $Li_{1.08}Mn_{1.92}O_4$ cathode electrode after 100 charge-discharge cycles shows a rough surface, and the surfaces of the counter anode (lithium

foil) and separator exhibit an obvious black slurry from cathode manganese dissolution.

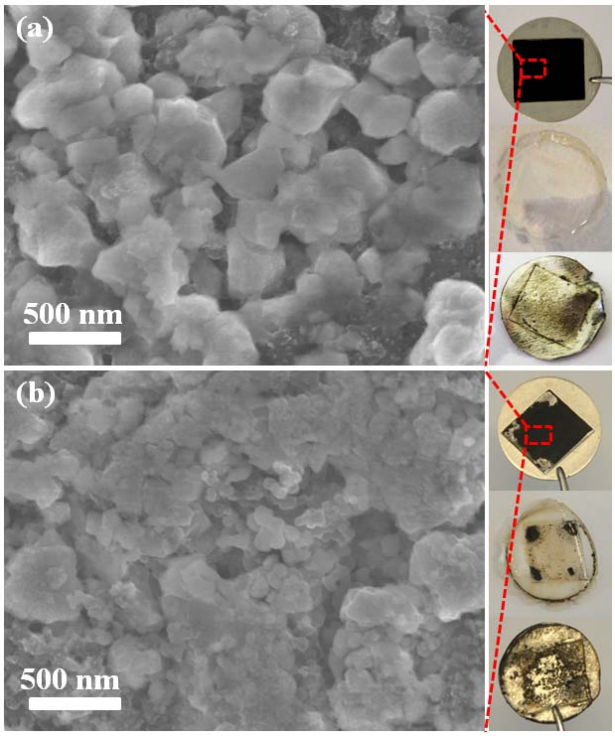

Figure 4.18 Images of electrodes collected after 100 cycles at 0.5 C and 25 ^{o}C: FESEM images of (a) $0.06LiNbO_3$-$0.97Li_{1.08}Mn_{1.92}O_4$ sample and (b) pristine $Li_{1.08}Mn_{1.92}O_4$ sample. The right sides of the FESEM images are the corresponding optical digital photographs for the cathode (top), separator (middle), and lithium anode (bottom).

Figure 4.18 (a) and (b) presents the respective FESEM images of the $0.06LiNbO_3$-$0.97Li_{1.08}Mn_{1.92}O_4$ and pristine $Li_{1.08}Mn_{1.92}O_4$ cathodes after100 cycles at 0.5 C and 25 ^{o}C. It can be found by comparing the two cathodes that the pristine $Li_{1.08}Mn_{1.92}O_4$ particles are separated from each other and shrunken within the secondary particles, but this did not occur in the $LiNbO_3$-coated cathode. Due to the sintering at high temperature, the primary particles (around 500 nm in size) were merged into secondary particles (about 1 μm), as shown in Figure S3. Similar to what was previously reported, the formation of Mn^{3+} leads to Mn dissolution, and Jahn-Teller crystallographic distortion causes the primary particles of $Li_{1.08}Mn_{1.92}O_4$ to separate and shrink [305, 306]. Therefore, the SSE-$LiNbO_3$ coating layer

prevents the soluble Mn^{2+} from passing into the electrolyte and allows the Li^+ ions free transportation among the cathode, OLE, and anode, while there are no reports that conventional coating layers can decrease the lithium ionic conduction and/or charge transfer reaction between the electrode and electrolyte [242, 275-283].

4.4 Conclusion

SSE-$LiNbO_3$ coating layers on manganese spinel cathode were successfully introduced into LIBs with an organic liquid electrolyte system using a facile solid-state reaction method. The $Li_{1.08}Mn_{1.92}O_4$ sample with a thin and uniform coating layer exhibited higher cycling stability, higher rate capability, and better high temperature cycling performance than the pristine $Li_{1.08}Mn_{1.92}O_4$. The SSE-$LiNbO_3$ coating layer effectively prevented Mn dissolution, and the $Li_{1.08}Mn_{1.92}O_4$ samples with $LiNbO_3$ coating layers showed much lower charge transfer resistance, lower apparent activation energy, and lower apparent diffusion activation energy than the pristine $Li_{1.08}Mn_{1.92}O_4$ sample, due to their high ionic conductivity. The successful combination of a SSE coating layer with OLE in LIBs provides a clear direction for designing next-generation large-scale LIBs.

Chapter 5 Solid-state electrolyte $LiNbO_3$ Additive for Improving Cycling and Rate Abilities of High-Voltage $LiNi_{0.5}Mn_{1.5}O_4$ Cathode Material

5.1 Introduction

Spinel $LiNi_{0.5}Mn_{1.5}O_4$ (LNMO) has received particularly attention as a potential cathode material for large-scale energy storage and electric vehicles (EVs), due to its high-voltage plateau (~ 4.7 V vs. Li^+/Li) offering high energy density [2, 3, 307]. In addition, LNMO shows several advantages, such as low cost, environmental friendliness, good rate capability due to its fast Li^+ diffusion within the three-dimensional spinel structure [15, 308]. The electrochemical performance of LNMO, however, depends on many factors related to the material itself, such as its crystalline structure (cation mixing and stoichiometry), particle morphology and size, and electrolyte type. It worth noting that the LNMO shows unsatisfactory electrochemical performance at high rate and does not have a long cycle life. This poor battery performance is partly owing to variations in lithium ion conductivity between different LMNO secondary particles and the high reactivity of the transition metal cations at the surface. The latter leads to the formation of cathode electrolyte interphase (CEI), which is a thick, resistive passivation layer and also limits the lithium ion intercalation/deintercalation [309-311].

One viable option is modification of the material by coating with an oxide, such as MgO [312], ZnO [313], or SiO_2 [314]. The coating layers can protect the electrolyte from the oxidative side reactions at high voltage, but it does not improve the lithium ion conductivity. Recently, Ohta et al. reported that oxide buffer layers ($Li_4Ti_5O_{12}$ [274], $LiNbO_3$ (LNO) [241], $LiTaO_3$ [315], and Li_2SiO_3 [316]) are interposed in all-solid-state lithium-ion batteries (LIBs) between the $LiCoO_2$ cathode and electrolyte by spray-coating or the sol-gel method, and reduce the lithium charge transfer resistance (related to lithium ion conductivity). In

particular, $LiCoO_2$ particles coated with solid-state electrolyte LNO exhibited the smallest lithium charge transfer resistance among them. Meanwhile, Haruyama et al. theoretically elucidated that the LNO interposition provides smooth lithium ion transport paths between the cathode and electrolyte [242].

Herein, I uniformly mixed solid-state electrolyte LNO and LNMO material using a simple solid-state reaction method. The solid-state reaction should consist of a two-phase synergistic nucleation and growth process, and the small amount of LNO has a preference for nucleation and growth at LNMO lattice defects, which are located at the crystal surface. During the sintering process at high temperature, the LNMO primary particles were merged into secondary particles. Solid-state electrolyte LNO additive acts as a bifunctional additive in LIBs with organic liquid electrolyte. The portion of LNO that is located in the interior of the secondary particles (due to nucleation and growth on the primary particles) effectively improves the lithium diffusion coefficient; and the portion of LNO that is located on the secondary particle surface protects the electrolyte from the oxidative side reactions at high voltage (Figure 5.1).

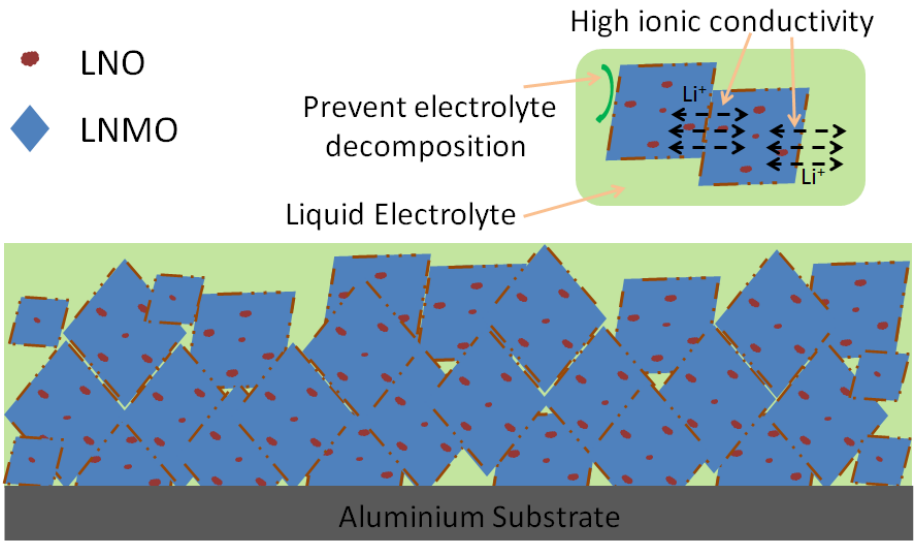

Figure 5.1 Schematic illustration of LNO-LNMO interface between secondary particles and

liquid electrolyte in a LIB.

In this report, LNMO was synthesized by a citric-acid-assisted sol-gel method, and LNO/LNMO composite was synthesized by the solid-state reaction method. The influence of the LNO additive has been investigated, including the influence on the crystal structure and electrochemical performance. The LNO additive effectively increases the lithium ion conductivity of LNMO cathode and inhibits the formation of CEI.

5.2 Experimental Section

5.2.1 Material Synthesis

LNMO was synthesized by a citric acid-assisted sol-gel method according to our previous report [317]. The starting materials, lithium acetate ($LiCH_3COO{\cdot}2H_2O$, ≥ 99% purity, Sigma-Aldrich), nickel acetate ($Ni(CH_3COO)_2{\cdot}4H_2O$, ≥ 99% purity, Sigma-Aldrich), manganese acetate ($Mn(CH_3COO)_2{\cdot}4H_2O$, ≥ 99% purity, Sigma-Aldrich), and citric acid ($C_6H_8O_7$, 99% purity, Sigma-Aldrich) were dissolved in an appropriate amount of distilled water under stirring. The mol ratio of Li/Ni/Mn is 1.1/0.5/1.5. The resulting solution was stirred for 12 h at room temperature, before heating at 80 ^oC to form a viscous gel. The viscous gel was then heated at 850 ◦C in a tube furnace for 10 h in air and subsequently annealed at 600 ^oC for another 5 h.

*x*LNO/LNMO (*x* =0, 0.02, 0.04, 0.06) composites were synthesized by the solid-state reaction method according to our previous report [318]. The stoichiometric amounts of starting materials, niobium pentoxide (Nb_2O_5, 99.8% purity, CBMM-Brazil), lithium carbonate ($LiCO_3$, ≥ 99% purity, Sigma-Aldrich), and LNMO, were ground in an agate mortar with a pestle until the mixture became homogeneous. After that, the mixture was pressed into pellets and preheated at 650 ^oC in air for 5 h in a tube furnace. Then, the mixture was again ground,

pressed into pellets, and heated at 750 ^oC in air for 24 h in the same tube furnace. All the samples were cooled to room temperature at the cooling rate of 1 ^oC/min after the second heat-treatment.

5.2.2 Material Characterization

The structures of the as-prepared materials were characterized by X-ray diffraction (XRD; GBC MMA) with Cu Kα radiation, and synchrotron X-ray diffraction (SXRD) with *in situ* SXRD conducted at the Powder Diffraction Beamline (wavelengths: 0.8257 Å, and 0.6887 Å; Australian Synchrotron, Clayton, Australia) with a Mythen detector. The morphologies of the as-prepared materials were examined by field emission scanning electron microscopy (FESEM; JEOL 7500, 30 kV), and transmission electron microscopy (TEM; JEOL JEM-2011, 200 kV) with high-resolution TEM (HRTEM). The specific areas of the as-prepared materials were calculated by Brunauer-Emmett-Teller (BET) analysis (Quanta Chrome Nova 1000). To test the electrodes after cycling, the cells were opened, and the electrodes were taken out and washed with dimethyl carbonate (DMC) three times. For the *in situ* synchrotron X-ray diffraction, Kapton film was used as a window to allow the penetration of the synchrotron beam into the *in situ* cell, which was assembled under the same conditions as the other cells in this work.

5.2.3 Electrochemical measurements

To test the electrochemical performance, the electrodes were prepared by mixing *x*LNO/LNMO (x = 0, 0.02, 0.04, and 0.06) composite materials with super P, and polyvinylidene fluoride (PVDF) in *N*-methyl-2-pyrrolidone (NMP), in a weight ratio of 80:10:10. The slurry was spread onto aluminum foil with a doctor blade with a thickness of 200 μm, followed by drying in a vacuum oven at 100 ^oC for 24 h. The working electrode was prepared by punching the electrode film into discs 1.2 cm in diameter (area = 1 cm^2). The

electrode was then pressed using a disc with a diameter of 14 mm to enhance the contact between the aluminum foil, active materials, and conductive carbon. The average active material loading rate was ~ 3 mg cm^{-2}. CR 2032 coin-type cells were assembled in an Ar-filled glove box (Mbraun, Unilab, Germany), using lithium foil as the counter electrode. The electrolyte was 1 M $LiPF_6$ in a mixture of ethylene carbonate (EC) and dimethyl carbonate (DMC) (1:1 by volume). The cells were galvanostatically charged and discharged in the voltage range of 5-3.5 V at different current densities using a computer-controlled charger system manufactured by Land Battery Testers. A Biologic VMP-3 electrochemical work station was used to perform cyclic voltammetry (CV; scanning rate 0.1 mV s^{-1}) and electrochemical impedance spectroscopy (EIS; ac amplitude 5 mV, frequency range 100 kHz-0.01 Hz).

5.3 Results and Discussion

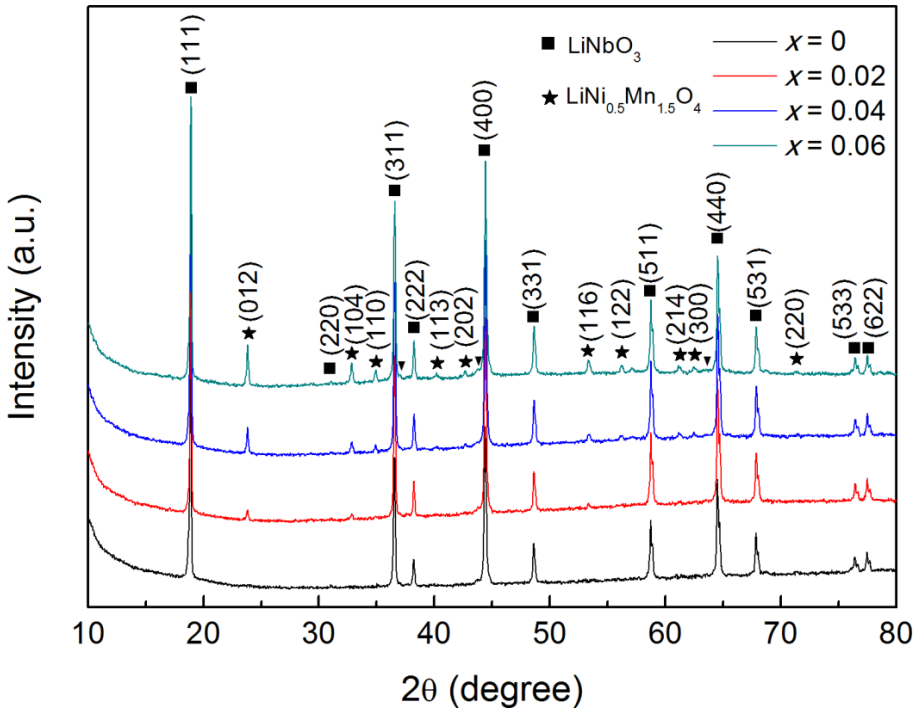

Figure 5.2 XRD patterns for as-prepared *x*LNO/LNMO (*x* = 0, 0.02, 0.04, and 0.06) composites.

The structures and phases of the as-prepared *x*LNO/LNMO (*x* = 0, 0.02, 0.04, and 0.06) composites were analyzed by X-ray diffraction (XRD; Figure 5.2) and synchrotron powder X-ray diffraction (SXRD, Figure 5.3). All peaks of *x*LNO/LNMO (*x* = 0, 0.02, 0.04, and 0.06) are sharp and well defined, indicating that the composites are well crystallized. The diffraction patterns can be indexed as mixed phases [LNMO $Fd\bar{3}m$ spinel structure (JPCDS card no. 80-2162) and LNO *R3c* structure (JPCDS card no. 20-0631)]. A common impurity phase, $Li_xNi_{1-x}O$, can be observed from the XRD patterns at 2θ angles of 37.5°, 43.7°, and 63.7°. In order to further identify the phases and phase composition, Rietveld refinements of the SXRD data on *x*LNO/LNMO (*x* = 0, 0.02, 0.04, and 0.06) were conducted, as shown in Figure 5.3. The refined lattice parameters are summarized in Table 5.1. The lattice parameters of LNMO remain stable with increasing amounts of the LNO phase, and peak shifts cannot be observed. That is to say, the Nb element only forms LNO phase on the surface of LNMO crystals and the LNMO phase structure is not affected by the LNO formation process.

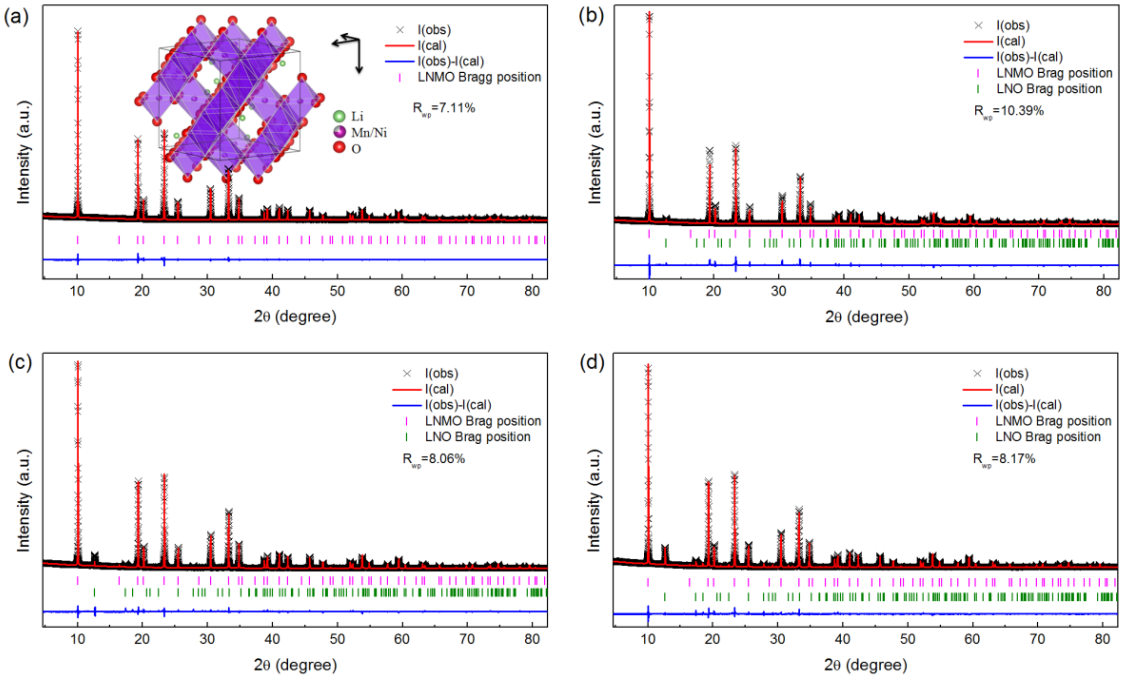

Figure 5.3 Rietveld refinement results for SXRD patterns: (a) LNMO, with the spinel structure of LNMO shown in the inset (space group $Fd\bar{3}m$); (b) 0.02LNO/LNMO; (c)

0.04LNO/LNMO; and (d) 0.06LNO/LNMO. I(obs) is observed data, I(cal) is calculated data, I(obs)-I(cal) is the difference curve between the observed and calculated intensities. R_{wp} is the weighted profile factor.

Table 5.1 Lattice parameters for the *x*LNO/LNMO (*x* = 0, 0.02, 0.04, and 0.06) composites.

Samples		a(Å)	b(Å)	c(Å)	Volume (Å^3)	Rwp[a] (%)
x=0	Phase1[b]	8.16486	8.16486	8.16486	544.31	7.11
	Phase2[c]	/	/	/	/	
x=0.03	Phase1	8.16034	8.16034	8.16034	543.406	10.39
	Phase2	5.14369	5.14369	13.8340	316.979	
x=0.06	Phase1	8.16139	8.16139	8.16139	543.616	8.06
	Phase2	5.14061	5.14061	13.8445	318.075	
x=0.10	Phase1	8.16290	8.16290	8.16290	543.918	8.17
	Phase2	5.15857	5.15857	13.8164	318.407	

[a] R_{wp} is the agreement factor for the *x*LNO/LNMO (*x* = 0, 0.02, 0.04, and 0.06) refinement.
[b] is LNMO phase. [c] is LNO phase.

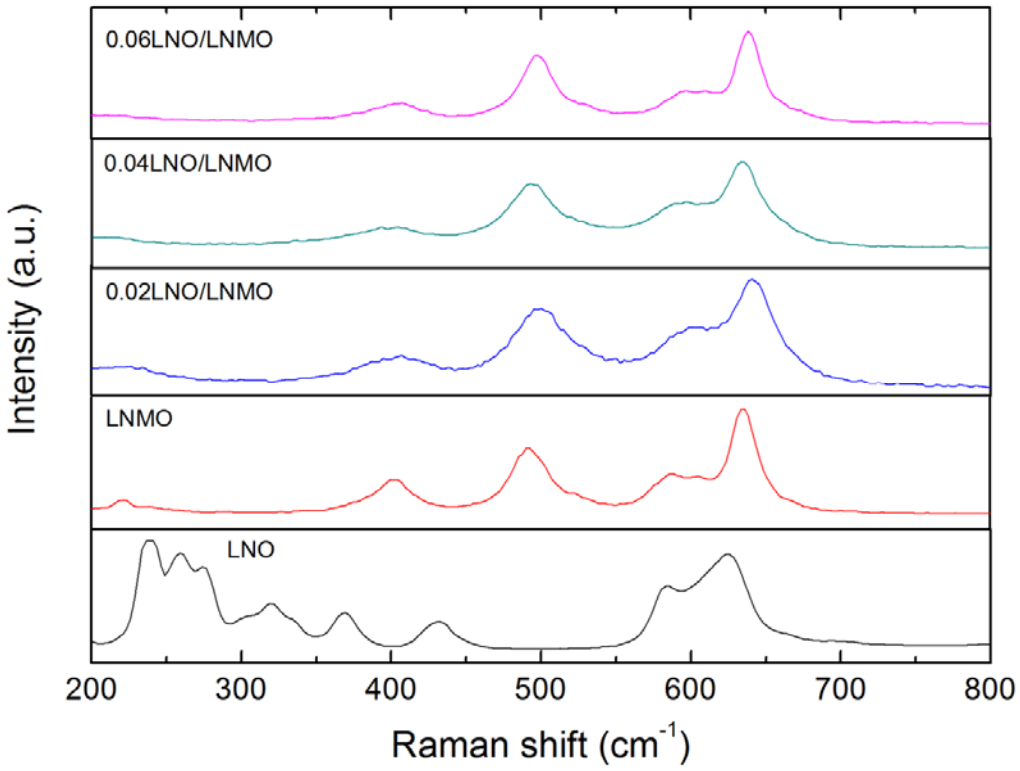

Figure 5.4 Raman spectra of *x*LNO/LNMO (*x* = 0, 0.02, 0.04, and 0.06) composites and pure LNO.

Raman spectroscopy was conducted to further confirm that the LNMO phase is $Fd\bar{3}m$ spinel structure. The Raman patterns of *x*LNO/LNMO (*x* = 0, 0.02, 0.04, and 0.06) are shown in

Figure 5.4. The spectra of the pristine LNMO sample exhibit a typical band at ~ 636 cm^{-1} corresponding to the Mn-O bond (belonging to the MnO_6 group) [319]. The bands at 404 and 496 cm^{-1} are assigned to the Ni^{2+}-O stretching band [320]. The bands at 580 and 605 cm^{-1} are related to nickel substitution [321]. In comparison, the spectra of LNMO phase in *x*LNO/LNMO (*x* = 0.02, 0.04, and 0.06) composites shows the same band positions as the pristine LNMO. The LNO peaks can be observed at 240, 253, 265, 334, 370, 433, 580 and 632 cm^{-1}, similar to other reports in the literature [322, 323].

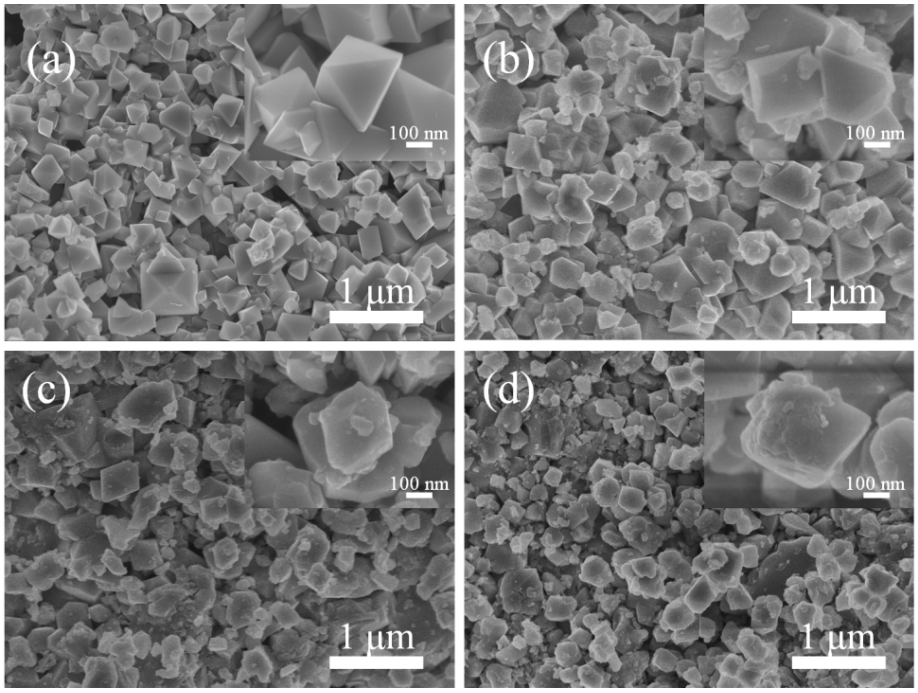

Figure 5.5 FESEM images of (a) LNMO; (b) 0.02LNO/LNMO; (c) 0.04LNO/LNMO; and (d) 0.06LNO/LNMO. The insets show corresponding high magnification images.

Typical morphologies of the *x*LNO/LNMO (*x* = 0.02, 0.04, and 0.06) composites are shown in Figure 5.5. The particle sizes of all four samples are approximately 500 nm. The pristine LNMO particles show a clear surface. After introducing the LNO, the particle sizes of the *x*LNO/LNMO (*x* = 0.02, 0.04, and 0.06) composites do not significantly increase, however, the small LNO particles can be observed on the surface of LNMO particles and in the gaps between the LNMO particles. The specific surface areas of the as-prepared samples were

measured by the 15-point Brunauer-Emmett-Teller (BET) N_2 adsorption method. The specific surface areas of the *x*LNO/LNMO (*x* = 0.02, 0.04, and 0.06) composites are slightly increased

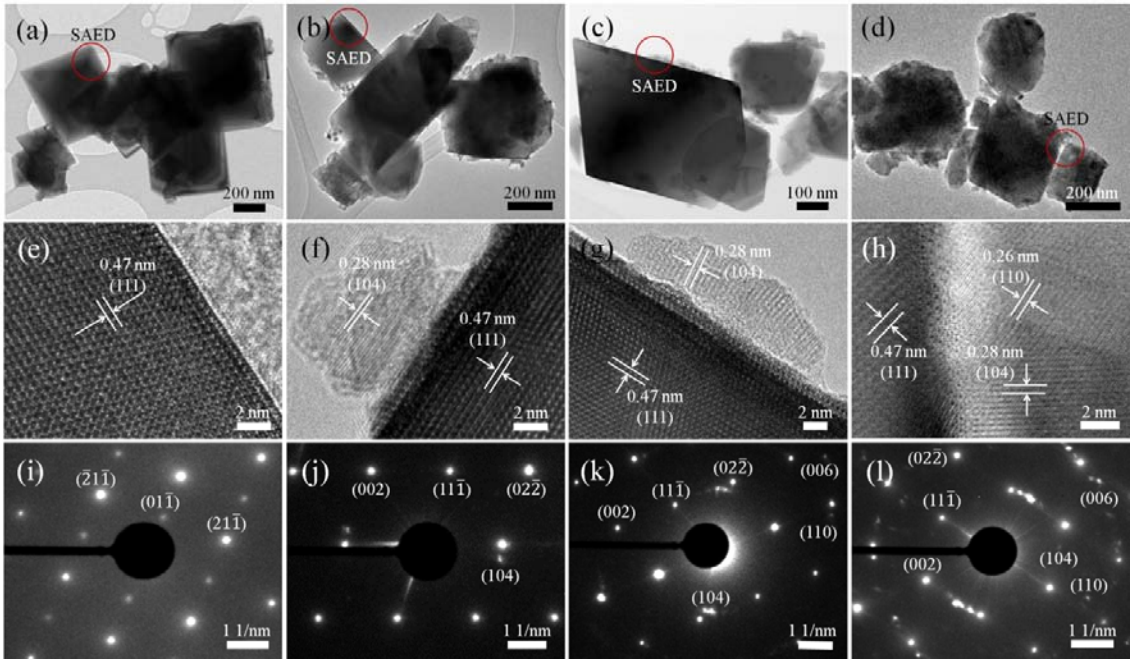

Figure 5.6 TEM images, HRTEM images, and SAED patterns, respectively: (a, c, i) LNMO; (b, f, j) 0.02LNO/LNMO; (c, g, k) 0.04LNO/LNMO; and (d, h, l) 0.06LNO/LNMO.

compared with the pristine LNMO particles (1.6, 2.1, 2.8, 2.3 m^2 g^{-1}, respectively). TEM investigations further revealed that the samples consisted of LNO and LNMO (Figure 5.6). The particles of the pristine LNMO sample showed very smooth edges, and there is no other phase on the surface in Figure 5.6(a). As can be seen from Figure 5.6(b) and (c), the 0.04LNO/LNMO composite features a uniform LNO net (consisting of small LNO nanoparticles) on the surface of the LNMO particles, while the 0.02LNO/LNMO composite features fewer LNO particles on the surface of the LNMO particles. Big particles are observed on the surface of LNMO particles when the *x* value for LNO is 0.06 [Figure 5.6(d)]. To gain structural information, HRTEM images and the corresponding selected area electron diffraction (SAED) patterns are shown in Figure 5.6(e-l). The pristine LNMO sample shows lattice fringes with a lattice spacing of 0.47 nm along the [111] direction, and the selected

area electron diffraction pattern presents well-defined spots which can be well indexed to the

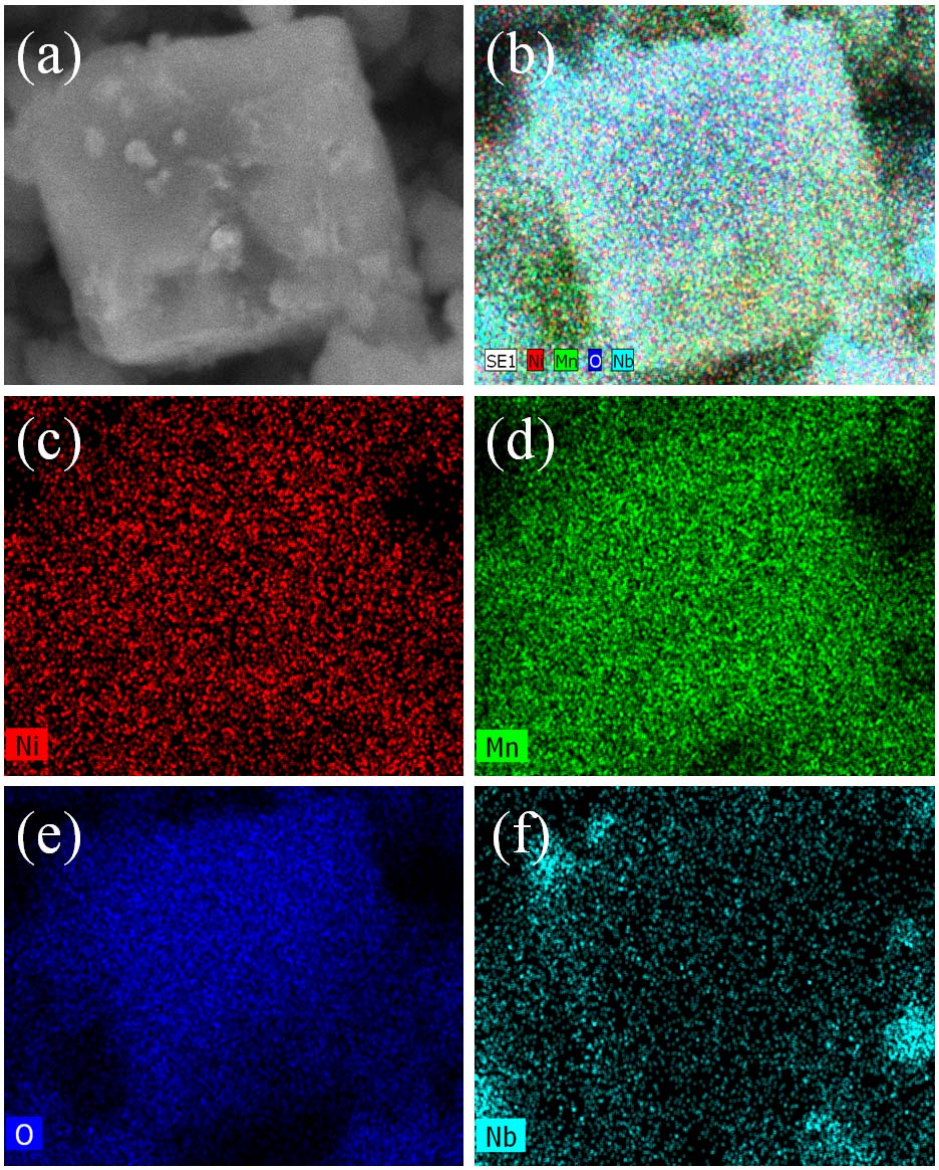

Figure 5.7 FESEM image of 0.02LNO/LNMO particle (a), and corresponding EDX mapping results: overall elements distribution (b), Ni (c), Mn (d), O (e), and Nb (f).

cubic spinel structure [Figure 5.6(e) and (i)]. The *x*LNO/LNMO (*x* = 0.02, 0.04, and 0.06) samples also show high crystallinity with clearly distinguished lattice fringes. Taking 0.04LNO/LNMO composite as an example [Figure 5.6(g) and (k)], the thickness of the LNO nanoplate is 3-6 nm, and the LNO nanoplates have different crystallographic directions (such

as the [104] direction with a lattice spacing of 0.28 nm and the [110] direction with a lattice spacing of 0.26 nm). Furthermore, the SAED pattern for the 0.04LNO/LNMO composite shows two sets of diffraction spots: 1) well-defined bright spots indexed to the cubic spinel structure; 2) weak spots corresponding to the LNO additive and indexed as (104), (110), and (006) from the inside out, respectively [Figure 5.6(k)]. In order to further investigate the distribution of LNO in 0.04LNO/LNMO composite, detailed information on the elements distribution was further acquired by energy dispersive X-ray (EDX) mapping (Figure 5.7). The results show that the LNO is distributed uniformly throughout the whole area, and some small particles are located at the edges of the LNMO particle. Therefore, it is found that the 0.04LNO/LNMO composite has the proper concentration of LNO compared with other samples, as it shows thin and uniformly dispersed LNO nanoplates on the surfaces of the LNMO particles.

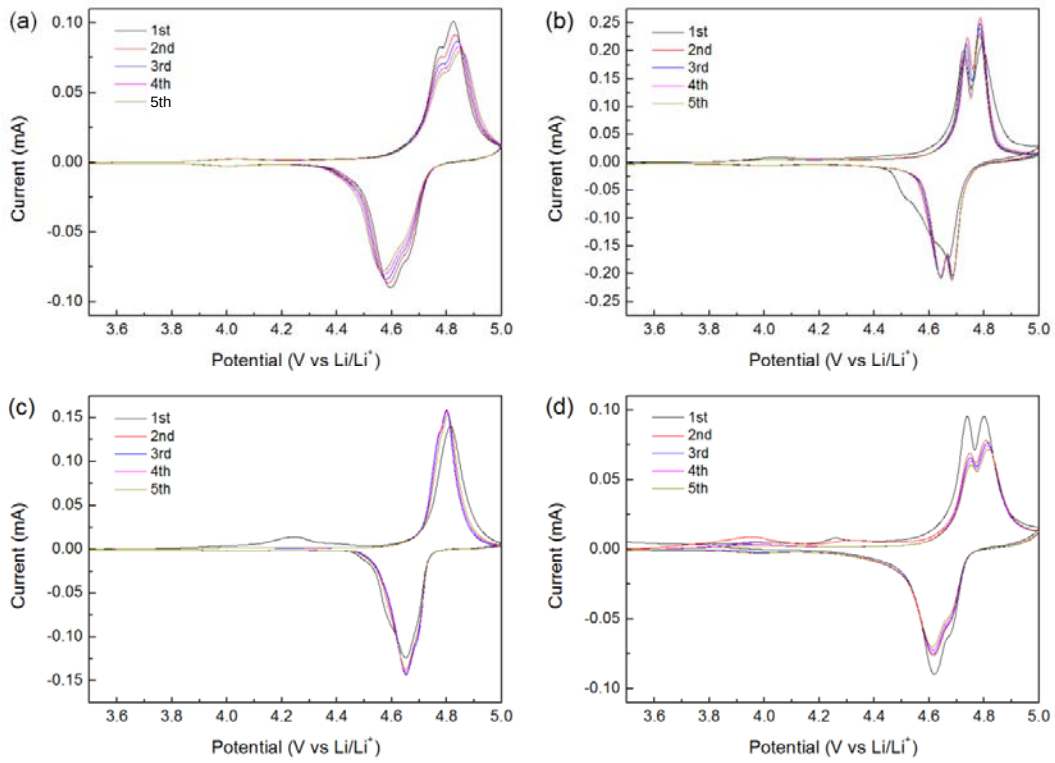

Figure 5.8 Cyclic voltammograms of *x*LNO/LNMO (*x* = 0.02, 0.04, and 0.06) electrodes for

the first 5 cycles with a scan rate of 0.1 mV s^{-1}: (a) LNMO; (b) 0.02LNO/LNMO; (c) 0.04LNO/LNMO; and (d) 0.06LNO/LNMO.

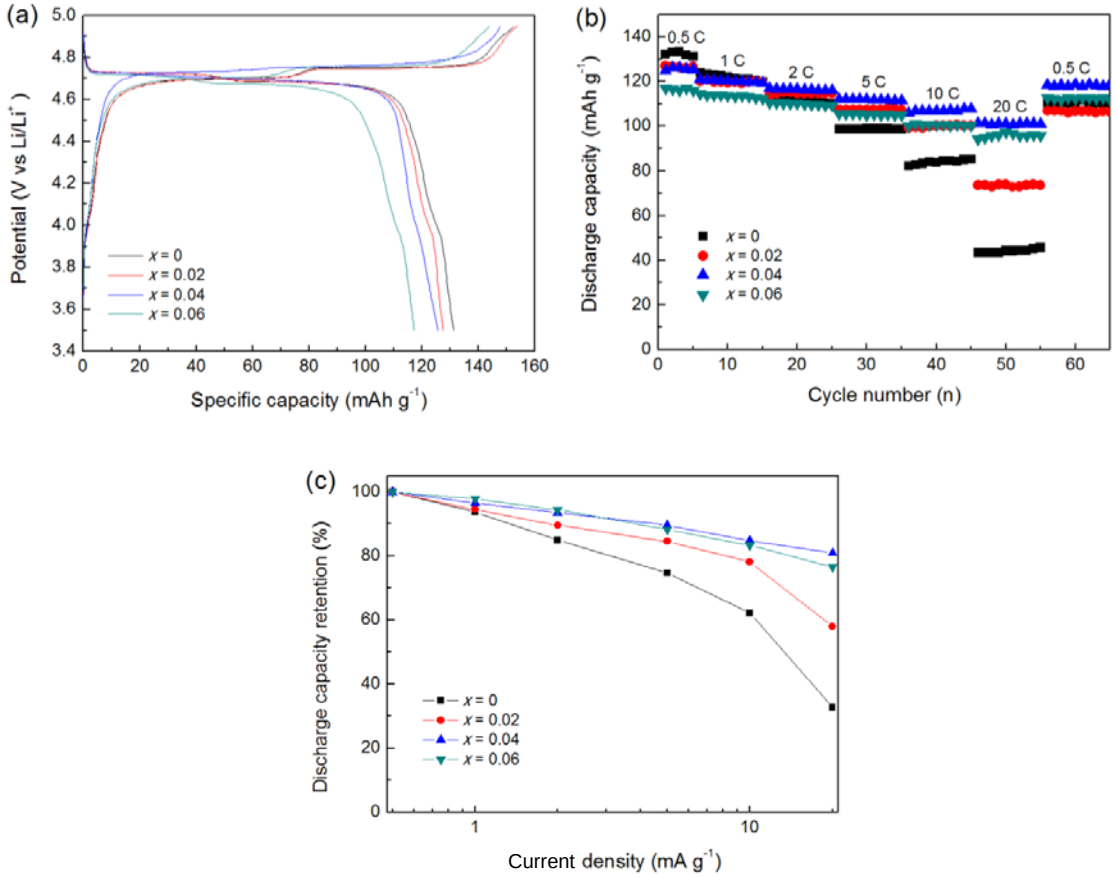

Figure 5.9 Charge-discharge curves of *x*LNO/LNMO (*x* = 0.02, 0.04, and 0.06) electrodes for the first cycle at 25 ^{o}C at a current density of 0.5 C (1 C = 148 mAh g^{-1}) (a); rate performance (b), and the corresponding capacity retention rate at different current densities from 0.5 C to 50 C at 25 ^{o}C (c). The rate capability in (c) is expressed as a relative specific discharge rate compared to that obtained at 0.5 C.

The influence of the LNO additive on LIBs was investigated as follows. Cyclic voltammetry (CV) was initially conducted for the cells with *x*LNO/LNMO (*x* = 0, 0.02, 0.04, and 0.06) composite electrodes in the first 5 cycles (Figure 5.8). In all of the four samples, the typical two redox peaks can be observed at ~ 4.7 V, corresponding to the two-step reaction of

Ni^{2+}/Ni^{3+} and Ni^{3+}/Ni^{4+} [324, 325], but the *x*LNO/LNMO (*x* = 0.02, 0.04, and 0.06) composite electrodes show merged Ni^{2+}/Ni^{3+} and Ni^{3+}/Ni^{4+} peaks (at ~ 4.7 V), which is related to the second sintering (LNO synthesis process). The two-phase reaction represent the lithium ion insertion/extraction into/from 8a tetrahedral sites of the cubic structure. After the second sintering, the LNMO phase is a disordered $Fd\bar{3}m$ spinel structure. A pair of peaks at ~ 4.0 V, corresponding to the redox peaks of Mn^{3+}/Mn^{4+} along with lithium ion insertion/extraction into/from 8a tetrahedral sites are observable at quite low intensity. This is related to the presence of a small amount of Mn^{3+} in LNMO [326]. As can be seen from Figure 5.8(c), the peak at ~ 4.0 V of the 0.04LNO/LNMO sample is much weaker than that of the pristine LNMO sample, which is ascribed to the LNO additive, which has inhibited the Mn dissolution or restrained the Jahn-Teller distortion [327-329]. Charge/discharge curves for the first cycle are also shown in Figure 5.9(a). In good agreement with the CV results, all of the *x*LNO/LNMO (*x* = 0, 0.02, 0.04, and 0.06) composite electrodes show a distinguishable two-step plateau (at ~ 4.7 V). A small plateau in the 4.0 V region is clearly observed for all of the four samples, while the 0.04LNO/LNMO sample shows the weakest plateau. Furthermore, the 0.04LNO/LNMO sample shows a higher discharge capacity than the other two electrodes (127.5 mAh g^{-1}, 125.7 mAh g^{-1}, and 117.3 mAh g^{-1}, corresponding to *x* = 0.02, 0.04, and 0.6, respectively). The pristine LNMO electrode shows the highest discharge capacity with 131.3 mAh g^{-1}, because the LNO additive counts as an active material in the electrodes. To further evaluate the rate capability, the *x*LNO/LNMO (*x* = 0, 0.02, 0.04, and 0.06) electrodes were cycled at various current densities ranging from 0.5 C to 20 C within a potential window of 4.95-3.5 V at room temperature, followed by a return to 0.5 C. A rate of *n* C corresponds to a full charge/discharge of the theoretical capacity in 1/*n* hours, and 1 C is 147 mAh g^{-1} for LNMO. As shown in Figure 5.9(b) and (c), the 0.04LNO/LNMO electrode and 0.06LNO/LNMO electrode exhibit excellent rate capability, such that when the C-rate

increases, even up to 20 C, the cell still retains 80.9% and 76.5% of the original capacity of 125.1 mAh g^{-1} and 117.1 mAh g^{-1}, respectively. Whereas, the 0.06LNO/LNMO electrode shows lower discharge capacity than that of the 0.04LNO/LNMO electrode, due to the high amount of LNO phase. Meanwhile, the pristine LNMO electrode and the 0.02LNO/LNMO electrode show inferior rate capability of only 32.7% and 57.9% of the original capacity of 132.2 mAh g^{-1} and 127.1 mAh g^{-1}, respectively, under the same conditions of increasing C-rate. These results indicate that the LNO additive afford intrinsically better rate performance.

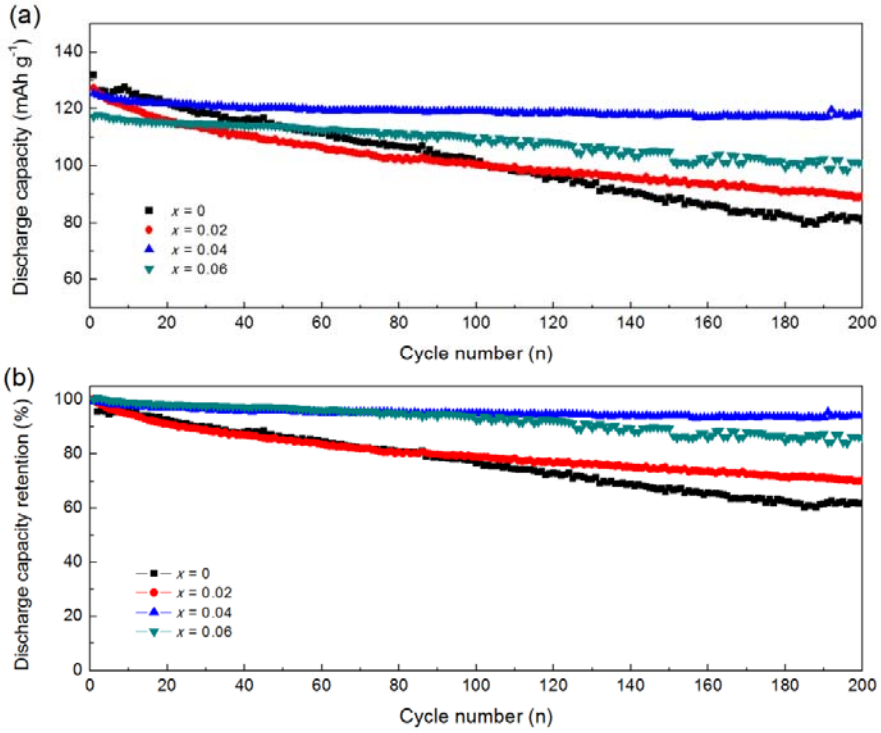

Figure 5.10 Cycling performance (a) and capacity retention rate (b) for *x*LNO/LNMO (*x* =0, 0.02, 0.04, and 0.06) electrodes at current density of 0.5 C with a potential window of 4.95-3.5 V at 25 ^{o}C. The cycling retention rate represents a relative specific discharge capacity compared to the discharge capacity at the first cycle.

To investigate the cycling stability, the variation in the discharge capacity of the electrodes over 200 cycles is shown in Figure 5.10, where there is a comparison between LNMO samples containing different amounts of LNO additive. The initial discharge specific

capacities, at a rate of 0.5 C, are 131.9 mAh g^{-1}, 127.3 mAh g^{-1}, 125.4 mAh g^{-1}, and 117.2 mAh g^{-1} for the *x*LNO/LNMO (*x* = 0, 0.02, 0.04, and 0.06) electrodes, respectively [Figure 5.10(a)]. The retained discharge capacity was 61.6%, 70.1%, 94%, and 86.1%, respectively, after 200 cycles, in comparison with the initial capacity (corresponding discharge capacity: 80.8 mAh g^{-1}, 89.2 mAh g^{-1}, 117.9 mAh g^{-1}, and 101 mAh g^{-1}) [Figure 5.10(b)]. In accordance with those cycling stability results, thin and uniform coating of LNO nanoplates on the surface of LNMO increases the cycling stability, prevents capacity fading and decreases the capacity loss caused by the weight percentage of LNO. The 0.04LNO/LNMO electrode is the optimal sample with high rate capability and stable cycling performance. To investigate the influence of LNO additive on the LIB's performance, we focused on the 0.04LNO/LNMO electrode which was further tested.

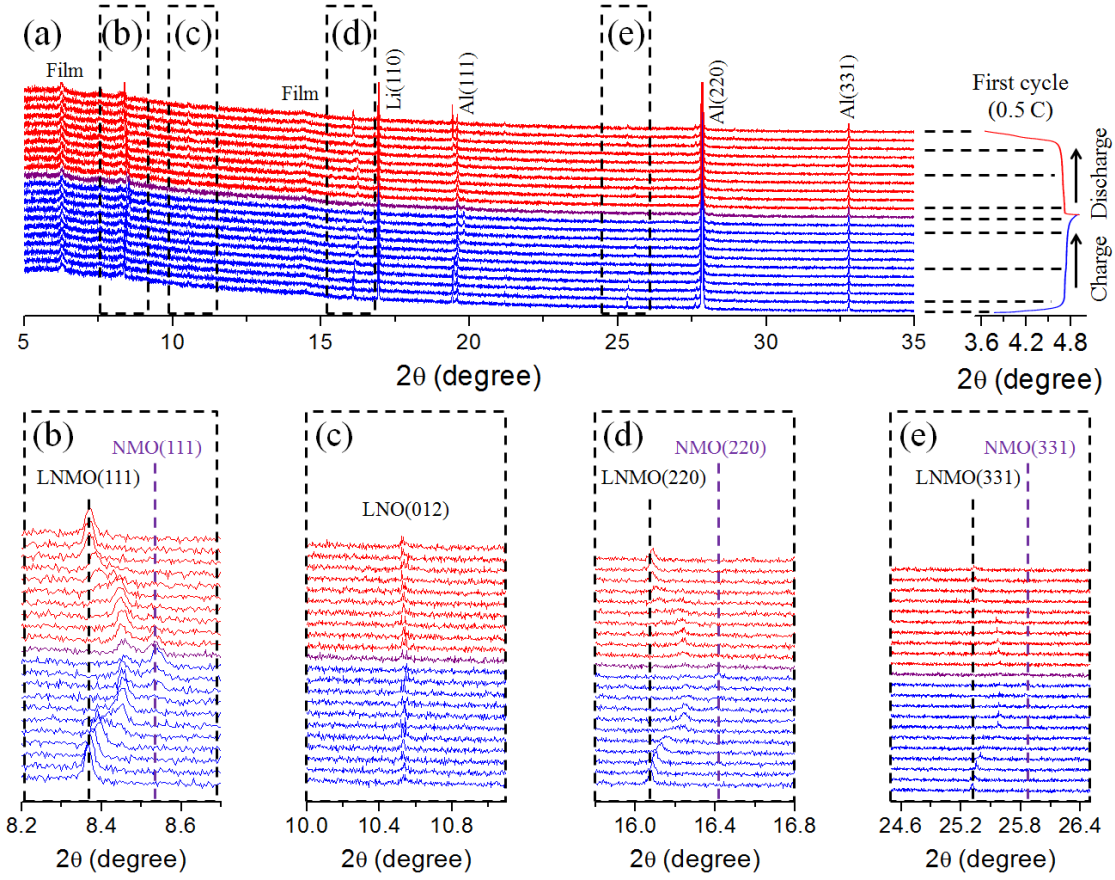

Figure 5.11 *In situ* SXRD patterns of 0.04LNO/LNMO electrode during the first cycle at 0.5C and 25 °C. (a) Selected individual diffraction patterns during the first cycle stacked

against the charge/discharge curve. The main peaks of LNMO correspond to (b) (111), (d) (220), and (e) (331) reflections. These regions are highlighted in the bottom columns and peaks corresponding to the $LiNi_{0.5}Mn_{1.5}O_4$ and $Ni_{0.5}Mn_{1.5}O_4$ phases are marked by black dotted lines and purple dotted lines, respectively. For the LNO phase, the main peak that corresponds to the (012) reflection is also highlighted in the bottom columns (c).

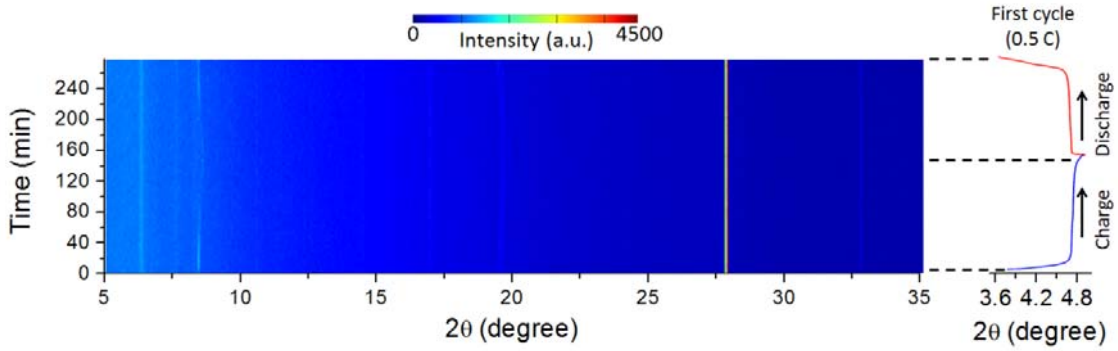

Figure 5.12 *In situ* SXRD patterns of 0.04LNO/LNMO electrode during the first cycle at 0.5 C.

The electrochemical delithiation/lithiation processes were also investigated via *in situ* SXRD. As can be seen from Figure 5.11 and Figure 5.12, the 0.04LNO/LNMO composite undergoes highly reversible changes in crystal structure during the 1st cycle at 0.5C and 25 ^{o}C. During the charge process, the lattice constant of LNMO decreases from a = 0.816 nm (voltage = 3.6 V, open circuit potential) to a = 0.801 nm (voltage = 4.95 V), corresponding to the SXRD peak shift from the peak at 8.374 ^{o} to higher angles (8.516 ^{o}) [Figure 5.11(b, d, e)]. The charge process includes two steps corresponding to the reaction of Ni^{2+}/Ni^{3+} and Ni^{3+}/Ni^{4+}. A similar phenomenon appears during the discharge process, in which the SXRD peaks are shifted backward from their initial position (a = 0.815 nm, voltage = 3.5 V). No new crystal structure is generated during the delithiation/lithiation processes. That is to say, there is no nucleation and growth of a second phase, so that the spinel structure avoids rearrangement and large volume changes [330-332]. From Figure 5.11(c), we can see that the solid-state

electrolyte (SSE) additive LNO shows a weak (012) reflection. No peak shifts of $LiNbO_3$ appear throughout the charge/discharge process. The dual composition of the cathode material, the stable LNO additive, and the highly reversible crystal structure of LNMO, effectively prevents the soluble Mn^{2+} from being generated and diffusing to the electrolyte, and avoids the splitting up of LNMO particles caused by the slight crystal volume change. Although solid-state-electrolyte presents a low lithium ion transfer rate in all solid state batteries, there is no obvious evidence that the LNO additive affects the lithium ion transfer rate between cathode and anode from the *in situ* SXRD results. Therefore, the highly reversible phase LNMO and the stable LNO additive can increase the high-rate capability and cycling stability.

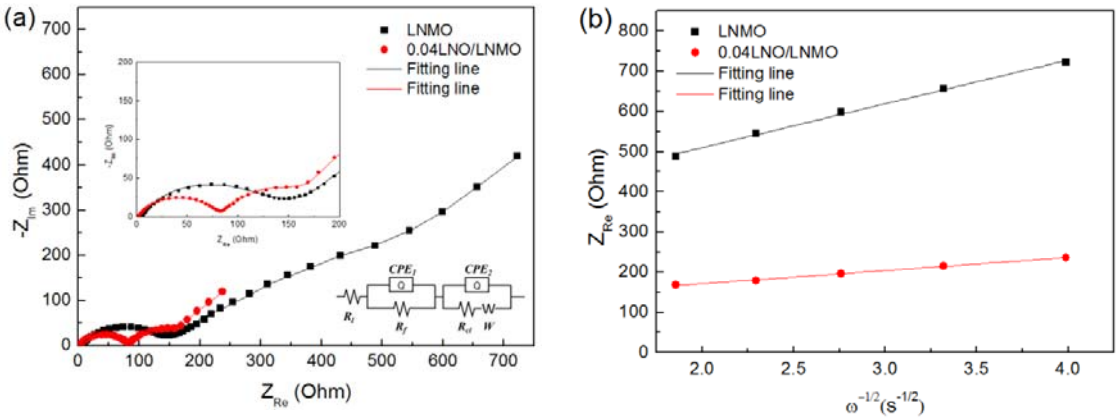

Figure 5.13 (a) Impedance plots of pristine LNMO and 0.04LNO/LNMO electrodes at discharge voltage of 4.7 V vs. Li/Li^+ after 5 cycles and frequencies from 100 kHz to 10 mHz. The equivalent circuit is shown in the lower right inset and the upper left inset is an enlargement of the higher frequency region. (b) Real part of the impedance for the electrodes versus $\omega^{-1/2}$ at discharge potential of 4.7 V vs. Li/Li^+.

To further investigate the influence of the LNO additive on the LIBs, the electrochemical kinetics for pristine LNMO and 0.04LNO/LNMO electrodes was examined by electrochemical impedance spectroscopy (EIS). Figure 5.13 shows the Nyquist plots at

discharge potential of 4.7 V vs. Li/Li^+ after 5 cycles. Both the impedance curves show two partially overlapping semicircles in the high to medium frequency region, which could be assigned to the film resistance (R_f), associated with the CEI, and the charge transfer resistance (R_{ct}), respectively.

Table 5.2 R_f, R_{ct}, and R_l values for pristine LNMO and 0.04LNO/LNMO electrodes calculated by Zview.

Electrodes	LNMO	0.04LNO/LNMO
R_f **(Ω)**	68.3	36.5
R_{ct} **(Ω)**	339.4	67.6
R_l **(Ω)**	0.8	1.2

A line inclined at approximately 45° reflects the Warburg impedance (W), which is associated with the lithium-ion diffusion in the LNMO compound. The high-frequency intercept of the semicircle reflects the uncompensated resistance (R_l), which includes the particle-particle contact resistance, the electrolyte resistance, and the resistance between the cathode materials and the current collector [333, 334]. The R_f, R_{ct}, and R_l values for the pristine LNMO and 0.04LNO/LNMO electrodes were obtained using the equivalent circuit shown in the inset of Figure 5.13(a) (calculated by Zview and shown in Table 5.2). The R_l of the 0.04LNO/LNMO electrode is slightly higher than that of the pristine $Li_{1.08}Mn_{1.92}O_4$ electrode, whereas the R_f and R_{ct} are apparently decreased after adding the LNO. This indicates that the LNO nanoplates effectively hinder CEI formation and increase the ionic conductivity caused by the shortened lithium ion diffusion distance. The lithium diffusion coefficients of the pristine LNMO and 0.04LNO/LNMO electrodes were calculated using the following Equation (5.1)[303]

$$D = R^2T^2/2A^2n^4F^4C^2\sigma^2 \quad (5.1)$$

Where D is the diffusion coefficient ($cm^2\ s^{-1}$), R is the gas constant, 8.314 J mol^{-1} K^{-1}, T is the absolute temperature (K), A is the surface area of the cathode (1 cm^2), n is the number of

electrons transferred in the half-reaction for the redox couple, which is equal to 1, F is the Faraday constant (96485 C mol^{-1}), C is the concentration of lithium ions in the solid LNMO (3.05×10^{-3} mol cm^{-3}), and σ is the Warburg factor, which is relative to Z_{re}. σ can be obtained from Figure 5.13(b).

$$Z_{re} = R_l + R_{ct} + \sigma\omega^{-1/2} \quad (5.2)$$

The lithium diffusion coefficients are calculated to be (3.2, and 36.3) $\times 10^{-11}$ cm^2 s^{-1} for the pristine LNMO and 0.04LNO/LNMO electrodes, respectively, at 25 ^oC. The 0.04LNO/LNMO composite electrode with a thin and uniform LNO additive exhibits a much higher lithium diffusion coefficient than that of the pristine LNMO, due to the high ionic conductivity of the LNO. During the sintering process at high temperature, the primary particles (around 500 nm in size) were merged into secondary particles (about 1 μm), as shown in Figure 5.5 and Figure 5.6. The portion of LNO that is located in the interior of the secondary particles (due to the growth on the primary particles) effectively improves the lithium diffusion coefficient. There will be a three-dimensional (3D) LiNO net structure in the secondary particles. This 3D LNO net structure provides fast lithium ion transport pathways.

The excellent electrochemical stability of the 0.04LNO/LNMO composite is also confirmed by the images of electrodes, which were collected after 200 cycles at 0.5 C and 25 ^oC (Figure 5.14). Figure 5.14(a) and (b) present the respective FESEM images of the pristine LNMO and 0.04LNO/LNMO cathodes. It can be found by comparing the two cathodes that the pristine LNMO particles are separated from each other and shrunken within the secondary particles, but this did not occur in the LNO-added cathode. As can been seen from the counter anode (lithium foil) and separator, the LNO-added cathode show much weaker decomposition than the pristine LNMO cathode (see the optical digital photographs, Figure 4.14: the bottom of the FESEM images). Similar to what was previously reported, the formation of Mn^{2+} leads to Mn

dissolution, and Jahn-Teller crystallographic distortion causes the primary particles of LNMO to separate and shrink [318]. Therefore, the LNO additive prevents the soluble Mn^{2+} from passing into the electrolyte and allows the Li^+ ions free transportation between the cathode and electrolyte.

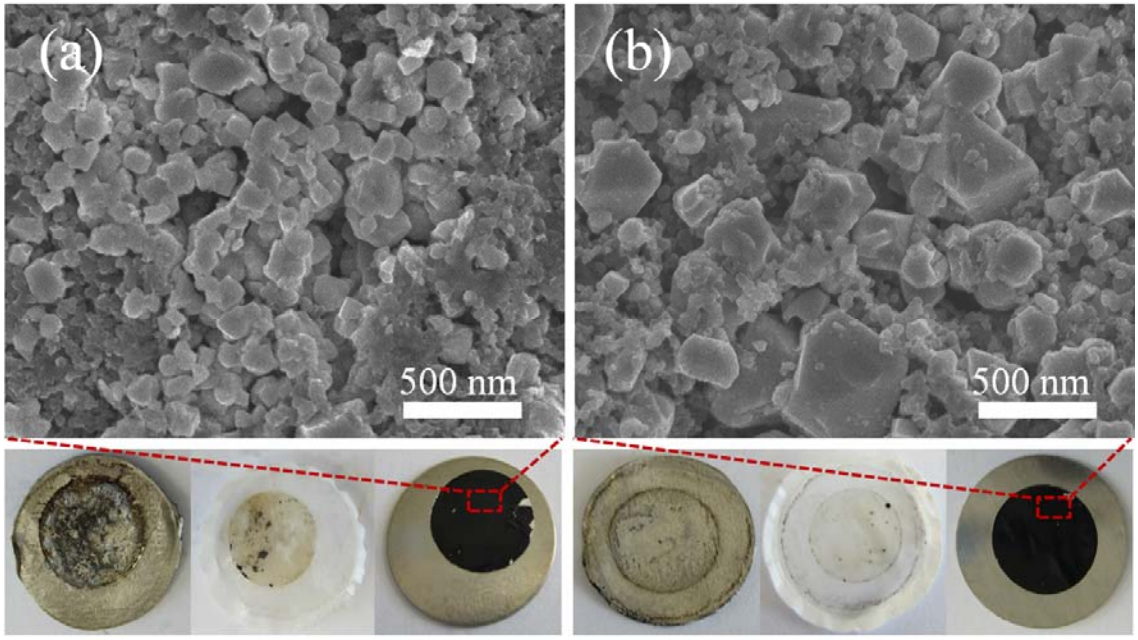

Figure 5.14 Images of electrodes collected after 200 cycles at 0.5 C and 25 ^oC: FESEM images of (a) pristine LNMO sample and (b) 0.4LNO/LNMO sample. At the bottom of the FESEM images are the corresponding optical digital photographs for the lithium anode (left), separator (middle), and cathode (right).

5.4 Conclusion

LNMO with LNO additive cathode was successfully prepared as a cathode material using a facile solid-state reaction method. The LNMO sample with a thin and uniform LNO additive exhibited higher cycling stability, higher rate capability, and better high temperature cycling performance than the pristine LNMO. The LNO nanoplates effectively prevented Mn dissolution, and the LNMO samples with LNO additive showed much lower charge transfer resistance than the pristine LNMO sample, due to their high ionic conductivity.

Chapter 6 Polypyrrole-Coated α-$LiFeO_2$ Nanocomposite with Enhanced Electrochemical Properties for Lithium-Ion Batteries

6.1 Introduction

Lithium ferrite ($LiFeO_2$), a layered cathode material, has attracted much attention because it is non-toxic, environmentally friendly, and low-cost [335, 336]. As is well known, α-$NaFeO_2$-type $LiCoO_2$ cathode materials are in widespread use in commercial LIBs. Layered $LiCoO_2$ has a rock-salt structure, where alternate layers of Li and Co occupy the octahedral sites of a cubic close packed oxygen array [337]. $LiCoO_2$ is more toxic and more expensive than oxides of other transition metals (Mn, Ni, Fe, etc.) [338-340]. $LiFeO_2$ has different forms, including the α-, β-, γ-forms, etc. α-$LiFeO_2$ has a disordered-cation cubic rock-salt structure with space group *Fm3m*. β-$LiFeO_2$ with space group *C2/c* is formed as an intermediate phase during the ordering process. γ-$LiFeO_2$ with space group $I4_1/amd$ is obtained by reducing the symmetry from cubic to tetragonal by ordering the Li^+ and Fe^{3+} ions at octahedral sites [335-337, 340].

α-$LiFeO_2$ has many advantages as a cathode material for the LIB as a substitute for $LiCoO_2$ in terms of lower price and environmental friendliness. The charging reaction can be written as:

$$LiFe^{III}O_2 \rightarrow xLi^+ + xe^- + Li_{1-x}Fe_{1-x}^{III}Fe_x^{IV}O_2 \quad (6.1)$$

With x = 1, this reaction provides a theoretical capacity of 282 mAh g^{-1}. Kanno et al. [337], however, reported a maximum value of x = 0.1 for the α-$NaFeO_2$-type structure. The charged electrodes should contain iron in a mixed oxidation state (III and IV). The first charge voltage plateau is above 4 V, corresponding to the Fe^{+3}/Fe^{+4} couple reaction, however, large voltage hysteresis is observed during the discharge step. Sakurai et al. reported that unusual Fe^{+4} ions

generated during charging may play an important role in the occurrence of voltage hysteresis [341]. Kanno et al. also pointed out that the conversion proceeds from the corrugated layered structure $LiFeO_2$ to an amorphous phase during the first charge, and the charge-discharge process after the second cycle proceeds in the amorphous phase [337]. According to the structural change in α-$LiFeO_2$ in the charge/discharge process, as determined by X-ray diffraction (XRD) and X-ray diffraction near-edge structure (XANES) spectroscopy, Morales et al. confirmed that Fe^{2+} may exist after the first discharge, and the strong exothermic peak close to 398 K in the differential scanning calorimetry (DSC) curve may result from the reaction of Fe^{4+} with electrolyte [342].

The electrical conductivity is extremely low, however, because the iron ions on lithium sites block the lithium diffusion pathways. There are mainly two ways to increase the electrical conductivity: one way is to fabricate nanosized α-$LiFeO_2$. Nanosized materials have short pathway lengths for lithium ion transport and a large contact area between the electrode and electrolyte for improving the reaction rate at the interface [343]. The other way is to coat a conductive material onto the surface of the α-$LiFeO_2$ [342]. Using the hydrothermal method, nanosized FeOOH can be prepared in different crystal phases and morphologies [344-348]. Later, FeOOH can be converted into α-$LiFeO_2$ via a solid-state reaction. Polypyrrole (PPy) is a popular conducting polymer due to its ability to act as a binder and store electric charge (C_{ppy} = 72 mAh g^{-1}) [349-351]. Our group has successfully used PPy to improve the performance of cathode and anode materials in LIBs, in such composites as S-PPy, SnO_2-PPy, and LiV_3O_8-PPy [352-354]. The theoretical capacity of polypyrrole-coated M (M = S, SnO_2, and LiV_3O_8) can be calculated as following according to the theoretical capacity of M and the theoretical capacity of PPy: C_M × wt.% of α-$LiFeO_2$ + C_{PPy} × wt.% of PPy. However, the synthesis of polypyrrole-coated α-$LiFeO_2$ composite for use in LIBs has not been explored yet.

In this study, α-$LiFeO_2$-PPy nanocomposite was synthesized using a chemical polymerization method. The structural characterization and electrochemical performance of the α-$LiFeO_2$-PPy composite are discussed and compared with the performance of bare α-$LiFeO_2$ cathode material.

6.2 Experimental Section

6.2.1 Preparation of β-FeOOH

The β-FeOOH was prepared by using a microwave autoclave method. 3.244 g of $FeCl_3$ (Sigma-Aldrich) was dissolved in 200 ml distilled water to obtain a final concentration of 0.1 M in a beaker. Then, the solution was sonicated to dissolve the $FeCl_3$ particles to achieve a homogeneous system. The solution was transferred into sealed Teflon vessels and reacted for 5 min at 120 ℃ using a Milestone Microsynth Microwave Labstation (Germany) [355]. After cooling down naturally and washing 3 times with distilled water, the brown product, β-FeOOH, was dried at 60 ℃ in a vacuum oven for 12 h. The collected powder was used for further characterization and as the precursor to prepare α-$LiFeO_2$.

6.2.2 Preparation of α-$LiFeO_2$

The α-$LiFeO_2$ was prepared by heating appropriate molar ratios of β-FeOOH and $LiOH{\cdot}H_2O$ (Sigma-Aldrich). A stoichiometric amount of each material was ground and heated at 400 ^oC for 3 h in air atmosphere in a tube furnace. The brown product was washed 3 times with distilled water and dried at 60 ^oC in a vacuum oven for 12 h. The synthesis procedure was repeated in order to obtain single α-$LiFeO_2$ phase.

6.2.3 Preparation of α-$LiFeO_2$-Polypyrrole Composite

The α-$LiFeO_2$-polypyrrole composite was prepared by the chemical polymerization method with sodium *p*-toluenesulfonate (pTSNa) as the dopant and $FeCl_3$ as the oxidant. The molar

ratio of monomer pyrrole to dopant was 3:1, and the molar ratio of monomer pyrrole to oxidant was 1:3 [354]. Firstly, α-$LiFeO_2$ was dispersed into a solution (50 ml) of pTSNa (0.01 M) and pyrrole (0.03 M). Secondly, the mixture was magnetically stirred while the oxidant agent, $FeCl_3$ solution, was slowly added to the aqueous solution. The gradual change of colour from brown to black indicated the formation of PPy. Stirring of the reaction mixture was maintained for 20 h. Finally, the black mass was washed 3 times with distilled water and dried at 60 ^oC in a vacuum oven for 12 h. In order to calculate the PPy content, pure PPy powder was also prepared using the same chemicals as mentioned above.

6.2.4 Materials Characterization

The products, β-FeOOH, α-$LiFeO_2$, and α-$LiFeO_2$-polypyrrole composite, were analysed by X-ray diffraction (XRD; GBC MMA) with Cu Kα radiation, as well as by field emission scanning electron microscopy (FESEM; JEOL 7500, equipped for energy dispersive X-ray (EDX) spectroscopy). For PPy analysis, Fourier transform infrared (FTIR) spectrographs were collected using a Nicolet Avatar 360 FTIR Fourier transform infrared spectrometer. Thermogravimetric analysis (TGA) was performed by using a SETARAM Thermogravimetric Analyzer (France) in air to determine the changes in sample weight with increasing temperature and to estimate the amount of polypyrrole in the sample.

6.2.5 Electrochemical Measurements

The electrodes were prepared by mixing 80 wt.% α-$LiFeO_2$ or α-$LiFeO_2$-polypyrrole composite with 15 wt.% carbon black and 5 wt.% carboxymethyl cellulose (CMC) binder. The slurry was spread onto aluminium foil substrates. The coated electrodes were dried at 60 ^oC in a vacuum oven for 24 h to remove water molecules. The electrode was then pressed using a disc with a diameter of 14 mm to enhance the contact between the aluminium foil, active materials, and conductive carbon. Subsequently, the electrodes were cut to a 1×1 cm^2

size. The average active material loading rate was around 5 mg cm^{-2}. CR 2032 coin-type cells were assembled in an Ar-filled glove box (M braun, Unilab, Germany) using lithium metal foil as the counter electrode. The electrolyte was 1 M $LiPF_6$ in a mixture of ethylene carbonate (EC) and dimethyl carbonate (DMC) (1:1 by volume, provided by MERCK KGaA, Germany). The cells were galvanostatically charged and discharged in the range of 4.5–1.5 V at different current densities using a computer-controlled charger system manufactured by Land Battery Testers. A Biologic VMP-3 electrochemical workstation was used to perform electrochemical impedance spectroscopy (EIS; ac amplitude 5 mV, frequency range 100 kHz-0.01 Hz).

6.3 Results and Discussion

The β-FeOOH precursor was prepared by using a microwave autoclave method. The X-Ray diffraction (XRD) pattern of β-FeOOH is presented in Figure 6.1(a). The β-FeOOH sample diffraction peaks are consistent with reported values (JCPDS 34-1266). Figure 6.1(b) shows a field emission scanning electron microscope (FESEM) image of β-FeOOH. The obtained β-FeOOH has rod-like nanoparticle morphology, with a nanorod diameter of about 50 nm and length of 100 nm.

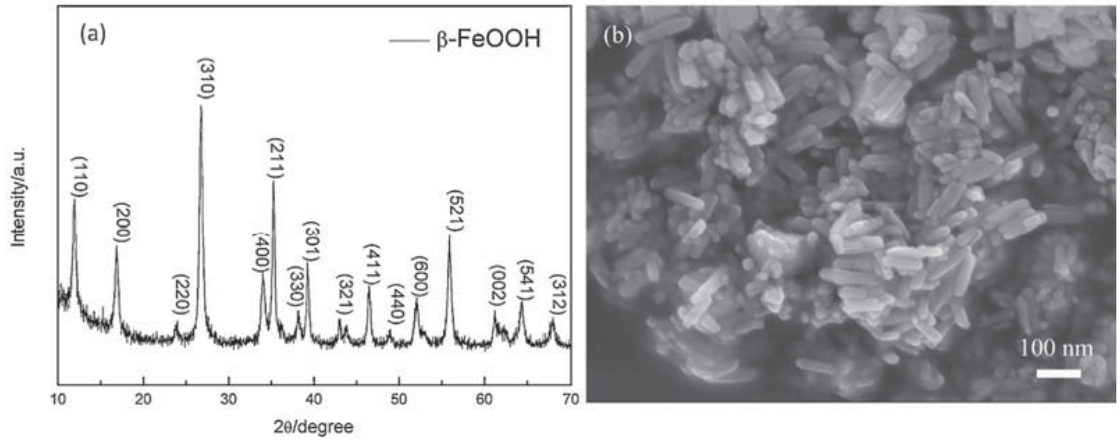

Figure 6.1 X-ray diffraction pattern (a) and FESEM image (b) of β-FeOOH.

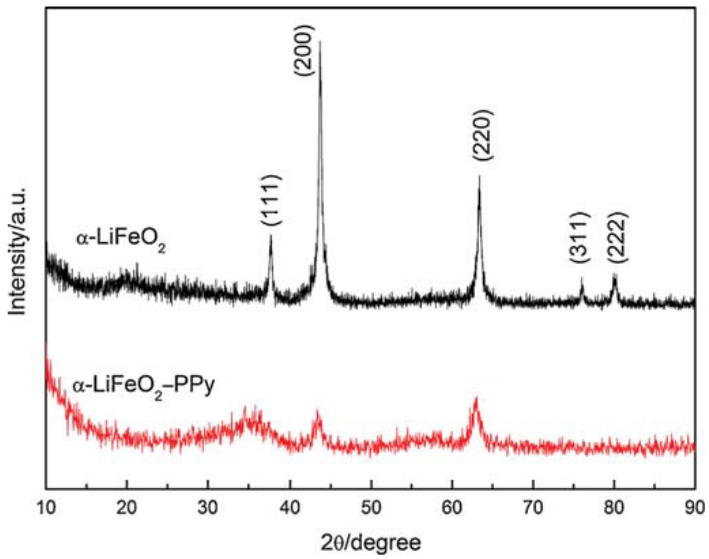

Figure 6.2 X-Ray diffraction patterns of α-$LiFeO_2$ and α-$LiFeO_2$-PPy composite.

Figure 6.2 shows the XRD patterns of α-$LiFeO_2$ and α-$LiFeO_2$-PPy. In the preparation of α-$LiFeO_2$, the sintering temperature and the excess lithium content in the starting mixture were critical parameters for obtaining pure-phase α-$LiFeO_2$ nanoparticles. The pure-phase α-$LiFeO_2$ was obtained under the conditions of Li/Fe = 3, 400 ^oC, and 3 h. The main peaks were indexed in the cubic system with lattice parameter a = 4.158 Å , which is quite consistent with the reported value (JCPDS 17-938). Figure 6.2 also reveals that the XRD pattern of the α-$LiFeO_2$-PPy composite is similar to that of α-$LiFeO_2$ in terms of peak positions. The main peaks in the pattern of the PPy-coated composite are broader than those of the uncoated material. This may be due to the reaction between $LiFeO_2$ and pyrrole to form the coating on the surface, which could reduce the crystal size of the pristine $LiFeO_2$ and cause part of the Li^+ loss [356]. No obvious diffraction peaks of any impurity phases were observed. In order to confirm that the PPy was coated on the α-$LiFeO_2$ particles, Fourier transform infrared (FTIR) analysis was conducted. The Fourier transform infrared (FTIR) spectra obtained for the PPy, α-$LiFeO_2$, and α-$LiFeO_2$-PPy are shown in Figure 6.3. The α-$LiFeO_2$-PPy has the typical absorption peaks of PPy, as shown in Figure 6.3. The band at 1546 cm^{-1} is due to aromatic C=C in PPy. C=N and C-N show peaks around 1190 cm^{-1} and 1300 cm^{-1},

respectively. The aromatic C-H in PPy is responsible for the peak at 1041 cm^{-1} [357-359]. The results demonstrate that the PPy was successfully coated onto the surface of the α-$LiFeO_2$ particles.

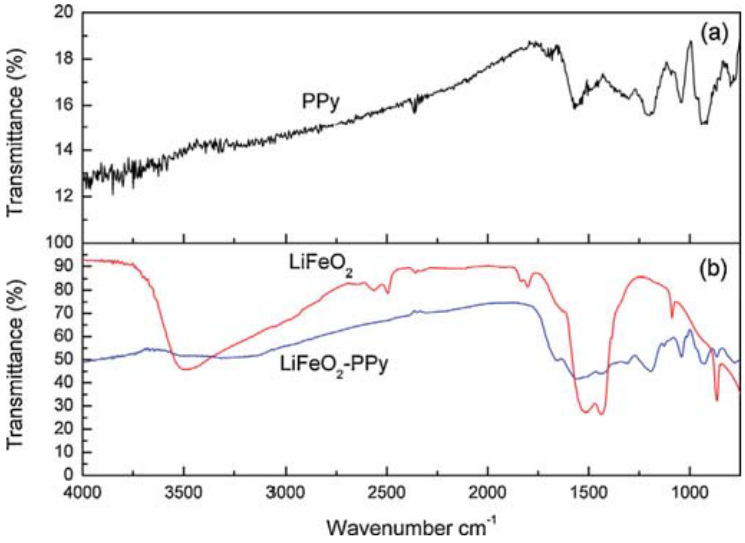

Figure 6.3 FTIR spectra of PPy, α-$LiFeO_2$, and α-$LiFeO_2$-PPy composite.

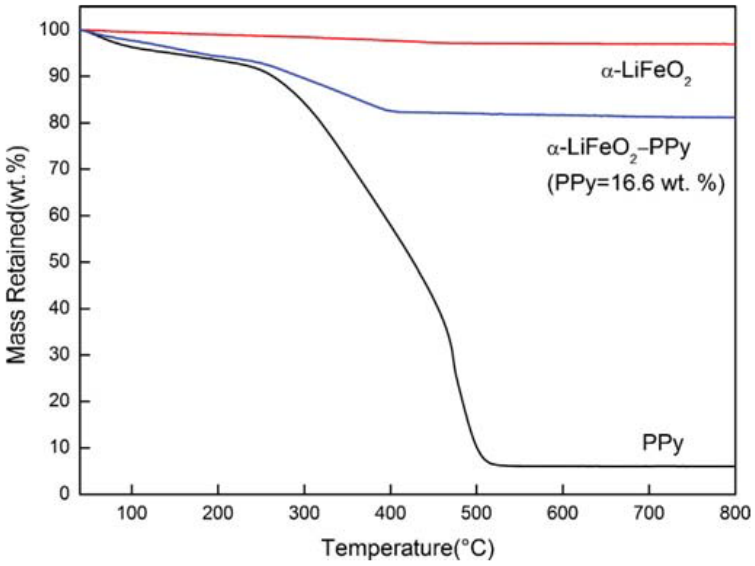

Figure 6.4 TGA curves of PPy, α-$LiFeO_2$, and α-$LiFeO_2$-PPy composite.

To quantify the amount of PPy in the α-$LiFeO_2$-PPy composite, TGA analysis was carried out in air. Figure 6.4 shows the TGA curve of the α-$LiFeO_2$-PPy composite along with those of

bare α-$LiFeO_2$ and PPy powder when heated from 40 to 800 ^oC at a rate of 10 ^oC min^{-1} in air. Bare PPy powder burns off at 520 ^oC, and there is around 6.0 wt.% dopant or oxidant remaining. While the bare α-$LiFeO_2$ powder maintains a constant weight throughout the temperature range used for this experiment, the α-$LiFeO_2$-PPy composite shows a single-step weight loss at a temperature of around 450 ^oC, which corresponds to the burning of PPy. There is no further weight loss after the initial decomposition of PPy. Therefore, the change in weight before and after the burning of PPy directly translates into the amount of PPy in the α-$LiFeO_2$-PPy. Using this method, it can be calculated that the weight percentage of PPy in this composite is 16.6 wt.%.

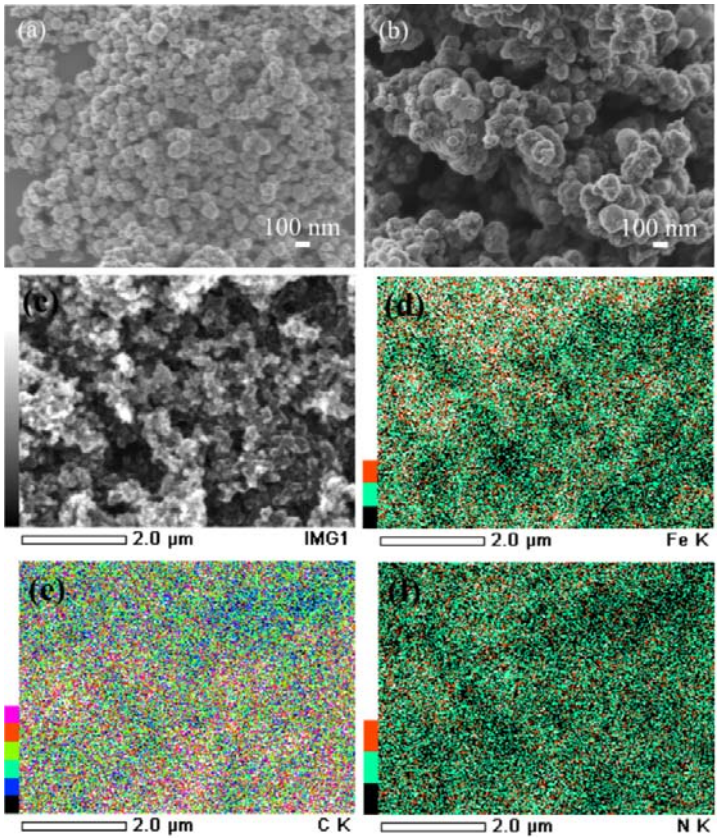

Figure 6.5 FESEM images of α-$LiFeO_2$ (a), α-$LiFeO_2$-PPy composite (b), and corresponding EDX mapping for the α-$LiFeO_2$-PPy composite image (c) as follows: Fe (d), C (e), and N (f).

FESEM images of the bare α-$LiFeO_2$ and the α-$LiFeO_2$-PPy composite are shown in Figure

6.5(a, b). The particle size of the bare α-$LiFeO_2$ ranges from 10 nm to 100 nm. After introducing the PPy, cauliflower-like nanoparticles of PPy were coated on the surfaces of the α-$LiFeO_2$ particles. The PPy matrix reduces the particle-to-particle contact resistance, thus significantly enhancing the electrical conductivity of the composite. In order to further confirm the presence of PPy, energy dispersive X-ray (EDX) mapping was used to observe the distribution of PPy (Figure 6.5(c-f)). The coloured points correspond to the presence of the elements Fe, C, and N, respectively. The N and C are elements of PPy. The results show that N and C are distributed uniformly throughout the whole area, which indicates that the PPy particles had uniformly coated the surfaces of the α-$LiFeO_2$ nanoparticles.

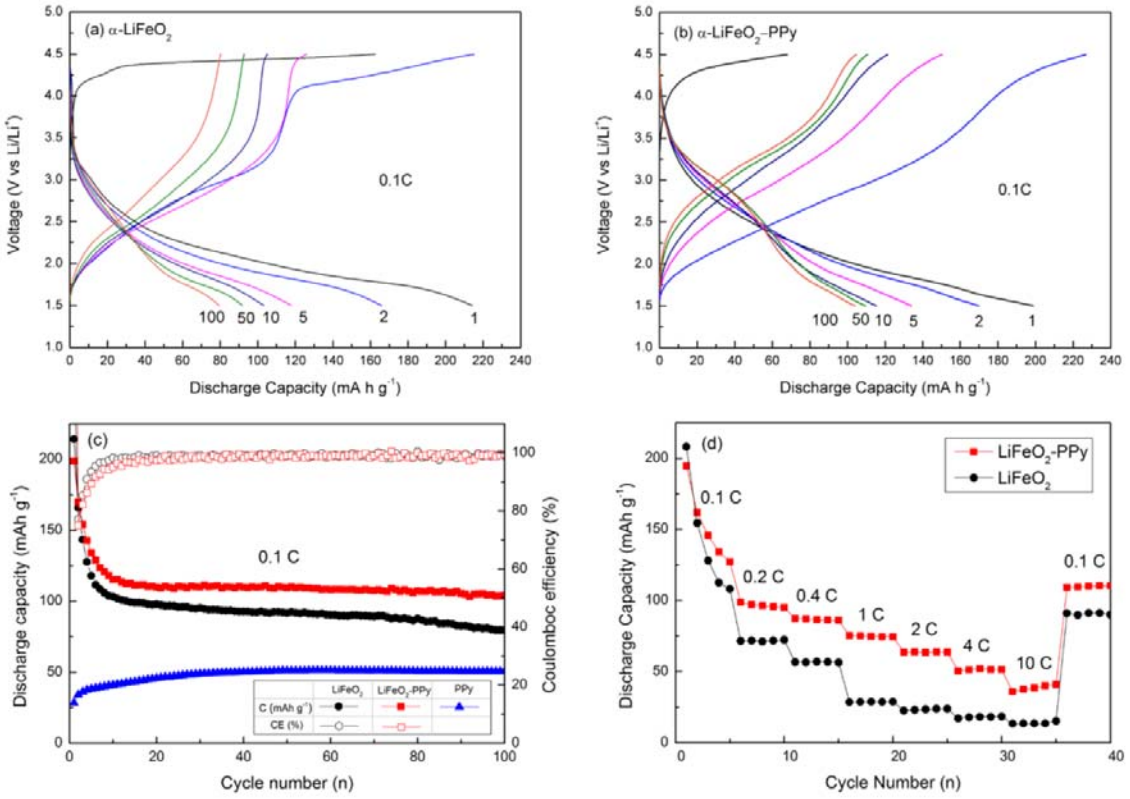

Figure 6.6 Charge-discharge curves for selected cycles for electrodes of (a) bare α-$LiFeO_2$, and (b) α-$LiFeO_2$-PPy composite; (c) cycling behaviour of bare α-$LiFeO_2$, α-$LiFeO_2$-PPy composite, and PPy electrodes; (d) rate capability for bare α-$LiFeO_2$ and α-$LiFeO_2$-PPy composite electrodes (C = 282 mA g^{-1}).

Figure 6.6(a, b) shows typical charge-discharge curves for different cycles of α-$LiFeO_2$ and α-$LiFeO_2$-PPy electrodes in coin test cells using lithium as the counter and reference electrode between 1.5 and 4.5 V (vs. Li^+/Li). From the first charge curves of the two samples, we can see that the charge capacity of α-$LiFeO_2$-PPy (67.9 mAh g^{-1}) is much lower than that of α-$LiFeO_2$ (162.5mAh g^{-1}). That is to say, a small amount of Li^+ was lost during the process of PPy coating. Although all the samples showed some irreversible capacity losses, the amount of irreversible capacity loss of α-$LiFeO_2$-PPy composite is much lower than that of the bare α-$LiFeO_2$. The cycling stabilities of bare α-$LiFeO_2$, α-$LiFeO_2$-PPy composite, and PPy electrodes at 0.1 C (C = 282 mA g^{-1}) are shown in Figure 6.6(c). The Coulombic efficiency (CE) in the first cycle for α-$LiFeO_2$ and α-$LiFeO_2$-PPy is 131.8% and 292.8%, respectively (CE = Discharge capacity/Charge capacity). The high Coulombic efficiency and the irreversible capacity in the first cycle are mainly due to the electrolyte decomposition and Li^+ loss. The first charge voltage plateau is above 4 V, corresponding to the Fe^{+3}/Fe^{+4} couple reaction. The active Fe^{+4} should react with the electrolyte and cause electrolyte decomposition in the following discharge process. At first discharge process, the active Fe^{+4} is consumed in the formation of the solid electrolyte interphase (SEI), so that the second charge curve is different from the first charge curve, but similar to the following charge curves. Furthermore, the Coulombic efficiency of α-$LiFeO_2$ and α-$LiFeO_2$-PPy is nearly 100% after 10 cycles. It can be seen that the discharge capacity of bare α-$LiFeO_2$ continuously decreases in the first 10 cycles and reaches 103.2 mAh g^{-1} after 10 cycles. The capacity retention after 100 cycles is around 75%, with reference to the 10^{th} cycle (78.4 mAh g^{-1}). In comparison, the α-$LiFeO_2$-PPy composite electrode shows great enhancement of the capacity retention. The α-$LiFeO_2$-PPy composite electrode shows an initial discharge capacity of 198.8 mAh g^{-1}, and after 10 cycles, it settles on a fairly stable capacity of 115.3 mAh g^{-1}. The capacity retention after 100 cycles is around 90%, with reference to the 10^{th}

cycle (103.7 mAh g^{-1}). The pure PPy electrode shows a low capacity of about 50 mAh g^{-1} at 0.1 C.

To further investigate the electrochemical performance of the bare α-$LiFeO_2$ and the α-$LiFeO_2$-PPy composite electrodes, the rate capability was tested, as shown in Figure 6.6(d). The α-$LiFeO_2$ and α-$LiFeO_2$-PPy composite electrodes were measured at different rates from 0.1 C to 10 C, followed by a return to 0.1 C. The specific capacity of α-$LiFeO_2$ was very low when the rate capability was more than 1 C. The α-$LiFeO_2$-PPy composite electrode, however, showed the highest specific capacity of 45.9 mAh g^{-1} at a current density of 10 C. There is less than a 15% capacity loss for the α-$LiFeO_2$-PPy composite electrode after changing the current density from 0.1 C to 10 C and back to 0.1 C over 40 cycles, showing the relatively good cycling stability.

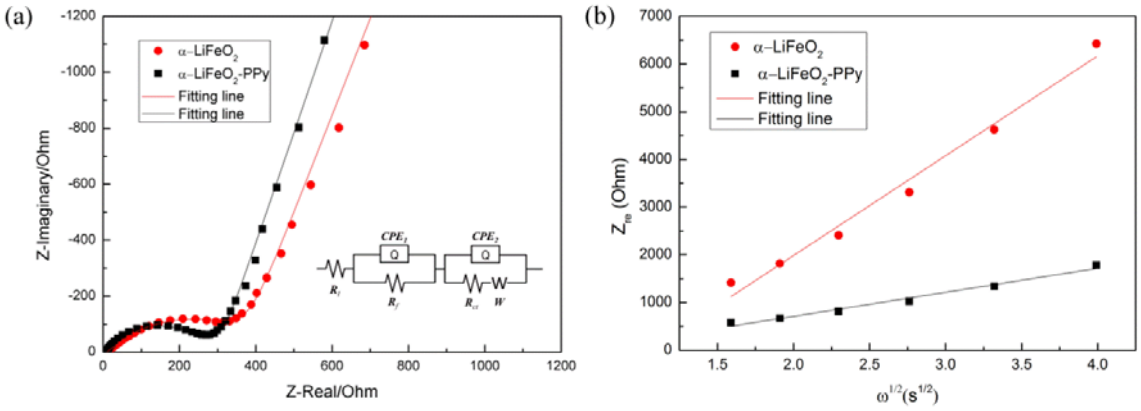

Figure 6.7 (a) Impedance plots of the cathodes containing α-$LiFeO_2$ and α-$LiFeO_2$-PPy composite after cycling over 10 cycles at a discharge potential of 2.0 V vs. Li/Li^+ at 25 ℃ at frequencies from 100 kHz to 10 mHz. The equivalent circuit is shown in the inset. (b) Real part of the complex impedance versus $\omega^{-1/2}$ at 25 ℃ at an anodic potential of 2.0 V vs. Li/Li^+.

In order to verify that the conductive PPy coating is responsible for the good performance of

the cell with the α-$LiFeO_2$-PPy electrode, electrochemical impedance spectroscopy (EIS) measurements were performed on the bare α-$LiFeO_2$ and α-$LiFeO_2$-PPy composite electrodes. Figure 6.7(a) shows the Nyquist plots of the electrodes at a discharge potential of 2.0 V vs. Li/Li^+ at 25 ^oC after cycling over 10 cycles. All the impedance curves show two compressed semicircles in the high to medium frequency region, which could be assigned to the film resistance (R_f) of the solid electrolyte interphase (SEI) and the charge transfer resistance (R_{ct}), respectively. A line inclined at approximately 45° reflects the Warburg impedance (W), which is associated with the lithium-ion diffusion in the bulk of the active material. The high-frequency intercept of the semicircle reflects the uncompensated resistance (R_l), which includes the particle-particle contact resistance, the electrolyte resistance, and the resistance between the electrode and the current collector [105, 360]. The R_f, R_{ct}, and R_l for the α-$LiFeO_2$ and α-$LiFeO_2$-PPy electrodes were obtained using the equivalent circuit shown in the inset of Figure 6.7(a) (calculated by Zview). The R_l of the α-$LiFeO_2$-PPy (8.9 Ω) is smaller than that of the α-$LiFeO_2$ (10.1 Ω) electrode due to the enhanced conductivity from the PPy coating. By comparing the diameters of the semicircles, the R_f of the α-$LiFeO_2$-PPy electrode is much smaller than that of the bare α-$LiFeO_2$ electrode, due to the PPy layer, which prevents the SEI formation (9.5×10^{-4} Ω and 7.5 Ω, respectively). The R_{ct} of the α-$LiFeO_2$-PPy electrode is also lower than that of the bare α-$LiFeO_2$ electrode due to the enhancement in electronic conductivity (231.7 Ω and 386.9 Ω, respectively).

The EIS can also be used to calculate the lithium diffusion coefficient using the following equation [302, 303, 361]

$$D = R^2T^2/2A^2n^4F^4C^2\sigma^2 \quad (6.2)$$

where R is the gas constant, T is the absolute temperature, A is the surface area of the cathode

(1 cm^2), n is the number of electrons transferred in the half-reaction for the redox couple, which is equal to 1, F is the Faraday constant, C is the concentration of Li ions in the solid (2.01×10^{-3} mol cm^{-3}), D is the diffusion coefficient (cm^2 s^{-1}), and σ is the Warburg factor, which is relative to Z_{re}. σ can be obtained from the slope of the lines in Figure 6.7(b).

$$Z_{re} = R_D + R_L + \sigma\omega^{1/2} \quad (6.3)$$

The lithium diffusion coefficients are calculated to be 2.0×10^{-15} cm^2 s^{-1} and 3.5×10^{-14} cm^2 s^{-1} for bare α-$LiFeO_2$ and α-$LiFeO_2$-PPy nanocomposite, respectively, at 25 °C. This indicates that the PPy coating layer on the α-$LiFeO_2$ particles can improve the electrochemical kinetics.

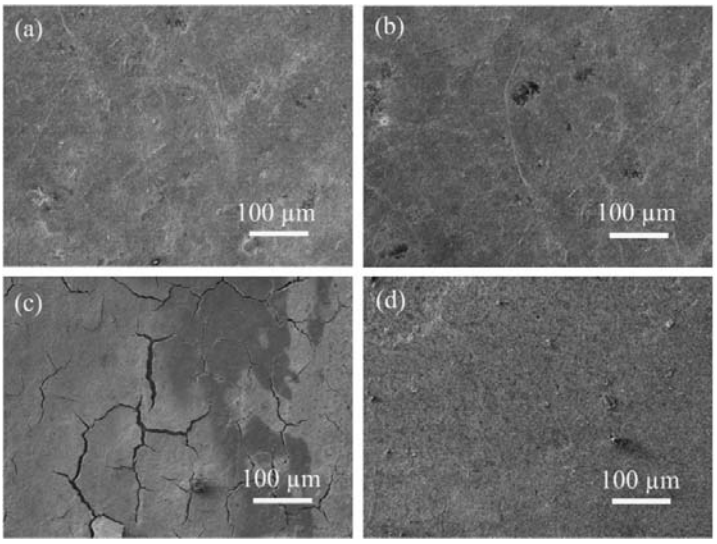

Figure 6.8 FESEM images of the electrode surface of α-$LiFeO_2$ (a, c) and α-$LiFeO_2$-PPy composite (b, d) before (a, b) and after (c, d) 100 cycles.

A morphological study of the electrodes before cycling and after 100 cycles was also conducted. The electrodes before cycling show a similar smooth surface (Figure 6.8(a, b)), while after cycling, the electrode morphology shows big differences. Figure 6.8(c) is a FESEM image showing the surface of the α-$LiFeO_2$ after 100 cycles. Big cracks can be clearly observed on the surface of the electrode. The α-$LiFeO_2$-PPy composite electrode surface is much smoother in Figure 6.8(d). There are no clear cracks that can be observed on

the surface, suggesting good structural stability of the composite electrode. This excellent stability of the electrode should be attributed to the presence of the well-dispersed PPy coating on the α-$LiFeO_2$ powders. The PPy coating could work as a protective layer to reduce the contact between the $LiFeO_2$ and the electrolyte, and thus form a better SEI layer [362, 363]. Moreover, PPy could prevent cracking and pulverization of the α-$LiFeO_2$ electrode [364].

6.4 Conclusions

In this chapter, nanosized α-$LiFeO_2$ has been synthesized at low temperature using a solid-state reaction method with β-FeOOH as the precursor. A novel α-$LiFeO_2$-PPy composite was then prepared by chemical polymerization. The α-$LiFeO_2$-PPy composite shows better capacity retention and higher rate capability than the bare α-$LiFeO_2$. The R_f and R_{ct} for the α-$LiFeO_2$-PPy nanocomposite electrode are much lower than for the bare α-$LiFeO_2$ electrode, indicating enhanced electron transfer due to the good conductivity of the PPy coating layer. The PPy can prevent the formation of cracks in electrodes during the charge/discharge process. The conductive PPy serves as both a conducting matrix and a protective coating.

Chapter 7 Facile Synthesis of Porous V_2O_3/C Composites as Lithium Storage Material with Enhanced Capacity and Good Rate Capability

7.1 Introduction

Over the decades, vanadium oxides have attracted special interest because of their outstanding structural flexibility combined with their interesting chemical and physical properties for catalytic and electrochemical applications [365, 366]. It is well known that vanadium oxides possess an exceptionally rich variety of structural motifs due to their different atomic configurations and the wide range of vanadium valence states, leaving us a broad scope for exploring new morphological and structural atomic configurations [144, 367, 368]. Among the various vanadium oxides, metastable oxides, such as V_2O_3, VO_2, $H_2V_3O_8$, $V_2O_{5-\delta}$, V_2O_5, $LiVO_2$, and LiV_3O_8, have been found to show interesting electrode properties in lithium cells [365, 369-373]. Vanadium sesquioxide (V_2O_3) is a multifunctional material frequently applied in conductive polymer composites and catalysis. Recently, it has been utilized in Li-based electrochemical energy storage systems, in both non-aqueous and aqueous systems, as an electrode material [141, 144]. V_2O_3 possesses a high theoretical capacity of 1070 mAh g^{-1} as an anode material in LIBs, much higher than that of the currently commercialized graphite [373, 374]. Besides the high specific capacity, V_2O_3 has other advantages such as abundant raw materials and low toxicity [373]. However, as a kind of transition metal oxide, their first discharge process leads to the amorphization of their host structures, and the poor kinetics associated with the energy barrier and breakage of the metal-oxygen (M-O) bonds causes a large electrode polarization [375]. All these issues could be circumvented, however, by applying different structures and adding the active materials in well-graphitized carbon layers

[373, 376].

Porous materials have attracted great research interest in the field of catalysts, molecular sieves, host materials, and battery materials, especially in electrochemistry-related applications [377-379], essentially because of their substantial advantages in terms of mass transport [380]. The nanostructured transition metal oxides have been proven to be advantageous compared to micrometer-sized structures for LIBs, owing to the shortened diffusion length for both Li ions and electrons, and the larger specific surface area for the electrode/electrolyte interaction. Drawbacks such as poor conductivity, however, as well as the expansion induced loss of contact points, remain problematic and require further improvement [381]. Employing the porous morphology could offer fast lithium diffusion pathways as well as enough electrical contact. Transport of electrons and Li^+ in a porous nanostructured system typically encompasses shorter path lengths, higher electrode–electrolyte contact area, and a better accommodation of the strain of Li^+ insertion/extraction [380]. The porous structure can form a strong supporting framework as well to avoid agglomeration of particles.

Furthermore, carbon coating has been successfully applied in many transition-metal oxides such as TiO_2, Co_3O_4, Fe_3O_4, and Cr_2O_3 to improve the conductivity and stability [382-384]. Because V_2O_3 exhibits an even higher specific capacity than these oxides the carbon coating process could further enhance the conductivity of V_2O_3 and protect the particles from agglomeration. However, so far, only a few V_2O_3/carbon composites have been reported in the literature, all exhibiting poor performance [141, 373, 385, 386].

Therefore, the successful design and synthesis of V_2O_3 composites based both porous

structure and carbon coating will be an important development for next-generation electrode materials for LIBs. This paper reports an in-situ rapid hydrothermal method for preparation of porous V_2O_3/C composites. The structure, morphology, and electrochemical properties of V_2O_3 and V_2O_3/C are also presented in this paper.

7.2 Experimental Section

7.2.1 Material Synthesis

The V_2O_3/C composite precursor was prepared by an *in-situ* hydrothermal process. In a typical synthesis, a suitable amount of glucose, 0.304 g of V_2O_3 powder (purissima, Riedel-de Haen), 20 mL of $NH_3 \cdot H_2O$ (~30%, Sigma–Aldrich), and 30 mL of de-ionized H_2O were mixed together for 4 h using an ultrasonic probe, which was followed by vigorous magnetic stirring at room temperature for 15 min. The resultant mixture was then transferred to a 100 mL autoclave and kept in an oven at 180 °C for 10 h. The product was washed with anhydrous ethanol and cyclohexane 3 times. The resultant V_2O_3/C composite precursor was dried at 80 °C in a vacuum oven for 12 h. The crystalline V_2O_3/C composite was obtained by annealing the precursor at 450 °C for 4 h under argon atmosphere.

7.2.2 Material Characterization

X-ray diffraction was performed using a GBC instrument (Bragg-Brentano configuration), with Cu-K_α radiation and graphite monochrometer at a scanning rate of 2° min^{-1} for 2θ in the range of 10 - 80°. Traces™ software in combination with the Joint Committee on Powder Diffraction Standards (JCPDS) powder diffraction files were used to identify the phases present. Raman analysis was performed using a Raman spectrometer (JobinYvon HR800) employing a 10 mW helium/neon laser at 632.8 nm. The amount of graphene in the samples was estimated using a Mettler-Toledo thermogravimetric analysis/differential scanning

calorimetry (TGA/DSC) 1 STARe System from 50 - 800 °C at 5 °C min^{-1} in air flux. Field emission scanning electron microscopy was performed using a JEOL 7500 cold FEG analytical instrument and transmission electrom microscopy was performed at 200 KeV using a JEOL 2011 analytical TEM/STEM instrument equipped with a JEOL EDS detector (EM-202207T JEC, 30mm^2 area and 144 eV Resolution), and JEOL Analysis Station Software. Samples for TEM analysis were prepared by direct dispersion of powders onto holey carbon support film. The specific surface area of the powders was examined by gas sorption analysis using the Brunayer-Emmett-Teller method (Quanta Chrome Nava 1000).

7.2.3 Electrochemical measurements

To test the electrochemical performance, electrodes were prepared by pasting a mixture of the V_2O_3 or V_2O_3/C anode material, carbon black, and sodium carboxymethyl cellulose (CMC) in a weight ratio of 75: 20: 5 on copper foil, followed by drying in a vacuum oven at 150 °C for 2 h. The loading mass of the electrodes is around 2.5 mg cm^{-2} for both of the V_2O_3 and V_2O_3/C electrodes. CR 2032 coin-type cells were assembled in an Ar-filled glove box (Mbraun, Unilab, Germany) using lithium metal foil as the counter electrode and 1 M $LiPF_6$ solution in ethylene carbonate/diethyl carbonate as the electrolyte (1: 1 by volume, provided by MERCK KGaA, Germany). The cells were galvanostatically charged and discharged in the range of 0 - 3 V at different rates using a computer-controlled charger system manufactured by Land Battery Testers. Electrochemical impedance spectroscopy (EIS) was performed on the electrodes using a Biologic VMP3 electrochemistry workstation. The AC amplitude was 5 mV, and the frequency range applied was 100 kHz to 0.01 Hz.

7.3 Results and Discussion

X-ray diffraction results obtained from both V_2O_3 and the V_2O_3/C composite (Figure 7.1) can be readily indexed to the rhombohedral crystalline phase (space group: R3c

167) of V_2O_3, in agreement with the literature values (JCPDS no. 34 0187). Possible impurity phases, includingV_3O_7, V_2O_5, VO_2 (M), and VO_2 (B), were below the level of detection, indicating that V_2O_3 of high purity had been synthesized [385, 387].

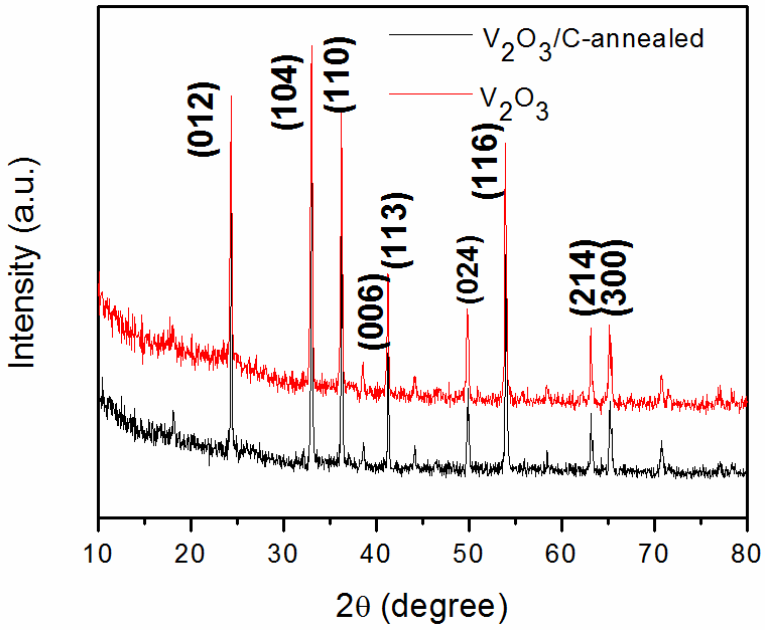

Figure 7.1 XRD patterns of the V_2O_3 and annealed V_2O_3/C composite.

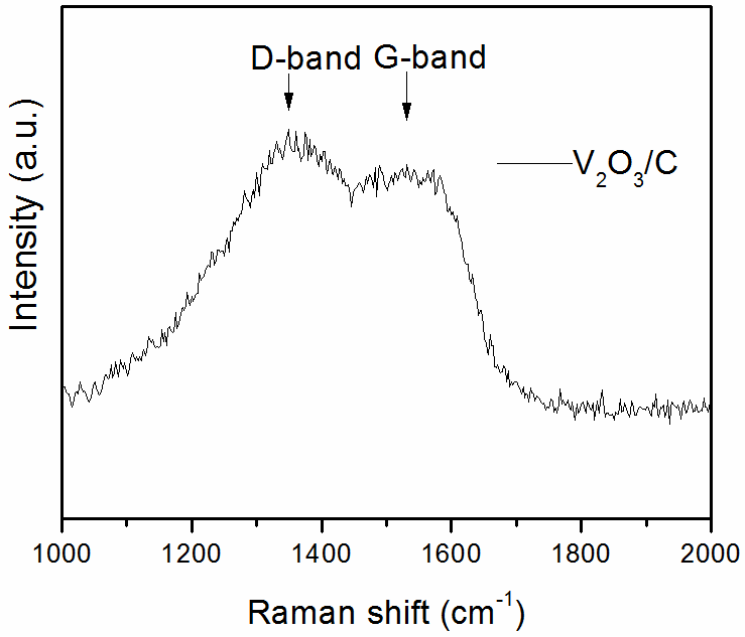

Figure 7.2 Raman spectrum of V_2O_3/C composite.

Raman spectroscopy (Figure 7.2) was applied to investigate the presence of a carbon layer and vanadium oxide. The bands in the range of 1200-1460 cm^{-1} and 1470-1730 cm^{-1} are attributed to the D-band (K-point phonons of A_{1g} symmetry) and G-band (E_{2g} phonons of sp^2 carbons). The intensity of the G-band is almost as strong as that of the D-band, implying that well graphitized carbon dominates the carbon coating layer.

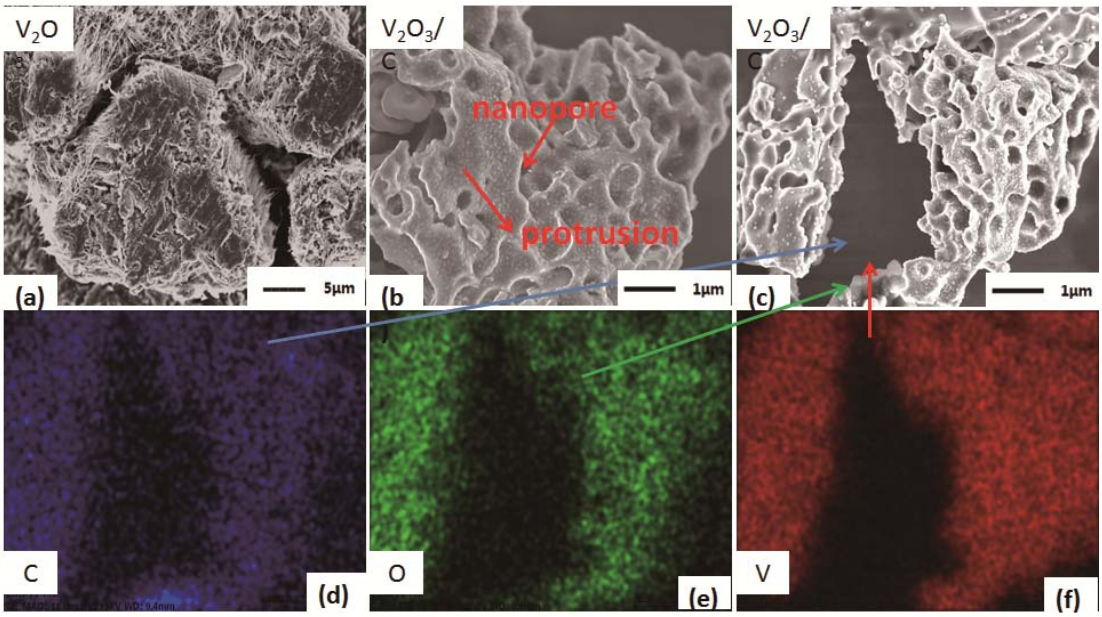

Figure 7.3 FESEM images obtained from the commercial V_2O_3 (a) and the V_2O_3/C composite (b, c) with corresponding EDS maps for C (d), O (e), and V (f).

Results of SEM examination combined with EDS mapping for different elements (V, O, and C) are shown in Figure 7.3. As shown in Figure 7.3(a), the commercial V_2O_3 has an irregular morphology, comprising particles tens of microns in size with smaller fibrous regions originating from the surfaces. After hydrothermal treatment (Figure 7.3(b) - (e)) and carbon coating, the V_2O_3morphology has converted into a network of smaller, irregular porous particles (Figure 7.3(b)-(c)), with cross-linking and inter penetration of the sub-micron diameter pores (Figure 7.3(b), where additional surface protrusions are also present). SEM combined with X-ray mapping (Figure 7.3(c) - (f))

confirmed that the particles were coated with a carbon-rich layer, and that V and O are distributed uniformly throughout the whole surface of each porous particle [388].

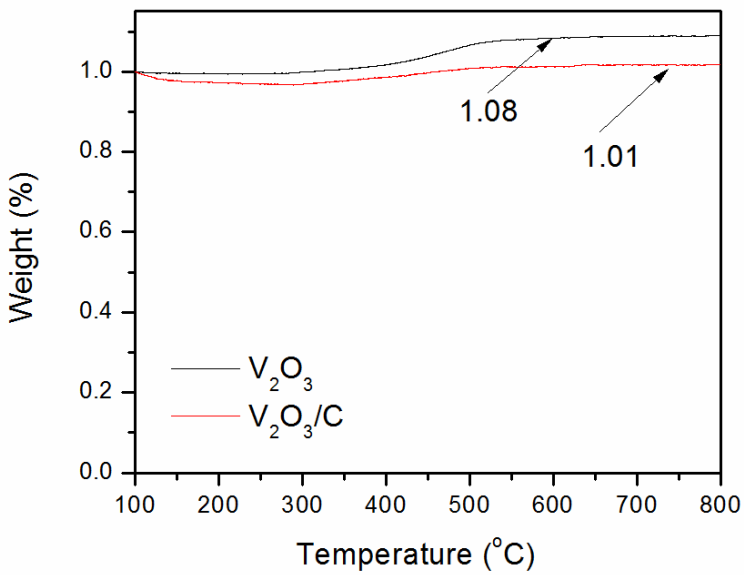

Figure 7.4 TGA curves of V_2O_3 and V_2O_3/C composite.

To estimate the amount of carbon in the V_2O_3/C composite, thermogravimetric analysis (TGA) was carried out in air flux (Figure 7.4). The results show a typical TGA curve obtained from the V_2O_3/C composite sample along with a sample of V_2O_3. The difference in weight between the V_2O_3 and the V_2O_3/C composite after oxidation could be translated into the amount of carbon in the V_2O_3/C composite. By this method, the amount of carbon in V_2O_3/C was estimated to be approximately 7 wt.%.

Transmission electron microscopy of V_2O_3/C composite, combined with EDS spot analyses imaging (Figure 7.5), confirmed the open porous microstructure of the product (Figure 7.5(a)), comprising of a carbon containing vanadium oxide structure with protrusions matching those in the SEM images. Protrusions in the TEM images (Figure 7.5(b) corresponded to the regions on the edges of the large particles in the SEM images. TEM-EDS spot analysis of such regions indicated that they regions comprised a nanostructured mixture of vanadium oxide and carbon. In addition, high

resolution TEM imaging consistently indicated contrast consistent with the presence of a layer of amorphous carbon on the surface of the V_2O_3, as indicated in (Figure 7.5(c) and the associated EDS analysis of that region (Figure 7.5(d)).

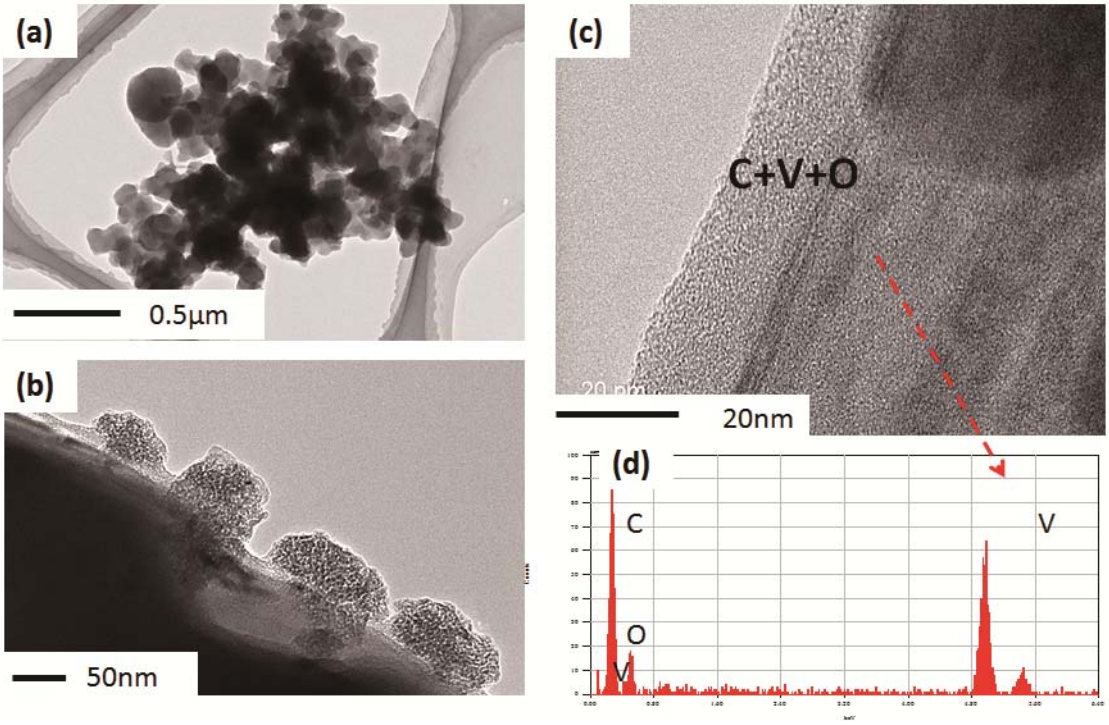

Figure 7.5 TEM and TEM-EDS spot analyses obtained from the V_2O_3/C composite: (a) TEM image at low magnification, (b) intermediate magnification image showing uneven protrusions, and (c) high magnification image with inset EDS analysis confirming the presence of C, V and O.

To gain further insight into the surface area of the V_2O_3/C composite, Brunauer-Emmett-Teller (BET) measurements were performed. A high specific surface area of 52.8 m^2 g^{-1} for the V_2O_3/C composite was obtained by nitrogen adsorption-desorption profiles compared with 2.1 m^2 g^{-1} for the commercial V_2O_3. Such a high surface area and porous structure provides efficient transport pathways to the interior voids of the particles and increases the electrode-electrolyte interfacial area, which is critical for high rate LIB applications.

It is proposed that the porous V_2O_3/C composites are formed by corrosive etching of the initial microfibers on the surfaces of the as-supplied V_2O_3, via an oxygen-engaged oxidation process. The trace oxygen dissolved in solution may gradually oxidize V_2O_3 into $VO_3(OH)^{2-}$ [389]. In the second step, glucose is believed to be absorbed on the surface of the porous structure and transformed to colloidal carbon through the hydrothermal method at 180 ^oC. The third step involves the graphitization of the carbon by annealing. Figure 7.6 summarizes all the major steps involved in the corrosive etching process [390].

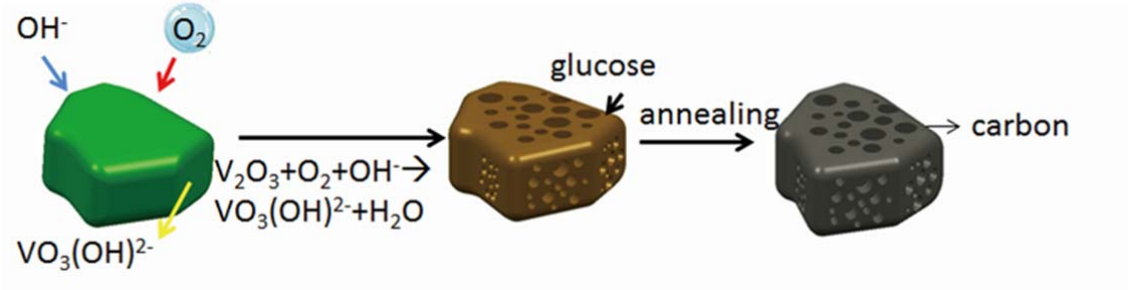

Figure 7.6 Schematic illustration of the synthesis of V_2O_3/C composite: (1) corrosive etching; (2) absorbing glucose; and (3) carbon coating.

To test the electrochemical performance, sample powders were mixed with carbon black and sodium carboxymethyl cellulose (CMC) in a weight ratio of 75: 20: 5, pasted on copper foil, and then dried in a vacuum oven at 150$^{\circ}C$ for 2 h. CR 2032 coin-type cells were assembled in an Ar-filled glove box (Mbraun, Unilab, Germany) using lithium metal foil as the counter electrode. The electrolyte was 1 M $LiPF_6$ in a mixture of ethylene carbonate (EC) and diethyl carbonate (DEC) (1: 1 by volume, provided by MERCK KGaA, Germany).

The cyclic voltammetry (CV) curves of the V_2O_3 and V_2O_3/C composite electrodes for the first five cycles are shown in Figure 7.7 (a) and (b), in the potential range of 0-3.0

V at a scan rate of 0.1 mV s^{-1}. The main feature of the CV curves is the presence of three pairs of redox peaks for each cycle. The first five CV curves of the V_2O_3/C composite electrode overlap much better. The positive shift and the change in shape of the oxidation/reduction potential peak may be attributed to structural change and polarization in the electrode. Better overlapping indicates that the V_2O_3/C composite electrode has better stability and reversibility for the insertion and extraction of lithium ions. In addition, the current density of V_2O_3/C composite electrode is more than two times that of V_2O_3 electrode, and the peaks are more obvious.

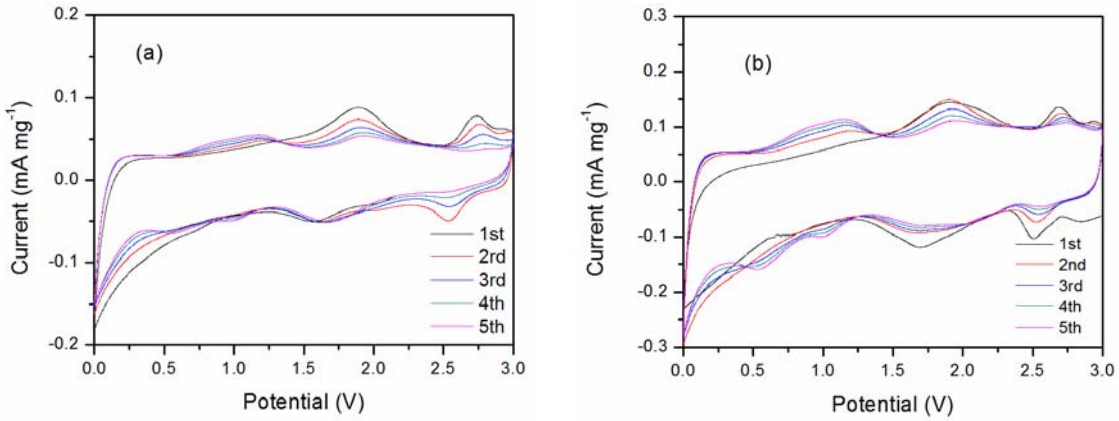

Figure 7.7 (a) cyclic voltammetry (CV) curves (for the first five cycles of V_2O_3 at a scan rate of 0.1 mV s^{-1}; (b) CV curves for the first five cycles of V_2O_3/C at a scan rate of 0.1 mV s^{-1}.

The cathodic/anodic peaks in the cyclic voltammograms (Figure 7.7 (a) and (b)) are in good agreement with the plateaus observed in the voltage-capacity profiles (Figure 7.7). In Figure 7.8, the V_2O_3 electrode shows a discharge capacity of 314 mAh g^{-1}, while the V_2O_3/C composite electrode exhibits a much higher capacity, 437 mAh g^{-1} higher than the V_2O_3 electrode. These results suggest that the V_2O_3/C composite electrode has better kinetic properties and electrochemical reactivity.

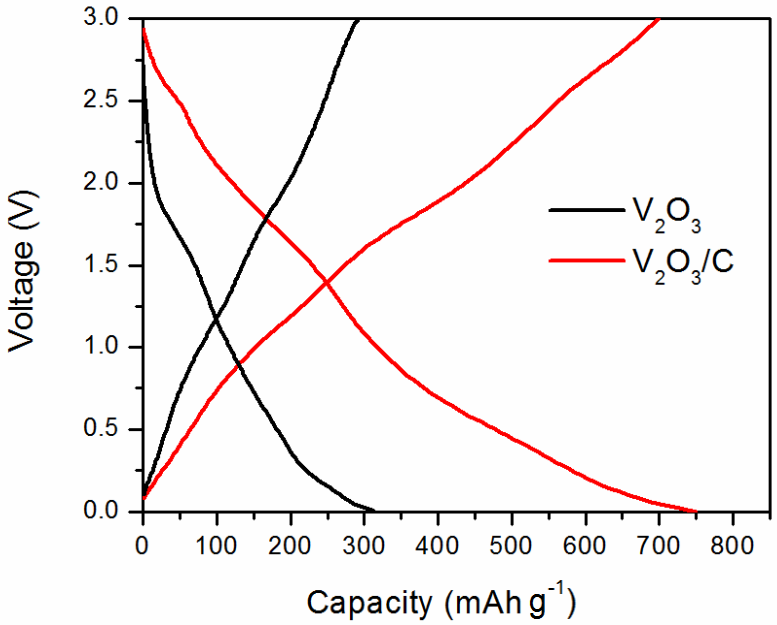

Figure 7.8 Typical discharge and charge profiles of the V_2O_3 and V_2O_3/C composite at the current density of 250 mA g^{-1} between 0 and 3 V, in 1 M $LiPF_6$ solution of EC/DEC.

According to the discharge/charge profiles and CV results, the V_2O_3/C composite is also an ideal electrode candidate for pseudo-capacitors. Its electrochemical performance at different scan rate has been tested and the capacitance has been calculated (Figure 7.9). Figure 7.9 shows the cyclic voltammograms of V_2O_3 and V_2O_3/C electrodes at various scan rates varying from 200 mV s^{-1} to 0.1 mV s^{-1}. It can be seen that the response changes from an almost square-like behaviour to a more distorted parallelogram as the scan rate increases. The specific capacitance of the V_2O_3 and V_2O_3/C composites was calculated at various scan rates using the following Equation [391]:

$$C = \int I \times dV/(s \times 2 \times V \times m) \quad (7.1)$$

where C is the capacitance of pseudo-capacitor (F g^{-1}), $\int I \times dV$ is Area of the cyclic voltammogram, s is scan rate (V s^{-1}), V is voltage window (0-3 V), m is the mass of active material (g).

It can be clearly observed that the capacitance of V_2O_3 and V_2O_3/C electrodes as expected decreases with increasing scan rate as the reaction kinetics of the pseudocapacitance reactions become evidently rate-limited [392]. The V_2O_3 electrode has a fade of capacitance from 321.5 F g^{-1} @ 0.1mV s^{-1} to 32.5 F g^{-1} @ 200 mV s^{-1}. In contrast, the capacitance of V_2O_3/C electrodes at the scan rate of 0.1 mA s^{-1} could be as high as 841F g^{-1} and still get the capacitance of 65.9 F g^{-1} at the scan rate of 200mA s^{-1}. The porous structure and the carbon coating could enhance the capacitance significantly.

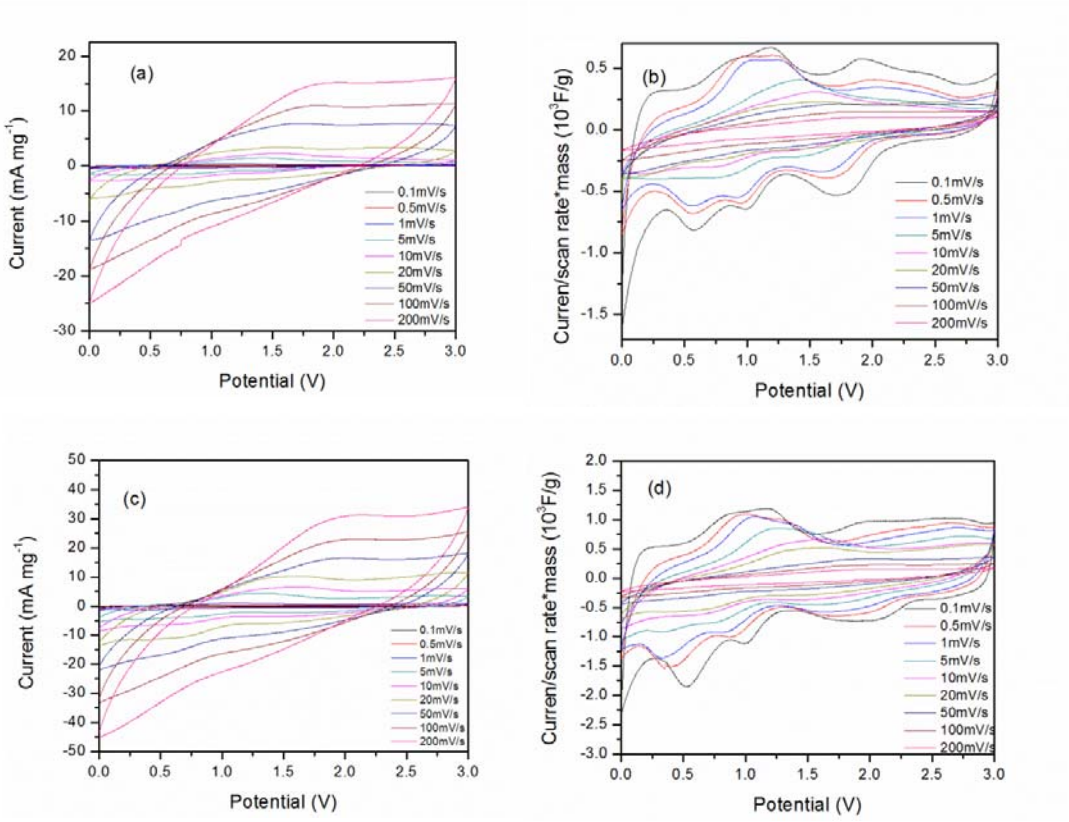

Figure 7.9 (a) Cyclic Voltammogram of V_2O_3 and at a number of scan rates from 200 mV s^{-1} to 0.1 mV s^{-1}; (b) CV curves of V_2O_3; (c) Cyclic Voltammogram of V_2O_3/C composites electrode and at a number of scan rates from 200 mV s^{-1} to 0.1 mV s^{-1}; (d) CV curves of V_2O_3/C.

Figure 7.10(a) displays the Nyquist plots (electrochemical impedance spectra) of the

pure V_2O_3 and V_2O_3/C composite electrodes after 5 cycles in the discharged state. They present one compressed semicircle in the high to medium frequency range, which describes the charge transfer resistance (R_{ct}) for both electrodes, and a line in the low-frequency range, which could be considered as Warburg impedance (Z_W) [105]. From comparing the diameters of the semicircles, the impedance of the V_2O_3 electrode is significantly larger than that of the V_2O_3/C composite electrode. The values of R_{ct} for the V_2O_3 and V_2O_3/C composite electrodes were calculated to be 351 Ω and 237 Ω, respectively. The R_{ct} of the V_2O_3/C composite electrode is only 67% of that of the V_2O_3 electrode, confirming that carbon in the composite reduces the charge transfer resistance and enhances the electronic conductivity of the V_2O_3/C composite. These results clearly reveal the enhanced stability, superior conductivity, and reversibility of this novel porous V_2O_3/C structure.

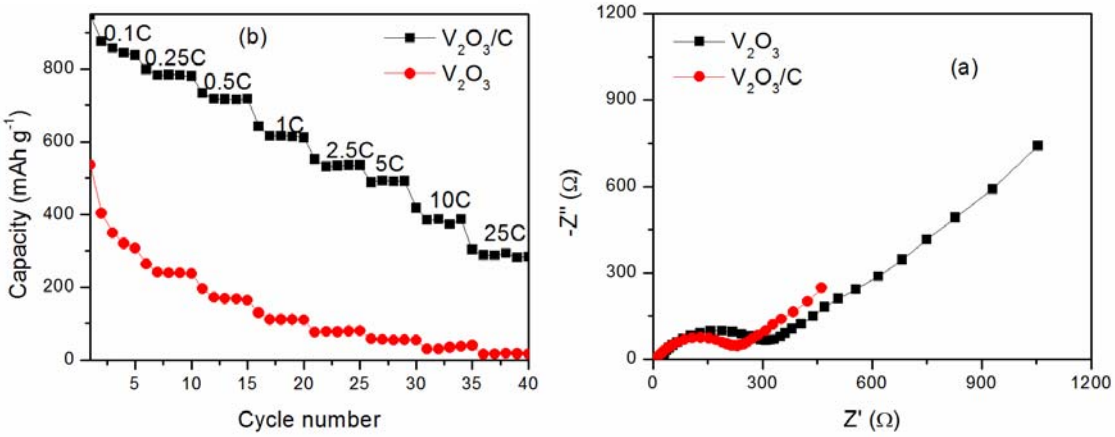

Figure 7.10 (a) Nyquist plots of V_2O_3 and V_2O_3/C composite after 5 cycles; and (b) rate performance of V_2O_3 and V_2O_3/C composite cycled in 1 M $LiPF_6$ solution of EC/DEC.

A comparison of the rate performance of the V_2O_3 and V_2O_3/C composite electrodes is shown in Figure 7.10(b). After the cells had been cycled for 5 cycles at the rate of 0.1

C (current density of 100 mA g^{-1}), the current density was increased stepwise to 25 C (current density is of 25 A g^{-1}). The V_2O_3/C composite exhibits obviously improved high rate performance over that of the V_2O_3. A high capacity of 283 mAh g^{-1} was obtained for the V_2O_3/C at the highest current density of 25 C, while V_2O_3 shows almost no capacity at this current density. These results are much better than the reported V_2O_3/C composites, which delivered 230 mAh g^{-1} at 5 A g^{-1} (5 C) [373] and 309mAh g^{-1}(2C) [386]. This can be explained by the high crystallinity and the unique morphology.

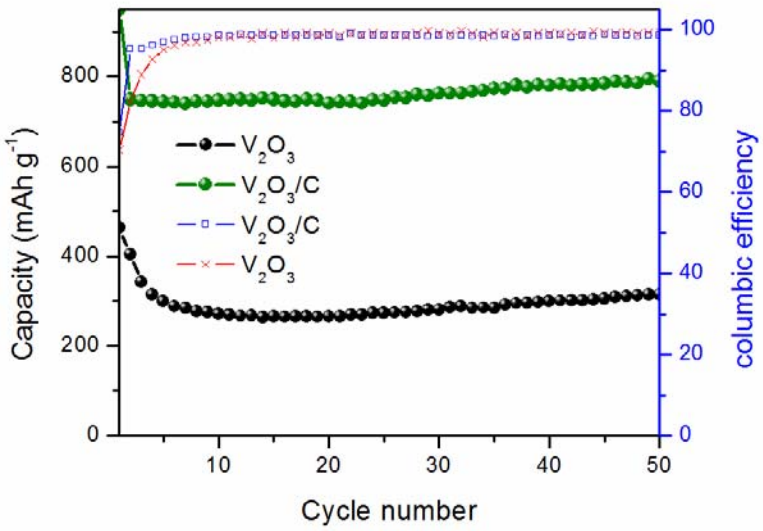

Figure 7.11 Cycling performance of the pure V_2O_3 and V_2O_3/C composite electrodes at the current density of 250 mA g^{-1} between 0 and 3 V.

The improvement of stability could also be demonstrated by cycling performance and by the lack of damage indicated by FESEM images of the electrodes after cycling. Discharge/charge cycling was carried out in the voltage range of 0-3.0 V (vs. Li) based on the reference current density of 250 mA g^{-1} up to 50 cycles (Figure 7.11). The discharge capacity is calculated in terms of the weight of composite. The large irreversible capacity observed in the first and second cycles may be caused by the

formation of amorphous Li_2O and the solid electrolyte interphase (SEI), as well as the amorphization of their host structures. The discharge capacity of the third cycle of V_2O_3 is 342.7 mAh g^{-1}, and it keeps decreasing to 272.7 mAh g^{-1} after 25 cycles. The carbon coated V_2O_3 composite electrode delivered more than two times the capacity of the commercial V_2O_3. The increasing capacity after several discharge/charge cycles as well as the 2% loss of columbic efficiency could be attributed to the decomposition of the electrolyte. The higher surface area of the V_2O_3/C composite may also amplify this effect.

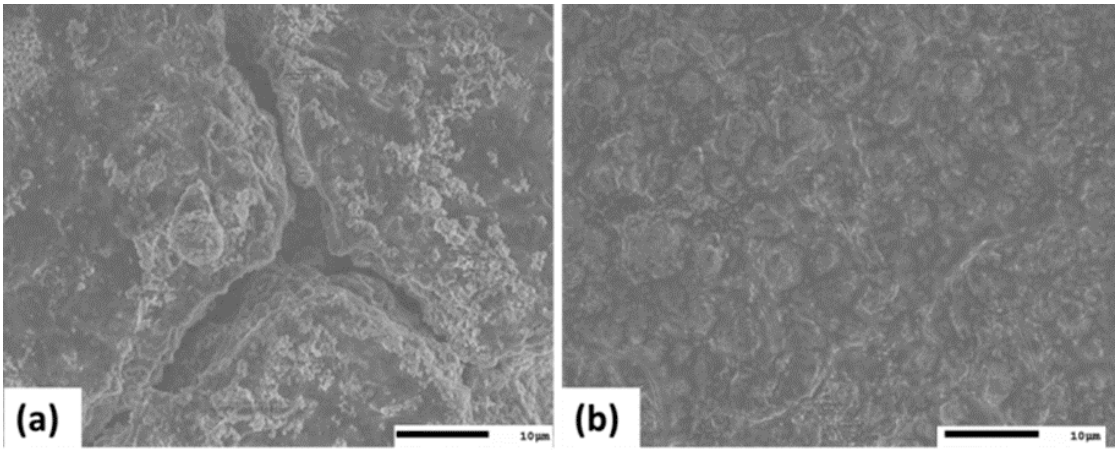

Figure 7.12 (a) FESEM image of the electrode of the V_2O_3 electrode after 50 cycles; and (b) FESEM image of the electrode of the V_2O_3/C composite after 50 cycles.

The morphology change of V_2O_3 and V_2O_3/C electrodes after cycling has been studied by using the FESEM (Figure 7.12 a and b). After 50 cycles, V_2O_3 electrode performed great cracks due to the agglomerate during the charge/discharge, while no obvious cracks of V_2O_3/C electrode could be observed which could be attributed to the carbon coating and the buffering of porous structure.

As an anode material in LIBs,V_2O_3 has a very high theoretical capacity of 1070 mAh g^{-1} [373, 374]. However, as a typical conversion type anode material, the first

discharge process of V_2O_3 leads to the amorphization of its host structure, and the poor kinetics associated with the energy barrier and breakage of the M-O bonds causes a large electrode polarization [375]. The resulting poor energy efficiency makes the use of conversion type material impractical in a high energy battery system. Carbon coating could partly solve this problem and result in significantly reduced contact resistance along with enhanced capacity and rate capability.

7.4 Conclusion

A composite of porous V_2O_3/C has been synthesized by a rapid novel corrosive-coating combined hydrothermal method. The resultant composite reveals a unique morphology in which porous V_2O_3 is coated by carbon. The porous structure could mitigate the stress/strain of Li^+ insertion/de-insertion, increase the surface area of the material, and reduce the effective diffusion distance for lithium ions, all of which would lead to improved capacity, rate capability, and cycling performance. Furthermore, this carbon-coated nano-architecture ensures not only high electronic conductivity for both facile mass transfer and facile charge transfer, but also protection from the agglomeration of nanoparticles. As one of the first reported composites of V_2O_3/C, it has highly desirable properties: a high specific capacity, reduced resistance, and exceptionally good rate capability. Therefore, V_2O_3/C electrode is a promising candidate for the development of high-performance, low-cost, and advanced LIBs.

Chapter 8 Tuning Three-Dimensional TiO_2 Nanotube Electrode to Achieve High Utilization of Ti Substrate for Lithium Storage

8.1 Introduction

Rechargeable LIBs have been widely used as power sources for portable electronic devices due to their high energy-storage density, high voltage, long cycle life, and operation at ambient temperature [200, 393, 394]. Most of the commercial LIBs use graphitic carbon as the anode material. There are safety concerns about this material, however. Graphite electrode is prone to growing lithium dendrites after repetitive charge-discharge, resulting in irreversible damage to the lithium ion battery. Compared to graphite, TiO_2 has a higher lithium intercalation potential (1.75 V vs. Li^+/Li), enabling it to avoid the deposition of metallic lithium, and it has higher capacity for Li^+ intercalation/de-intercalation [395, 396]. These properties make TiO_2 suitable for large-scale energy storage, when coupled with high-voltage cathode materials ($LiMn_2O_4$, $LiNi_{0.5}Mn_{1.5}O_4$, $LiNi_{1/3}Mn_{1/3}Co_{1/3}O_4$, etc.) [148, 320, 329, 396]. Moreover, TiO_2 is non-toxic, low-cost, abundant in nature, and has good electronic properties, as well as stable physical and chemical properties [397, 398].

Nanostructured TiO_2 anodes have been successfully used to improve cycling stability and high rate capability over those of their bulk counterparts. Compared with nanoparticles, nanowires, and nanoribbons, self-organized TiO_2 nanotube arrays possess larger specific surface areas and faster Li^+ transport [399-401]. The traditional TiO_2 nanotube arrays, however, only have a low surface area and a small aspect ratio of length to diameter, because they are grown on Ti foil by electrochemical anodization and the length of TiO_2 nanotube is only around 500 nm, so the traditional TiO_2/Ti foil electrode shows low area capacity [396, 402]. Moreover, the use of Ti foil is expensive and wasteful. Liao et al. reported that only around 2 wt% of the Ti was converted into TiO_2 nanotubes [403]. TiO_2 nanotube array

electrode grown on Ti mesh is a good choice to avoid these disadvantages. The TiO_2 nanotubes extend radially in a 3D array on a grid of fine Ti wires, so the TiO_2/Ti mesh electrode has high surface area, a large aspect ratio, and a high Ti conversion rate (M_{Ti-1} (Ti converted into TiO_2 nanotubes)/ M_{Ti-0} (Ti mesh substrate)) [404-406]. Meanwhile, the 3D TiO_2 nanotube arrays allow Li^+ to more easily access the TiO_2 surface from the electrolyte [407, 408]. Some reports have shown real benefits from the 3D electrode design, such as in LIBs using Sn/graphene in a 3D multilayer structure and 3D ordered porous Sn-Ni alloy as anode to improve the specific area capacity, conductivity, and cycling stability [409, 410]. The benefits for LIBs associated with 3D nanotube arrays of TiO_2 grown on Ti mesh, however, have not been studied to date.

Here, TiO_2/Ti mesh as a new type of anode material was prepared by the electrochemical anodization method. TiO_2/Ti mesh can be applied directly as an electrode material in a test cell without the need for a current collector or binder. 3D TiO_2 radial nanotube arrays with different lengths were grown on Ti mesh by controlling the anodization time. The special architecture of the 3D nanotube arrays with large surface area can provide effective contact between the active materials and the electrolyte, and shorten the lithium diffusion length. Moreover, the thin Ti wires at the centre of the nanotubes can maintain good conductivity. In this work, we tested the properties of TiO_2/Ti mesh electrodes with different anodization processing times. When the anodization processing time was 600 min, the investigated TiO_2/Ti mesh electrode possessed both high electrochemical performance and good mechanical behaviour.

8.2 Experimental Section

8.2.1 Material Synthesis and Characterization

3D TiO_2 nanotube arrays on Ti mesh were prepared following our previous method [411]. A

polished piece of Ti mesh (30 × 55 mm^2, 100 mesh, 0.1 mm thick, purity 99.5 wt%) was anodized in organic electrolyte consisting of ammonium fluoride (NH_4F, 0.25 wt%) and ethylene glycol (EG; $(HOCH_2)_2$, 98 vol%; H_2O, 2 vol%). The potential was supplied by a laboratory DC power supply (TPR-6405, LWDQGS). The nanotube length could be increased by increasing the anodization time of the Ti mesh at 20 V in organic electrolyte. The as-prepared TiO_2/Ti meshes were annealed at 500 ^oC under ambient air for 3 h to induce TiO_2 crystallization. The TiO_2/Ti meshes were analysed by X-ray diffraction (XRD; GBC MMA) with Cu Kα radiation, as well as by field emission scanning electron microscopy (FESEM; JEOL 7500).

8.2.2 Electrochemical Measurements

The TiO_2/Ti mesh electrodes were cut to 1 × 1 cm^2 in size and then dried at 80 ^oC in a vacuum oven for 24 h. CR 2032 coin-type cells were assembled in an Ar-filled glove box (Mbraun, Unilab, Germany), using lithium metal foil as the counter electrode. The electrolyte was 1 M $LiPF_6$ in a mixture of ethylene carbonate (EC) and diethyl carbonate (DEC) (1:1 by volume, provided by MERCK KGaA, Germany). The cells were galvanostatically charged and discharged in the range of 3.0-1.0 V at different current densities using a computer-controlled charger system manufactured by Land Battery Testers. A Biologic VMP-3 electrochemical workstation was used to perform cyclic voltammetry (CV; scanning rate 0.1 mV s^{-1}).

8.3 Results and Discussion

Figure 8.1 shows the XRD patterns of the 3D TiO_2 nanotube arrays on Ti mesh prepared by anodization in organic electrolyte over periods ranging from 60 min to 720 min, with the samples designated as TiO_2/Ti-*t* mesh (*t* = 0, 60, 180, 420, 600, 720 min; the different anodization time intervals were used to obtain more comprehensive results and are also

mentioned in our previous report) [411]. After annealing at 500 ºC, the TiO_2 nanotubes on Ti mesh (JCPDS 44-1294) are mainly anatase phase (JCPDS 21-1272). Some weak peaks related to the rutile phase (JCPDS 44-1276) appear in the XRD patterns of the TiO_2/Ti-*t* mesh samples, but the nanotubes are mostly still composed of anatase phase [404]. Varghese et al. reported that rutile phase mainly existed in the barrier layer underlying the TiO_2 nanotube arrays [412]. With increasing anodization processing time, the intensity of the rutile phase peaks decreases, while the intensity of the anatase phase peaks increases because the weight percentage of TiO_2 nanotubes is increased.

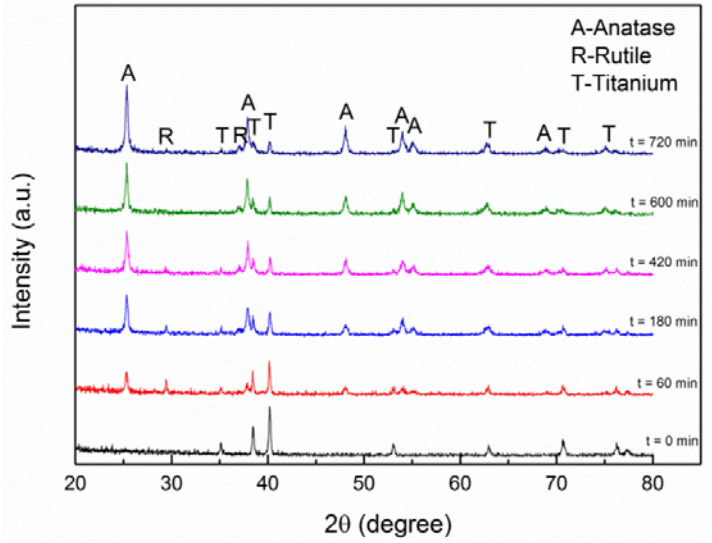

Figure 8.1 XRD patterns of TiO_2/Ti-*t* mesh (*t* = 0, 60, 180, 420, 600, 720 min) annealed at 500 ºC.

FESEM images of the anodic TiO_2 nanotubes on the Ti mesh substrates are presented in Figure 8.2. Figure 8.2 shows that the diameter of the TiO_2/Ti wire increases with prolonged anodization processing time. When the anodization processing time is 60 min, the morphology of the TiO_2/Ti-60min mesh has only slightly changed compared with the Ti mesh, because the additional diameter of the TiO_2/Ti wire is only around 10 μm, while the diameter of the bare Ti wire is 90.2 μm [Figure 8.2(a, b)]. With increasing anodization

processing time, the TiO_2 nanotube arrays are interspaced with fissures at irregular intervals [Figure 8.2(c-f)]. This can be attributed to van der Waals attraction and capillary forces during drying [404-406]. Meanwhile, we can see from the Figure 8.2(b-f) insets that the TiO_2 nanotube arrays and the Ti wire substrates have been separated at their interfaces due to the stress when the TiO_2/Ti mesh was cut down during the FESEM characterization.

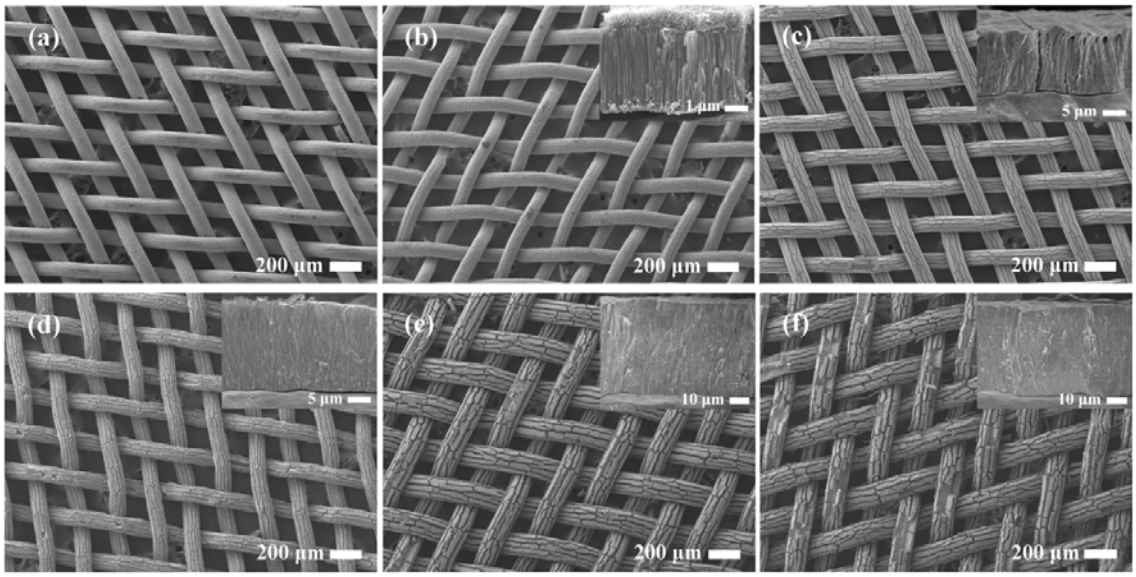

Figure 8.2 FESEM images of TiO_2/Ti mesh prepared by anodization in EG electrolyte containing 0.25 wt% NH_4F with different anodization processing times: a) 0 min; b) 60 min; c) 180 min; d) 420 min; e) 600 min; f) 720 min. The corresponding cross-sections of TiO_2 nanotubes on Ti mesh are shown in the insets.

From Figure 8.2, we can measure the diameters of the Ti and TiO_2/Ti wires and the length of the TiO_2 nanotubes. Figure 8.3(a) shows the geometric parameters of the TiO_2/Ti mesh obtained by anodization in organic electrolyte. The diameters of the Ti and TiO_2/Ti wires and the length of the TiO_2 nanotubes have a linear relationship with the anodization processing time [Figure 8.3(b)]. The Ti mesh did not react with the organic electrolyte when *t* was 0 min, so the intercepts for the TiO_2/Ti wire diameter and the Ti wire diameter have the same value (90.2 μm, the diameter of the Ti wire before anodization), and the intercept for the TiO_2

nanotube length is 0. The linear fit results can be written as the following equations

$$D = k_1 \times t + B \tag{8.1}$$

$$d = - k_2 \times t + B \tag{8.2}$$

$$h = k_3 \times t \tag{8.3}$$

where D is the diameter of the TiO_2/Ti wire (μm), d is the diameter of the Ti wire (μm), h is the length of the TiO_2 nanotubes (μm), t is the anodization processing time (min), k_1, k_2, k_3 is the growth rate with processing time of the TiO_2/Ti wire diameter, the Ti wire diameter, and the TiO_2 nanotube length, respectively, and B is the TiO_2/Ti wire and Ti wire diameter intercept (B = 90.2 μm). From the linear fit results, the absolute values of the slopes have similar values ($|K| \approx 0.08$; k_1 = 0.081 (± 0.007), k_2 = -0.079 (± 0.004), k_3 = 0.080 (± 0.005)). Therefore, the relationship between D and d can be written as in the following equation

$$D = |K| \times t + B \tag{8.4}$$

For the Ti mesh used here, the distance between two adjacent Ti wires ($a_{\text{Ti-Ti}}$) is 257.1 μm for Ti mesh. There will be no void regions between two adjacent TiO_2/Ti wires in the TiO_2/Ti mesh when D approaches 257.1 μm. That is to say, the void regions in the Ti mesh will be fully filled with TiO_2 nanotube arrays, so that the TiO_2/Ti mesh shows the highest specific surface area. Meanwhile, the electrolyte can penetrate to the entire surface of the TiO_2 nanotubes due to the nanotube arrays that are radially grown on the Ti wires [Figure 8.3(a, c-e)]. For the TiO_2/Ti mesh samples, however, the TiO_2 nanotube arrays are easily detached from the Ti mesh when t is 720 min, because the length of the TiO_2 nanotubes (h_{TiO2} = 61.4 μm) is around two times the diameter of the Ti wire (d_{Ti} = 30.1 μm; Figure 8.2(f)). The TiO_2/Ti-720min mesh electrode shows poor mechanical behavior. Figure 8.2(e) shows that the TiO_2/Ti mesh with 600 min anodization processing has been uniformly covered with TiO_2

nanotubes, and the ratio of h_{TiO2}/d_{Ti} is 1.2 (h_{TiO2} = 50.5 μm, d_{Ti} = 43.6 μm). The Ti conversion rate can be calculated from the masses of the Ti mesh and the TiO_2/Ti-600min mesh for 1 cm^2 electrode area (18.1 mg and 11.56 mg, respectively). The Ti conversion rate is 22 wt%, much higher than that previously reported (2 wt%) [404]. Therefore, the TiO_2/Ti-600min mesh electrode is the most promising electrode, as it has high surface area, good mechanical behavior, and a high Ti conversion rate. Furthermore, by controlling the distance between two adjacent Ti wires and controlling the anodization processing time, we can obtain higher surface area and better mechanical behavior in TiO_2/Ti mesh electrode for lithium-ion batteries.

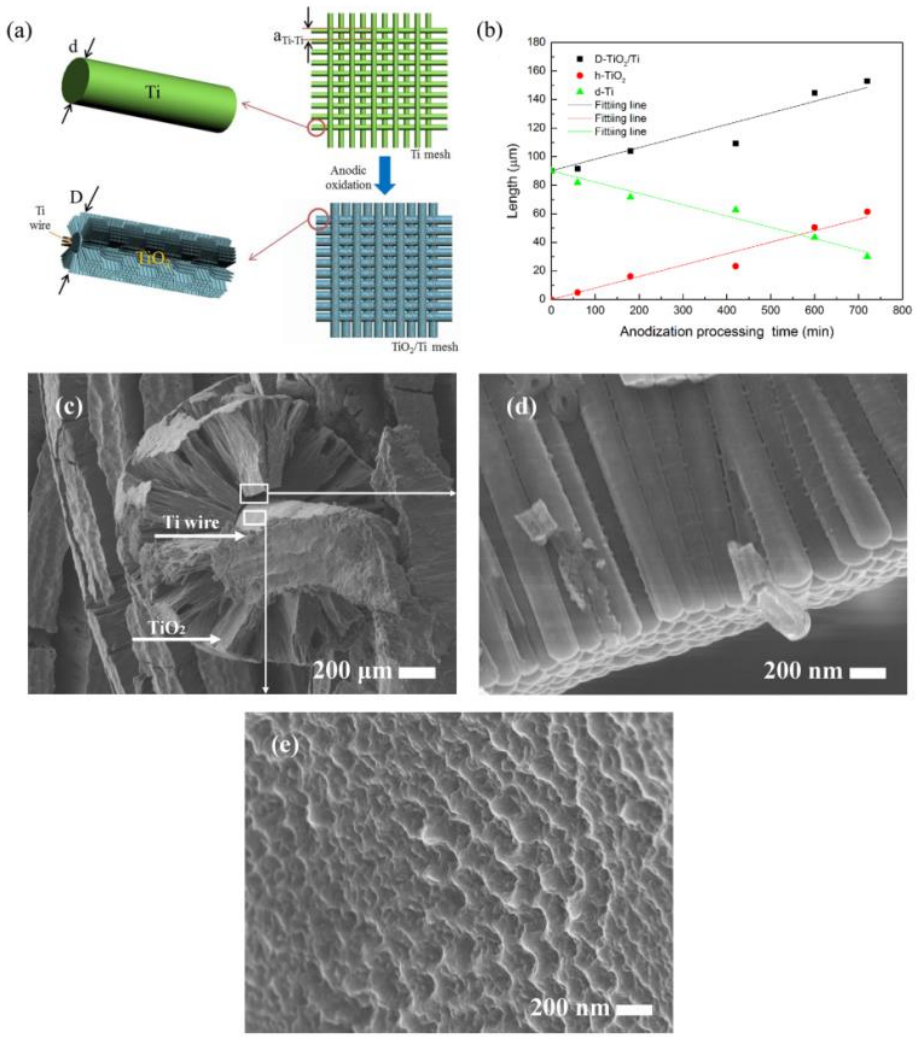

Figure 8.3 (a) Geometric parameters of Ti mesh and TiO_2/Ti mesh obtained with anodization

in EG electrolyte containing 0.25 wt% NH_4F. (b) Length and diameter parameters of TiO_2/Ti mesh versus anodization processing time. (c) FESEM image of single wire of mesh from TiO_2/Ti-600min (cross-section); high magnification images of (d) TiO_2 nanotube and (e) Ti wire for selected areas in (c).

In order to compare TiO_2/Ti mesh electrode prepared over a short time (60 min) and a longer time (600 min), we conducted FESEM using high magnification. FESEM images of anodic TiO_2 nanotubes on the Ti mesh substrates are presented in Figure 8.2(b, e), and high magnification FESEM images are presented in Figure 8.4(a, b). After the 60 min anodization process, the mesh retained sufficient void regions, and the TiO_2 nanotubes grew perpendicularly to the surface of the Ti wire and covered the entire wire uniformly [Figure 8.2(b)]. The Ti wires act as the current collector during LIB testing. The length and inner diameter of the TiO_2 nanotubes are ~4.9 μm and ~100 nm, respectively [Figure 8.2(b) and Figure 8.4(a)]. The length and inner diameter of the TiO_2 nanotubes are ~50.5 μm and ~100 nm, respectively, when the anodization processing time is 600 min [Figure 8.2(e) and Figure 8.4(b)].

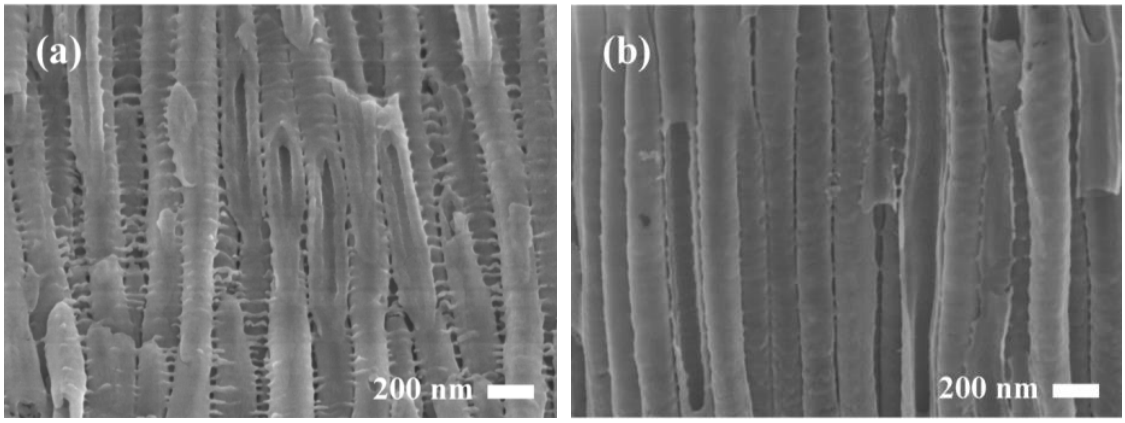

Figure 8.4 High magnification FESEM images of TiO_2/Ti mesh prepared by anodization in EG electrolyte containing 0.25 wt% NH_4F: a) cross-sectional image of TiO_2 nanotubes from TiO_2/Ti-60min mesh; b) cross-sectional image of TiO_2 nanotubes from TiO_2/Ti-600min mesh.

The TiO_2/Ti-60min mesh electrode and TiO_2/Ti-600min mesh electrode were selected to test their performance in LIBs. Figure 8.5(a, b) shows cyclic voltammograms of TiO_2/Ti mesh for the first five cycles at the scan rate of 0.1 mV s^{-1}. In the first cycle, the TiO_2/Ti-60min mesh

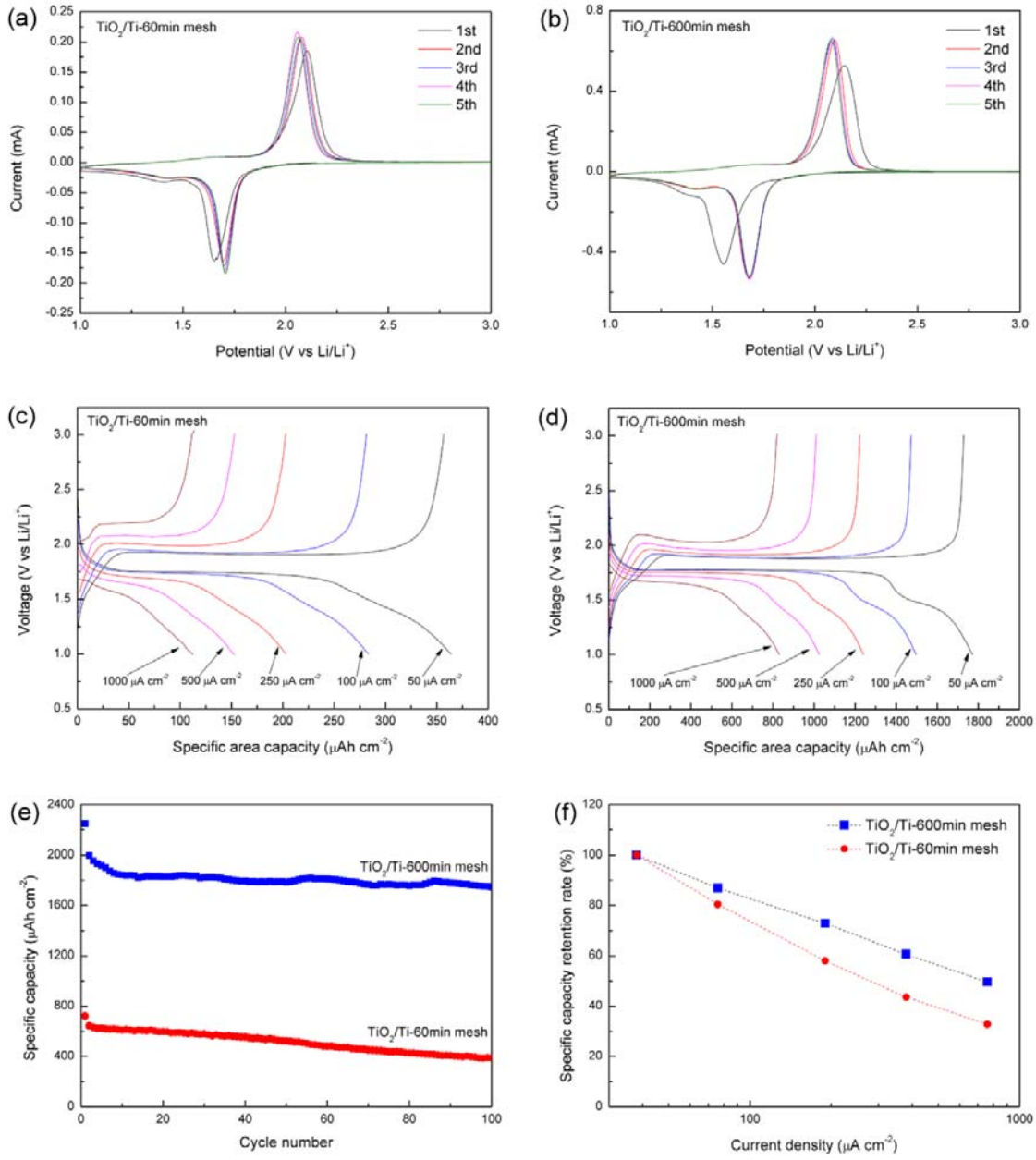

Figure 8.5 Electrochemical behaviour of the TiO_2/Ti-60min mesh and TiO_2/Ti-600min mesh electrodes: (a, b) cyclic voltammograms for the first 5 cycles at a scan rate of 0.1 mV s^{-1}; (c, d) 5th cycle discharge and charge curves at different current densities from 50 μA cm^{-2} to

1000 μA cm^{-2}; (e) cycling performance at 50 μA cm^{-2}; (f) rate capability at different current densities.

electrode presents a pair of cathodic/anodic peaks centred at 1.65 V and 2.10 V (vs. Li/Li^+), corresponding to lithium insertion/extraction into/from the anatase TiO_2 lattice, respectively, while the TiO_2/Ti-600min mesh electrode's cathodic/anodic peaks are centred at 1.55 V and 2.15 V (vs. Li/Li^+). In the following cycles, however, both the TiO_2/Ti-60min mesh and the TiO_2/Ti-600min mesh electrodes show a single pair of cathodic/anodic peaks at about 1.70 V and 2.05 V (vs. Li/Li^+), consistent with a two-phase redox reaction of $xLi^+ + xe^- + TiO_2 \leftrightarrow Li_xTiO_2$ ($x \approx 0.5$) [395, 413]. A similar observation has been previously reported, and it has been ascribed to an activation effect during the initial cycling of the TiO_2 nanotubes [414]. It should be noted that there is a pair of broad and low cathodic/anodic peaks that appear around 1.4 V and 1.6 V (vs. Li/Li^+) [Figure 8.5(a, b)]. These peaks correspond to lithium insertion/extraction into/from the rutile TiO_2 lattice, respectively [200]. These cathodic and anodic peaks are in accordance with the plateaus in the discharge/charge curves. Figure 8.5(c, d) displays typical discharge/charge curves for the TiO_2/Ti-60min mesh and TiO_2/Ti-600min mesh electrodes at different current densities from 50 to 1000 μA cm^{-2}. The TiO_2/Ti-60min mesh electrode starts to show sloping discharge curves from 250 μA cm^{-2}, whereas the TiO_2/Ti-600min mesh electrode still shows a flat plateau, even at 500 μA cm^{-2}. Those results suggest that the kinetic properties of the TiO_2/Ti mesh electrode have remained stable with increasing length of the TiO_2 nanotubes.

Figure 8.5(e) shows the cycling performances of the TiO_2/Ti-60min mesh and TiO_2/Ti-600min mesh electrodes at 50 μA cm^{-2}. The TiO_2/Ti-60min mesh electrode shows an initial discharge capacity of 720.9 μA h cm^{-2}. After the second cycle, the capacity retention remains stable at around 600 μA h cm^{-2}. After 30 cycles, however, the discharge capacity continuously

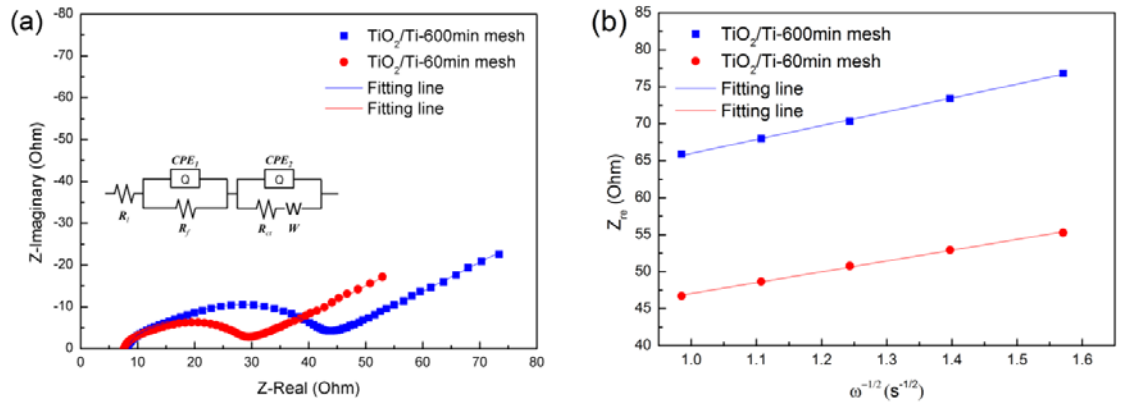

Figure 8.6 (a) Impedance plots of the TiO_2/Ti-60min mesh and TiO_2/Ti-600min mesh anodes after cycling over 10 cycles at a discharge potential of 1.7 V vs. Li/Li^+ at 25 ˚C at frequencies from 100 kHz to 10 mHz. The equivalent circuit is shown in the inset. (b) Real part of the complex impedance versus $\omega^{-1/2}$ at 25 ˚C at a discharge potential of 1.7 V vs. Li/Li^+.

decreases to 388.9 μA h cm^{-2}. The capacity retention after 100 cycles is around 54% of the initial discharge capacity. In comparison, the TiO_2/Ti-600min mesh electrode shows great enhancement of the capacity retention. The TiO_2/Ti-600min mesh electrode shows an initial discharge capacity of 2249.9 μA h cm^{-2}, and after 100 cycles, it was measured to be 1745.5 μA h cm^{-2}, which is around 78% of the initial discharge capacity. For comparing specific capacity with other reported nanostructured TiO_2 anodes, the specific capacity of the TiO_2/Ti-600min mesh (1 cm^{-2}) based on its mass (11.56 mg) was calculated. The initial discharge capacity and the discharge capacity after 100 cycles were 195.3 mAh g^{-1} and 151.5 mAh g^{-1}, respectively, and the discharge current density was 4.3 mA g^{-1}, similar to other reports in the literature (where the capacity is between 100 mAh g^{-1} and 170 mAh g^{-1} after 100 cycles at 20 mA g^{-1} [200, 393, 395, 400, 415]). Figure 8.5(f) shows the specific capacity retention rate as a function of current density for lithium cells containing the TiO_2/Ti-60min mesh and TiO_2/Ti-600min mesh electrodes. As shown in Figure 8.5(f), the specific capacity retention rate of the TiO_2/Ti-600min mesh electrode decreases much more slowly with increasing discharge rate

than that of the TiO_2/Ti-60min mesh electrode. Although the 3D TiO_2 nanotube arrays on the Ti mesh are as long as 50.5 μm, the TiO_2/Ti mesh cell always maintains its high area capacity, stable cycling performance, and high rate capability. The cycling stability and rate performance of the TiO_2/Ti-600min mesh electrode could be attributed to the particular geometry, in which the TiO_2 nanotubes extend radially in a 3D array on a grid of Ti wires, allowing e^- and Li^+ to more easily access the TiO_2 surface.

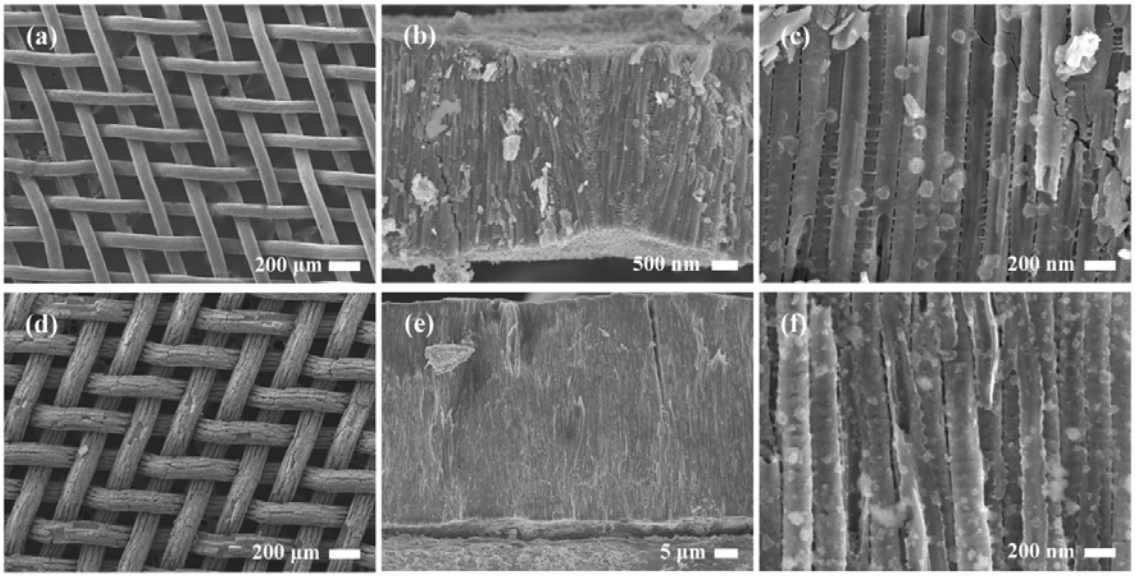

Figure 8.7 FESEM images of TiO_2/Ti mesh after 100 cycles: (a) top view of theTiO_2/Ti-60min mesh; (b) cross-sectional image of the TiO_2/Ti-60min mesh; (c) high magnification image of the TiO_2 nanotubes from (b); (d) top view of the TiO_2/Ti-600min mesh; (e) cross-sectional image of the TiO_2/Ti-600min mesh; (f) high magnification image of TiO_2 nanotubes from (e).

To further understand the kinetic processes of the electrode reactions, electrochemical impedance spectroscopy (EIS) measurements were performed on the TiO_2/Ti-60min and TiO_2/Ti-600min mesh electrodes. Figure 8.6(a) shows the Nyquist plots of the electrodes at a discharge potential of 1.7 V vs. Li/Li^+ at 25 °C after cycling over 10 cycles. All the impedance curves show two partly overlapping semicircles in the high to medium frequency region,

which could be assigned to the film resistance (R_f) of the solid electrolyte interphase (SEI) and the charge transfer resistance (R_{ct}), respectively. A line inclined at approximately 45° reflects the Warburg impedance (W), which is associated with the lithium-ion diffusion in the TiO_2 nanotubes. The high-frequency intercept of the semicircle reflects the uncompensated resistance (R_l), which includes the particle-particle contact resistance, the electrolyte resistance, and the resistance between the TiO_2 nanotube arrays and the Ti wire [105, 415]. The R_f, R_{ct}, and R_l for the TiO_2/Ti-60min and TiO_2/Ti-600min mesh electrodes were obtained using the equivalent circuit shown in the inset of Figure 8.6(a) (calculated by Zview). The R_l of the TiO_2/Ti-60min mesh electrode (7.8 Ω) is similar to that of the TiO_2/Ti-600min mesh electrode (8.3 Ω), indicating that the interface between the nanotube arrays and the Ti wire is stable and adhesive. On comparing the diameters of the semicircles, the R_f of the TiO_2/Ti-60min mesh electrode is similar to that of the TiO_2/Ti-600min mesh electrode (15.7 Ω and 24.2 Ω, respectively), due to the particular geometry, which hinders SEI formation. The thickness of the TiO_2 nanotubes is about 20 nm, so the R_{ct} values of the TiO_2/Ti-60min mesh and the TiO_2/Ti-600min mesh electrodes are very small (3.1 Ω and 6.8 Ω, respectively). The EIS can also be used to calculate the lithium diffusion coefficient using the following equation [279, 303, 416]

$$D = R^2T^2/2A^2n^4F^4C^2\sigma^2 \quad (8.5)$$

where R is the gas constant, T is the absolute temperature, A is the surface area of the cathode (1 cm^2), n is the number of electrons transferred in the half-reaction for the redox couple, which is equal to 0.5, F is the Faraday constant, C is the concentration of Li ions in the solid material (1.39×10^{-3} mol cm^{-3}), D is the diffusion coefficient ($cm^2\ s^{-1}$), and σ is the Warburg factor, which is relative to Z_{re} [417]. σ can be obtained from the slope of the lines in Figure 8.6(b).

$$Z_{re} = R_l + R_{ct} + \sigma\omega^{-1/2} \quad (8.6)$$

The lithium diffusion coefficients are calculated to be 6.0×10^{-9} cm^2 s^{-1} and 3.3×10^{-9} cm^2 s^{-1} for the TiO_2/Ti-60min mesh and the TiO_2/Ti-600min mesh, respectively, at 25 °C. This indicates that the TiO_2/Ti-600min mesh electrode can maintain good electrochemical kinetics.

A morphological study of the electrodes before cycling and after 100 cycles was also conducted. The TiO_2/Ti-60min mesh electrode before cycling shows a smooth surface [Figure 8.2(b) and Figure 8.4(a)], while the TiO_2/Ti-600min mesh electrode shows some TiO_2 nanotube arrays interspaced with fissures at irregular intervals on the Ti wire surface [Figure 8.2(e) and Figure 8.4(b)]. Compared with before cycling, the electrodes after cycling show similar morphology. Figure 8.7(a) is a FESEM image showing the surface of the TiO_2/Ti-60min mesh after 100 cycles. No changes can be observed on the surface of the electrode. The high magnification image of the cross-section shows that some electrolyte particles have not been washed off, and the surface of the TiO_2 nanotube is very smooth due to the particular geometry [Figure 8.7(b, c)]. The TiO_2/Ti-600min mesh electrode surface shows the same morphology as before cycling, and the SEI layer can be seen on the inside and outside of the TiO_2 nanotubes [Figure 8.7(e, f)] [362, 418]. This excellent stability of the electrode should be attributed to the particular architecture. Traditional nanostructured electrodes are easy to damage after long cycling, however, for the TiO_2/Ti mesh electrodes used here, the Ti wires act as the current collector and as a frame to protect the TiO_2 nanotube arrays from being damaged and detached [183, 367]. As can be seen from the cross-section of the TiO_2/Ti-600min mesh electrode, the 3D TiO_2 nanotube arrays efficiently prevent the SEI layer from increasing, even though the length of the TiO_2 nanotube is 50.5 μm [Figure 8.7(e)].

8.4 Conclusions

In summary, a new type of electrode consisting of long 3D TiO_2 nanotube arrays on Ti mesh was manufactured using the electrochemical anodization method. The TiO_2 nanotubes extend radially in a 3D array on a grid of Ti wires. The Ti wires acted as the current collector during LIB testing. The Ti conversion rate was increased to around 22wt%. This electrode, which does not need a current collector or binder, has flat potential plateaus, high specific area capacity, and high rate capability, on the same level as reported for nanostructured TiO_2 anode. Therefore, this novel 3D structured TiO_2/Ti mesh is a very promising anode material for LIBs.

Chapter 9 General Conclusions and Outlook

9.1 General Conclusions

This doctoral work investigates nanostructured and composite electrode materials for LIBs with AN emphasis on high rate capability and stable capacity retention, including $LiNbO_3$ coated $Li_{1.08}Mn_{1.92}O_4$ composite, $LiNbO_3/LiNi_{0.5}Mn_{1.5}O_4$ composite, PPy-coated α-$LiFeO_2$ nanocomposite, V_2O_3/C composite, and3D TiO_2/Ti mesh. The aim was to broaden our understanding of their surface structural evolution and related electrochemical behavior. The composite electrode materials showed highly enhanced electron or lithium ion transport within the electrode, with improved high temperature stability and high rate capability, and buffering of the volume changes to increase the capacity retention. The as-synthesized nanostructured electrode materials showed improved electrochemical performance due to their high surface area, shortened electronic and lithium diffusion pathways, and enhanced reactivity. A summary of the outcomes will be elaborated in the following sections.

9.1.1 Cathode materials

$Li_{1.08}Mn_{1.92}O_4$ samples with a solid-state electrolyte (SSE) coating layer were successfully synthesized by a facile solid-state reaction method. Based on the as-prepared $LiNbO_3$ coated $Li_{1.08}Mn_{1.92}O_4$ composites, a novel LIB system was developed which consists of a manganese spinel cathode, a $LiNbO_3$-coating layer, OLE, and a lithium foil anode. In this novel LIB system, $LiNbO_3$-coated $Li_{1.08}Mn_{1.92}O_4$ composite electrode showed enhanced high temperature electrochemical performance, including long cycling stability, high rate capability, and a good lithium-ion diffusion coefficient. From the *in situ* SXRD results, the SSE $LiNbO_3$ coating layer functioned effectively to prevent Mn dissolution and maintain high ionic conductivity between the electrode and the organic liquid electrolyte, due to the dual structure of the cathode material (low-energy non-equilibrium solid solution phase

[$Li_{x+0.08}Mn_{1.92}O_4$ ($0 < x < 1$)] and the stable SSE $LiNbO_3$ coating layer). The $0.06LiNbO_3$-$0.97Li_{1.08}Mn_{1.92}O_4$ cathode displayed the best electrochemical properties, with the highest capacity of 111 mAh g^{-1} up to 100 cycles at a current density of 74 mA g^{-1} and at 55 ^oC.

$LiNi_{0.5}Mn_{1.5}O_4$ cathode material was synthesized by a sol-gel method, and $LiNbO_3$ additive with high ionic conductivity was uniformly mixed with $LiNi_{0.5}Mn_{1.5}O_4$ by a solid-state reaction. Electrochemical measurements show that the additive affects the cycling performance and high rate capability of the electrode. The *in situ* SXRD patterns show that the as-prepared $LiNi_{0.5}Mn_{1.5}O_4$ cathode material has a highly reversible $P4_332$ phase. The $LiNbO_3$ phase structure remains stable throughout the charge-discharge process, and the $LiNbO_3$ acts as a bifunctional additive in LIBs with liquid electrolyte. This bifunctional additive can improve the lithium diffusion coefficient and protect the electrolyte from the oxidative side reactions at high voltage. The $0.04LiNbO_3/LiNi_{0.5}Mn_{1.5}O_4$ cathode displayed the best electrochemical performance, in terms of the capacity of 118 mAh g^{-1} after 200 cycles with capacity retention of 94% at 25 ^oC and high rate capability (101 mAh g^{-1}, 20 C).

Cauliflower-like α-$LiFeO_2$-PPy nanocomposite was successfully prepared using a chemical polymerization method. The electrochemical performance of the α-$LiFeO_2$-PPy electrode was improved over that of the bare α-$LiFeO_2$, especially the capacity retention and high rate capability. The conductive PPy acts as both a conducting matrix and a protective coating layer. The α-$LiFeO_2$-PPy electrode with 16.6 wt.% PPy showed good cycling stability (104 mAh g^{-1} at 0.1 C after 100 cycles) and rate capability (50 mAh g^{-1} at 10 C).

9.1.2 Anode materials

Porous V_2O_3/C composites were synthesized by a rapid novel corrosive-coating method combined with the hydrothermal method. The resultant composite exhibits a unique morphology, in terms of the porous V_2O_3 coated with carbon. The porous structure

provides shortened lithium ion diffusion pathways, a large specific surface area, and a high tolerance for the volume changes. The coated carbon layer effectively increases the composite's conductivity and prevents the formation of SEI during the cycling procedure. The V_2O_3/C composite electrode showed a significantly improved electrochemical performance over that of bare V_2O_3, and it delivered an impressive capacity of 283 mAh g^{-1} at the current density of 25 A g^{-1} (more than two times the capacity of V_2O_3). In addition, this carbon-coated nano-architecture ensures protection from the agglomeration of nanoparticles. As one of the first reported V_2O_3/C composites, it exhibits very promising electrochemical properties: a high specific capacity, reduced resistance, and exceptionally good rate capability.

3D TiO_2 nanotube arrays on Ti mesh were prepared for LIBs by using the electrochemical anodization method. The 3D TiO_2 radial nanotube arrays were grown on Ti mesh by controlling the anodization time. They feature large surface area and provide effective contact between the active materials and the electrolyte, while also shortening the lithium diffusion length. The thin Ti wires at the center of the nanotubes can maintain good conductivity, and the Ti conversion rate was ~ 22wt%. The TiO_2/Ti mesh anode exhibited superior electrochemical performance, with the high specific area capacity of 1745.5 μAh cm^{-2} after 100 cycles at a current density of 50 μA cm^{-2}. This TiO_2/Ti mesh anode does not need a current collector, conductive carbon, or a binder. In addition, this electrode showed very stable lithiation/delithiation processes, while the 3D architecture still retained its morphology after 100 cycles. This novel 3D structured TiO_2/Ti mesh is a very promising anode material for LIBs.

9.2 Outlook

This doctoral work has been mainly focused on the synthesis of nanostructured or composite

electrode materials and on characterizing the electrochemical performance of the corresponding LIBs. The synthesis methods for the electrode materials presented in this experimental work, including the hydrothermal and microwave hydrothermal, solid-state reaction, sol-gel, chemical polymerization, and anodic oxidation methods, are also suitable for the preparation of other nanostructured or composite electrode materials.

A SSE coating layer is a novel surface modification for electrodes used in LIBs with liquid electrolyte, but it needs to be deeply investigated in terms of their electrochemical properties and for other substitute solid-state electrolytes such as $LiTaO_3$, Li_2SiO_3, and $Li_{3x}La_{(2/3)-x}TiO_3$. Furthermore, the high ionic conductivity materials that can act as additives in the LIB system, including $LiNbO_3$, $LiTaO_3$, Li_2SiO_3, and $Li_{3x}La_{(2/3)-x}TiO_3$, also need attention because of their potential for improving the electrochemical performance of LIBs, especially the liquid electrolyte stability at high voltage (5 V) and lithium ion transportation.

Electronically conducting coating layers, such as polymers, carbons, and noble metals, also need extensive investigation with other cathode and anode materials to improve the high rate capability and capacity retention. The electronically conducting coating layers are also potential candidates for other energy storage systems, for example, lithium-sulphur batteries, sodium-ion batteries, and supercapacitors.

3D metal-oxide nanotube arrays grown on metal mesh substrate, including TiO_2, SnO_2, and MnO_2, are still worth further investigation for use in LIBs. On the one hand, the 3D metal-oxide nanotube arrays exhibit a large surface area, shortened lithium ion diffusion pathways, and high structural stability. On the other hand, the metal mesh substrate with good electronic conductivity acts as current collector, which simplifies the battery design and saves a series of electrode preparation processes, because the conductive carbon, binder, solvent, and current collector are now unnecessary. These features make for LIBs with splendid electrochemical

performance.

The *in situ* synchrotron technique is a powerful tool to investigate structural changes in electrodes during cycling process due to the sensitivity of high energy X-rays to light elements, such as lithium, oxygen, etc. In particular, conventional techniques cannot collect some information during the conversion reaction because the crystallinity of the electrode materials has changed. Therefore, the *in situ* synchrotron technique is an ideal tool for analysing the lithiation/delithiation processes. To fully understand the electrochemical reaction mechanism, other *in situ* measurement techniques are also necessary, such as *in situ* Raman spectroscopy, *in situ* TEM, or *in situ* neutron diffraction.

In addition, it should be noted that the nanostructured materials show some intrinsic disadvantages due to their high surface area and nanosize effects. Usually, the nanostructured electrode materials exhibit low density and high reactivity in side reactions, which directly generates more irreversible capacity and safety issues. In order to avoid those disadvantages, particle size control and surface modification should be further investigated for different electrode materials. Further research will also need to emphasize the safety issues related to the nanosize effect.

References

[1] B. Dunn, H. Kamath, J. M. Tarascon, Science, 334 (2011) 928-935.

[2] V. Etacheri, R. Marom, R. Elazari, G. Salitra, D. Aurbach, Energy & Environmental Science, 4 (2011) 3243-3262.

[3] A. Kraytsberg, Y. Ein-Eli, Advanced Energy Materials, 2 (2012) 922-939.

[4] L. Lu, X. Han, J. Li, J. Hua, M. Ouyang, Journal of Power Sources, 226 (2013) 272-288.

[5] W. J. Zhang, Journal of Power Sources, 196 (2011) 13-24.

[6] B. Scrosati, Electrochimica Acta, 45 (2000) 2461-2466.

[7] E. Yoo, J. Kim, E. Hosono, H. S. Zhou, T. Kudo, I. Honma, Nano Letters, 8 (2008) 2277-2282.

[8] B. Scrosati, J. Hassoun, Y. K. Sun, Energy & Environmental Science, 4 (2011) 3287-3295.

[9] F. Croce, M. L. Focarete, J. Hassoun, I. Meschini, B. Scrosati, Energy & Environmental Science, 4 (2011) 921-927.

[10] I.D. Scott, Y. S. Jung, A. S. Cavanagh, Y. Yan, A. C. Dillon, S. M. George, S. H. Lee, Nano Letters, 11 (2010) 414-418.

[11] Y. Ma, Y. Zhu, Y. Yu, T. Mei, Z. Xing, X. Zhang, Y. Qian, International Journal of Electrochemical Science, 7 (2012) 4657-4662.

[12] K. S. Park, D. Im, A. Benayad, A. Dylla, K. J. Stevenson, J. B. Goodenough, Chemistry of Materials, 24 (2012) 2673-2683.

[13] Q. Qu, L. Fu, X. Zhan, D. Samuelis, J. Maier, L. Li, S. Tian, Z. Li, Y. Wu, Energy & Environmental Science, 4 (2011) 3985-3990.

[14] J. Y. Luo, Y. G. Wang, H. M. Xiong, Y. Y. Xia, Chemistry of Materials, 19 (2007) 4791-4795.

[15] J. H. Kim, S. T. Myung, C. Yoon, S. Kang, Y. K. Sun, Chemistry of Materials, 16 (2004)

906-914.

[16] X. Ma, B. Kang, G. Ceder, Journal of The Electrochemical Society, 157 (2010) A925-A931.

[17] D. Bar-Tow, E. Peled, L. Burstein, Journal of The Electrochemical Society, 146 (1999) 824-832.

[18] N. Dimov, S. Kugino, M. Yoshio, Electrochimica Acta, 48 (2003) 1579-1587.

[19] W. M. Zhang, J. S. Hu, Y. G. Guo, S. F. Zheng, L. S. Zhong, W. G. Song, L. J. Wan, Advanced Materials, 20 (2008) 1160-1165.

[20] P. Poizot, S. Laruelle, S. Grugeon, L. Dupont, J. Tarascon, Nature, 407 (2000) 496-499.

[21] L. Ji, Z. Lin, M. Alcoutlabi, X. Zhang, Energy & Environmental Science, 4 (2011) 2682-2699.

[22] A. Dey, Journal of The Electrochemical Society, 118 (1971) 1547-1549.

[23] Y. Matsuda, H. Nakashima, M. Morita, Y. Takasu, Journal of The Electrochemical Society, 128 (1981) 2552-2556.

[24] S. R. Hui, J. Roller, S. Yick, X. Zhang, C. Deces-Petit, Y. Xie, R. Maric, D. Ghosh, Journal of Power Sources, 172 (2007) 493-502.

[25] Y. Mo, S. P. Ong, G. Ceder, Chemistry of Materials, 24 (2011) 15-17.

[26] P. H. Notten, F. Roozeboom, R. A. Niessen, L. Baggetto, Advanced Materials, 19 (2007) 4564-4567.

[27] M. Armand, J. M. Tarascon, Nature, 451 (2008) 652-657.

[28] M. Dresselhaus, I. Thomas, Nature, 414 (2001) 332-337.

[29] R. Marom, S. F. Amalraj, N. Leifer, D. Jacob, D. Aurbach, Journal of Materials Chemistry, 21 (2011) 9938-9954.

[30] J. Cao, N. Schofield, A. Emadi, in: Proceedings of the IEEE Vehicle Power and Propulsion Conference, 2008. (VPPC'08). IEEE, 2008, pp. 1-6.

[31] J. B. Goodenough, Y. Kim, Chemistry of Materials, 22 (2009) 587-603.

[32] G. Armstrong, A. R. Armstrong, P. G. Bruce, P. Reale, B. Scrosati, Advanced Materials, 18 (2006) 2597-2600.

[33] W. van Schalkwijk, B. Scrosati, Advances in lithium-ion batteries, Springer, 2002.

[34] M. S. Whittingham, Science, 192 (1976) 1126-1127.

[35] F. W. Dampier, Journal of The Electrochemical Society, 121 (1974) 656-660.

[36] C. R. Walk, J. S. Gore, J. Electrochem. Soc., 122 (1975) C68-C68.

[37] K. Mizushima, P. Jones, P. Wiseman, J. Goodenough, Materials Research Bulletin, 15 (1980) 783-789.

[38] J. Goodenough, K. Mizushima, T. Takeda, Japanese Journal of Applied Physics, 19 (1980) 305.

[39] M. Okuno, S. Kojima, R. Matsushima-Nishiwaki, H. Tsurumi, Y. Muto, S. L. Friedman, H. Moriwaki, Current Cancer Drug Targets, 4 (2004) 285-298.

[40] T. Nagaura, K. Tozawa, Prog. Batteries Solar Cells, 9 (1990) 209.

[41] J. M. Tarascon, M. Armand, Nature, 414 (2001) 359-367.

[42] M. Winter, R. J. Brodd, Chemical Reviews, 104 (2004) 4245-4270.

[43] Y. S. Meng, M. E. Arroyo-de Dompablo, Energy & Environmental Science, 2 (2009) 589-609.

[44] B. L. Ellis, K. T. Lee, L. F. Nazar, Chemistry of Materials, 22 (2010) 691-714.

[45] D. Aurbach, B. Markovsky, G. Salitra, E. Markevich, Y. Talyossef, M. Koltypin, L. Nazar, B. Ellis, D. Kovacheva, Journal of Power Sources, 165 (2007) 491-499.

[46] L. X. Yuan, Z. H. Wang, W. X. Zhang, X. L. Hu, J. T. Chen, Y. H. Huang, J. B. Goodenough, Energy & Environmental Science, 4 (2011) 269-284.

[47] M. S. Whittingham, Chemical Reviews, 104 (2004) 4271-4302.

[48] T. Tan, S. Soo, A. Rahmat, J. Shamsul, R. A. Osman, Z. Jamal, M. Idris, Advanced

Materials Research, 795 (2013) 245-250.

[49] S. Luo, K. Wang, J. Wang, K. Jiang, Q. Li, S. Fan, Advanced Materials, 24 (2012) 2294-2298.

[50] P. He, H. Yu, H. Zhou, Journal of Materials Chemistry, 22 (2012) 3680-3695.

[51] J. Dahn, U. Von Sacken, M. Juzkow, H. Al-Janaby, Journal of The Electrochemical Society, 138 (1991) 2207-2211.

[52] A. R. Armstrong, P. G. Bruce, Nature, 381 (1996) 499-500.

[53] M. Tabuchi, K. Ado, H. Kobayashi, H. Kageyama, C. Masquelier, A. Kondo, R. Kanno, Journal of The Electrochemical Society, 145 (1998) L49-L52.

[54] R. Kanno, T. Shirane, Y. Kawamoto, Y. Takeda, M. Takano, M. Ohashi, Y. Yamaguchi, Journal of The Electrochemical Society, 143 (1996) 2435-2442.

[55] Y. Wang, J. Wang, H. Liao, X. Qian, M. Wang, G. Song, S. Cheng, RSC Advances, 4 (2014) 3753-3757.

[56] C. Thomas, C. Z. Ag, C. Hafner, T. Bernthaler, V. Knoblauch, G. Schneider, "Fast Structural and Compositional Analysis of Aged Li-Ion Batteries with 'shuttle & Find'" (2011).

[57] I. Saadoune, C. Delmas, Journal of Solid State Chemistry, 136 (1998) 8-15.

[58] T. Ohzuku, Y. Makimura, Chemistry Letters, (2001) 642-643.

[59] T. Ohzuku, Y. Makimura, Chemistry Letters, (2001) 744-745.

[60] H. Sclar, D. Kovacheva, E. Zhecheva, R. Stoyanova, R. Lavi, G. Kimmel, J. Grinblat, O. Girshevitz, F. Amalraj, O. Haik, Journal of The Electrochemical Society, 156 (2009) A938-A948.

[61] W. Luo, F. Zhou, X. Zhao, Z. Lu, X. Li, J. Dahn, Chemistry of Materials, 22 (2009) 1164-1172.

[62] L. Cahill, S. C. Yin, A. Samoson, I. Heinmaa, L. Nazar, G. Goward, Chemistry of

Materials, 17 (2005) 6560-6566.

[63] N. Yabuuchi, K. Yoshii, S. T. Myung, I. Nakai, S. Komaba, Journal of the American Chemical Society, 133 (2011) 4404-4419.

[64] J. Choi, A. Manthiram, Journal of The Electrochemical Society, 152 (2005) A1714-A1718.

[65] X. Li, Y. Wei, H. Ehrenberg, F. Du, C. Wang, G. Chen, Solid State Ionics, 178 (2008) 1969-1974.

[66] T. F. Yi, Y. R. Zhu, X. D. Zhu, J. Shu, C. B. Yue, A. N. Zhou, Ionics, 15 (2009) 779-784.

[67] Z. S. Zheng, Z. L. Tang, Z. T. Zhang, W. C. Shen, Journal of Inorganic Materials, 2 (2003) 079-083.

[68] J. Y. Luo, H. M. Xiong, Y. Y. Xia, The Journal of Physical Chemistry C, 112 (2008) 12051-12057.

[69] A. Wills, N. Raju, J. Greedan, Chemistry of Materials, 11 (1999) 1510-1518.

[70] E. Hosono, T. Kudo, I. Honma, H. Matsuda, H. Zhou, Nano Letters, 9 (2009) 1045-1051.

[71] M. Okubo, Y. Mizuno, H. Yamada, J. Kim, E. Hosono, H. Zhou, T. Kudo, I. Honma, ACS Nano, 4 (2010) 741-752.

[72] S. Mandal, R. Rojas, J. Amarilla, P. Calle, N. Kosova, V. Anufrienko, J. Rojo, Chemistry of Materials, 14 (2002) 1598-1605.

[73] K. Kushida, K. Kuriyama, Applied Physics Letters, 77 (2000) 4154-4156.

[74] B.G. Park, S. Kim, I. D. Kim, Y. J. Park, Journal of Materials Science, 45 (2010) 3947-3953.

[75] Y. Kim, J. Lim, S. Kang, International Journal of Quantum Chemistry, 113 (2013) 148-154.

[76] N. Treuil, C. Labrugère, M. Menetrier, J. Portier, G. Campet, A. Deshayes, J. C. Frison, S. J. Hwang, S. W. Song, J. H. Choy, The Journal of Physical Chemistry B, 103 (1999) 2100-

2106.

[77] K. M. Shaju, P. G. Bruce, Chemistry of Materials, 20 (2008) 5557-5562.

[78] K. Y. Chung, W. S. Yoon, K. B. Kim, B. W. Cho, X. Q. Yang, Journal of Applied Electrochemistry, 41 (2011) 1295-1299.

[79] R. Benedek, M. Thackeray, Electrochemical and Solid-State Letters, 9 (2006) A265-A267.

[80] S. B. Chikkannanavar, D. M. Bernardi, L. Liu, Journal of Power Sources, 248 (2014) 91-100.

[81] Y. Dai, L. Cai, R. E. White, Journal of The Electrochemical Society, 160 (2013) A182-A190.

[82] B. M. Hwang, S. J. Kim, Y. W. Lee, B. Han, S. B. Kim, W. S. Kim, K. W. Park, Int. J. Electrochem. Sci., 8 (2013) 9449-9458.

[83] J. M. Kim, G. Lee, B. H. Kim, Y. S. Huh, G. W. Lee, H. J. Kim, Ultrasonics Sonochemistry, 19 (2012) 627-631.

[84] Y. Lin, Y. Yang, H. Ma, Y. Cui, W. L. Mao, The Journal of Physical Chemistry C, 115 (2011) 9844-9849.

[85] X. Xie, D. Su, B. Sun, J. Zhang, C. Wang, G. Wang, Chemistry-A European Journal, 20 (2014) 17125-17131.

[86] J. Cho, G. B. Kim, H. S. Lim, C. S. Kim, S. I. Yoo, Electrochemical and Solid-State Letters, 2 (1999) 607-609.

[87] H. W. Ha, N. J. Yun, K. Kim, Electrochimica Acta, 52 (2007) 3236-3241.

[88] J. Cho, Journal of Materials Chemistry, 18 (2008) 2257-2261.

[89] S. Lee, Y. Cho, H. K. Song, K. T. Lee, J. Cho, Angewandte Chemie, International Edition, 51 (2012) 8748-8752.

[90] P. Dyah, S. Hari, L. Dewi Yuanita, in: Proceeding of the International Conference on

Research, Implementation and Education of Mathematics And Sciences 2014, Yogyakarta State University, 2014.

[91] H. Wu, J. Tu, X. Chen, Y. Li, X. Zhao, G. Cao, Journal of Solid State Electrochemistry, 11 (2007) 173-176.

[92] T. Tsuji, H. Umakoshi, Y. Yamamura, Journal of Physics and Chemistry of Solids, 66 (2005) 283-287.

[93] G. M. Song, W. J. Li, Y. Zhou, Materials Chemistry and Physics, 87 (2004) 162-167.

[94] L. Guohua, H. Ikuta, T. Uchida, M. Wakihara, Journal of The Electrochemical Society, 143 (1996) 178-182.

[95] R. Thirunakaran, B.R. Babu, N. Kalaiselvi, P. Periasamy, T. P. Kumar, N. Renganathan, M. Raghavan, N. Muniyandi, Bulletin of Materials Science, 24 (2001) 51-55.

[96] H. Shigemura, H. Sakaebe, H. Kageyama, H. Kobayashi, A. West, R. Kanno, S. Morimoto, S. Nasu, M. Tabuchi, Journal of The Electrochemical Society, 148 (2001) A730-A736.

[97] H. Shigemura, M. Tabuchi, H. Kobayashi, H. Sakaebe, A. Hirano, H. Kageyama, Journal of Materials Chemistry, 12 (2002) 1882-1891.

[98] F. Zhou, X. Zhao, A. van Bommel, X. Xia, J. Dahn, Journal of The Electrochemical Society, 158 (2011) A187-A191.

[99] Y. Ein-Eli, J. T. Vaughey, M. M. Thackeray, S. Mukerjee, X. Q. Yang, J. McBreen, Journal of The Electrochemical Society, 146 (1999) 908-913.

[100] E. McCalla, A. Rowe, R. Shunmugasundaram, J. Dahn, Chemistry of Materials, 25 (2013) 989-999.

[101] M. Imazaki, K. Ariyoshi, T. Ohzuku, Journal of The Electrochemical Society, 156 (2009) A780-A786.

[102] A. K. Padhi, K. Nanjundaswamy, J. B. Goodenough, Journal of The Electrochemical

Society, 144 (1997) 1188-1194.

[103] C. Delacourt, L. Laffont, R. Bouchet, C. Wurm, J. B. Leriche, M. Morcrette, J. M. Tarascon, C. Masquelier, Journal of The Electrochemical Society, 152 (2005) A913-A921.

[104] J. Yang, J. J. Xu, Journal of The Electrochemical Society, 153 (2006) A716-A723.

[105] A. V. Murugan, T. Muraliganth, A. Manthiram, Journal of The Electrochemical Society, 156 (2009) A79-A83.

[106] O. Garcia-Moreno, M. Alvarez-Vega, F. Garcia-Alvarado, J. Garcia-Jaca, J. Gallardo-Amores, M. Sanjuán, U. Amador, Chemistry of Materials, 13 (2001) 1570-1576.

[107] A. Yamada, S. C. Chung, K. Hinokuma, Journal of The Electrochemical Society, 148 (2001) A224-A229.

[108] H. Huang, S. C. Yin, L. S. Nazar, Electrochemical and Solid-State Letters, 4 (2001) A170-A172.

[109] X. L. Wu, L. Y. Jiang, F. F. Cao, Y. G. Guo, L. J. Wan, Advanced Materials, 21 (2009) 2710-2714.

[110] J. Molenda, J. Marzec, Functional Materials Letters 1 (2008) 97-104.

[111] L. Laffont, C. Delacourt, P. Gibot, M. Y. Wu, P. Kooyman, C. Masquelier, J. M. Tarascon, Chemistry of Materials, 18 (2006) 5520-5529.

[112] S. Y. Chung, J. T. Bloking, Y. M. Chiang, Nature Materials, 1 (2002) 123-128.

[113] D. Wang, H. Li, S. Shi, X. Huang, L. Chen, Electrochimica Acta, 50 (2005) 2955-2958.

[114] N. Meethong, Y. H. Kao, S. A. Speakman, Y. M. Chiang, Advanced Functional Materials, 19 (2009) 1060-1070.

[115] D. Arumugam, G. P. Kalaignan, P. Manisankar, Journal of Solid State Electrochemistry, 13 (2009) 301-307.

[116] S. T. Myung, S. Komaba, N. Kumagai, Journal of The Electrochemical Society, 148 (2001) A482-A489.

[117] G. Wang, S. Bewlay, S.A. Needham, H. Liu, R. Liu, V. Drozd, J. F. Lee, J. Chen, Journal of The Electrochemical Society, 153 (2006) A25-A31.

[118] C. Delacourt, C. Wurm, L. Laffont, J. B. Leriche, C. Masquelier, Solid State Ionics, 177 (2006) 333-341.

[119] H. Liu, C. Li, Q. Cao, Y. Wu, R. Holze, Journal of Solid State Electrochemistry, 12 (2008) 1017-1020.

[120] G. Wang, L. Yang, S. Bewlay, Y. Chen, H. K. Liu, J. H. Ahn, Journal of Power Sources, 146 (2005) 521-524.

[121] X. Zhou, F. Wang, Y. Zhu, Z. Liu, J. Mater. Chem., 21 (2011) 3353-3358.

[122] C. R. Sides, F. Croce, V. Y. Young, C. R. Martin, B. Scrosati, Electrochemical and Solid-State Letters, 8 (2005) A484-A487.

[123] G. Li, H. Azuma, M. Tohda, Electrochemical and Solid-State Letters, 5 (2002) A135-A137.

[124] C. Delacourt, P. Poizot, M. Morcrette, J. M. Tarascon, C. Masquelier, Chemistry of Materials, 16 (2004) 93-99.

[125] D. Choi, D. Wang, I. T. Bae, J. Xiao, Z. Nie, W. Wang, V. V. Viswanathan, Y. J. Lee, J. G. Zhang, G. L. Graff, Nano Letters, 10 (2010) 2799-2805.

[126] D. Wang, C. Ouyang, T. Drézen, I. Exnar, A. Kay, N. H. Kwon, P. Gouerec, J. H. Miners, M. Wang, M. Grätzel, Journal of The Electrochemical Society, 157 (2010) A225-A229.

[127] S. M. Oh, S. W. Oh, C. S. Yoon, B. Scrosati, K. Amine, Y. K. Sun, Advanced Functional Materials, 20 (2010) 3260-3265.

[128] D. Choi, J. Xiao, Y. J. Choi, J. S. Hardy, M. Vijayakumar, M. Bhuvaneswari, J. Liu, W. Xu, W. Wang, Z. Yang, Energy & Environmental Science, 4 (2011) 4560-4566.

[129] M. Pivko, M. Bele, E. Tchernychova, N. Z. Logar, R. Dominko, M. Gaberscek,

Chemistry of Materials, 24 (2012) 1041-1047.

[130] N. Kumagai, K. Tanno, T. Nakajima, N. Watanabe, Electrochimica Acta, 28 (1983) 17-22.

[131] D. Murphy, P. Christian, F. DiSalvo, J. Carides, Journal of The Electrochemical Society, 126 (1979) 497-499.

[132] M. S. Whittingham, Journal of The Electrochemical Society, 123 (1976) 315-320.

[133] N. A. Chernova, M. Roppolo, A. C. Dillon, M. S. Whittingham, Journal of Materials Chemistry, 19 (2009) 2526-2552.

[134] S. L. Chou, J. Z. Wang, J. Z. Sun, D. Wexler, M. Forsyth, H. K. Liu, D. R. MacFarlane, S. X. Dou, Chemistry of Materials, 20 (2008) 7044-7051.

[135] D. Yu, C. Chen, S. Xie, Y. Liu, K. Park, X. Zhou, Q. Zhang, J. Li, G. Cao, Energy & Environmental Science, 4 (2011) 858-861.

[136] M. E. Spahr, P. Stoschitzki-Bitterli, R. Nesper, O. Haas, P. Novák, Journal of The Electrochemical Society, 146 (1999) 2780-2783.

[137] V. Mohan, B. Hu, W. Qiu, W. Chen, Journal of Applied Electrochemistry, 39 (2009) 2001-2006.

[138] B. Li, Y. Xu, G. Rong, M. Jing, Y. Xie, Nanotechnology, 17 (2006) 2560.

[139] N. Pinna, M. Willinger, K. Weiss, J. Urban, R. Schlögl, Nano Letters, 3 (2003) 1131-1134.

[140] Z. Chen, V. Augustyn, J. Wen, Y. Zhang, M. Shen, B. Dunn, Y. Lu, Advanced Materials, 23 (2011) 791-795.

[141] A. Odani, V. G. Pol, S. V. Pol, M. Koltypin, A. Gedanken, D. Aurbach, Advanced Materials, 18 (2006) 1431-1436.

[142] M. Giorgetti, M. Berrettoni, W. H. Smyrl, Chemistry of Materials, 19 (2007) 5991-6000.

[143] F. Coustier, J. Hill, B.B. Owens, S. Passerini, W. H. Smyrl, Journal of The Electrochemical Society, 146 (1999) 1355-1360.

[144] Y. Xu, L. Zheng, C. Wu, F. Qi, Y. Xie, Chemistry-A European Journal, 17 (2011) 384-391.

[145] H. Li, P. He, Y. Wang, E. Hosono, H. Zhou, Journal of Materials Chemistry, 21 (2011) 10999-11009.

[146] Y. C. K. Chen-Wiegart, P. Shearing, Q. Yuan, A. Tkachuk, J. Wang, Electrochemistry Communications, 21 (2012) 58-61.

[147] T. Patey, S.H. Ng, R. Büchel, N. Tran, F. Krumeich, J. Wang, H.K. Liu, P. Novák, Electrochemical and Solid-State Letters, 11 (2008) A46-A50.

[148] Y. Shi, J. Z. Wang, S. L. Chou, D. Wexler, H. J. Li, K. Ozawa, H. K. Liu, Y. P. Wu, Nano Letters, 13 (2013) 4715-4720.

[149] M. S. Whittingham, Y. Song, S. Lutta, P. Y. Zavalij, N. A. Chernova, Journal of Materials Chemistry, 15 (2005) 3362-3379.

[150] M. Winter, J. O. Besenhard, M. E. Spahr, P. Novak, Advanced Materials, 10 (1998) 725-763.

[151] D. Aurbach, Journal of Power Sources, 89 (2000) 206-218.

[152] J. Besenhard, J. Yang, M. Winter, Journal of Power Sources, 68 (1997) 87-90.

[153] L. Dai, D. W. Chang, J. B. Baek, W. Lu, Small, 8 (2012) 1130-1166.

[154] N. A. Kaskhedikar, J. Maier, Advanced Materials, 21 (2009) 2664-2680.

[155] D. S. Su, R. Schlögl, ChemSusChem, 3 (2010) 136-168.

[156] H. Chang, H. Wu, Advanced Functional Materials, 23 (2013) 1984-1997.

[157] T. Kuila, A. K. Mishra, P. Khanra, N. H. Kim, J. H. Lee, Nanoscale, 5 (2013) 52-71.

[158] D. Aurbach, E. Zinigrad, Y. Cohen, H. Teller, Solid State Ionics, 148 (2002) 405-416.

[159] H. Ota, Y. Sakata, A. Inoue, S. Yamaguchi, Journal of The Electrochemical Society, 151

(2004) A1659-A1669.

[160] Y. Ein-Eli, Electrochemical and Solid-State Letters, 2 (1999) 212-214.

[161] D. M. Guldi, V. Sgobba, Chem. Commun., 47 (2010) 606-610.

[162] E. Frackowiak, F. Beguin, Carbon, 40 (2002) 1775-1787.

[163] E. T. Thostenson, Z. Ren, T. W. Chou, Composites Science and Technology, 61 (2001) 1899-1912.

[164] J. Zhao, A. Buldum, J. Han, J. P. Lu, Physical Review Letters, 85 (2000) 1706.

[165] R. S. Morris, B. G. Dixon, T. Gennett, R. Raffaelle, M. J. Heben, Journal of Power Sources, 138 (2004) 277-280.

[166] S. Y. Chew, S. H. Ng, J. Wang, P. Novák, F. Krumeich, S. L. Chou, J. Chen, H. K. Liu, Carbon, 47 (2009) 2976-2983.

[167] A. K. Geim, K. S. Novoselov, Nature Materials, 6 (2007) 183-191.

[168] K. Novoselov, A. K. Geim, S. Morozov, D. Jiang, M. K. I. Grigorieva, S. Dubonos, A. Firsov, Nature, 438 (2005) 197-200.

[169] W. S. Hummers, R. E. Offeman, Journal of the American Chemical Society, 80 (1958) 1339-1339.

[170] Y. Zhang, T. T. Tang, C. Girit, Z. Hao, M. C. Martin, A. Zettl, M. F. Crommie, Y. R. Shen, F. Wang, Nature, 459 (2009) 820-823.

[171] G. Wang, X. Shen, J. Yao, J. Park, Carbon, 47 (2009) 2049-2053.

[172] R. A. Huggins, Journal of Power Sources, 81 (1999) 13-19.

[173] C. K. Chan, H. Peng, G. Liu, K. McIlwrath, X. F. Zhang, R. A. Huggins, Y. Cui, Nature Nanotechnology, 3 (2007) 31-35.

[174] Y. Idota, T. Kubota, A. Matsufuji, Y. Maekawa, T. Miyasaka, Science, 276 (1997) 1395-1397.

[175] C. K. Chan, X. F. Zhang, Y. Cui, Nano Letters, 8 (2008) 307-309.

[176] M. R. Palacín, Chemical Society Reviews, 38 (2009) 2565-2575.

[177] J. Wolfenstine, Journal of Power Sources, 79 (1999) 111-113.

[178] A. R. Kamali, D.J. Fray, Journal of New Materials for Electrochemical Systems, 2 (2010) 147-160.

[179] Z. Huang, N. Geyer, P. Werner, J. De Boor, U. Gösele, Advanced Materials, 23 (2011) 285-308.

[180] J. Rath, Solar Energy Materials and Solar Cells, 76 (2003) 431-487.

[181] H. Y. Lee, Y. L. Kim, M. K. Hong, S. M. Lee, Journal of Power Sources, 141 (2005) 159-162.

[182] C. M. Park, J. H. Kim, H. Kim, H. J. Sohn, Chemical Society Reviews, 39 (2010) 3115-3141.

[183] H. Wu, G. Chan, J. W. Choi, Y. Yao, M. T. McDowell, S. W. Lee, A. Jackson, Y. Yang, L. Hu, Y. Cui, Nature Nanotechnology, 7 (2012) 310-315.

[184] M. H. Park, K. Kim, J. Kim, J. Cho, Advanced Materials, 22 (2010) 415-418.

[185] M. H. Park, Y. Cho, K. Kim, J. Kim, M. Liu, J. Cho, Angewandte Chemie, 123 (2011) 9821-9824.

[186] Y. J. Cho, C. H. Kim, H. S. Im, Y. Myung, H. S. Kim, S. H. Back, Y. R. Lim, C. S. Jung, D. M. Jang, J. Park, Physical Chemistry Chemical Physics, 15 (2013) 11691-11695.

[187] G. Cui, L. Gu, L. Zhi, N. Kaskhedikar, P. A. van Aken, K. Müllen, J. Maier, Advanced Materials, 20 (2008) 3079-3083.

[188] K. H. Seng, M. H. Park, Z. P. Guo, H. K. Liu, J. Cho, Angewandte Chemie, International Edition, 51 (2012) 5657-5661.

[189] M. S. Park, G. X. Wang, Y. M. Kang, D. Wexler, S. X. Dou, H. K. Liu, Angewandte Chemie, International Edition, 119 (2007) 764-767.

[190] Z. Wen, Q. Wang, Q. Zhang, J. Li, Advanced Functional Materials, 17 (2007) 2772-

2778.

[191] H. X. Zhang, C. Feng, Y. C. Zhai, K. L. Jiang, Q. Q. Li, S. S. Fan, Advanced Materials, 21 (2009) 2299-2304.

[192] Z. Wang, H. Zhang, N. Li, Z. Shi, Z. Gu, G. Cao, Nano Research, 3 (2010) 748-756.

[193] Y. Yu, C. H. Chen, Y. Shi, Advanced Materials, 19 (2007) 993-997.

[194] X. W. Lou, D. Deng, J. Y. Lee, L. A. Archer, Chemistry of Materials, 20 (2008) 6562-6566.

[195] X. M. Yin, C. C. Li, M. Zhang, Q. Y. Hao, S. Liu, L. B. Chen, T.H. Wang, The Journal of Physical Chemistry C, 114 (2010) 8084-8088.

[196] J. Liu, W. Li, A. Manthiram, Chemical Communications, 46 (2010) 1437-1439.

[197] Y. Wang, H. C. Zeng, J. Y. Lee, Advanced Materials, 18 (2006) 645-649.

[198] S. Han, B. Jang, T. Kim, S.M. Oh, T. Hyeon, Advanced Functional Materials, 15 (2005) 1845-1850.

[199] L. Ji, Z. Lin, B. Guo, A. J. Medford, X. Zhang, Chemistry-A European Journal, 16 (2010) 11543-11548.

[200] D. Wang, D. Choi, J. Li, Z. Yang, Z. Nie, R. Kou, D. Hu, C. Wang, L. V. Saraf, J. Zhang, ACS Nano, 3 (2009) 907-914.

[201] Y. Ren, Z. Liu, F. Pourpoint, A. R. Armstrong, C. P. Grey, P. G. Bruce, Angewandte Chemie, 124 (2012) 2206-2209.

[202] J. Xu, C. Jia, B. Cao, W. Zhang, Electrochimica Acta, 52 (2007) 8044-8047.

[203] K. Wang, M. Wei, M. A. Morris, H. Zhou, J. D. Holmes, Advanced Materials, 19 (2007) 3016-3020.

[204] J. Cabana, L. Monconduit, D. Larcher, M. R. Palacin, Advanced Materials, 22 (2010) E170-E192.

[205] C. Li, X. D. Lou, Chemical Communications, 47 (2011) 8061-8063.

[206] Y. Li, B. Tan, Y. Wu, Nano Letters, 8 (2008) 265-270.

[207] Y. Sun, S. Jiang, W. Bi, C. Wu, Y. Xie, Journal of Power Sources, 196 (2011) 8644-8650.

[208] Z. Yang, P. Cai, L. Chen, Y. Gu, L. Shi, A. Zhao, Y. Qian, Journal of Alloys and Compounds, 420 (2006) 229-232.

[209] K. Xu, Chemical Reviews, 104 (2004) 4303-4418.

[210] J. F. Oudenhoven, L. Baggetto, P. H. Notten, Advanced Energy Materials, 1 (2011) 10-33.

[211] K. Murata, S. Izuchi, Y. Yoshihisa, Electrochimica Acta, 45 (2000) 1501-1508.

[212] A. Manuel Stephan, European Polymer Journal, 42 (2006) 21-42.

[213] S. S. Zhang, Journal of Power Sources, 162 (2006) 1379-1394.

[214] M. Tatsumisago, M. Nagao, A. Hayashi, Journal of Asian Ceramic Societies, 1 (2013) 17-25.

[215] J. Song, Y. Wang, C. Wan, Journal of Power Sources, 77 (1999) 183-197.

[216] V. Koch, S. Brummer, Electrochimica Acta, 23 (1978) 55-62.

[217] K. I. Takata, M. Morita, Y. Matsuda, K. Matsui, Journal of The Electrochemical Society, 132 (1985) 126-128.

[218] J. Tarascon, D. Guyomard, Solid State Ionics, 69 (1994) 293-305.

[219] M. Ue, S. Mori, Journal of The Electrochemical Society, 142 (1995) 2577-2581.

[220] J. Foropoulos, D. D. DesMarteau, Inorganic Chemistry, 23 (1984) 3720-3723.

[221] R. Aroca, M. Nazri, G. Nazri, A. Camargo, M. Trsic, Journal of Solution Chemistry, 29 (2000) 1047-1060.

[222] R. Murugan, V. Thangadurai, W. Weppner, Angewandte Chemie, International Edition, 46 (2007) 7778-7781.

[223] K. Hayashi, Y. Nemoto, S. I. Tobishima, J. I. Yamaki, Electrochimica Acta, 44 (1999)

2337-2344.

[224] R. Imhof, P. Novák, Journal of The Electrochemical Society, 146 (1999) 1702-1706.

[225] R. Fong, U. von Sacken, J. Dahn, Journal of The Electrochemical Society, 137 (1990) 2009-2013.

[226] R. Yazami, Electrochimica Acta, 45 (1999) 87-97.

[227] S. Lux, I. Lucas, E. Pollak, S. Passerini, M. Winter, R. Kostecki, Electrochemistry Communications, 14 (2012) 47-50.

[228] G. J. Janz, M. R. Lorenz, Journal of The Electrochemical Society, 108 (1961) 1052-1058.

[229] A. J. Gmitter, I. Plitz, G. G. Amatucci, Journal of The Electrochemical Society, 159 (2012) A370-A379.

[230] I. Stassen, G. Hambitzer, Journal of Power Sources, 105 (2002) 145-150.

[231] B. Garcia, S. Lavallée, G. Perron, C. Michot, M. Armand, Electrochimica Acta, 49 (2004) 4583-4588.

[232] V. Baranchugov, E. Markevich, E. Pollak, G. Salitra, D. Aurbach, Electrochemistry Communications, 9 (2007) 796-800.

[233] V. Koch, L. Dominey, C. Nanjundiah, M. Ondrechen, Journal of The Electrochemical Society, 143 (1996) 798-803.

[234] J. Fuller, R. T. Carlin, R. A. Osteryoung, Journal of The Electrochemical Society, 144 (1997) 3881-3886.

[235] H. J. Ha, E. H. Kil, Y. H. Kwon, J. Y. Kim, C. K. Lee, S. Y. Lee, Energy & Environmental Science, 5 (2012) 6491-6499.

[236] E. Quartarone, P. Mustarelli, Chemical Society Reviews, 40 (2011) 2525-2540.

[237] O. Bohnke, Solid State Ionics, 179 (2008) 9-15.

[238] Y. Iriyama, C. R. Park, A Novel All-Solid-State Thin-Film-Type Lithium-Ion Battery

with In-Situ Prepared Electrode Active Materials, InTech Publishing, (2010) 75-91.

[239] F. Mizuno, A. Hayashi, K. Tadanaga, M. Tatsumisago, Advanced Materials, 17 (2005) 918-921.

[240] A. Glass, K. Nassau, T. Negran, Journal of Applied Physics, 49 (1978) 4808-4811.

[241] N. Ohta, K. Takada, I. Sakaguchi, L. Zhang, R. Ma, K. Fukuda, M. Osada, T. Sasaki, Electrochemistry Communications, 9 (2007) 1486-1490.

[242] J. Haruyama, K. Sodeyama, L. Han, K. Takada, Y. Tateyama, Chemistry of Materials, 26 (2014) 4248-4255.

[243] A. Manuel Stephan, K. Nahm, Polymer, 47 (2006) 5952-5964.

[244] G. Jiang, S. Maeda, Y. Saito, S. Tanase, T. Sakai, Journal of The Electrochemical Society, 152 (2005) A767-A773.

[245] A. A. Peterson, F. Vogel, R. P. Lachance, M. Fröling, M. J. Antal Jr, J. W. Tester, Energy & Environmental Science, 1 (2008) 32-65.

[246] H. Jacobs, J. A. Delcour, Journal of Agricultural and Food Chemistry, 46 (1998) 2895-2905.

[247] L. Noerochim, J. Z. Wang, D. Wexler, Z. Chao, H. K. Liu, Journal of Power Sources, 228 (2013) 198-205.

[248] A. Vadivel Murugan, T. Muraliganth, A. Manthiram, Electrochemistry Communications, 10 (2008) 903-906.

[249] S. R. Shi, M. E. Key, K. L. Kalra, Journal of Histochemistry & Cytochemistry, 39 (1991) 741-748.

[250] J. S. Wang, K. Matyjaszewski, Journal of the American Chemical Society, 117 (1995) 5614-5615.

[251] R. M. Carvalho, J. C. Pereira, M. Yoshiyama, D. H. Pashley, Operative Dentistry, 21 (1995) 17-24.

[252] E. Vivaldo-Lima, P. E. Wood, A. E. Hamielec, A. Penlidis, Industrial & Engineering Chemistry Research, 36 (1997) 939-965.

[253] D. P. Debecker, V. Hulea, P. H. Mutin, Applied Catalysis A: General, 451 (2013) 192-206.

[254] R. Ciriminna, A. Fidalgo, V. Pandarus, F.o. Béland, L.M. Ilharco, M. Pagliaro, Chemical Reviews, 113 (2013) 6592-6620.

[255] C. J. Brinker, G.W. Scherer, Sol-gel science: the physics and chemistry of sol-gel processing, Gulf Professional Publishing, 1990.

[256] D. Gong, C.A. Grimes, O.K. Varghese, W. Hu, R. Singh, Z. Chen, E. C. Dickey, Journal of Materials Research, 16 (2001) 3331-3334.

[257] Q. Cai, M. Paulose, O. K. Varghese, C. A. Grimes, Journal of Materials Research, 20 (2005) 230-236.

[258] J. M. Macak, H. Tsuchiya, P. Schmuki, Angewandte Chemie, International Edition, 44 (2005) 2100-2102.

[259] C. Weidenthaler, Nanoscale, 3 (2011) 792-810.

[260] S. Brunauer, P. H. Emmett, E. Teller, Journal of the American Chemical Society, 60 (1938) 309-319.

[261] G. Du, Nanostructured anode materials for lithium-ion batteries，University of Wollongong Thesis Collection, (2011).

[262] M. E. Orazem, B. Tribollet, Electrochemical impedance spectroscopy, John Wiley & Sons, 2011.

[263] M. J. Lindsay, Data analysis and anode materials for lithium ion batteries，University of Wollongong Thesis Collection, (2004).

[264] R. Zhang, Y. Zhang, K. Zhu, F. Du, Q. Fu, X. Yang, Y. Wang, X. Bie, G. Chen, Y. Wei, ACS Applied Materials & Interfaces, 6 (2014) 12523-12530.

[265] M. S. Islam, C. A. Fisher, Chemical Society Reviews, 43 (2014) 185-204.

[266] D. Luo, G. Li, C. Fu, J. Zheng, J. Fan, Q. Li, L. Li, Advanced Energy Materials, (2014).

[267] X. Hao, X. Lin, W. Lu, B. M. Bartlett, ACS Applied Materials & Interfaces, (2014).

[268] S. Mishra, G. Ceder, Physical Review B, 59 (1999) 6120.

[269] Y. Xia, Y. Zhou, M. Yoshio, Journal of The Electrochemical Society, 144 (1997) 2593-2600.

[270] M. J. Lee, S. Lee, P. Oh, Y. Kim, J. Cho, Nano Letters, 14 (2014) 993-999.

[271] G. A. Nazri, G. Pistoia, Lithium batteries: science and technology, Springer Science & Business, 2008.

[272] O. K. Park, Y. Cho, S. Lee, H. C. Yoo, H. K. Song, J. Cho, Energy & Environmental Science, 4 (2011) 1621-1633.

[273] M. Aubrey, R. Ameloot, B. M. Wiers, J. R. Long, Energy & Environmental Science, 7 (2014) 667-671.

[274] N. Ohta, K. Takada, L. Zhang, R. Ma, M. Osada, T. Sasaki, Advanced Materials, 18 (2006) 2226-2229.

[275] J. Gnanaraj, V. Pol, A. Gedanken, D. Aurbach, Electrochemistry Communications, 5 (2003) 940-945.

[276] S. T. Myung, K. Izumi, S. Komaba, Y. K. Sun, H. Yashiro, N. Kumagai, Chemistry of Materials, 17 (2005) 3695-3704.

[277] Y. Fan, J. Wang, Z. Tang, W. He, J. Zhang, Electrochimica Acta, 52 (2007) 3870-3875.

[278] S. K. Hu, G. H. Cheng, M. Y. Cheng, B. J. Hwang, R. Santhanam, Journal of Power Sources, 188 (2009) 564-569.

[279] Z. J. Zhang, J. Z. Wang, S. L. Chou, H. K. Liu, K. Ozawa, H. J. Li, Electrochimica Acta, 108 (2013) 820-826.

[280] R. Gangopadhyay, A. De, Chemistry of Materials, 12 (2000) 608-622.

[281] S. H. Ng, J. Wang, D. Wexler, K. Konstantinov, Z. P. Guo, H. K. Liu, Angewandte Chemie, International Edition, 45 (2006) 6896-6899.

[282] Y. Shi, S. L. Chou, J. Z. Wang, D. Wexler, H. J. Li, H. K. Liu, Y. Wu, Journal of Materials Chemistry, 22 (2012) 16465-16470.

[283] H. K. Noh, H. S. Park, H. Y. Jeong, S. U. Lee, H. K. Song, Angewandte Chemie, 126 (2014) 5159-5163.

[284] Z. Ma, G. Shao, Y. Fan, G. Wang, J. Song, T. Liu, ACS Applied Materials & Interfaces, (2014).

[285] Y. Xia, T. Sakai, T. Fujieda, X. Yang, X. Sun, Z. Ma, J. McBreen, M. Yoshio, Journal of The Electrochemical Society, 148 (2001) A723-A729.

[286] C. X. Guo, M. Wang, T. Chen, X. W. Lou, C. M. Li, Advanced Energy Materials, 1 (2011) 736-741.

[287] J. Tarascon, W. McKinnon, F. Coowar, T. Bowmer, G. Amatucci, D. Guyomard, Journal of The Electrochemical Society, 141 (1994) 1421-1431.

[288] M. R. Laskar, D. N. Nath, L. Ma, E. W. Lee II, C. H. Lee, T. Kent, Z. Yang, R. Mishra, M. A. Roldan, J. C. Idrobo, Applied Physics Letters, 104 (2014) 092104.

[289] Y. Gao, J. Dahn, Journal of The Electrochemical Society, 143 (1996) 100-114.

[290] J. Xu, S. L. Chou, M. Avdeev, M. Sale, H. K. Liu, S. X. Dou, Electrochimica Acta, (2012).

[291] J. Tarascon, D. Guyomard, Electrochimica Acta, 38 (1993) 1221-1231.

[292] C. Masquelier, M. Tabuchi, K. Ado, R. Kanno, Y. Kobayashi, Y. Maki, O. Nakamura, J. B. Goodenough, Journal of Solid State Chemistry, 123 (1996) 255-266.

[293] Y. Xia, M. Yoshio, Journal of The Electrochemical Society, 143 (1996) 825-833.

[294] F. Cheng, H. Wang, Z. Zhu, Y. Wang, T. Zhang, Z. Tao, J. Chen, Energy & Environmental Science, 4 (2011) 3668-3675.

[295] H. Chan, J. Duh, S. Sheen, Journal of Power Sources, 115 (2003) 110-118.

[296] R. Jiang, Y. Huang, D. Jia, L. Wang, L. Wang, Journal of The Electrochemical Society, 154 (2007) A698-A702.

[297] H. Liu, F. C. Strobridge, O. J. Borkiewicz, K. M. Wiaderek, K. W. Chapman, P. J. Chupas, C. P. Grey, Science, 344 (2014) 1252817.

[298] Y. Sun, L. Zhao, H. Pan, X. Lu, L. Gu, Y. . Hu, H. Li, M. Armand, Y. Ikuhara, L. Chen, Nature Communications, 4 (2013) 1870.

[299] S. Mukerjee, T. Thurston, N. Jisrawi, X. Yang, J. McBreen, M. Daroux, X. Xing, Journal of The Electrochemical Society, 145 (1998) 466-472.

[300] J. E. Greedan, Functional Oxides, (2010) 41-117.

[301] E. Barsoukov, J. R. Macdonald, Impedance Spectroscopy: Theory, Experiment, and Applications, Wiley, 2005.

[302] N. Takami, A. Satoh, M. Hara, T. Ohsaki, Journal of The Electrochemical Society, 142 (1995) 371-379.

[303] S. L. Chou, J. Z. Wang, H. K. Liu, S. X. Dou, The Journal of Physical Chemistry C, 115 (2011) 16220-16227.

[304] A. J. Bard, L. R. Faulkner, Hoboken: Wiley and Sons, (2001).

[305] B. Li, L. Xing, M. Xu, H. Lin, W. Li, Electrochemistry Communications, 34 (2013) 48-51.

[306] D. H. Jang, Y. J. Shin, S. M. Oh, Journal of The Electrochemical Society, 143 (1996) 2204-2211.

[307] J. Cabana, M. Casas-Cabanas, F. O. Omenya, N. A. Chernova, D. Zeng, M. S. Whittingham, C. P. Grey, Chemistry of Materials, 24 (2012) 2952-2964.

[308] T. F. Yi, Y. Xie, M. F. Ye, L. J. Jiang, R. S. Zhu, Y. R. Zhu, Ionics, 17 (2011) 383-389.

[309] K. Edström, T. Gustafsson, J. O. Thomas, Electrochimica Acta, 50 (2004) 397-403.

[310] H. Duncan, Y. Abu-Lebdeh, I. J. Davidson, Journal of The Electrochemical Society, 157 (2010) A528-A535.

[311] D. Montinaro, V. Sglavo, M. Bertoldi, T. Zandonella, A. Arico, M. Lo Faro, V. Antonucci, Solid State Ionics, 177 (2006) 2093-2097.

[312] G. Alva, C. Kim, T. Yi, J. Cabana, in: Meeting Abstracts, The Electrochemical Society, 2013, pp. 993-993.

[313] Y. K. Sun, K. J. Hong, J. Prakash, K. Amine, Electrochemistry Communications, 4 (2002) 344-348.

[314] Y. Fan, J. Wang, Z. Tang, W. He, J. Zhang, Electrochimica Acta, 52 (2007) 3870-3875.

[315] M. Nagino, T. Takada, M. Miyazaki, S. Miyakawa, K. Tsukada, S. Kondo, J. Furuse, H. Saito, T. Tsuyuguchi, T. Yoshikawa, Journal of Hepato-Biliary-Pancreatic Surgery, 15 (2008) 25-30.

[316] A. Sakuda, H. Kitaura, A. Hayashi, K. Tadanaga, M. Tatsumisago, Journal of The Electrochemical Society, 156 (2009) A27-A32.

[317] X. W. Gao, C. Q. Feng, S. L. Chou, J. Z. Wang, J. Z. Sun, M. Forsyth, D. R. MacFarlane, H. K. Liu, Electrochimica Acta, 101 (2013) 151-157.

[318] Z. Zhang, S. L. Chou, Q. F. Gu, H. K. Liu, H. Li, K. Ozawa, J. Z. Wang, ACS Applied Materials & Interfaces, 6 (2014) 22155-22165.

[319] X. Zhang, F. Cheng, J. Yang, J. Chen, Nano Letters, 13 (2013) 2822-2825.

[320] J. Yang, X. Han, X. Zhang, F. Cheng, J. Chen, Nano Research, 6 (2013) 679-687.

[321] N. Amdouni, K. Zaghib, F. Gendron, A. Mauger, C. Julien, Ionics, 12 (2006) 117-126.

[322] X. Liu, K. Kitamura, Q. Yu, J. Xu, M. Osada, N. Takahiro, J. Li, G. Cao, Science and Technology of Advanced Materials, 14 (2013) 055011.

[323] A. Bartasyte, V. Plausinaitiene, A. Abrutis, S. Stanionyte, S. Margueron, P. Boulet, T. Kobata, Y. Uesu, J. Gleize, Journal of Physics: Condensed Matter, 25 (2013) 205901.

[324] J. C. Arrebola, A. Caballero, M. Cruz, L. Hernán, J. Morales, E. R. Castellón, Advanced Functional Materials, 16 (2006) 1904-1912.

[325] Y. Lee, Y. Sun, S. Ota, T. Miyashita, M. Yoshio, Electrochemistry Communications, 4 (2002) 989-994.

[326] J. Xiao, X. Chen, P. V. Sushko, M. L. Sushko, L. Kovarik, J. Feng, Z. Deng, J. Zheng, G. L. Graff, Z. Nie, Advanced Materials, 24 (2012) 2109-2116.

[327] H. Wu, I. Belharouak, A. Abouimrane, Y. Sun, K. Amine, Journal of Power Sources, 195 (2010) 2909.

[328] G. Zhao, Y. Lin, T. Zhou, Y. Lin, Y. Huang, Z. Huang, Journal of Power Sources, 215 (2012) 63-68.

[329] L. Zhou, D. Zhao, X. D. Lou, Angewandte Chemie, 124 (2012) 243-245.

[330] J. H. Kim, A. Huq, M. Chi, N. P. Pieczonka, E. Lee, C.A. Bridges, M. M. Tessema, A. Manthiram, K. A. Persson, B. R. Powell, Chemistry of Materials, 26 (2014) 4377-4386.

[331] M. R. Jo, Y. I. Kim, Y. Kim, J. S. Chae, K. C. Roh, W. S. Yoon, Y. M. Kang, ChemSusChem, 7 (2014) 2248-2254.

[332] W. Chen, R. Du, H. Liang, Z. Zhou, L. Shao, J. Shu, Z. Wang, Journal of Power Sources, 272 (2014) 622-628.

[333] M. Mohamedi, M. Makino, K. Dokko, T. Itoh, I. Uchida, Electrochimica Acta, 48 (2002) 79-84.

[334] R. Alcantara, M. Jaraba, P. Lavela, J. Tirado, Journal of Electroanalytical Chemistry, 566 (2004) 187-192.

[335] Y. Lee, S. Sato, Y. Sun, K. Kobayakawa, Y. Sato, Journal of Power Sources, 119 (2003) 285-289.

[336] J. Li, J. Li, J. Luo, L. Wang, X. He, International Journal of Electrochemical Science, 6 (2011) 1550-1561.

[337] R. Kanno, T. Shirane, Y. Inaba, Y. Kawamoto, Journal of Power Sources, 68 (1997) 145-152.

[338] M.M. Rahman, J. Z. Wang, M. F. Hassan, S. Chou, Z. Chen, H. K. Liu, Energy & Environmental Science, 4 (2011) 952-957.

[339] C. Delmas, G. Prado, A. Rougier, E. Suard, L. Fournès, Solid State Ionics, 135 (2000) 71-79.

[340] J. Morales, J. Santos-Pena, Electrochemistry Communications, 9 (2007) 2116-2120.

[341] Y. Sakurai, H. Arai, S. Okada, J. I. Yamaki, Journal of Power Sources, 68 (1997) 711-715.

[342] J. Morales, J. Santos-Peña, R. Trócoli, S. Franger, E. Rodríguez-Castellón, Electrochimica Acta, 53 (2008) 6366-6371.

[343] M. Hirayama, H. Tomita, K. Kubota, H. Ido, R. Kanno, Materials Research Bulletin, 47 (2012) 79-84.

[344] B. Wang, H. Wu, L. Yu, R. Xu, T. T. Lim, Advanced Materials, 24 (2012) 1111-1116.

[345] J. Yue, X. Jiang, Y. V. Kaneti, A. Yu, Journal of Colloid and Interface Science, 367 (2012) 204-212.

[346] T. Sugimoto, Y. Shimotsuma, H. Itoh, Powder Technology, 96 (1998) 85-89.

[347] S. Musić, S. Krehula, S. Popović, Materials Letters, 58 (2004) 444-448.

[348] H. Morimoto, K. Takeno, Y. Uozumi, K. I. Sugimoto, S. I. Tobishima, Journal of Power Sources, 196 (2011) 6512-6516.

[349] A. H. Gemeay, H. Nishiyama, S. Kuwabata, H. Yoneyama, Journal of The Electrochemical Society, 142 (1995) 4190-4195.

[350] J. Harreld, H. Wong, B. Dave, B. Dunn, L. Nazar, Journal of Non-Crystalline Solids, 225 (1998) 319-324.

[351] G. Wang, L. Yang, Y. Chen, J. Wang, S. Bewlay, H. Liu, Electrochimica Acta, 50

(2005) 4649-4654.

[352] S. Y. Chew, C. Feng, S. H. Ng, J. Wang, Z. Guo, H. Liu, Journal of The Electrochemical Society, 154 (2007) A633-A637.

[353] J. Wang, J. Chen, K. Konstantinov, L. Zhao, S. H. Ng, G. Wang, Z. Guo, H. K. Liu, Electrochimica Acta, 51 (2006) 4634-4638.

[354] L. Yuan, J. Wang, S. Y. Chew, J. Chen, Z. Guo, L. Zhao, K. Konstantinov, H. K. Liu, Journal of Power Sources, 174 (2007) 1183-1187.

[355] C. Zhong, J. Wang, Z. Chen, H. Liu, The Journal of Physical Chemistry C, 115 (2011) 25115-25120.

[356] O. Jarjayes, P. Fries, C. Bidan, Synthetic Metals, 69 (1995) 343-344.

[357] I. Sultana, M. Rahman, J. Wang, C. Wang, G. G. Wallace, H. K. Liu, Solid State Ionics, 215 (2012) 29-35.

[358] H. T. Ham, Y. S. Choi, N. Jeong, I. J. Chung, Polymer, 46 (2005) 6308-6315.

[359] N. V. Blinova, J. Stejskal, M. Trchová, J. Prokeš, M. Omastová, European Polymer Journal, 43 (2007) 2331-2341.

[360] T. Osaka, K. Naoi, S. Ogano, S. Nakamura, Journal of The Electrochemical Society, 134 (1987) 2096-2102.

[361] H. Liu, Q. Cao, L. J. Fu, C. Li, Y. Wu, H. Wu, Electrochemistry Communications, 8 (2006) 1553-1557.

[362] S. L. Chou, X. W. Gao, J. Z. Wang, D. Wexler, Z. X. Wang, L. Q. Chen, H. K. Liu, Dalton Transactions, 40 (2011) 12801-12807.

[363] Q. Gong, Y. S. He, Y. Yang, X. Z. Liao, Z. F. Ma, Journal of Solid State Electrochemistry, 16 (2012) 1383-1388.

[364] Z. Guo, J. Wang, H. Liu, S. Dou, Journal of Power Sources, 146 (2005) 448-451.

[365] M. Rahman, J. Z. Wang, N. H. Idris, Z. Chen, H. Liu, Electrochimica Acta, 56 (2010)

693-699.

[366] C. V. Subba Reddy, E. H. Walker Jr, S. Wicker Sr, Q.L. Williams, R. R. Kalluru, Current Applied Physics, 9 (2009) 1195-1198.

[367] Y. Shi, S. L. Chou, J. Z. Wang, H. J. Li, H. K. Liu, Y. P. Wu, Journal of Power Sources, 244 (2013) 684-689.

[368] Q. Zhao, L. Jiao, W. Peng, H. Gao, J. Yang, Q. Wang, H. Du, L. Li, Z. Qi, Y. Si, Journal of Power Sources, 199 (2012) 350-354.

[369] A. Kannan, A. Manthiram, Solid State Ionics, 159 (2003) 265-271.

[370] H. Qiao, X. Zhu, Z. Zheng, L. Liu, L. Zhang, Electrochemistry Communications, 8 (2006) 21-26.

[371] F. Zhang, S. Passerini, B. B. Owens, W. H. Smyrl, Electrochemical and Solid-State Letters, 4 (2001) A221-A223.

[372] A. R. Armstrong, C. Lyness, P. M. Panchmatia, M. S. Islam, P. G. Bruce, Nature Materials, 10 (2011) 223-229.

[373] Y. Wang, H. J. Zhang, A. S. Admar, J. Luo, C. C. Wong, A. Borgna, J. Lin, RSC Advances, 2 (2012) 5748-5753.

[374] H. Li, P. Balaya, J. Maier, Journal of The Electrochemical Society, 151 (2004) A1878-A1885.

[375] P. G. Bruce, B. Scrosati, J. M. Tarascon, Angewandte Chemie, International Edition, 47 (2008) 2930-2946.

[376] B. Oschmann, D. Bresser, M. N. Tahir, K. Fischer, W. Tremel, S. Passerini, R. Zentel, Macromolecular Rapid Communications, 34 (2013) 1693-1700.

[377] Y. Tao, H. Kanoh, L. Abrams, K. Kaneko, Chemical Reviews, 106 (2006) 896-910.

[378] Y. Wang, L. Yin, O. Palchik, Y. R. Hacohen, Y. Koltypin, A. Gedanken, Langmuir, 17 (2001) 4131-4133.

[379] B. Lee, D. Lu, J. N. Kondo, K. Domen, Journal of the American Chemical Society, 124 (2002) 11256-11257.

[380] S. J. Bao, Q. L. Bao, C. M. Li, Z. L. Dong, Electrochemistry Communications, 9 (2007) 1233-1238.

[381] X. Huang, X. Qi, F. Boey, H. Zhang, Chemical Society Reviews, 41 (2012) 666-686.

[382] L. Y. Jiang, S. Xin, X. L. Wu, H. Li, Y. G. Guo, L. J. Wan, Journal of Materials Chemistry, 20 (2010) 7565-7569.

[383] Y. Wang, H. J. Zhang, L. Lu, L.P. Stubbs, C. C. Wong, J. Lin, ACS Nano, 4 (2010) 4753-4761.

[384] P. Wu, N. Du, H. Zhang, C. Zhai, D. Yang, ACS Applied Materials & Interfaces, 3 (2011) 1946-1952.

[385] Y. Zhang, M. Fan, X. Liu, C. Huang, H. Li, European Journal of Inorganic Chemistry, 2012 (2012) 1650-1659.

[386] L. Zeng, C. Zheng, J. Xi, H. Fei, M. Wei, Carbon, 62 (2013) 382-388.

[387] X. Sun, J. Liu, Y. Li, Chemistry of Materials, 18 (2006) 3486-3494.

[388] J. Wang, S. Chew, Z. Zhao, S. Ashraf, D. Wexler, J. Chen, S. Ng, S. Chou, H. Liu, Carbon, 46 (2008) 229-235.

[389 C. Lu, L. Qi, J. Yang, X. Wang, D. Zhang, J. Xie, J. Ma, Advanced Materials, 17 (2005) 2562-2567.

[390] L. W. Zhang, H. B. Fu, Y. F. Zhu, Advanced Functional Materials, 18 (2008) 2180-2189.

[391] P. Simon, Y. Gogotsi, Nature Materials, 7 (2008) 845-854.

[392] B. Conway, Scientific Fundamentals and Technological Applications, Kluwer Academic/Plenum Publishers, New York, (1999).

[393] J. Wang, Y. Bai, M. Wu, J. Yin, W. Zhang, Journal of Power Sources, 191 (2009) 614-

618.

[394] D. Nan, J. G. Wang, Z. H. Huang, L. Wang, W. Shen, F. Kang, Electrochemistry Communications, 34 (2013) 52-55.

[367] Y. Wang, M. Wu, W. Zhang, Electrochimica Acta, 53 (2008) 7863-7868.

[395] G. F. Ortiz, I. Hanzu, P. Knauth, P. Lavela, J. L. Tirado, T. Djenizian, Electrochimica Acta, 54 (2009) 4262-4268.

[396] J. S. Kim, K. Kim, W. Cho, W.H. Shin, R. Kanno, J.W. Choi, Nano Letters, 12 (2012) 6358-6365.

[397] P. M. Dziewoński, M. Grzeszczuk, Electrochimica Acta, 55 (2010) 3336-3347.

[398] F. Wu, X. Li, Z. Wang, H. Guo, L. Wu, X. Xiong, X. Wang, Journal of Alloys and Compounds, 509 (2011) 3711-3715.

[399] Z. Sun, J. H. Kim, Y. Zhao, F. Bijarbooneh, V. Malgras, Y. Lee, Y. M. Kang, S. X. Dou, Journal of the American Chemical Society, 133 (2011) 19314-19317.

[400] Z. Liu, V. Subramania, M. Misra, The Journal of Physical Chemistry C, 113 (2009) 14028-14033.

[401] Y. Liang, Z. Cui, S. Zhu, Y. Liu, X. Yang, Journal of Catalysis, 278 (2011) 276-287.

[402] Y. Ohsaki, N. Masaki, T. Kitamura, Y. Wada, T. Okamoto, T. Sekino, K. Niihara, S. Yanagida, Physical Chemistry Chemical Physics, 7 (2005) 4157-4163.

[403] J. Liao, S. Lin, L. Zhang, N. Pan, X. Cao, J. Li, ACS Applied Materials & Interfaces, 4 (2011) 171-177.

[404] W. He, J. Qiu, F. Zhuge, X. Li, J. H. Lee, Y. D. Kim, H. K. Kim, Y. H. Hwang, Nanotechnology, 23 (2012) 225602.

[405] Z. Liu, Q. Zhang, T. Zhao, J. Zhai, L. Jiang, Journal of Materials Chemistry, 21 (2011) 10354-10358.

[406] Y. B. Xie, X. Li, Materials Chemistry and Physics, 95 (2006) 39-50.

[407] Z. Wei, Z. Liu, R. Jiang, C. Bian, T. Huang, A. Yu, Journal of Solid State Electrochemistry, 14 (2010) 1045-1050.

[408] G. K. Mor, K. Shankar, M. Paulose, O. K. Varghese, C. A. Grimes, Nano Letters, 6 (2006) 215-218.

[409] G. Wang, B. Wang, X. Wang, J. Park, S. Dou, H. Ahn, K. Kim, Journal of Materials Chemistry, 19 (2009) 8378-8384.

[410] F. S. Ke, L. Huang, H. H. Jiang, H. B. Wei, F. Z. Yang, S. G. Sun, Electrochemistry Communications, 9 (2007) 228-232.

[411] Q. Y. Zeng, M. Xi, W. Xu, X. J. Li, Materials and Corrosion, 64 (2013) 1001-1006.

[412] O. K. Varghese, D. Gong, M. Paulose, C. A. Grimes, E. C. Dickey, Journal of Materials Research, 18 (2003) 156-165.

[413] F. Bonino, L. Busani, M. Lazzari, M. Manstretta, B. Rivolta, B. Scrosati, Journal of Power Sources, 6 (1981) 261-270.

[414] H. Zhang, G. Li, L. An, T. Yan, X. Gao, H. Zhu, The Journal of Physical Chemistry C, 111 (2007) 6143-6148.

[415] C. Lai, G. Li, Y. Dou, X. Gao, Electrochimica Acta, 55 (2010) 4567-4572.

[389] B. L. He, B. Dong, H. L. Li, Electrochemistry Communications, 9 (2007) 425-430.

[416] N. Takami, A. Satoh, M. Hara, T. Ohsaki, Journal of The Electrochemical Society, 142 (1995) 2564-2571.

[417] A. J. Bard, L. R. Faulkner, Electrochemical Methods: Fundamentals and Applications, Wiley New York, 1980.

[418] D. Deng, M. G. Kim, J. Y. Lee, J. Cho, Energy & Environmental Science, 2 (2009) 818-837.

Appendix

Appendix A: List of Publication

1] **Z. J. Zhang,** J. Z. Wang,* S. L. Chou, H. K. Liu, K. Ozawa, H. J. Li,* Polypyrrole-coated α-$LiFeO_2$ nanocomposite with enhanced electrochemical properties for lithium-ion batteries, *Electrochimica Acta*, 2013, 108, 820-826.

[2] **Z. J. Zhang,** Q. Y. Zeng, S. L. Chou, X. J. Li, H. J. Li,* K. Ozawa, H. K. Liu, K. Ozawa, J. Z. Wang,* Tuning three-dimensional TiO_2 nanotube electrode to achieve high utilization of Ti substrate for lithium storage, *Electrochimica Acta*, 2014, 133, 570-577.

[3] **Z. J. Zhang,** S. L. Chou, Q. F. Gu, H. K. Liu, H. J. Li,* K. Ozawa , J. Z. Wang,* Enhancing the High Rate Capability and Cycling Stability of $LiMn_2O_4$ by a Solid-State-Electrolyte LiNbO3 Layer, *ACS applied materials & interfaces*, 2014, 6(24), 22155-22165.

[4] **Z. J. Zhang**, Y. X. Wang, S. L. Chou, H. J. Li,* H. K. Liu, J. Z. Wang,* Rapid synthesis of α-Fe_2O_3/rGO nanocomposites as superior anodes for sodium-ion batteries by microwave autoclave strategy, *Journal of Power Sources*, 2015, 280, 107-113.

[5] **Z. J. Zhang,** S. L. Chou, Q. F. Gu, J. Wang, J. F. Li, H. K. Liu, H. J. Li,* J. Z. Wang,* Solid-state electrolyte $LiNbO_3$ Additive Improving Cycling and Rate Abilities of High-Voltage $LiNi_{0.5}Mn_{1.5}O_4$ Cathode Material, To Be Submitted.

[6] Y. Shi, **Z. J. Zhang**, D. Wexler, S. L. Chou, J. Gao, H. D. Abruña, H. J. Li, H. K. Liu, Y. P. Wu, J. Z. Wang, Facile synthesis of porous V2O3/C composites as lithium storage material with enhanced capacity and good rate capability, *Journal of Power Sources*, 2015, 275, 392-398.

[7] J. F. Li, J. Z. Wang,* X. Liang, **Z. J, Zhang**, H. K. Liu, Y. T. Qian, S. L. Xiong, Hollow

$MnCo_2O_4$ Submicrospheres with Multilevel Interiors: From Mesoporous Spheres to Yolk-in-Double-Shell Structures, *ACS applied materials & interfaces*, 2014, 6 (1), 24-30.

[8] X. Li, J. Xu, L. Mei, **Z. J. Zhang**, C. Cui, H. K. Liu, J. Ma,* S. X. Dou, Electrospinning of Crystalline MoO_3@C Nanofibers for High-Rate Lithium Storage, *Journal of Materials Chemistry A*, 2015, 3, 3257-3260.

[9] Z. D. Zhang, R. H. Fan,* Z. C. Shi, K. L. Yan, **Z. J. Zhang**, X. L. Wang,* S. X. Dou, Microstructure and metal-dielectric transition behaviour in a percolative Al_2O_3-Fe composite via selective reduction; *Rsc Advances*, 2013, 3, 26110-26115.

Appendix B: Received Awards

1. International Postgraduate Tuition Award (IPTA), 2011-2014, University of Wollongong;

2. Chinese Government Scholarship, 2011-2014, China Scholarship Council;

3. Excellent Research Top-Up Award, 2014, University of Wollongong;

4. Student Travel Grant to attend international conference, 2014, University of Wollongong;

5. Postgraduate Student Merit Award, 2014, University of Wollongong.